EXPERIMENTAL CHARACTERIZATION OF VISCOELASTIC FLOW INSTABILITIES

by

Jeffrey Alan Byars

B. S. Chemical Engineering
Northwestern University, 1989

Submitted to the Department of Chemical Engineering
in partial fulfillment of the requirements for the degree of

DOCTOR OF PHILOSOPHY IN CHEMICAL ENGINEERING

at the

MASSACHUSETTS INSTITUTE OF TECHNOLOGY

February 1996

Author ....
Department of Chemical Engineering
November 9, 1995

Certified by ....
Robert C. Armstrong
Professor of Chemical Engineering
Thesis Supervisor

Certified by ....
Robert A. Brown
Professor of Chemical Engineering
Thesis Supervisor

Accepted by ....
Robert E. Cohen
Graduate Officer, Department of Chemical Engineering

Experimental Characterization of Viscoelastic Flow Instabilities

by

Jeffrey Alan Byars

Submitted to the Department of Chemical Engineering
on November 9, 1995 in Partial Fulfillment
of the Requirements for the Degree of
Doctor of Philosophy in Chemical Engineering

Abstract

The effects of elasticity on flow stability were studied in three types of test geometries that model more complex polymer processing operations: *1*) the rotational flow between parallel plates or a cone and a plate, *2*) the stagnation flow behind a cylinder or other obstacle confined in a channel and *3*) superposed plane Poiseuille flow of two fluids in a channel. Laser Doppler velocimetry (LDV) and digital image analysis were used to quantitatively characterize the onset conditions and the spatial and temporal characteristics of the instabilities. Experimental stability diagrams were constructed to show the dependence of the onset conditions on geometric aspect ratios and the elasticity of the flow as measured by the Deborah number, *De*, which is the ratio of a characteristic timescale of the fluid to a characteristic timescale of the flow. The experimental results are compared to the predictions of a linear stability analysis as a means of testing the ability of constitutive equations to determine the onset and form of elastic instabilities. Semidilute solution of a high molecular weight polyisobutylene in a solvent of tetradecane and a low molecular weight polybutene were used as test fluids. These 'Boger' fluids are characterized by their nearly constant viscosity and high elasticity.

In the parallel plate geometry, the flow was unstable to a spiral disturbance consisting of nested Archimedean spirals that occupied only an annular region between the plates due to the shear-rate dependence of the normal stress coefficient. The wavelength and radial extent of the spiral cells were found to scale with the separation between the plates. A similar instability occurred in the cone-and-plate geometry, but the lack of a characteristic length scale and the uniform shear rate throughout the gap resulted in a logarithmic spiral that filled the entire gap.

LDV was used to characterized the wake instability for flow past a cylinder confined in a channel for a wide range of cylinder radius to channel half-height ratios. The instability consisted of periodic variations in the streamwise velocity along the axis of the cylinder. The critical Deborah number increased for small aspect ratios, and the shearing flow between the cylinder and the channel walls did not determine the onset conditions for large aspect ratios. The wavelength of the instability was comparable to the cylinder radius, but the ratio of the wavelength to the radius increased for small aspect ratios. A qualitatively similar instability was observed for a geometry without an upstream stagnation point, and no instability was found for an axisymmetric stagnation flow.

Image analysis of experiments in the superposed plane Poiseuille flow geometry showed that the system was capable of determining the stability of the interface for a wide range of experimental conditions. Although an experimental stability diagram has not been established for this system, present results show that quantitative measures of the growth rate can be obtained.

Thesis Supervisors:	Robert C. Armstrong Professor Chemical Engineering	Robert A. Brown Professor Chemical Engineering

Acknowledgements

I would like to thank my thesis advisors, Professors Bob Armstrong and Bob Brown, for their guidance and support during this research. They have helped me learn to understand and appreciate polymer fluid mechanics and rheology, and to conscientiously avoid split infinitives. Thank you also to Professors Edward Merrill and Greg Rutledge for serving on my thesis committee. This work has also benefited greatly from my collaboration with Gareth McKinley and Alp Öztekin. None of this would have been possible without Arline, Nancy, Janet and Elaine, who keep things running so smoothly. I would also like to acknowledge the National Science Foundation and 3M for the financial support of this work.

Fortunately, there is more to MIT than research, and I would like to thank all the roommates, officemates and friends whose company I have enjoyed. To acknowledge them individually would be too long a list, so stop looking for your name. A special thanks to the members of the MIT cycling team, and everyone else I've biked or run with over the years, for providing a much-needed diversion. Never once during a race did I catch myself daydreaming about being in group seminar.

Table of Contents

List of Figures

List of Tables

Chapter 1

Introduction

1.1 Motivation

Understanding the causes of viscoelastic flow instabilities is important to the polymer processing industry, where instabilities often limit the processing rates that can be achieved. Instabilities such as sharkskinning and melt fracture can dramatically distort the surface of an extruded polymer, and any instability that changes the flow history of the polymer can lead to nonuniformities in the processing conditions and therefore the properties of the final product. A more thorough understanding of the causes of flow instabilities can eventually lead to the ultimate goal of being able to determine *a priori* necessary modifications to either the fluid's rheological properties or process design in order to reach higher throughput in the absence of instabilities.

This thesis contains experimental characterizations of viscoelastic flow instabilities in three different types of test flows that model portions of more complex polymer processing operations. Furthermore, the experiments provide sufficient detail of the onset conditions and structure of the instabilities to serve as a basis of comparison with linear stability calculations and thereby test the ability of constitutive equations to accurately capture the relevant physics of the instability mechanism.

Before any reliable numerical predictions can be made, it is first necessary to demonstrate the ability of the constitutive equation and solution method to produce accurate results in simpler test geometries, and detailed experimental data for these flows is therefore necessary for comparison. Benchmark problems such as the flow past a cylinder in a channel or a sphere in a tube and the axisymmetric contraction have been chosen as bases for comparison (Brown and McKinley 1994), and considerable progress has been made in recent years in the ability to accurately calculate the flow field in these geometries. Experimentally, laser Doppler velocimetry (LDV) and flow-induced birefringence allow for quantitative measures of the velocity and stress fields, respectively. Flow visualization experiments using a sheet of light to illuminate a cross-section of the flow also can be used to obtain streak photographs in which particle tracks approximate streamlines of the flow. This method has been applied to a wide variety of non-Newtonian flows; see Boger and

Walters (1993). This method allows qualitative features of the flow to be observed simply, although it cannot provide quantitative measures of the velocity and is not useful for time-dependent flows. Flow visualization is combined with digital image analysis in this work to measure quantitatively the structure of flow instabilities, and LDV can be used to measure temporally- or spatially-varying velocities.

A meaningful comparison also requires that the experiments be performed with a well-characterized test fluid in order to determine values of the parameters in the constitutive equations. All models of viscoelastic fluids require at least a measure of the fluid's zero-shear-rate viscosity and relaxation time, and many models contain additional parameters that can be determined from knowledge of the shear-rate dependence of the material properties. Newtonian fluids are completely characterized by their viscosity, but viscoelastic fluids also show normal stress differences, which manifest themselves in experiments such as rod-climbing and the tubeless siphon (Bird *et al.* 1987a). Polymeric fluids retain a 'fading memory' of their flow history that is characterized by a spectrum of relaxation times. Furthermore, the extensional viscosity of polymer solutions can be 1000 times or more greater than the viscosity at high strain rates, whereas for Newtonian fluids the extensional viscosity is three times the viscosity. The fluids used in this work are 'Boger' fluids (Boger 1977/78) consisting of a small amount of high molecular weight polyisobutylene in a Newtonian solvent of low molecular weight polybutene and tetradecane. These fluids are designed to be highly elastic while maintaining a nearly constant viscosity in order to isolate elastic effects. Polymer melts and concentrated solutions typically have viscosities that decrease dramatically with increasing shear rate, and although the Boger fluids used here are sufficiently concentrated to exhibit a shear-thinning viscosity, this effect is masked by the high solvent viscosity. These fluids are well-suited for the optical experiments conducted here since they are transparent, and they can also be used at room temperature and low pressures.

The effects of elasticity in a flow can be measured in terms of the Deborah number, *De*, which is the ratio of the fluid's longest relaxation time, λ, to a characteristic timescale of the process, $\mathcal{T}$:

$$De = \lambda/\mathcal{T}, \tag{1.1}$$

where $\mathcal{T}$ is taken to be a residence time or reciprocal rotation rate. For small values of the Deborah number, the fluid is able to relax fully on the timescale of the flow, and elastic effects will be negligible. However, for Deborah numbers of order unity, the fluid retains a memory of its past deformations, and elasticity can begin to affect the flow, either by modifying the velocity or stress fields, or by leading to an elastic instability. Elastic effects can also be measured in terms of a Weissenberg number, *We*, which is the product of the fluid's relaxation time and a characteristic strain rate in the flow. The Deborah and Weissenberg numbers are often related to one another by geometric ratios of the experimental system. Due to the high viscosity of most polymeric fluids, the Reynolds number is usually small and inertial effects can be neglected.

1.2 Viscoelastic Flow Instabilities

Instabilities have been observed for a wide range of flows, and previous work has been reviewed by Petrie and Denn (1976) and Larson (1992). Although many questions remain unanswered regarding the cause of instabilities such as extrudate distortions, others such as the instabilities due to draw resonance and necking in fiber spinning are well understood. The most thoroughly studied instability for Boger fluids is in Taylor-Couette flow between two concentric, rotating cylinders. An inertial instability also exists for this geometry, and small levels of elasticity have been shown to stabilize the flow, whereas higher levels of elasticity and shear-thinning destabilize the flow, and elasticity can also change the form of the instability from standing cells to an oscillatory mode. Larson *et al.* (1990) showed that a purely elastic (*i. e.*, in the limit of small Taylor number) instability consisting of axially-periodic toroidal cells existed for a Boger fluid, and that its onset could be predicted by the Oldroyd-B model. The theory predicted a shallow neutral stability curve for the critical Deborah number as a function of the wavenumber of the disturbance, and flow visualization experiments showed that the structure evolved from a single wavelength near onset to a much finger structure, in agreement with the calculations of Northey *et al.* (1992). The importance of the fluid's rheological properties was shown by Shaqfeh *et al.* (1992), who found that negative second normal stress differences and higher solvent viscosity ratios both stabilized the flow. LDV measurements by Muller *et al.* (1993) showed that the instability was oscillatory, in agreement with theoretical predictions. Many other studies have been conducted for this flow, but the work described above demonstrates that a simple test flow can be used to determine both theoretically and experimentally the characteristics of a flow instability.

Although each of the instabilities studied in this thesis has been previously observed experimentally, prior studies have not characterized the instabilities in sufficient detail to provide a basis for comparison with theoretical studies.

The rotational flows between parallel plates or a cone and a plate are commonly used for measuring the rheology of fluids, and the presence of an instability will lead to erroneously high measures of the viscosity or normal stress coefficient. Rotational flows are also encountered in polymer processing applications involving extrusion or spin coating. The instability has been previously reported by Jackson *et al.* (1984) and Magda and Larson (1988). McKinley *et al.* (1991a) established an experimental stability diagram by varying the gap between the plates or the cone angle, and showed a series of images of the development of spiral vortices beyond the critical Deborah number. However, no quantitative measures of the structure of the instability were obtained, and it is the goal of this thesis to determine the spatial and temporal characteristics of the instability in both the parallel pale and cone-and-plate geometries. Experimental observations of the instability provides not only a basis for comparison with theoretical studies, but can also guide analyses by ensuring that the correct form of the instability is studied. For example, the analysis of Phan-Thien (1983) assumed that the instability for the flow between parallel plates took the form of a single toroidal vortex, whereas the instability is actually found to consist of nested spiral vortices.

The only previous study of the elastic wake instability for flow past a confined cylinder is that of McKinley *et al.* (1993), who showed that the instability took the form of axially periodic fluctuations in the streamwise velocity downstream of the rear stagnation point. The present work extends on these experiments by determining the onset conditions for a wider range of cylinder radius to channel half-height aspect ratios, examining further the structure of the instability near the cylinder, and studying the sensitivity of the instability to changes in the upstream flow conditions. Stagnation flows are important since the strong extensional flow near the stagnation point can result in large elongational stresses in the downstream wake.

The interfacial instability for superposed plane Poiseuille flow of two elastic liquids has received considerable theoretical study, but no experimental data exist for Boger fluids. This flow model the commercial process of coextrusion, where the desired uniform thickness of the layers is disrupted by the instability. Wilson and Khomami (1992, 1993a,b) have obtained detailed experimental data for the flow of two polymer melts, and the experimental system used in this thesis is based on their system. By using Boger fluids, the effects of elasticity on the instability can be more easily studied, and the experimental system can also be used to study the instability for Newtonian fluids, for which no data exist.

Chapter 2 provides more detail of previous work for each of the three flows mentioned above, and Chapter 3 describes the fluids, the test geometries and the experimental techniques. Experimental results and comparison to the linear stability analysis of Öztekin are given in Chapter 4 for the rotational flow instabilities and in Chapter 5 for the stagnation flows, and Chapter 6 describes the experimental results for the interfacial instability.

Chapter 2

Literature Review

This thesis considers viscoelastic flow instabilities in three different types of flows that model important aspects of polymer processing: the rotational flow between parallel disks or a disk and a cone, the stagnation flow behind a constrained cylinder or axisymmetric obstacle, and the interfacial instability between superposed fluids in plane Poiseuille flow. This chapter discusses each of these flows and reviews previous studies of viscoelastic flow in each geometry.

2.1 Rotational Flows of Viscoelastic Fluids

2.1.1 Parallel-Plate Geometry

The torsional motion of a non-Newtonian fluid between coaxial parallel disks is one of the most common geometries employed in rheological measurements. Fluid samples are placed in a narrow gap of height H between two coaxial parallel disks of radius R, as shown in figure 2.1*(a)* and measurements of the torque and normal force exerted by the fluid on the upper plate are used to calculate the shear-rate-dependent material functions of the fluid, as a steady or oscillatory shear flow is driven by rotating the other plate. A key assumption in the subsequent analysis of such measurements, however, is that the flow is always steady and purely azimuthal for all rotation rates. Centrifugal effects, which produce inertial secondary flows in such geometries, are usually negligible because of the high viscosities of most viscoelastic solutions and melts; however, it has recently become clear that secondary flows can develop even in simple geometries at vanishingly small Reynolds number due to *purely elastic instabilities* that are entirely absent in the corresponding flows of Newtonian liquids. Such instabilities have been documented in circular Couette flows and Taylor-Dean flows as well as in torsional flows between coaxial disks or between a cone-and-disk, and have recently been reviewed by Larson (1992). Although the detailed mechanism and characteristic features of the elastic instability may vary in each geometry, the driving force in each case is the large difference between the extra normal stresses in the streamwise direction and the direction of the velocity gradient.

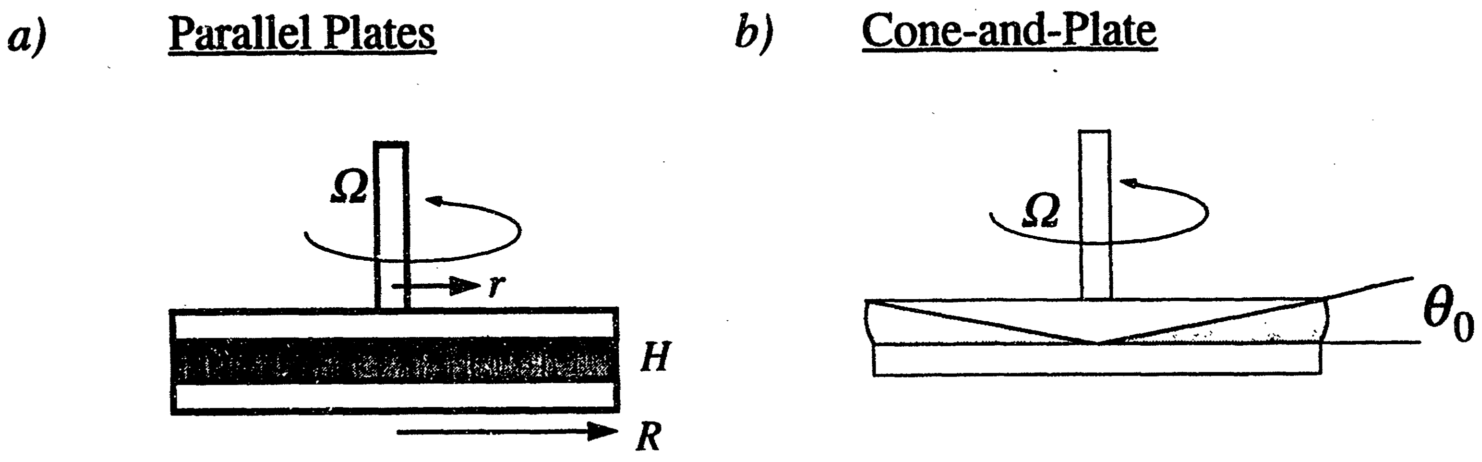

$$\dot{\gamma} = \Omega r/H$$

$$\dot{\gamma} \cong \frac{\Omega}{\theta_0}$$

Figure 2.1 Schematic diagrams of the *(a)* parallel-plate and *(b)* cone-and-plate geometries.

This *first normal stress difference* acts normal to the curvilinear streamlines in the flow and drives a secondary motion.

Viscoelastic modifications to the steady, inertially-driven, secondary recirculation that is present in confined rotating flows at finite Reynolds numbers have been known to exist since the early observations of Giesekus (1965) and Griffiths *et al.* (1969). Detailed experimental and theoretical studies (Hill 1972; Chiao and Chang 1990) in rotational flows such as the disk-and-cylinder system with low geometric aspect ratios, $(R/H) \sim O(1)$, show that as the rotation rate increases and viscoelastic effects become increasingly important, the weak centrifugal outward motion near the rotating disk reverses direction and becomes directed radially *inwards* towards the center of the disks. At still higher rotation rates, time-dependent unsteady motions are observed and calculated.

However, in systems with higher aspect ratios, such secondary motions are typically negligible and the fluid motion is steady and one-dimensional. The first experimental indications of a purely elastic instability in the creeping torsional flow of a viscoelastic fluid were observed by Jackson *et al.* (1984). Measurements of the torque and normal force exerted by a highly elastic polyacrylamide Boger fluid at high shear rates in a parallel-plate rheometer showed a steady monotonic increase over a period of 20 minutes. This time-dependent response resulted in an increase in the apparent viscosity and first normal stress coefficient calculated for the fluid sample, and was interpreted as a time-dependent shear-thickening or *anti-thixotropic* change associated with the microstructure of the fluid. Subsequent measurements by Magda and Larson (1988) with a number of different Boger fluids containing high molecular weight polystyrene (PS) or polyisobutylene (PIB) showed that the critical shear rate required for the onset of this apparent anti-thixotropic transition was not constant, but varied inversely with the separation H between the plates, and therefore corresponded to an approximately constant critical angular velocity Ω_{crit}. Figure 2.2 shows the time dependence of the measured shear and normal stresses for a PIB Boger fluid. After an initial rise to a seemingly steady value, the stresses rise dramatically at ~2100 s and then fluctuate about a much higher value. This observation was found to be in good qualitative agreement with calculations performed by Phan-Thien (1983) for the hydrodynamic stability of torsional motions of the Upper-Convected Maxwell and Oldroyd-B models. In this analysis, Phan-Thien used the von Kármán similarity forms for the velocity and stress fields which are valid when the disks are infinite in extent and examined the linear stability of the base rotational shear flow with respect to disturbances that can also be represented in similarity form. Infinitesimal perturbations were found to grow exponentially in time for values of the Deborah number, $De = \lambda_1 \Omega$, that exceeded the critical value given by $De_{\text{crit}} \equiv \pi[(1-\beta)(5-2\beta)]^{-1/2}$. In this

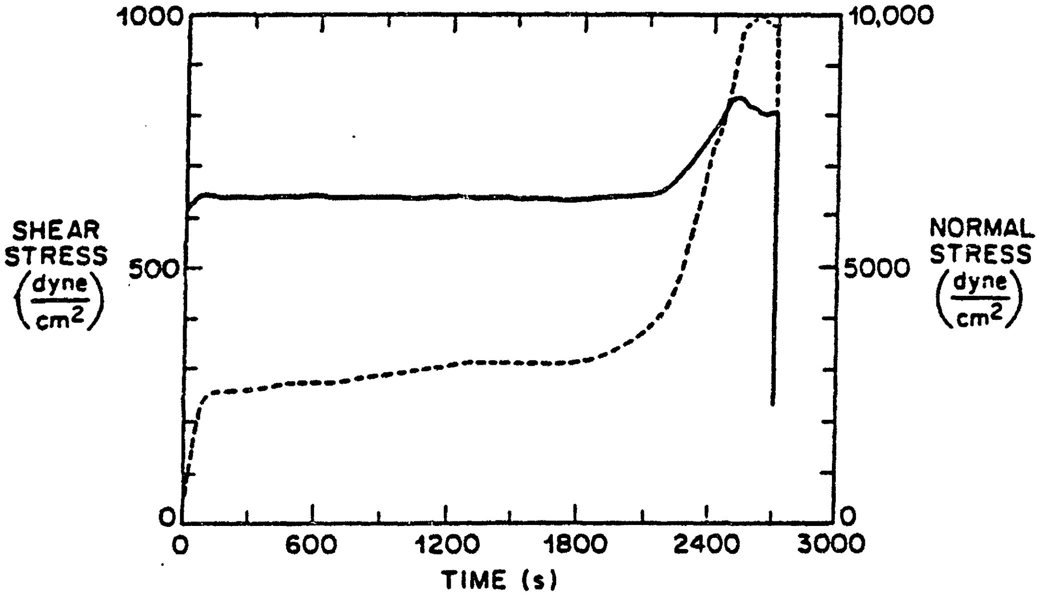

Figure 2.2 Time dependence of the normal stress (- - -) and the shear stress (——) for a PIB Boger fluid (from Magda and Larson 1988).

expression, λ_1 is the single relaxation time in the constitutive model and $\beta \equiv \eta_s/\eta_0$ is the dimensionless ratio of the solvent viscosity to the total viscosity in the Oldroyd-B model. Hence, the critical rotation rate Ω_{crit} for the onset of this secondary motion is predicted to be a function of the relaxation time and viscosity ratio of the fluid between the plates, but is independent of the gap H between the plates.

Subsequent flow visualization experiments with another PIB Boger fluid (McKinley *et al.* 1991a) showed that a number of the characteristics of this elastic instability cannot be described even qualitatively by the analysis of Phan-Thien. In particular, flow visualization and dynamic measurements of the shear stress and normal stresses exerted on the plates clearly demonstrated that the flow transition is nonaxisymmetric, overstable in time and corresponds to a subcritical bifurcation. Most importantly, the spatial structure of the developing secondary flow consists of a radially periodic structure that scales approximately with the gap H between the plates and *not* of a single toroidal vortex extending across the entire radial span of the disks, as is expected from perturbations of the similarity form considered by Phan-Thien. As the Deborah number was increased beyond a critical value, these vortices increased in intensity with time and propagated both radially outwards from the center of the disks and inwards from the free surface at the outer edge of the test geometry. By constructing an experimental stability curve for a number of different aspect ratios R/H and rotation rates, McKinley *et al.* also showed that the instability is a function of both the rotation rate Ω and the characteristic shear rate $\dot{\gamma}_R \equiv \Omega R/H$ between the plates, as shown in figure 2.3. This latter variation was attributed to the complex shear-rate-dependence of the viscoelastic material functions of the test fluid studied.

Highly elastic fluids, such as polymer melts, also can undergo another, entirely different, type of rotational flow instability known as *edge fracture* in a parallel-plate rheometer (Hutton 1969). Above a critical shear rate, a narrow concave indentation appears in the free surface of the fluid near the midplane between the two disks. This indentation rapidly propagates radially inwards in the form of a crack and the viscoelastic sample is torn into two halves, one attached to each plate. Tanner and Keentok (1983) conjectured that this instability is driven by the negative second normal stress difference $N_2 = (\tau_{zz} - \tau_{rr})$ measured in many polymeric systems. This observation has been verified by Lee *et al.* (1992), who showed that the critical second normal stress difference $N_{2\text{crit}}$ required for edge fracture in one particular cone-and-plate geometry remained almost constant for five different polymer solutions.

Both the purely elastic instability discussed by McKinley *et al.* (1991a) and edge fracture can severely limit the operating range of rotational rheometers for polymeric fluids,

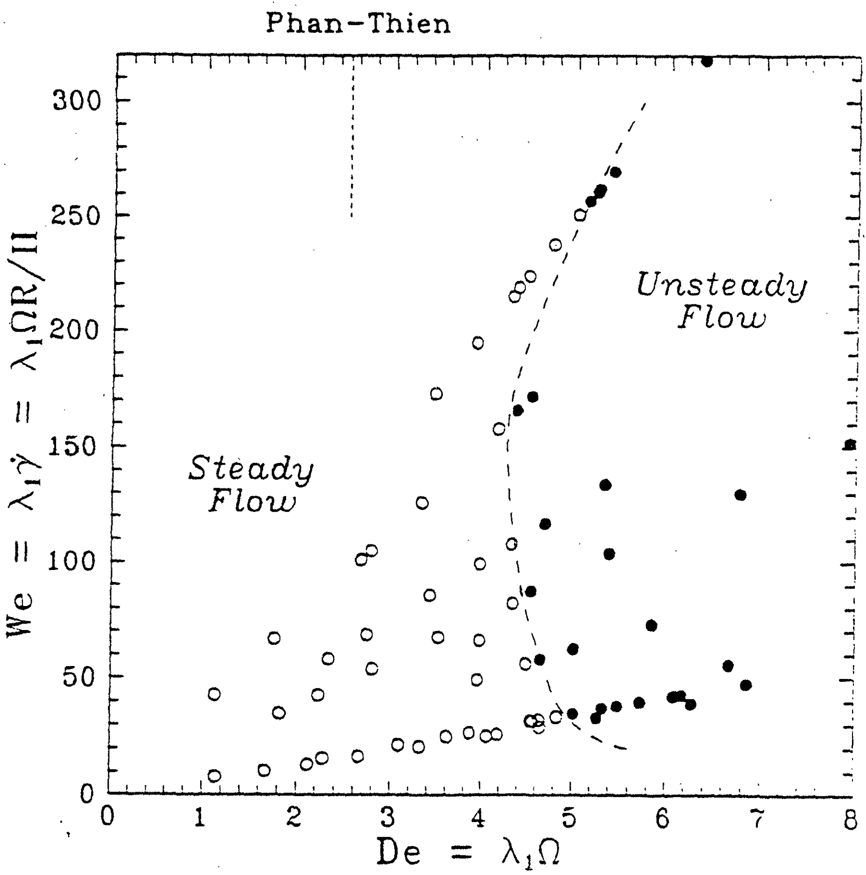

Figure 2.3 Stability diagram for the flow of a PIB Boger fluid between parallel plates. Stable (○) and unstable (●) experimental points are shown, as well as the critical Deborah number predicted by Phan-Thien (from McKinley *et al.* 1991).

and the particular ordering of the transitions depends on the relative magnitudes of the first and second normal stress coefficients and the surface tension for a given polymeric fluid. Dilute or weakly-entangled polymer solutions, such as the Boger fluids used in the present experiments, typically have vanishingly small second normal stress coefficients and are not prone to the edge-fracture instability. In their previous experiments, Lee *et al.* (1992) were not able to observe edge fracture in a polystyrene-based Boger fluid over a wide range of shear rates.

Although inertial transitions and secondary motions in the flow of Newtonian liquids between co- and counter-rotating parallel disks have been the subject of extensive theoretical and experimental attention (see the review by Zandbergen and Dijkstra 1987), much less is known about the corresponding flow of viscoelastic fluids. Most of the theoretical analyses have only considered the existence and stability of secondary flows described by the von Kármán similarity form first analyzed by Phan-Thien (1983). Walsh (1987) employed a numerical scheme to show the presence of a subcritical bifurcation from the base torsional flow of an Upper-Convected Maxwell fluid at zero Reynolds number. Similar results showing turning points in dynamic quantities such as the total torque exerted on the plates and the presence of multiple axisymmetric steady-state solutions of similarity form have been found by Ji *et al.* (1990) for the rotational flow of an Oldroyd-B fluid between infinite co-axial parallel plates at finite Reynolds numbers. Figure 2.4 shows the velocity components as functions of the axial position z for two different solution families for $\beta = 0$ and 0.5 for $De = 4$. For Branch I, the radial velocity is antisymmetric and the axial velocity is symmetric about the center of the gap, and the maximum azimuthal velocity is at the bottom, faster moving plate. Branch II corresponds to an unstable solution, with the maximum azimuthal velocity no longer at the bottom plate. Crewther *et al.* (1991) give a detailed review and mathematical study of both axisymmetric and nonaxisymmetric flows for the Oldroyd-B fluid and present examples of some of the hundreds of steady-state solutions they obtained using a bifurcation tracking scheme.

The first analysis that considered disturbances not of the similarity form was presented by Öztekin and Brown (1993) for the inertialess torsional flow of the Oldroyd-B model between infinite parallel plates. These authors considered the linear stability of infinitesimal normal mode disturbances to the base velocity and stress fields of the form

$$F(r,\theta,z,t) = f(z)e^{i\alpha r+im\theta+\sigma t}. \qquad (2.1)$$

Where F indicates any dimensionless disturbance variable, and all kinematic variables have been nondimensionalized with the length scale H and the time scale Ω^{-1}. In equation 2.1

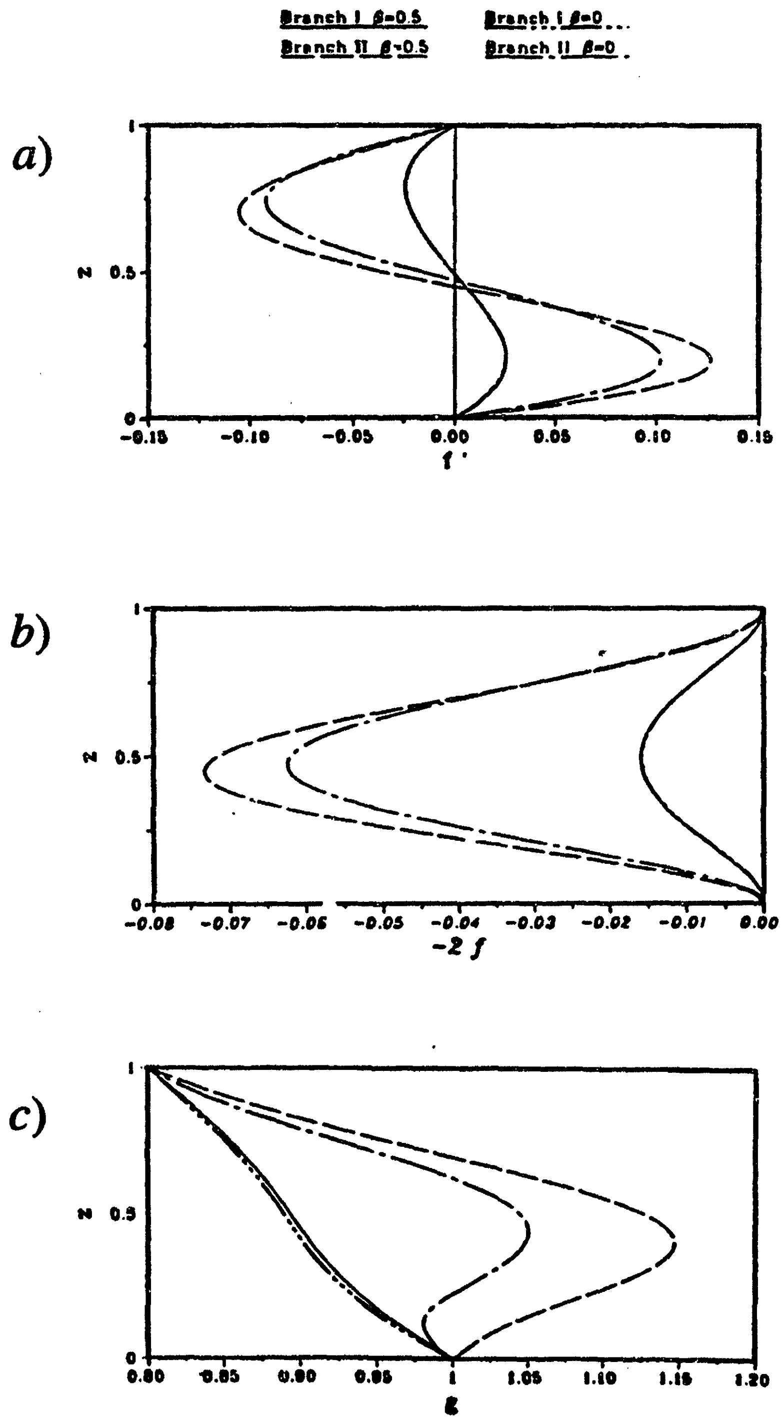

Figure 2.4 Nondimensional *(a)* radial, *(b)* axial and *(c)* azimuthal velocity components for flow between parallel disks as functions of the gap position. Branch I is stable, while Branch II is unstable (from Ji *et al.* 1990).

the dimensionless wavenumber α characterizes the radial form of disturbance, and m is an integer describing the azimuthal dependence of the disturbance. Nonaxisymmetric instabilities are incorporated by choosing $m \neq 0$. The dimensionless growth rate of the disturbance is given by the complex growth rate $\sigma = \sigma_r + i\sigma_i$. By linearizing the resulting disturbance equations about a critical dimensionless radial location R^*, the authors obtained a separable matrix eigenvalue problem which they solved to find the spatial form of the most unstable disturbance as a function of the local radial position R^*, the Deborah number, *De,* and the fluid rheology, as measured by the solvent viscosity ratio β. Figure 2.5 shows the critical Weissenberg number (= R^*De) for axisymmetric disturbances. Calculations showed that the most dangerous perturbations led to spiral vortices with positive or negative angle that traveled either radially outwards or inwards, respectively. The critical rotation rate for growth of these disturbances and the azimuthal dependence of the most unstable mode were sensitive functions of the fluid rheology and the local radial position. Most significantly, these disturbances were unstable at large R^* for Deborah numbers considerably below the critical condition predicted by the Phan-Thien analysis, and thus are more likely to be observed experimentally. The critical radial wavenumber α at the onset of the instability was in good agreement with the few photographs presented by McKinley *et al.*, but quantitative comparison of the azimuthal structure and wavespeed were inhibited by the lack of data.

The calculations of Öztekin and Brown were performed with the quasi-linear Oldroyd-B model which predicts a constant viscosity η_0 and a constant first normal stress coefficient $\Psi_{1,0}$ in steady torsional shear flows at all rotation rates. However, for Boger fluids such as those used in the experiments of Magda and Larson and McKinley *et al.*, it is well known that although the viscosity is almost constant across many decades of shear rate, the first normal stress coefficient is only constant at low shear rates and decreases monotonically even at moderate shear rates (Prilutski *et al.* 1983; Quinzani *et al.* 1990). Despite this limitation, the predicted form of the neutral stability curve obtained by Öztekin and Brown for the critical onset radius as a function of the Deborah number adequately described the experimental measurements of McKinley *et al.* when the effective relaxation time $\lambda_1(\dot{\gamma})$ for the test fluid was evaluated using the viscometric properties measured at the shear rate corresponding to the maximum value of R^* in the experimental apparatus and this value was used as the single relaxation time in the Oldroyd-B model.

Since it is the relative magnitude of the first normal stress coefficient $\Psi_1(\dot{\gamma})$ compared to the viscosity which provides the driving force for these purely elastic instabilities, Larson (1992) pointed out that shear-thinning phenomena may be expected to have profound stabilizing effects on the bifurcation structure and stability of highly elastic

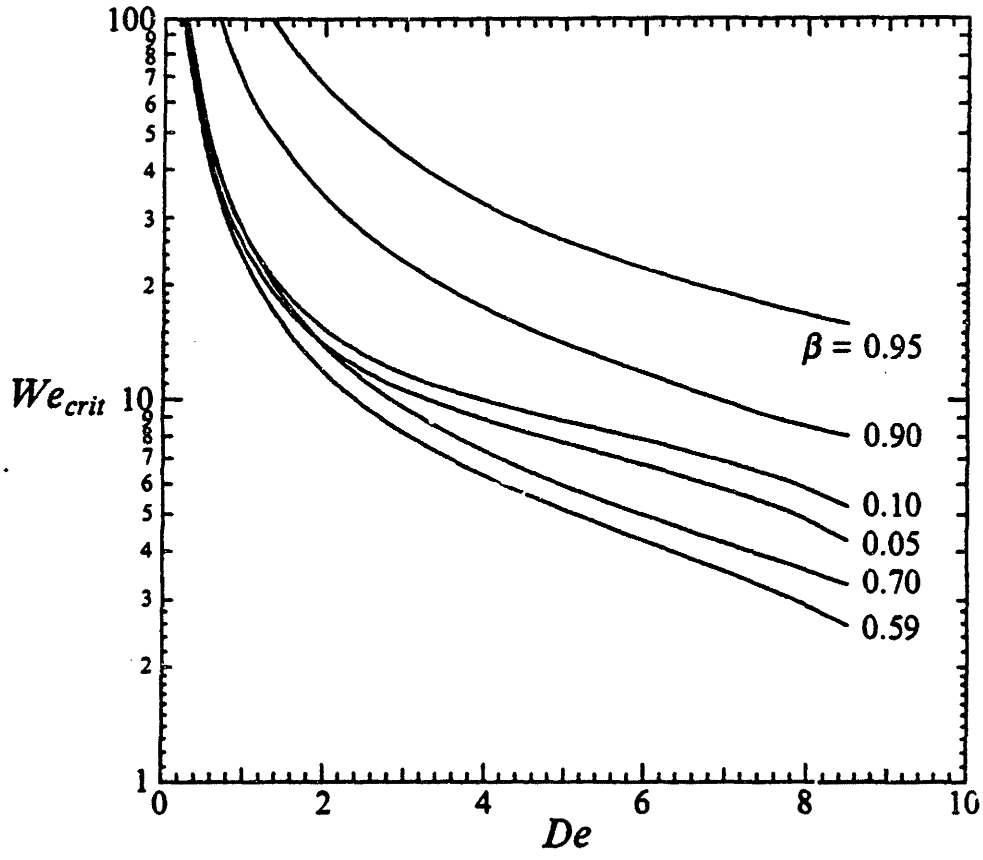

Figure 2.5 The critical Weissenberg number, $We_{crit} = R^*De$, for the onset of the axisymmetric instability as a function of the Deborah number and the solvent viscosity ratio (from Öztekin and Brown 1993).

flows. McKinley *et al.* (1991a) demonstrated that when the aspect ratio *R/H* of the plates was increased at a fixed rotation rate, the increasing importance of shear-thinning effects led to a progressive decrease in the amplitude of the ultimate unstable flow developing between the plates. However, to date, few analytical studies of the stabilizing effects of shear-thinning on purely elastic instabilities have appeared, primarily because of the greatly increased complexity of the analysis which results. Phan-Thien (1985) briefly reported on a linear stability analysis for the inertialess torsional motion of a fluid described by the Phan-Thien–Tanner (PTT) constitutive equation between an infinite cone and disk, and showed that whereas the flow of an Oldroyd-B fluid was unstable beyond a critical rotation rate for a particular form of the disturbance kinematics, the corresponding motion of the PTT model was always stable at all Deborah numbers. Larson *et al.* (1994) considered the effects of shear-thinning in the viscoelastic material functions, the presence of a Newtonian solvent contribution to the viscosity, and the effects of a distribution of relaxation times on the stability of Taylor-Couette flows to axisymmetric disturbances using the K-BKZ model. They showed that each of these effects increased the critical Deborah number based on the longest relaxation time for the onset of the purely elastic instability. Comparison with experimental observations gave reasonable agreement; however, the experimentally determined critical conditions were consistently lower than experimental measurements, and it was speculated that the most likely reason for this discrepancy was that the most unstable disturbance is nonaxisymmetric.

2.1.2 Cone-and-Plate Geometry

The torsional motion of a fluid in the narrow gap between a plate and an inverted cone is one of the most common viscometric flows used in the measurement of rheological material functions. A typical cone-and-plate rheometer configuration is shown in figure 2.1(*b*) and consists of a precision machined conical fixture which is mounted with its symmetry axis perpendicular to a flat circular disk. For creeping flow conditions and small cone angles $\theta_0 << 1$, the motion between the fixtures is purely azimuthal with no recirculating secondary flow. Measurements of the total torque and normal force exerted by the fluid on the lower plate as a function of the imposed rotation rate Ω of the cone are used to determine the viscous and elastic material functions of the fluid sample as a function of the deformation rate in the gap. Analysis of the dynamic quantities measured in this geometry is simplified because, in contrast to the corresponding motion between coaxial parallel plates, the circular base flow between the cone and plate is *homogeneous* (at least for slow flows and small cone angles), and the shear rate throughout the fluid is constant with a value given by $\dot{\gamma} = -\dot{\gamma}_{\theta\phi} = \Omega/\theta_0$ (Bird *et al.* 1987a).

For larger cone angles and/or finite Reynolds numbers, it is well known that the purely circumferential flow cannot satisfy the equations of motion and a weak secondary flow consisting of an axisymmetric toroidal vortex develops between the cone and plate (Turian 1972; Heuser and Krause 1979). In Newtonian fluids this secondary motion is driven by centrifugal forces and is directed radially outwards near the surface of the moving fixture. However, early flow visualization experiments by Giesekus (1963) and Walters and coworkers (Walters and Waters 1968; Griffiths and Walters 1970) with polymer solutions in devices with large cone angles ($\theta_0 = 30°$, $60°$) showed that elastic hoop stresses directed along the curved streamlines can lead to a steady axisymmetric secondary flow that is *inwardly*-directed near the moving fixture.

Such secondary motions in the cone-and-plate geometry have been accurately described analytically by considering perturbation expansions of the governing momentum and constitutive equations in terms of the cone angle θ_0, the Reynolds number $Re \equiv \rho\Omega R^2/\eta$, and, for viscoelastic fluids, in terms of the Deborah number $De \equiv \lambda_1\Omega$ which measures the relative importance of elastic effects to viscous effects in the flow. In these expressions, ρ is the fluid density, η is the fluid viscosity and λ_1 is a characteristic relaxation time for the viscoelastic fluid. Early numerical solutions for a cone-and-plate system of infinite radial extent were obtained by Giesekus (1963) and by Walters and Waters (1968) using second order fluid models (Bird *et al.* 1987a). Closed-form analytic expressions for the axisymmetric secondary motions of the Oldroyd-B constitutive model have been obtained for both the unbounded case (Olagunju and Cook 1992) and for a finite cone-and-plate geometry incorporating a deformable free surface (Olagunju 1993). These calculations corroborate the flow visualization results described above and also indicate that if both inertial and elastic effects are important in the flow, then two distinct recirculations may develop; an interior, elastically-dominated vortex that is inwardly-directed near the moving surface and a second, inertially-driven recirculation at larger radii that is outwardly directed.

All of the observations and calculations discussed above indicate that for viscous fluids with $Re < 1$ and for small cone angles, $\theta_0 \leq 10°$ (0.175 rad), these steady secondary flows have a negligible effect (*i.e.* less than 1%) on the experimentally-measured material properties of the fluid in a rheometric device. Consequently the flow in a cone-and-plate rheometer is assumed to be steady and one-dimensional at all rotation rates. However, recent analyses have indicated that the presence of elastic normal stresses along the closed circular streamlines can destabilize the torsional motion even under creeping flow and small-gap conditions, and ultimately lead to the onset of more complex non-viscometric motions (Larson 1992). Phan-Thien (1985) considered the stability of the creeping motion between a cone-and-plate for a viscoelastic fluid described by the quasilinear Oldroyd-B model (Bird *et al.* 1987a). By considering axisymmetric disturbances that could be represented in a similarity form, Phan-Thien showed that there exists a critical Deborah number $De_{\text{crit}} \equiv \lambda_1 \Omega_{\text{crit}}$ beyond which the base azimuthal motion is unstable to infinitesimal perturbations. This stability criterion was found to be independent of the cone angle θ_0 and to depend only on the solvent viscosity ratio of the fluid defined as $\beta \equiv \eta_s / \eta_0$, where η_s is the viscous contribution of the Newtonian solvent, and η_0 is the total viscosity predicted by the constitutive model. More recent calculations by Olagunju and Cook (1993) extended this analysis for the Oldroyd-B model to include $O(1)$ inertial effects and axisymmetric disturbance kinematics of a more general form. Asymptotic solutions of the governing equations again indicate that at a critical Deborah number, De_{crit}, there is an exchange of stability and loss of uniqueness in the steady solution. Incorporating inertial effects was found to destabilize the steady axisymmetric base solution and to reduce the critical Deborah number below the value found by Phan-Thien.

Experimental measurements also have suggested the presence of viscoelastic flow instabilities in cone-and-plate geometries. Early qualitative flow visualization photographs were presented by Kocherov *et al.* (1973) for polyethylene melts in a disc-type extruder containing a cone-and-plate fixture at the exit. No torque or normal force measurements were presented, but the introduction of tracer particles showed that the fluid pathlines were not concentric circles but of a non-axisymmetric spiral form. The extent of this secondary flow was found to depend on the rotation rate of the conical fixture and on the cone angle θ_0. Although no quantitative measurements were presented, these spiral patterns were labeled by Kocherov *et al.* as 'spirals of Archimedes'. A similar flow instability in cone-and-plate geometries with cone angles $\theta_0 \leq 10^\circ$ was reported later by Kulicke and Porter (1979) in rheological studies of shear-thinning polymer solutions. The unstable motion that they observed resulted in a time-dependent increase in the normal force exerted by the fluid on the plates beyond a critical shear rate $\dot{\gamma}_{\text{crit}}$ which was found to vary with the molecular weight and concentration of the polymer. No observations of the spatial structure of the flow between the cone and plate were provided; however, the authors did present photographs of the deformable fluid surface at the edge of the conical fixtures. Following the onset of unsteady motion, spatially-periodic surface irregularities were observed at the interface which were interpreted in terms of recirculating secondary vortices. These vortices scaled in size with the gap height at the edge of the cone-and-plate rheometer and slowly processed in the direction of imposed rotation at a rate slower than the rotation rate of the device.

Magda and Larson (1988) performed the first experiments connecting rheological measurements in a cone-and-plate geometry with the linear stability analysis of Phan-Thien. The experiments utilized highly-elastic, constant-viscosity Boger fluids to eliminate viscous shear-thinning effects, and conical fixtures with angles in the range $2.5^\circ \le \theta_0 \le 10^\circ$. In addition to documenting the time-dependent increase in the torque and normal forces measured in the device, Magda and Larson also demonstrated that the critical shear-rate for onset of instability varied inversely with the cone angle and thus corresponded to an approximately constant critical value of the rotation rate, in accord with the analysis of Phan-Thien. Subsequent measurements by Laun and Hingmann (1990) and McKinley *et al.* (1991a) corroborated these observations; however, these studies also showed that the detailed dynamics of the elastic cone-and-plate instability that are observed experimentally are not of the form predicted by the Phan-Thien–Olagunju analyses, but correspond to a subcritical Hopf bifurcation from the steady base flow.

No quantitative observations of the azimuthal spatial variation of the secondary flow between a cone and a plate have ever been performed; however, the early work of Kocherov *et al.* (1973) suggests that the unsteady flow observed will not be axisymmetric but also will consist of spiral recirculating vortices. The close similarities between the critical conditions and time-dependent torque/normal-force measurements in cone-and-plate and parallel-plate geometries that have been observed by previous investigators (Magda and Larson 1988; McKinley *et al.* 1991a) suggest that the elastic flow instabilities in both configurations may be very similar. There are, however, a number of very important differences between the cone-and-plate and parallel-plate geometries which make the previous analysis for the coaxial-disk geometry inappropriate. Most importantly, in the limit of small cone angles ($\theta_0 << 1$) the base shear flow between the cone and plate is a *homogeneous* shear flow with a shear rate, $\dot{\gamma} \equiv \Omega / \theta_0$, that is independent of radial location across the disk. Thus, at any given set of experimental conditions, both the shear rate *and* the Deborah number will be uniform throughout the fluid, and it is not appropriate to consider localized disturbances about a given critical radius R^*, as was the case for the parallel-plate geometry. In addition, there is no characteristic length scale H between the cone and the plate on which to base the scale of the secondary vortices, and the wavelength of the most unstable, nonlocal disturbance mode may be expected to vary throughout the fluid sample.

2.2 Viscoelastic Stagnation Flows

The geometry of flow past a cylinder to be considered in this thesis is shown in figure 2.6. The cylinder is centered between two parallel channel walls, and the ratio of the cylinder radius to the channel half-height is defined as R/H. Far upstream and downstream the flow is fully-developed plane Poiseuille flow. The points S_1 and S_2 are stagnation points, where all velocity components and their derivatives are zero. Polymer molecules will have long residence times near the stagnation points, which can lead to large molecular extensions and high elastic stresses, which in turn affect the flow field and drag.

Although the focus of this thesis is on viscoelastic flow past a cylinder, an understanding of Newtonian flow past a cylinder is important for comparison with flows at nonzero *De*. A brief review of Newtonian flow past a cylinder is therefore presented in §2.2.1, followed by a more complete review of viscoelastic flow past a cylinder in §2.2.2. Furthermore, the axisymmetric stagnation flow past a sphere is considered in §§2.2.3-4, and stagnation flow instabilities are reviewed in §2.2.5.

2.2.1 Newtonian Flow Past a Cylinder

The inertialess equations of motion can be solved for uniform flow past a circular cylinder to yield the stream function (Batchelor 1967)

$$\psi = U\sin\theta\left[Ar + \frac{B}{r} - \frac{C}{2} r\ln r \right], \tag{2.2}$$

where U is the far-field velocity and the origin of the coordinate system is at the center of the cylinder and A, B and C are constants. The drag force per unit length of the cylinder is

$$\frac{F}{l} = 2\pi\mu UC, \tag{2.3}$$

where μ is the fluid viscosity. In equations 2.2-3, no choice of the constant C can simultaneously provide a bounded velocity far from the cylinder and a nonzero drag force on the cylinder. This inconsistency is known as Stokes' paradox, and exists for all unbounded two-dimensional creeping flows (Happel and Brenner 1973).

Lamb (1932) used Oseen's linearization of the inertial terms to obtain an approximate function which is accurate near the cylinder for distances up to $r/R \approx 1/Re$:

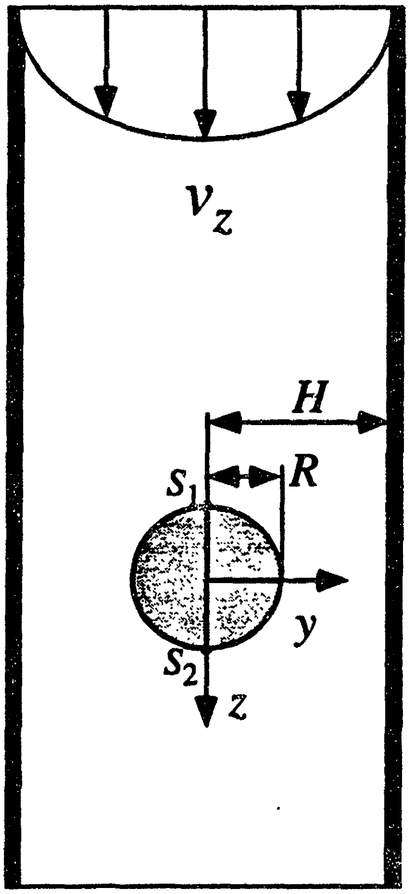

Figure 2.6 Schematic diagram of viscoelastic flow past a cylinder. The cylinder of radius R is centered in a channel of half-height H. A Cartesian coordinate system is defined with its origin at the center of the cylinder.

$$\psi = \frac{U\sin\theta}{\frac{1}{2} - \gamma + \ln 8 - \ln Re}\left[\frac{r}{2} - r\ln\left(\frac{r}{R_c}\right) - \frac{R_c^2}{2r}\right], \tag{2.4}$$

where γ is Euler's constant (≈ 0.577) and the drag coefficient for this solution is

$$C_D = \frac{8\pi}{Re\left[\frac{1}{2} - \gamma + \ln 8 - \ln Re\right]}. \tag{2.5}$$

Stokes' paradox can also be avoided by the introduction of walls to bound the freestream flow, in which the solution will depend on the aspect ratio R_c/H between the cylinder radius and the channel half-height, H. Faxén (1946) presented series expansions for the drag force and pressure drop in creeping flow up to order $(R_c/H)^8$. The drag coefficient for a cylinder moving through a channel with a velocity U normal to its axis can be expressed as

$$C_D\left(\frac{R_c}{H}\right) = \frac{8\pi}{\left[-0.9157 - \ln\left(\frac{R_c}{H}\right) + 1.7244\left(\frac{R_c}{H}\right)^2 + O\left(\frac{R_c}{H}\right)^4\right]}. \tag{2.6}$$

The complete solutions are shown in figure 2.7 for both the case of a cylinder moving through a channel (subscript '1') and a fixed cylinder with plane Poiseuille flow with maximum velocity U in the channel (subscript '2'). The drag force is given by $F_i = \mu U r_i$ and the pressure drop is $P_i = \mu U p_i$. As the aspect ratio increases and the presence of the walls becomes more important, the drag force increases dramatically.

The focus of this work is on the effect of elasticity on the flow field at low Reynolds number, but the flow past a cylinder also changes with increasing Re. At low Re, the streamlines are symmetric about the cylinder, but when inertial effects become important near $Re = 1$, the streamlines begin to shift downstream. At $Re \sim 6$ a pair of recirculating vortices appear downstream of the cylinder, as shown in figure 2.8, and they extend further downstream with increasing Re. At $Re \sim 40$ the wake downstream of the cylinder becomes unstable and oscillates with an amplitude that increases with distance downstream of the cylinder. As Re is increased, the oscillation moves closer to the cylinder, and at $Re \sim 60$ the vortices behind the cylinder begin to oscillate and shed from alternate sides of the cylinder, resulting in the von Kármán vortex street shown in figure 2.9. These oscillations continue until $Re \approx 2500$, and at $Re \approx 4 \times 10^5$ the boundary layer near the cylinder becomes unstable.

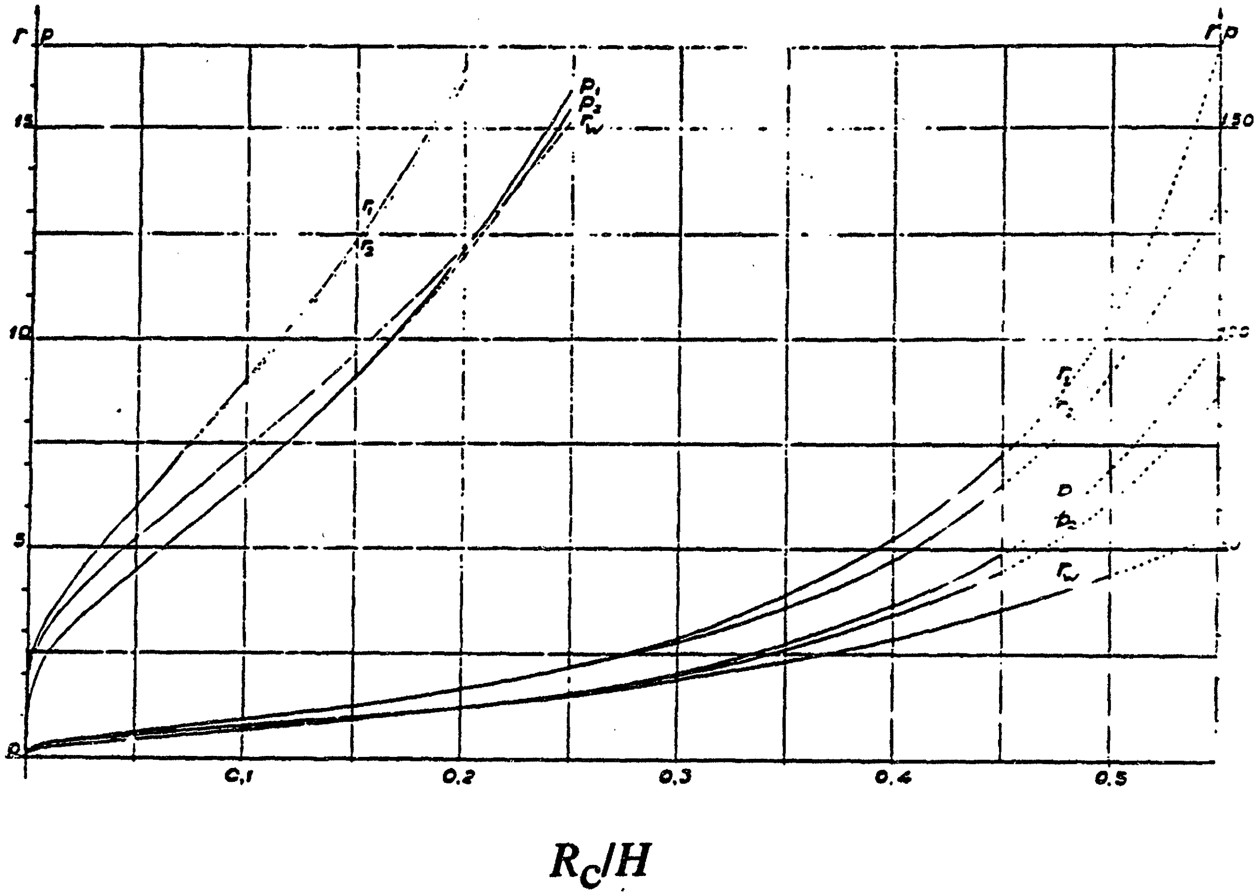

Figure 2.7 Drag force and pressure drop caused by the presence of walls for Newtonian flow past a cylinder (from Faxén 1946) as functions of the cylinder-channel ratio. The drag force is $F = \mu U r_i$ and the pressure drop is $P = \mu U p_i$, where i = 1 is for a cylinder moving through a channel, and i = 2 is for plane Poiseuille flow. The drag for a cylinder moving normal to the channel walls is given by r_w.

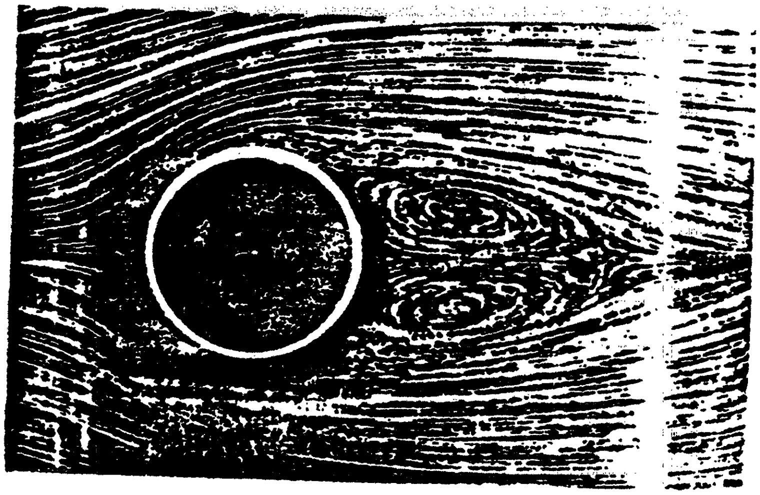

Figure 2.8 Streaklines of Newtonian flow past a cylinder at $Re = 26$ (from Taneda, in Van Dyke 1982).

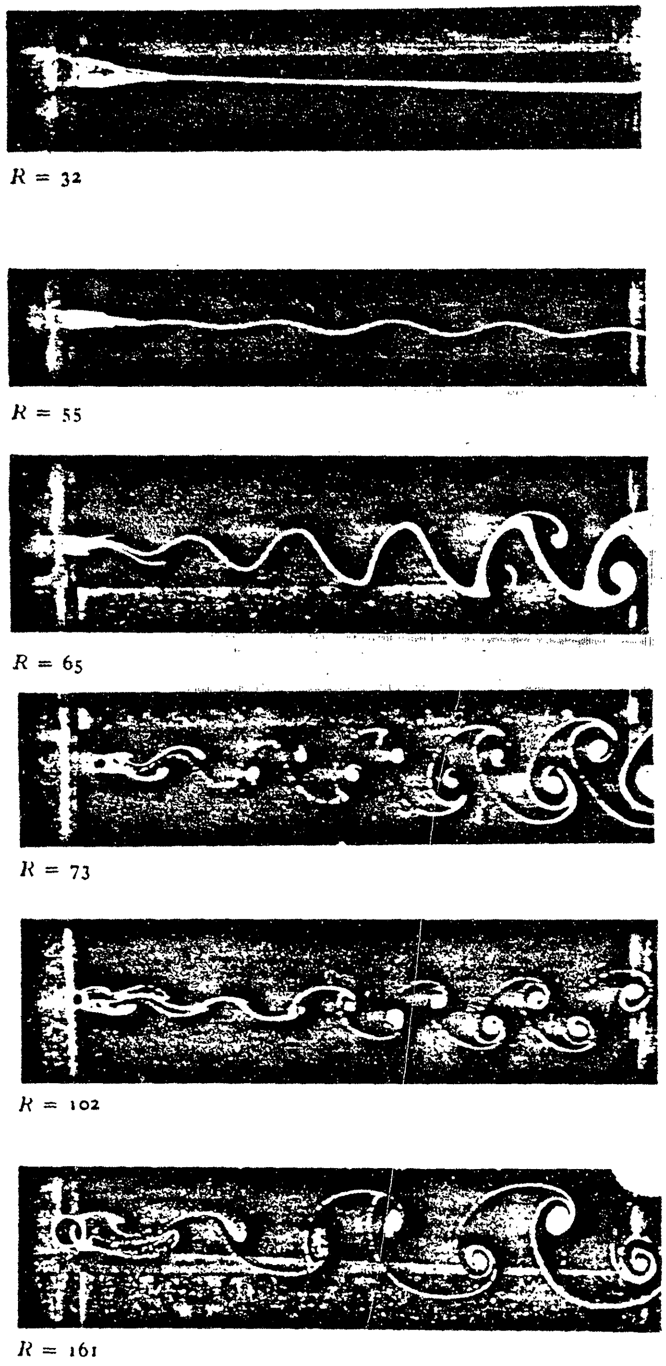

Figure 2.9 Streaklines of the wake behind a cylinder for increasing Reynolds number (from Homann, in Batchelor 1967).

The drag coefficient for flow past a cylinder as a function of the Reynolds number is shown in figure 2.10. It follows equation 2.5 at low *Re*, approaches a nearly constant value at intermediate *Re* and drops sharply when the point of detachment of the wake shifts from in front of the equator of the sphere to in back of the equator.

2.2.2 Viscoelastic Flow Past a Cylinder

Early studies of viscoelastic flow past a cylinder sought analytic solutions for the stream function and drag coefficient at low *De*. Ultman and Denn (1971) used the Oseen approximation to linearize both the equations of motion and the Upper Convected Maxwell model about the streaming velocity. Further restricting the flow to small deformations yielded the infinitesimal Maxwell model of linear viscoelasticity. Their analysis showed that for $ReDe < 1$ the equation set is elliptic and has a continuous solution. However, for $ReDe > 1$ the equation set becomes hyperbolic and discontinuities can propagate along streamlines. They also predicted drag reduction of $O(ReDe)$ and a large upstream shift of streamlines. Their experiments with a cylinder suspended in a cylindrical pipe showed a large upstream shift of the streamlines for aqueous solutions of carboxymethyl cellulose (CMC) and polyacrylamide (PAA). Their analytical technique was criticized by Mena and Caswell (1974) and Zana *et al.* (1975) since it reduced the order of the equations and led to an approximation which was not uniformly valid.

Instead, Mena and Caswell matched outer (Oseen) and inner (Stokes) solutions to obtain a solution valid for the entire flow field for $Re \ll 1$ and $De \ll 1$. They found an $O(De^2)$ decrease in the drag coefficient and downstream shift of the streamlines for an Oldroyd fluid.

Broadbent and Mena (1974) measured the drag on a cylinder in a square duct for an aqueous PAA solution using a linear displacement transducer. Their results showed a quadratic reduction in the drag relative to values for Newtonian fluids for $Re < 0.1$. However, their flow visualization experiments were unable to detect any differences in the streamlines between the PAA fluid and glycerol. Later experiments by Manero and Mena (1981) used fluids consisting of PAA in water and glycerol/water to cover a wide range of *De*. They observed a downstream shift of the streamlines for $De < 1$ and $Re < 0.01$, whereas for $De > 1$ the streamlines were shifted *upstream.*

Dhahir and Walters (1989) examined the effects of fluid rheology on drag force and streamlines by using Newtonian fluids, Boger fluids of PAA in a solvent consisting of corn syrup and water, shear-thinning solutions of PAA/H_2O and solutions of the rigid rod

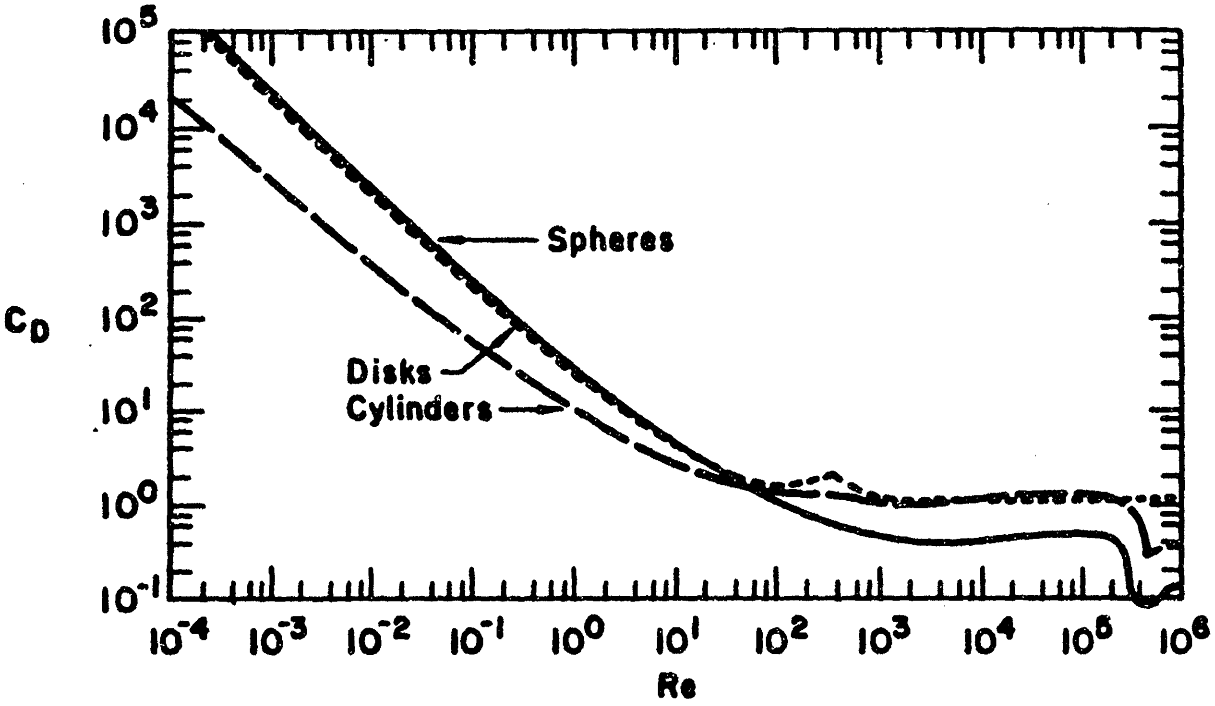

Figure 2.10 Drag coefficient as a function of Reynolds number for flow past a cylinder, sphere and disk (from Lapple and Shepherd 1940).

molecule Xanthan gum, which have a shear-thinning viscosity, but lower normal stresses than the PAA solutions and also a strain-thinning extensional viscosity. Their experiments used a square duct and a cylinder with $R/H = 0.6$ that could be positioned asymmetrically between the channel walls. They found that for an asymmetric arrangement fluid elasticity resulted in relatively less fluid passing through the narrow gap, thereby exaggerating the asymmetry. All fluids showed a decrease in the drag force as the eccentricity of the cylinder was increased, and the viscoelastic fluids also showed a lift force normal to the flow and directed toward the near wall that increased for larger eccentricities. Their calculations using the Generalized Newtonian Fluid and Upper Convected Maxwell models provided qualitative agreement for drag measurements as a function of *De* and eccentricity.

McKinley *et al.* (1993) used LDV to measure quantitatively the effects of elasticity on the flow field past a cylinder centrally mounted in a rectangular channel. They used a PIB Boger fluid and cylinder-channel aspect ratios between 0.17 and 0.50. Measurements of the streamwise velocity along the centerplane showed no changes in the upstream velocity profile with increasing *De*, while the downstream wake was extended with increasing *De*. Flow visualization and LDV were used to show that beyond a critical *De* a flow instability developed in the downstream wake. A steady, cellular structure was formed in which the streamwise velocity became periodic along the neutral direction of the cylinder axis. In figure 2.11, the centerplane of the flow cell has been illuminated by a sheet of laser light, and the periodically spaced bright bands correspond to regions of higher scattering particle density, and therefore higher streamwise velocity. This instability was characterized in terms of its onset conditions and the spatial wavelength of the velocity fluctuations, and it was found that the critical *De* and the ratio of the wavelength to the cylinder radius both increased as the cylinder to channel height ratio was decreased. A second flow transition was also observed at higher *De* when the flow became time-dependent, and the previously stationary cells began to travel outward from the center of the cylinder.

LDV was combined with flow induced birefringence (FIB) by Baaijens *et al.* (1994) to provide the first simultaneous measurements of the velocity and stress for flow past a cylinder. They used a shear-thinning solution of PIB/tetradecane and an aspect ratio of $R/H = 0.49$. Their velocity and first normal stress difference measurements upstream of the cylinder agreed well with their simulations for $De = 0.22$ using a single-mode Phan-Thien–Tanner (PTT) model. However, downstream of the cylinder the measured stresses have different profiles than the calculated values across the channel and relax much more slowly downstream. This discrepancy was attributed to problems with the experimental system that were later corrected.

Studies have also been conducted on the flow of viscoelastic fluids through an array of cylinders. In this geometry, molecules at the upstream stagnation point have already been extended by previous cylinders and the molecular extension can be accumulated through the array. Georgiou *et al.* (1991) studied a single line of eccentrically positioned cylinders in a duct, with alternate cylinders offset to opposite sides of the centerplane. Flow visualization experiments with fluids similar to those used by Dhahir and Walters showed little effect of viscoelasticity on the streamlines for the Boger fluid, whereas less of the aqueous PAA solution passed through the narrow gap between the cylinder and the near wall as *De* was increased. Pressure drop measurements across the geometry showed drag reduction for the PAA solutions, whereas the Boger fluid showed initial drag reduction followed by a large increase in the pressure drop at higher *De*. This same trend was shown qualitatively for calculations with the Oldroyd-B constitutive equation.

Chmielewski and Jayaraman (1993) used flow visualization and LDV to study the flow of a PIB Boger fluid and a PIB/decalin solution through square and hexagonal arrays of cylinders. Beyond a critical Deborah number, streaklines for the Boger fluid become asymmetric, indicating the presence of an elastic instability. The asymmetry was much more pronounced for the square array, and no measurements were take to determine if this was a three-dimensional instability similar to that observed by McKinley *et al.* Flow resistance measurements for the Boger fluid showed increased resistance relative to the Newtonian value for both arrays, with no initial decrease.

Numerical simulations of the flow past a cylinder have also been concerned with the effect of elasticity on the streamlines and drag force. Townsend (1980) used a four-constant Oldroyd model to study flow past a cylinder in an infinite domain with a uniform flow imposed at a distance of 20 cylinder radii. Elasticity was found to cause a small downstream shift of the streamlines, and incorporating a shear-thinning viscosity resulted in a larger downstream shift. The drag was found to decrease for low *Re* (< 0.1) and increase for $Re > 5$, in contrast to the results for a Newtonian fluid, for which the drag coefficient decreases with increasing *Re*. For the range of parameters considered, shear-thinning had little effect on the drag. Townsend (1984) also solved time-dependent flows with the Oldroyd-B model in order to continue calculations up to $De = 5$. A further downstream shift of the streamlines and a greater drag increase were found, as well as a recirculation region behind the cylinder at $Re = 2.5$.

Chilcott and Rallison (1988) proposed a FENE dumbbell constitutive equation for use in time-dependent calculations of creeping viscoelastic flow past cylinders, spheres and bubbles. The fluid was considered to be a dilute solution of noninteracting dumbbells, and separate equations were used for the evolution of the dumbbell extension and the polymeric

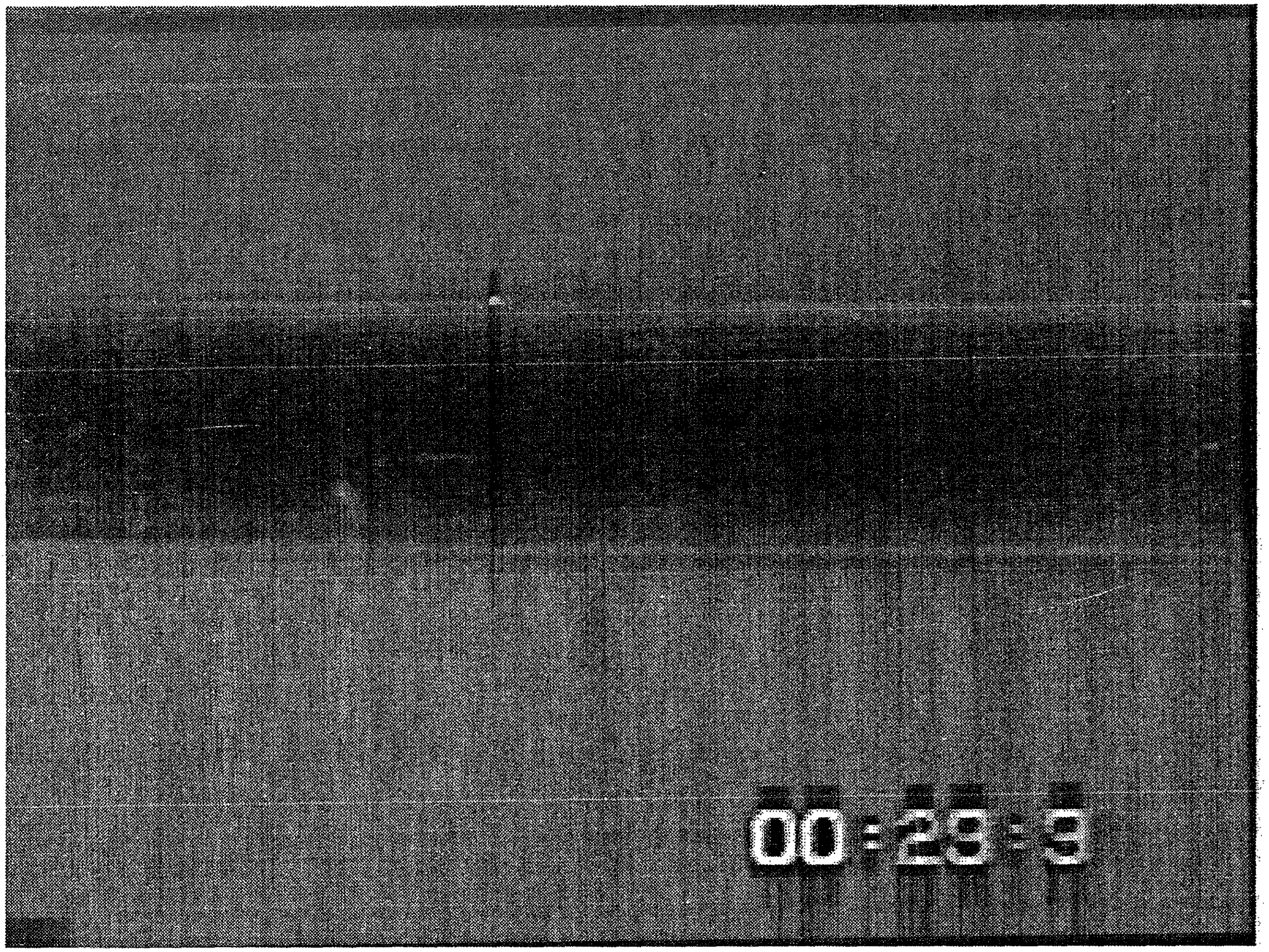

Figure 2.11 Video-image of the cellular structure in the downstream wake of the cylinder for $R/H = 0.5$ and $De = 0.50$ (from McKinley *et al.* 1993).

stress. The flow considered was similar to that of Townsend, in that the cylinder was taken to be in an infinite medium with uniform flow imposed at a constant radial position far from the cylinder. Figure 2.12 shows contours of constant molecular extension for flow past a cylinder at $De = 8$ with flow from left to right. Molecules are highly extended as they approach the upstream stagnation point, in the region of high shear rates along the sides of the cylinder and in the downstream wake. Because the velocity gradients vanish at the stagnation points, molecules at the stagnation points are fully relaxed, and the regions of highest deformation occur slightly away from the stagnation points. The drag was found to increase for $De > 1$ and approach an asymptotic value at high De. The asymptotic value increased when the fully extended length of the dumbbells was increased, due to a higher value of the extensional viscosity. The streamwise velocity accelerated slightly relative to that for a Newtonian fluid immediately downstream of the rear stagnation point, but further downstream there was a large downstream shift of the streamlines.

Carew and Townsend (1991) used both the Oldroyd-B and the PTT models to study the effects of elasticity and shear-thinning in flow past a cylinder in a channel. The cylinder-channel aspect ratio was 0.58, and both symmetrically and asymmetrically positioned cylinders were considered. They found no differences in the streamlines for the Newtonian and Oldroyd-B cases, and the shear-thinning of the PTT model led to a slight upstream shift that increased for high eccentricity. The drag force for both models decreased with increasing De or eccentricity, with the PTT value lower than the Oldroyd-B value for $De > 0.1$. As observed in the experiments of Dhahir and Walters, they also found a transverse force toward the near wall for eccentrically positioned cylinders.

2.2.3 Newtonian Flow Past a Sphere

Stokes obtained an analytic expression for the streamlines of the uniform flow of an unbounded Newtonian fluid of viscosity μ past a stationary sphere for $Re = 0$. He showed that

$$\psi = \frac{1}{4} U_0 R_s^2 \left[\frac{r}{R_s} - \frac{3R_s}{r} + 2\left(\frac{R_s}{r}\right)^2 \right] \sin^2\theta \; . \qquad (2.7)$$

Integration of normal and shear stresses over the surface of the sphere yields the drag force on the sphere

$$F_{St} = 6\pi\mu R_s U_\infty . \qquad (2.8)$$

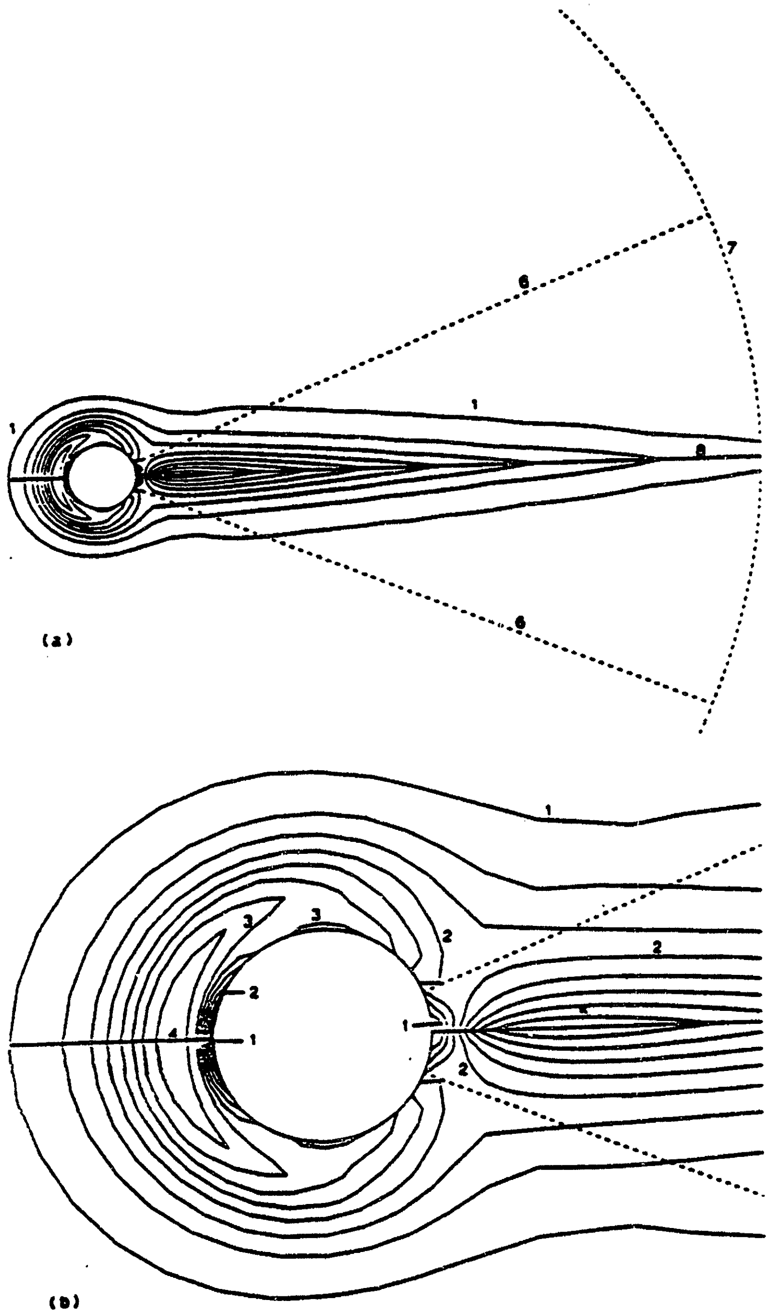

Figure 2.12 Contours of tr[τ_p] for flow past a cylinder for *De* = 8 and *L* = 10. *a)* Overall view showing the extent of the wake and *b)* detail showing high stress gradients near the cylinder (from Chilcott and Rallison 1988).

For a sphere falling through an unbounded liquid at steady state, this force must be balanced by gravity

$$F_{\mathrm{St}} = \frac{4}{3}\pi R_s^3(\rho_s - \rho_f), \tag{2.9}$$

where ρ_s and ρ_f are the densities of the sphere and the fluid, respectively. Knowing the densities and the radius and measuring the terminal velocity of the sphere thus leads to a simple way of measuring the viscosity of a Newtonian fluid in creeping flow.

The drag coefficient of Stokes' flow past a sphere is

$$C_{\mathrm{DS}} = \frac{6\pi\mu R_s U}{\frac{1}{2}\rho U^2 \pi R_s^2} = \frac{24}{Re}, \tag{2.10}$$

where Re is the Reynolds number based on the sphere diameter and unbounded fluid velocity, $2\rho_s R_s U_\infty/\mu$.

A correction to equation 2.10 was obtained by Oseen to account for the effect of a finite Re. Using a singular perturbation technique and matching inner and outer solutions gives

$$C_{\mathrm{D}} = \frac{24}{Re}\left(1 + \frac{3}{16}Re + O(Re \ln Re)\right). \tag{2.11}$$

A far more important correction that must be made to C_{DS} is that required by the presence of the cylinder walls near the sphere. The effect of walls is to increase the drag on the sphere, and the drag enhancement increases with the aspect ratio of the sphere radius to the cylinder radius, R_s/R_c, as was seen above for the presence of channel walls near a cylinder.

Equation 2.8 can be rewritten for a bounded fluid as

$$F = 6\pi\mu R_s(K_1 U_s + K_2 U_0), \tag{2.12}$$

where K_1 and K_2 are the wall correction factors for stagnant fluid and Poiseuille flow, respectively. Bohlin (1960) extended on Faxén's work (1946) using the method of reflections, which gives K_1 and K_2 as an expansion in R_s/R_c.

Haberman and Sayre (1958) expanded the stream function in both cylindrical and spherical coordinates. Matching terms yields an infinite set of algebraic equations, but keeping only the first two gives good agreement with the exact theory for $R_s/R_c \leq 0.5$.

This thesis will be concerned with understanding the effect of increasing the Deborah number at low Reynolds number. The problem of flow evolution with increasing Reynolds number has been the subject of much previous work (See Clift *et al.* 1978). The drag coefficient as a function of Re is shown in figure 2.10. For $Re < 1$ Stokes' law is closely followed, and the streamlines are symmetric fore and aft. As Re increases, the streamlines are shifted downstream, and at $Re = 20$ a steady wake forms behind the sphere and grows with Re.

At higher Re this wake becomes unstable, and vortices are shed from the sphere. Kim and Pearlstein (1990) solved the linear stability problem, and showed that the flow is stable up to at least $Re = 190$ for axisymmetric disturbances, but that a Hopf bifurcation occurs at $Re = 175$ for nonaxisymmetric disturbances.

Vortices are shed at higher frequency at increasing Re, and the drag coefficient is nearly constant over two decades from $Re = 10^3$ to 10^5. At $Re = 3.5\times10^5$, there is a sudden drop in the drag coefficient associated with the boundary layer becoming turbulent, which delays boundary layer separation. Achenbach (1972) has shown that C_D increases slightly at higher Re as the angle of the laminar/turbulent transition moves forward on the sphere.

2.2.4 Viscoelastic Flow Past a Sphere

The goal of past studies of viscoelastic flow past spheres has been to understand the effect of elasticity on velocity profiles, the drag coefficient and wall effects. Only limited efforts have been made toward understanding the stability of the flow with increasing Deborah number.

The earliest study of viscoelastic flow past a sphere was that of Leslie and Tanner (1961), who found that for creeping flow, an expansion in De in the Oldroyd 6-constant model predicts a slight downstream shift in streamlines and an $O(De^2)$ decrease in the drag from the Newtonian case. Caswell and Schwarz (1962) obtained similar results from their study of creeping flow of a third-order Rivlin-Erickson fluid by matching inner and outer expansions of the stream function.

The first experimental study aimed at determining the effects of elasticity on the drag coefficient and streamlines for flow past a sphere was that of Broadbent and Mena (1974). The sphere was held in place in an open channel by a shaft, and the drag was measured by a linear inductance displacement transducer. Using a 2% polyacrylamide (PAA)/H_2O solution, they found that the drag reduction from the Stokes drag was quadratic in velocity for $Re < 0.3$.

Acharya *et al.* (1976) solved for an approximate stream function for flow of a power law fluid past a sphere, from which they obtained an expression for the drag coefficient as a function of the power law index. The drag coefficients for balls falling in solutions of carboxymethylcellulose (CMC) and Carbopol followed their predictions for $Re < 1$. They also studied shear-thinning solutions of PAA and poly(ethylene oxide) (PEO), and found that the drag reduction would be accounted for simply by the shear rate-dependent viscosity and their theory for inelastic fluids.

Numerical simulations have also predicted drag reduction for viscoelastic fluids. Hassager and Bisgaard (1983) used a Lagrangian finite element method and the Upper Convected Maxwell (UCM) model to predict the drag as a function of R_S/R_C and De. They found little deviation from Stokes' law for $R_S/R_C < 0.3$, but at $R_S/R_C = 0.5$ the wall correction factor decreased rapidly with De.

Sugeng and Tanner (1986) obtained similar results for $R_S/R_C = 0.5$ using the modified Phan-Thien–Tanner model. Drag reduction of 40% occurred for a shear-thinning fluid, while a UCM fluid showed drag reduction of 25%.

All of the above studies used shear-thinning polymer solutions. A lower viscosity will lead to drag reduction with respect to the drag calculated based on the zero-shear viscosity, and this can lead to seemingly diminished wall effects. In order to isolate the effects of elasticity from viscous shear-thinning effects, recent efforts toward determining the role of elasticity in drag reduction have focused on Boger fluids, which are highly elastic with a nearly constant viscosity.

Chhabra *et al.* (1980) used a series of PAA/corn syrup (CS) Boger fluids with zero-shear-rate relaxation times of $0.037\ \text{s} \leq \lambda_0 \leq 0.51\ \text{s}$ in falling-ball experiments. Since their largest sphere radius to tube radius ratio, R_S/R_C, was 0.07, no wall correction was made. For $De < 0.1$ they observed no drag reduction, but beyond this De, the ratio of the measured drag to that expected for Stokes' flow decreased to an asymptotic value of 0.74 for $De \geq 0.7$. They observed that drag reduction occurred only at shear rates for which Ψ_1 was shear-thinning. Similar results are reported by Chhabra and Uhlherr (1988) for other PAA/CS Boger fluids.

A careful study of the effect of fluid rheology on drag was carried out by Mena *et al.* (1987) using four types of fluids: Newtonian (glycerol and glycerol/water); an inelastic, shear-thinning fluid (Carbopol/ethylene glycol); an elastic shear-thinning PAA/H_2O solution; and a constant viscosity, elastic PAA/CS Boger fluid. Spheres were suspended from thin wires, and the force required to pull the spheres through the fluids at a constant velocity was measured. At low values of R_S/R_C, the drag reduction for both elastic solutions followed an $O(De^2)$ dependence, as predicted by perturbation theories. However, for the PAA/H_2O solution, the O(De^2) dependence was followed to $De \sim 3$. For R_S/R_C values of 0.375 and 0.5, the drag reduction for the PAA/H_2O solution followed an O(De) dependence. No high R_S/R_C results were reported for the Boger fluid. It was shown that the drag reduction for the inelastic fluid and the shear-thinning PAA/H_2O could be accounted for by considering the shear rate-dependent viscosity. Furthermore, the drag reduction of the Boger fluid followed exactly the trend of Chhabra *et al.* (1980).

In contrast to the drag reduction found for PAA/CS Boger fluids, drag *enhancement* has been observed for polyisobutylene (PIB)/PB Boger fluids. Chmielewski *et al.* (1990) used both PAA/CS and PIB/PB Boger fluids in falling-ball experiments. The drag reduction for the PAA/CS fluid was similar to that of Chhabra *et al.*, while for $De > 0.3$ the drag ratio of the PIB/PB fluid increased, reaching 1.15 at $De = 0.7$. In experiments by Tirtaatmadja *et al.* (1990), test fluid M1 (a PIB/PB Boger fluid) showed a slight decrease in drag for $De > 0.1$, followed by an increase in drag with respect to the Newtonian value for $De > 0.6$. Based on intrinsic viscosity measurements, Chmielewski *et al.* note that PAA molecules in corn syrup are more fully extended relative to their contour length than are PIB molecules in polybutene. In terms of the calculations of Chilcott and Rallison (1988), this implies a higher value of their parameter L for PIB, which has been shown (Lunsmann *et al.* 1993) to lead to drag enhancement. Calculations by Harlen (1990) using the birefringent strand technique also predicted an initial decrease in the drag, followed by an increase at higher De. This method assumes that molecules in a narrow region downstream of the stagnation point (the 'birefringent strand') are fully extended, while molecules outside the region are not extended.

Lunsmann *et al.* (1993) compared the Oldroyd-B, UCM and Chilcott-Rallison models for a sphere falling through a tube. The Oldroyd-B model showed a small downstream shift in the velocity field, but a more pronounced shift in the stress field for both $R_S/R_C = 0.5$ and 0.125. For $R_S/R_C = 0.5$, the modified drag coefficient, K, decreased monotonically with increasing De for all values of the solvent viscosity ratio, as seen in figure 2.13, where $K = K(R_S/R_C, De)$ is the ratio of the drag for a falling sphere in a tube to the drag for a sphere falling through a Newtonian fluid of the same viscosity. The maximum decrease was for the UCM limit of no solvent viscosity, yielding a 30% decrease at $De = 1.5$. A small decrease followed by a larger increase was found for all solvent viscosity ratios for $R_S/R_C = 0.125$, although the maximum deviation from the Newtonian value was 5% at $De = 2$. Calculations with the Chilcott-Rallison model showed that loss of convergence for the Oldroyd-B model was not due to an unbounded extensional viscosity, but rather to the steep stress boundary layers in the sphere wake. The drag coefficient for

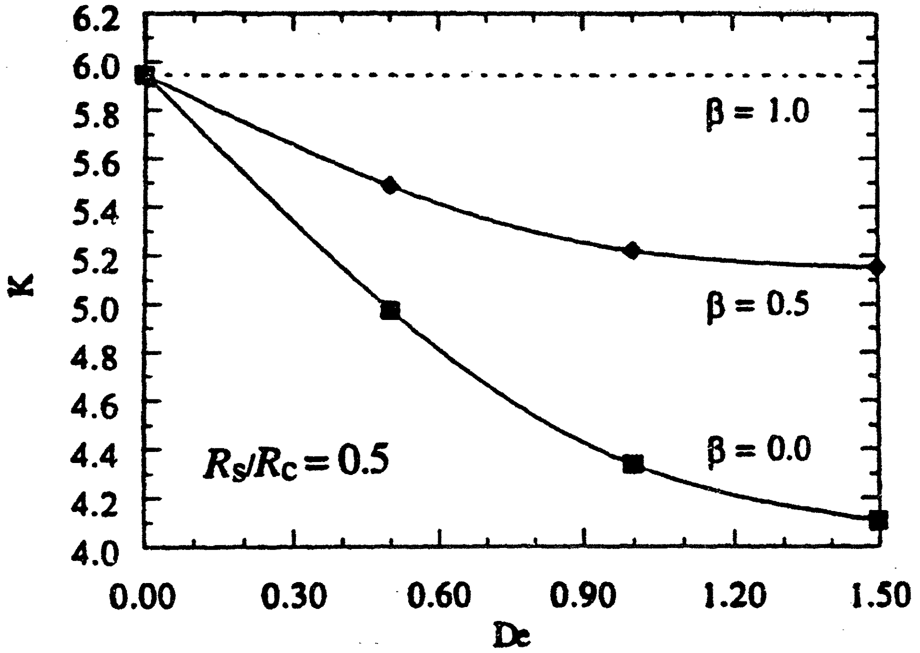

Figure 2.13 Drag coefficient as a function of Deborah number for a falling sphere for the Oldroyd-B model and $R_S/R_C = 0.5$ (from Lunsmann *et al.* 1993).

$R_s/R_c = 0.5$ decreased monotonically with *De*, but for $R_s/R_c = 0.125$ the initial decrease was followed by either an increase for $L \geq 10$, or a further decrease for $L = 5$.

Similar results for the dependence of the drag coefficient on the viscosity ratio, aspect ratio and *L* were obtained by Satrape and Crochet (1994) for the Chilcott-Rallison model. They also showed that for extremely small values of *L* ($L = 3.24$) it was possible to obtain a negative wake for the Chilcott-Rallison model, whereas all previous observations of a negative wake had been for constitutive models or fluids with shear-thinning viscosity. Furthermore, introduction of a second normal stress coefficient with a magnitude as large as 30% of the first normal stress coefficient was found to increase the drag coefficient by just 2%.

While most studies show at least initial drag reduction, there is less agreement on the effect of elasticity on streamlines. Broadbent and Mena's flow visualization by dye injection failed to show any shift in streamlines with respect to Newtonian glycerol/H_2O solutions. A slight upstream shift of the streamlines was observed by Zana *et al.* (1975) for PAA/H_2O solutions. However, the magnitude of the shift was much smaller than that predicted by Ultman and Denn. They found that the amount of the shift and the distance away from the flow axis at which elastic effects could be observed both increased with *De*.

Sigli and Contenceau (1977) obtained axial velocity profiles for spheres falling through a cylinder of $R_s/R_c = 0.5$ past a camera fixed in the laboratory reference frame. The flow is symmetric about the center of the sphere for a Newtonian oil, while the flow pattern is markedly different for a PEO/H_2O solution. The disturbance caused by the sphere in the viscoelastic fluid at the same *Re* extends over a larger distance and is no longer symmetric. Furthermore, near the sphere the fluid moves in the same direction as the sphere, whereas farther downstream the fluid velocity is directed away from the sphere. This has been termed a 'negative wake' by Hassager (1979), who observed the same phenomenon for a bubble rising through a PAA/glycerol solution. The negative wake is a possible explanation for the observation of Riddle *et al.* (1977) that two spheres falling along their centerline converge for small initial separations, but diverge for large initial separations. Figure 2.14 shows the velocity profiles measured by Sigli and Contenceau for their PEO solution as a function of the Deborah number based on the sphere velocity V_0. The velocities are relative to a reference frame moving with the sphere (at $-V_0$ with respect to a laboratory reference frame). $V/V_0 = 1$ is therefore stagnant fluid, while $V/V_0 > 1$ indicates a negative wake. Increasing *De* leads to a greater velocity overshoot and causes the maximum negative velocity to move closer to the sphere. Experiments with different sphere/tube radius ratios showed that increasing R_s/R_c also led to a greater overshoot closer to the sphere.

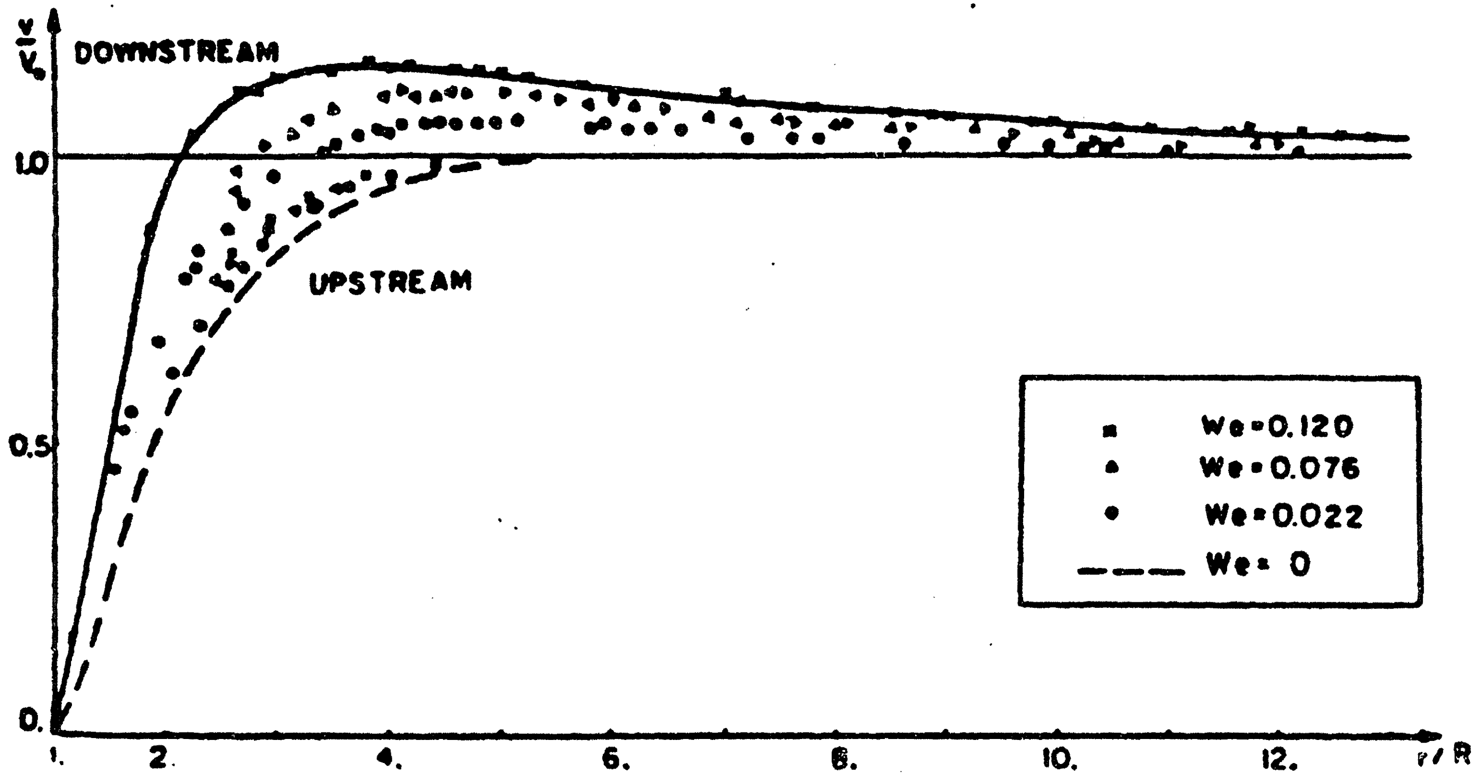

Figure 2.14 Axial velocity profile of a sphere falling through a tube with $R_s/R_c = 0.25$. $V/V_0 > 1$ indicates the presence of a negative wake (from Sigli and Coutanceau 1977).

Bisgaard (1983) used a one-color LDV system focused at a point on the axis of a cylinder filled with 1% PAA in glycerol, and the fluid velocity at that point was measured as a function of time as a sphere fell along the axis. Knowing the sphere velocity allows the data to be converted to velocity as a function of position. The velocity increases as the sphere approaches the measuring volume, and then decreases and becomes negative behind the sphere. The ratio of the magnitude of the maximum negative velocity to the magnitude of the sphere velocity was about 0.04 for $11.4 \leq De \leq 66.5$ and $0.04 \leq R_S/R_C \leq 0.16$. At $De > 40$, oscillations were observed in the axial velocity downstream of the sphere, while the radial velocity remained zero, as seen in figure 2.15. The Fourier spectrum of the velocity signal was calculated, but no dominant frequency was found. By measuring the velocity at a single point as the sphere passes by, it is impossible to distinguish spatial and temporal instabilities in the sphere wake. No such oscillations were observed in a Newtonian fluid (glycerol/H_2O) at a comparable *Re*, and the viscoelastic oscillations were damped at higher Reynolds (and Deborah) number.

An upstream shift in the streamlines very close to the downstream stagnation point followed by a downstream shift was found by Bush (1993) for flow past a sphere held in place on the centerline of a cylinder. LDV measurements of Newtonian fluids and PAA Boger fluids past a sphere with $R_S/R_C = 0.5$ showed an initial acceleration for all *De*, but over a shorter distance downstream as *De* was increased. Similar results were found for finite element calculations using both the Oldroyd-B and PTT constitutive equations, although for the PTT model the extent of the downstream shift was less sensitive to *De*, which was in better agreement with the experimental results. Calculations for a sphere falling through a cylinder showed that the acceleration was greatly reduced at all *De* due to the fact that for the sphere fixed relative to the walls there are higher peak values of the velocity and stress in the downstream wake. Figure 2.16 compares the contours of the tensile stress σ_{zz} for the Oldroyd-B model for the two cases for $De = 0.6$, $R_S/R_C = 0.5$ and $\beta = 0.6$. Bush (1994) extended this work to shear-thinning fluids. Elasticity was again found to cause an initial upstream shift, but a high extensional viscosity was found to reduce the shift. Increasing the ratio *De*/*Tr* was also shown to enhance the negative wake, where *Tr* is the Trouton ratio, $\bar{\eta}(\dot{\varepsilon})/\eta(\sqrt{3}\dot{\varepsilon})$, where $\dot{\varepsilon} = U_S/\sqrt{3}\,R_S$.

Becker *et al.* (1993) used a digital imaging system to measure the transient velocity of a sphere released from rest. An aspect ratio of 0.24 was used for all spheres, and the test fluid was a PIB Boger fluid. An initial overshoot in the sphere velocity was observed, followed by a monotonic decrease to a steady value. At the highest *De*, the velocity overshoot was nearly 50% of the steady value. Based on the steady settling velocity, it was found that there was a drag decrease at low *De*, followed by an increase at higher *De*. A

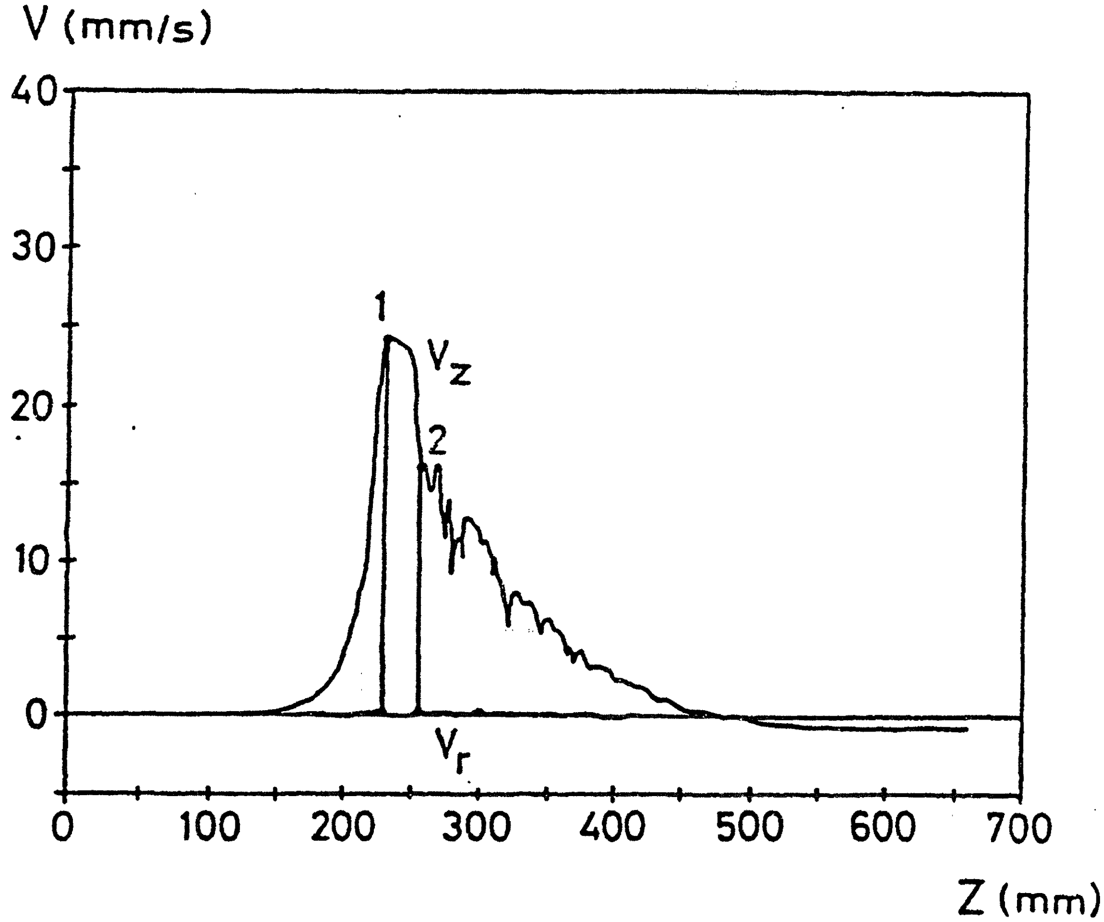

Figure 2.15 Instability in the axial velocity in the wake of a falling sphere, $R_s/R_c = 0.12$, $De = 47.6$ (from Bisgaard 1983).

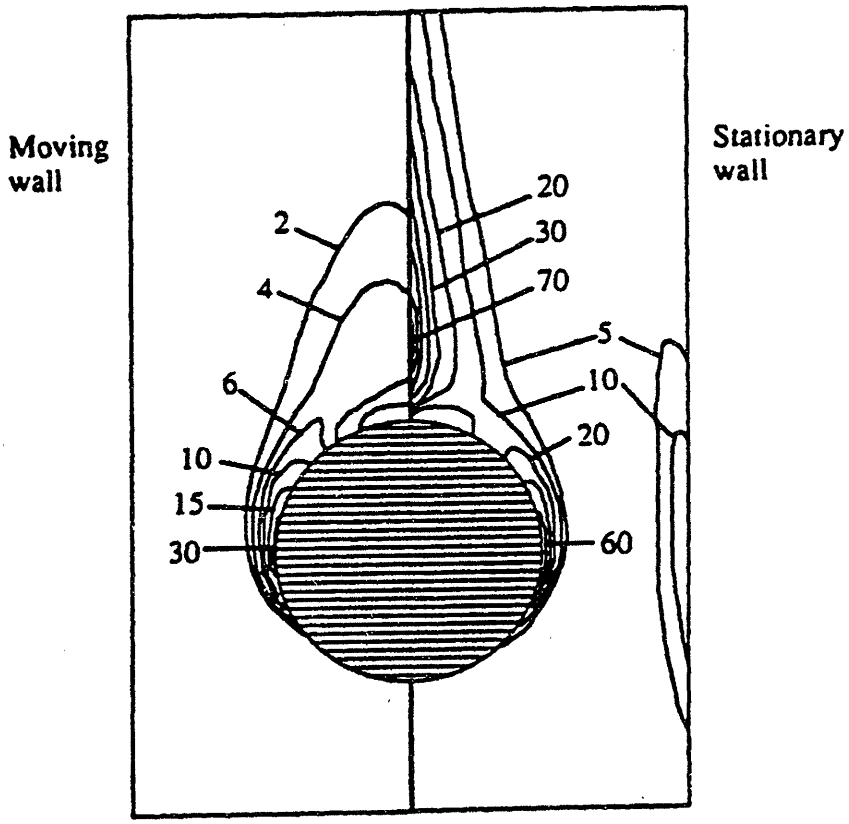

Figure 2.16 Contours of axial stress σ_{zz} for a falling sphere and a stationary sphere for the Oldroyd-B model with $\beta = 0.6$ and $De = 0.6$ (from Bush 1993).

Lagrangian finite element method was also used with both single- and multimode Oldroyd-B models to calculate the transient velocity profile. The single mode calculations show an initial overshoot, although its magnitude is much higher than experimentally observed and nearly independent of *De*. The four-mode model was able to incorporate both the short time constants that determine the initial velocity overshoot, and the long time constants that influence the velocity decay rate, thereby giving much better quantitative agreement, especially at high *De*.

2.2.5 Stagnation Flow Instabilities

Flow past a sphere and flow past a cylinder are both complex mixtures of shearing and extensional flows, although as seen in §§2.1-4, one of the most important features of these flows is the rear stagnation point in each geometry. This section briefly considers studies of purely extensional flow as it relates to flow instabilities.

Lagnado *et al.* (1984) considered the stability of the entire class of unbounded two-dimensional linear flows that can be generated in a four-roll mill. By varying the relative rotation speeds and directions of the rollers, pure rotational, simple shear and pure extensional flows can be generated, as well as all intermediate flows. For the special case of pure extensional flow, they showed that vorticity disturbances that are aperiodic in the direction of the inlet streamlines will grow in time provided that the wavenumber in the neutral direction is sufficiently small. In this case, the growth rate of the disturbance vorticity from vortex line stretching in the base flow is greater than the decay rate due to viscous diffusion in the neutral direction.

This analysis was extended (Lagnado *et al.* 1985) to a general Oldroyd model in which the fluid rheology was varied by using a time derivative in the constitutive equation that was allowed to vary from corotational (yielding a shear-thinning viscosity and constant extensional viscosity) to codeformational (yielding constant viscosity and strain-thickening extensional viscosity). For the codeformational derivative, the Oldroyd-B model was recovered, and the Newtonian solution was modified by extending slightly the range of unstable wavenumbers. However, for intermediate forms of the time derivative, there was less destabilization or even stabilization at low *De*, but beyond a critical *De* the flow was unstable to all wavenumbers in the neutral direction.

Flow visualization experiments of the flow of a Newtonian fluid (glycerol/water) in a four-roll mill by Lagnado and Leal (1990) showed that for a finite geometry the transition to three-dimensional flow was primarily an end effect. For a value of the roller length to gap width between rollers aspect ratio of 3.4, the flow was nearly two-dimensional throughout the geometry for $Re < 5$, but as the Reynolds number was increased, pairs of vortices formed at the ends of the geometry and grew until they met at the horizontal midplane at $Re = 37$. At higher Re the flow lost its symmetry about the horizontal and vertical midplanes, and for $Re > 60$, the flow became unsteady. For an aspect ratio of 12.7, the end vortices did not grow enough to touch one another, and cells did not form along the entire length of the rollers. For $Re > 37$ the vortices at each end became asymmetric, and for $Re > 55$ vortices were periodically shed inward from each end.

Kerr and Dold (1994) also considered a two-dimensional linear stagnation flow, $U = (0, Ay, -Az)$, and showed that it was unstable to three-dimensional disturbances. They showed that any nonlinear disturbance that initially had no component in the direction of the outgoing streamlines (y) would not develop a streamwise component, and that solutions existed that consisted of periodic rows of steady conterrotating vortices with their axes parallel to the outgoing flow direction, as shown in figure 2.17. The vortices were characterized in terms of two parameters: the strength of the converging flow relative to the rate of viscous dissipation and the amplitude of the solutions, A. As the strength of the flow was increased, the vortices were confined to a smaller region near the plane $z = 0$, and as the amplitude was increased, the vortices developed into a spiral flow.

The stability of a planar extensional flow of a dilute solution of linear-locked dumbbells was studied by Harris and Rallison (1994) using the birefringent strand technique of Harlen *et al.* (1990) At high De, dumbbells along the outgoing flow axis are assumed to be fully extended with a narrow region known as the birefringent strand, while outside the strand the dumbbells are fully relaxed. Two different instabilities of the strand were found. At moderate De, the strand is unstable to varicose disturbances in which the strand width is unsteady. The perturbations to the strand width affects the extension of dumbbells entering the strand, which in turn reinforces the perturbation. At higher De, a sinuous instability occurred in which the strand lost its symmetry about the midplane of the flow. Both of these instabilities were shown to agree qualitatively with instabilities observed in the experiments of Müller *et al.* (1988) for flow in an axisymmetric opposed jet.

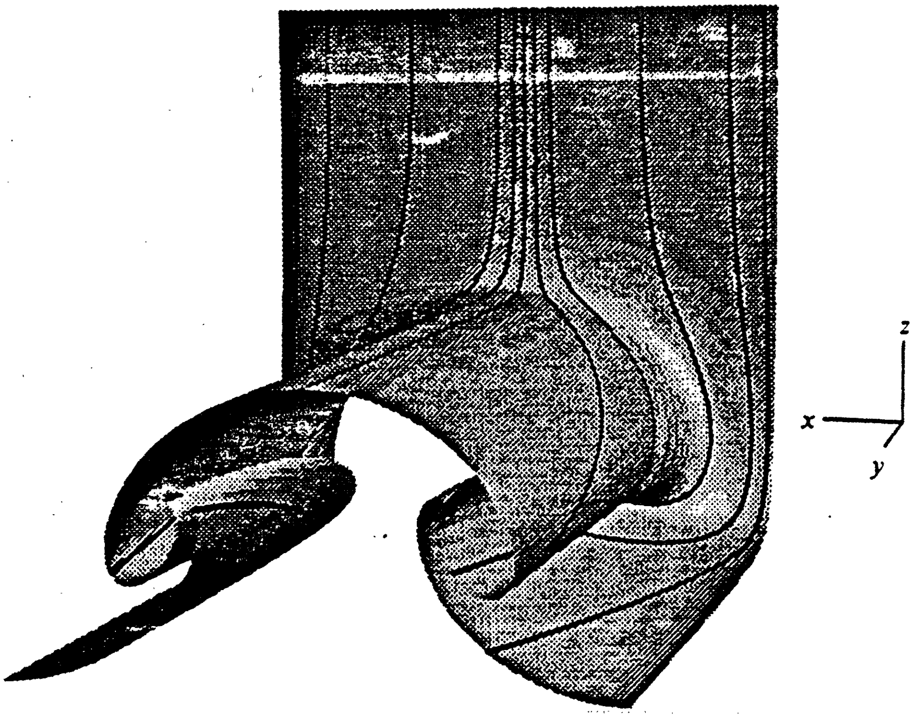

Figure 2.17 Three-dimensional representation of the periodic vortices, showing a sheet of fluid being swept into the vortices (from Kerr and Dold 1994).

2.3 Plane Poiseuille Flow of Superposed Fluids

The flow of two superposed Newtonian fluids in plane Poiseuille flow is shown schematically in figure 2.18. The interface of the fluids is defined as $y = 0$, and the velocity profile for the fluids is determined by the ratio of the viscosities of the fluids, $m = \mu_2/\mu_1$, and the depth ratio, $n = d_2/d_1$ as

$$U_1 = 1 + a_1 y + b_1 y^2, \tag{2.13a}$$
$$U_2 = 1 + a_2 y + b_2 y^2, \tag{2.13b}$$

where $a_1 = (m - n^2)/(n^2 + n)$, $b_1 = -(m + n)/(n^2 + n)$, $a_2 = a_1/m$ and $b_2 = b_1/m$, and the velocities are nondimensionalized with respect to the interface velocity, U_0. The maximum velocity occurs in the less viscous fluid, and because the velocities are lower in the more viscous fluid, it occupies a greater depth than the less viscous fluid for equal flowrates. Figure 2.18 shows the stable base flow with the interface between the fluids located at $y = 0$ for all x, and this section reviews previous studies of instabilities of the interface. In contrast to the purely elastic instabilities discussed above, an interfacial instability can occur even for Newtonian fluids at $Re = 0$, although elasticity modifies the neutral stability diagram. The interfacial instability also depends on a wide range of other parameters, including the viscosity ratio, the depth ratio, the density ratio ($r = \rho_2/\rho_1$) and surface tension. Previous efforts to determine the dependence of the interfacial instability on these parameters for Newtonian fluids are discussed in §2.3.1, and the effects of shear-thinning viscosity and elasticity are shown in §2.3.2.

2.3.1 Newtonian Fluids

The stability of the interface between two fluids in plane Poiseuille flow to long wavelength disturbances of the form $\psi = f(y)\exp[i\alpha(x - ct)]$ was considered for Newtonian fluids of different viscosities by Yih (1967). It was shown that for fluids of equal depths and equal density ($n = r = 1$), the flow was unstable if the two fluids had different viscosities.

Yiantsios and Higgins (1988) extended Yih's results to unequal layer depths, and showed that the interface is in general neutrally stable if the shear rate is continuous across the interface, which occurs when the depth ratio is equal to the square root of the viscosity ratio, $n_{\text{crit}} = m^{1/2}$. The neutral stability diagram for longwave disturbances is shown in figure 2.19. They studied a wide range of parameters affecting the interfacial stability, and

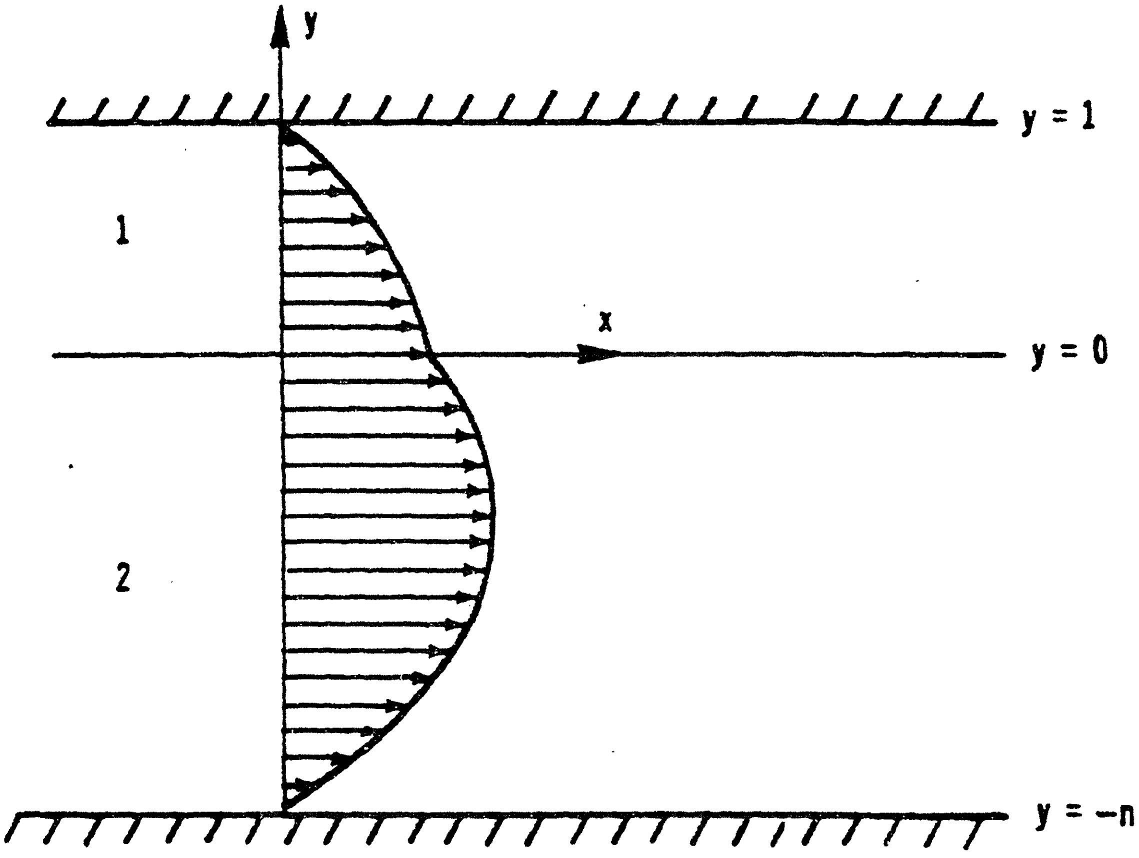

Figure 2.18 Schematic diagram of plane Poiseuille flow of two superposed fluids (from Yiantsios and Higgins 1988).

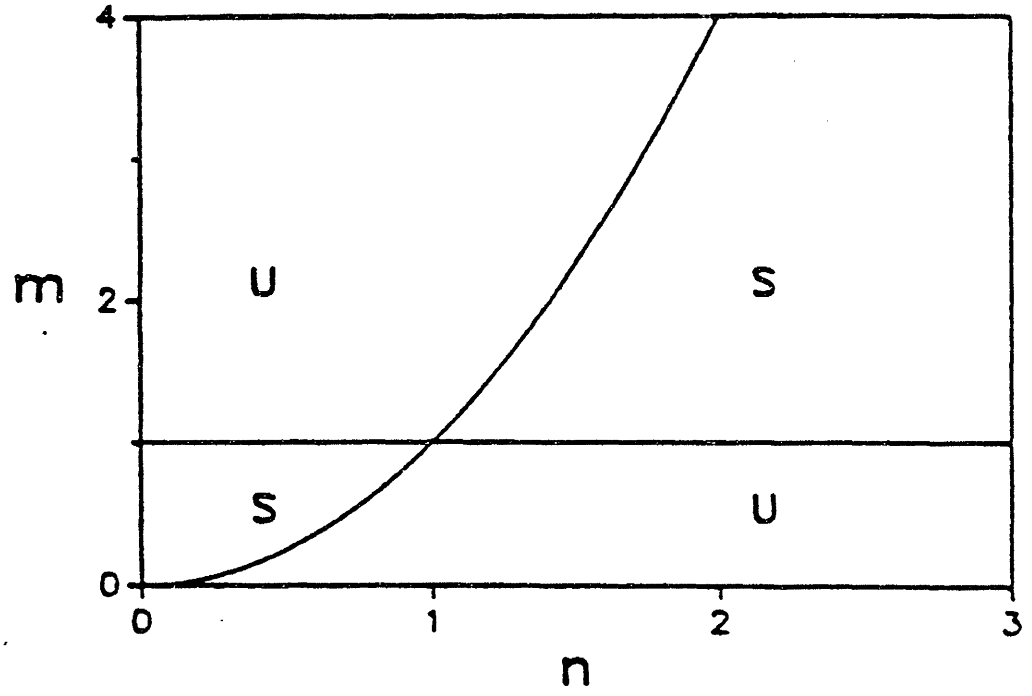

Figure 2.19 Neutral stability diagram for long-wavelength disturbances in Newtonian fluids for $r = 1$; S denotes stable regions, U denotes unstable regions (from Yiantsios and Higgins 1988).

also considered large wavenumber disturbances. The neutral stability diagram in the α-n plane is shown in figure 2.20 for a viscosity ratio of $m = 20$ and $F = \Sigma = 0$, where $F = (r - 1)gd_1/U_0^2$ and $\Sigma = \sigma/\rho_1 d_1 U_0^2$ express the effects of gravity g and surface tension σ, respectively. The results are shown for $Re = 10$, but the neutral stability diagram was not significantly altered for $0 \leq Re \leq 20$. The flow was neutrally stable to all wavenumbers for $n_{\text{crit}} = m^{1/2}$, and for small wavenumbers, the neutral stability diagram was the same as figure 2.19. However, for wavenumbers of $O(1)$ or greater the flow was stabilized when the depth of the more viscous fluid was below the critical value, *i.e.* $n < m^{1/2}$, although the flow was unstable for thin layers of the more viscous fluid ($n \ll m^{1/2}$). For shortwave disturbances ($\alpha \gg 1$), the stable region decreased, and the flow was asymptotically unstable everywhere except for $n = m^{1/2}$. The stabilizing effect of interfacial tension is shown in figure 2.21, which is for the same parameters as figure 2.20, except $\Sigma \neq 0$. All wavenumbers were stabilized by surface tension, although the amount of stabilization decreased for small wavenumbers. Gravity stabilized the flow at all wavenumbers when the lower fluid was the more dense ($r > 1$), but was destabilizing if the upper fluid was the more dense ($r < 1$), as shown in figure 2.22.

Hooper and Grimshaw (1985) considered the nonlinear evolution of the instability, and they found that surface tension and nonlinear effects would cause the instability either to return to the undisturbed state or to evolve to a finite amplitude steady state. They showed that surface tension stabilized disturbances with wavenumbers above $\alpha_c = (d/s)^{1/2}$, where d is the growth rate of the linear instability and s is a dimensionless surface tension. Unstable waves were shown to grow initially and evolve to a steady state containing just a few harmonics or to a quasiperiodic state in which energy was exchanged between several two-mode states.

Anturkar *et al.* (1990) showed that the introduction of a third layer could significantly alter the neutral stability curves. If the middle fluid were more viscous than the outer fluids (which had equal viscosity), the flow became more stable to large wavenumber disturbances for small values of the ratio of the flowrates of the middle and bottom layers (q_2/q_1, analogous to n above) as the flowrate of the third layer (q_3) was increased. The neutral stability curve at $n = m^{1/2}$ for the two-fluid case also shifted to lower values of q_2/q_1 as q_3 was increased. As seen above in figure 2.22, gravity was able to stabilize the flow for all wavenumbers at certain ratios of the flowrates, but only if each layer were more dense than the one above it; otherwise, gravity was destabilizing.

Very little experimental data is available for the interfacial instability for Newtonian fluids. Yu and Sparrow (1969) showed photographs of interfacial waves for a mineral oil/water system with a viscosity ratio of $m = 30$, but neither the onset conditions nor the

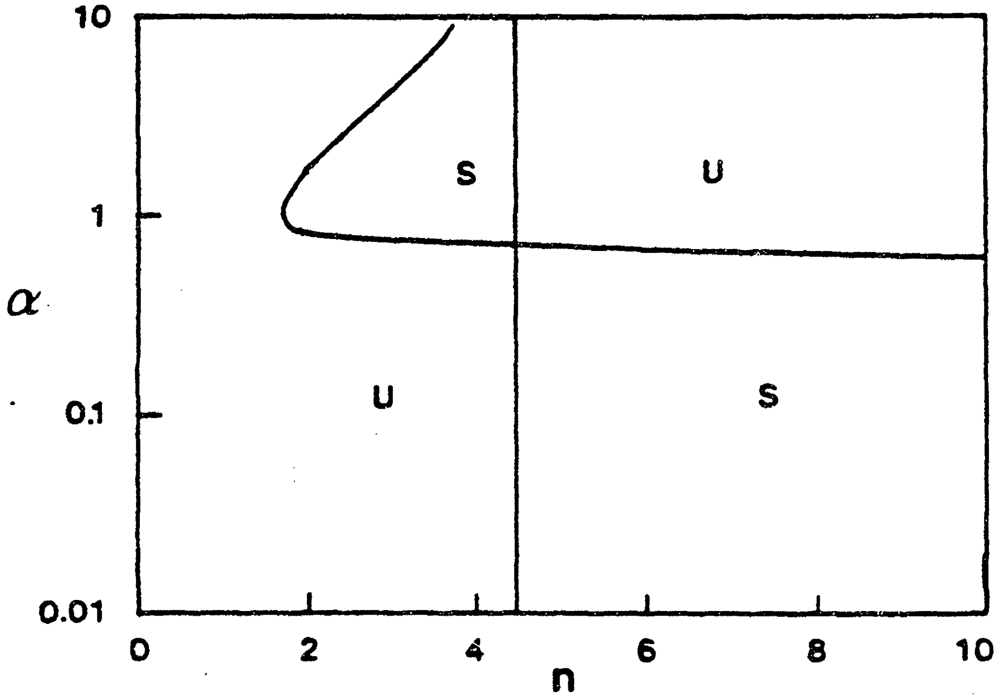

Figure 2.20 Neutral stability diagram for Newtonian fluids for $Re = 10$, $m = 20$, $r = 1$, $F = \Sigma = 0$; S denotes stable regions, U denotes unstable regions (from Yiantsios and Higgins 1988).

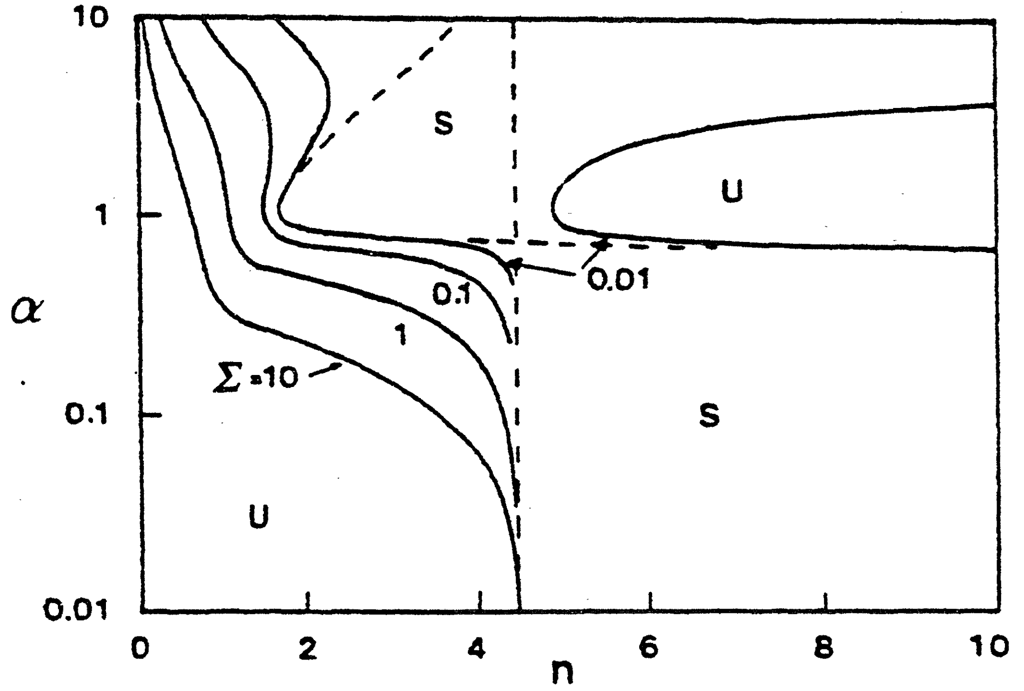

Figure 2.21 Effect of interfacial tension on the neutral stability diagram for Newtonian fluids for $Re = 10$, $m = 20$, $r = 1$, $F = 0$. The dashed curve is for $\Sigma = 0$; S denotes stable regions, U denotes unstable regions (from Yiantsios and Higgins 1988).

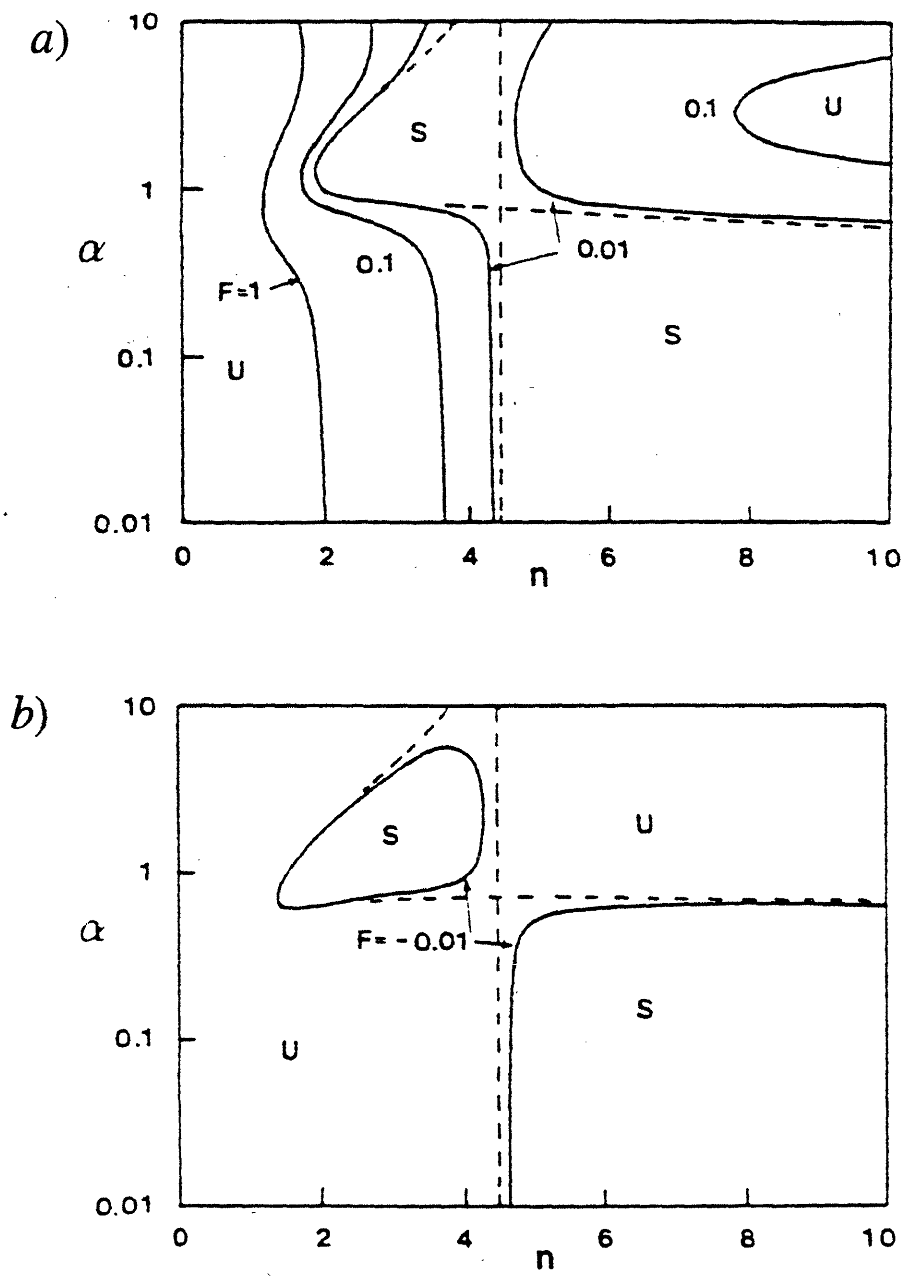

Figure 2.22 Effect of density stratification on the neutral stability diagram for Newtonian fluids for $Re = 10$, $m = 20$, $\Sigma = 0$ and $a)$ $r = 1.5$ and $b)$ $r = 0.5$. The dashed curves are for $F = 0$; S denotes stable regions, U denotes unstable regions (from Yiantsios and Higgins 1988).

disturbance wavenumber was reported. The only quantitative experimental study of instabilities of plane Poiseuille flow of Newtonian fluids was conducted by Kao and Park (1972) using a mineral oil/water system with $m = 20$ and $n = 1$. A mechanical exciter was used to introduce sinusoidal disturbances of varying frequency and amplitude, and the downstream amplitude was measured by a wave gauge. They were able to measure the growth or decay rates of disturbances over a wide range of Reynolds numbers and constructed an experimental neutral stability diagram in terms of the wavenumber and Reynolds number. They showed that the flow was stable to all disturbances below $Re = 2300$, based on the properties of water and the channel perimeter. However, the instability that they observed was not the interfacial instability discussed above, but rather a shear instability mode that exists only at high Re, and is also unstable for the case of a single fluid for $Re \sim 5800$. A careful interpretation of these results by Yiantsios and Higgins showed that for the parameters of the experiment, both surface tension and gravity were sufficiently strong stabilizing forces that the interfacial mode was in fact expected to be stable at lower Re.

2.3.2 Non-Newtonian Fluids

The effects of inelastic non-Newtonian fluids and viscoelastic fluids on the interfacial stability has also been studied. The stability boundaries are sensitive to shear-thinning of the viscosity, and even small levels of elasticity influence the instability. Experiments with polymer melts have shown agreement with analyses that have been conducted for the Oldroyd-B model, although no systematic study of the effects of elasticity has been conducted.

Khomami (1990a, b) showed that the longwave asymptotic stability diagram of Yih for two Newtonian fluids was significantly altered for the flow of power-law fluids or truncated power-law fluids, which have a constant viscosity below a critical shear rate. For these models, the viscosity ratio was defined based on the shear rate at the interface, which presented difficulties for the power-law model if the shear rate was too low, since the less viscous fluid could become the more viscous fluid. It was found that the truncated power-law fluids were more unstable than Newtonian fluids, especially at high depth ratios. In this case the shear rate at the interface was high, and the effects of shear-thinning were the greatest.

Pirarbasi and Liakopoulos (1995) presented the linear stability analysis for the superposed flow of two Carreau-Yasuda fluids (Bird *et al.* 1987a). The viscosity for the Carreau-Yasuda model can be written as

$$\eta(\dot{\gamma}) = \eta_0\left[1 + (\lambda\dot{\gamma})^a\right]^{(v+1/a)} \tag{2.14}$$

for each layer, where λ determines the shear rate at which shear-thinning begins, v is the power-law index and the value of a determines the transition region between the zero-shear-rate and power-law regions. The stability diagram as a function of v and the depth ratio n is shown in figure 2.23 for $m = 20$, $\lambda = 1$ and $a = 3$ for each fluid and neglecting gravity and surface tension. The Carreau-Yasuda model is similar to the truncated power-law model, and in agreement with Khomami's results, longwaves were destabilized as the degree of shear-thinning increased, and it was further shown that shortwaves were also destabilized. Increasing the value of λ stabilized shortwaves below the critical depth ratio while destabilizing the longwaves above the critical depth ratio, and increasing the viscosity ratio destabilized the flow at all wavenumbers.

The effects of elasticity on the interfacial instability were incorporated by Su and Khomami (1992a) by using the Oldroyd-B model. In order to study purely elastic instabilities, they used fluids of equal viscosity and density in each layer. Their longwave asymptotic analysis showed that the interface was unstable if the more elastic fluid occupied less than half the channel height, and their pseudospectral numerical technique further showed that all wavenumbers were unstable. Furthermore, shortwaves were destabilized even when the more elastic fluid occupied more than half the channel ($n < 1$). Calculations of the growth rates showed that the magnitude of the growth or decay rate increased when the jump in the normal stress difference across the interface was increased, and that the fastest growing wavenumber was always of $O(1)$.

This analysis was extended (Su and Khomami 1992b) by using a modified Oldroyd-B model, in which the constant viscosity was replaced by a shear-thinning viscosity described by a truncated power-law function. Figure 2.24 shows that for two elastic fluids at low (and equal) Deborah numbers, all wavenumbers were stabilized for depth ratios above the critical value $n > m^{1/2}$, while shortwaves were destabilized for depth ratios just below $m^{1/2}$. Figure 2.25 shows similar neutral stability diagrams, but in this case the Deborah number of the more viscous fluid was one-tenth of that for the more viscous fluid. Comparing figures 2.25(*a*) with 2.24(*b*) and 2.25(*b*) with 2.24(*c*) shows that reducing the relaxation time of the more viscous layer substantially stabilizes the flow. Whereas for Newtonian fluids Yiantsios and Higgins showed that inertia had little effect on the stability for $Re \leq 20$, $Re = 0.5$ was shown to overcome the stabilizing effect of elasticity for $De = 0.01$ and destabilize the interface for depth ratios above the critical value,

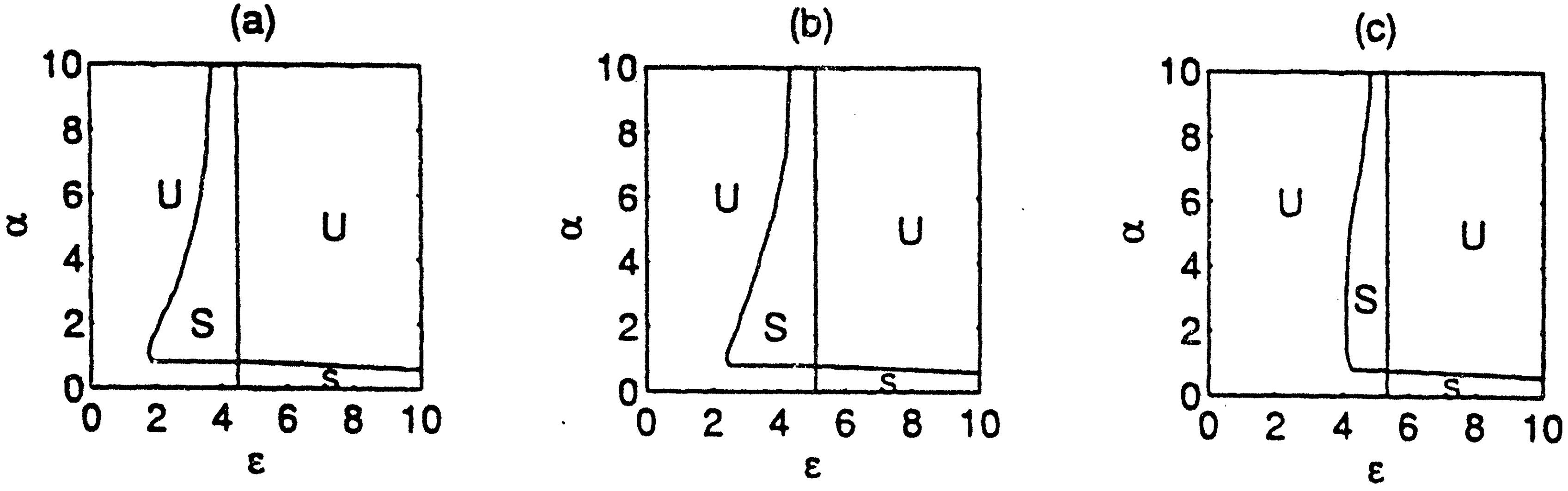

Figure 2.23 Neutral stability diagrams for two Carreau-Yasuda fluids for $Re = 0.1$, $m = 20$, $r = 1$, $F = \Sigma = 0$, $\lambda_1 = \lambda_2 = 1$, $a_1 = a_2 = 3$ and *a)* $\nu_1 = \nu_2 = 1$, *b)* $\nu_1 = \nu_2 = 0.5$ and *c)* $\nu_1 = \nu_2 = 0.25$; S denotes stable regions, U denotes unstable regions (from Pinarbasi and Liakopoulos 1995).

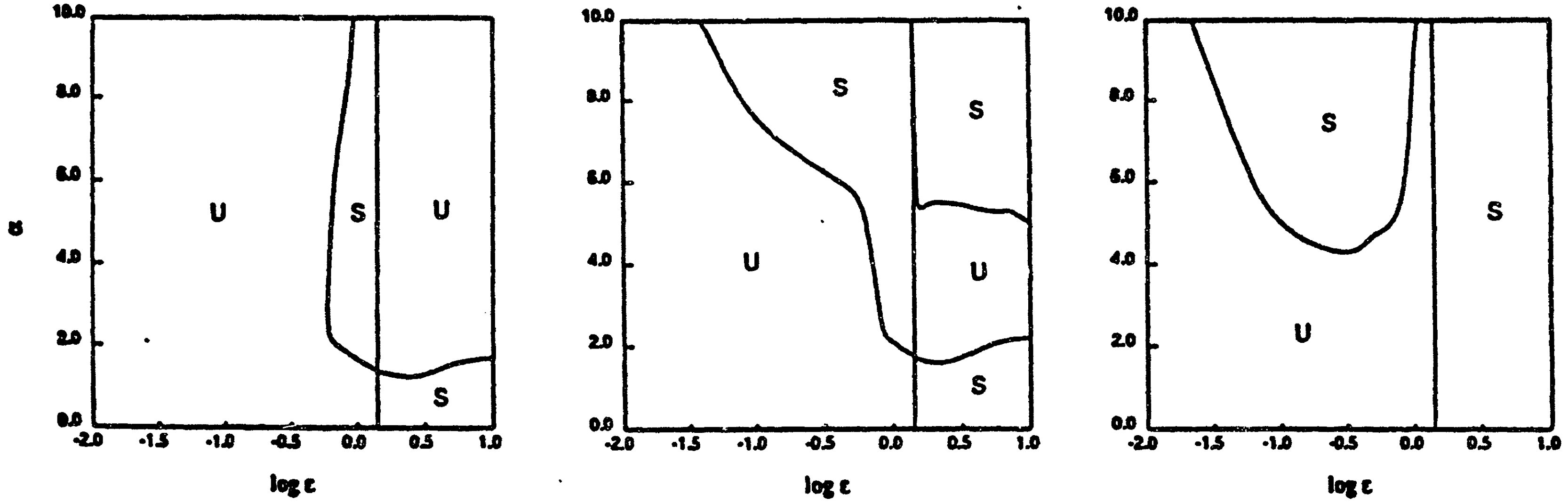

(a) (b) (c)

Figure 2.24 Neutral stability diagrams for Newtonian and Oldroyd-B fluids for $Re = 0.1$, $m = 2$, $r = 1$, $F = \Sigma = 0$. *a*) Newtonian, *b*) Oldroyd-B, $De_1 = De_2 = 0.003$, $\beta_1 = \beta_2 = 0.1$ and *c*) Oldroyd-B, $De_1 = De_2 = 0.01$, $\beta_1 = \beta_2 = 0.1$; S denotes stable regions, U denotes unstable regions (from Su and Khomami 1992a).

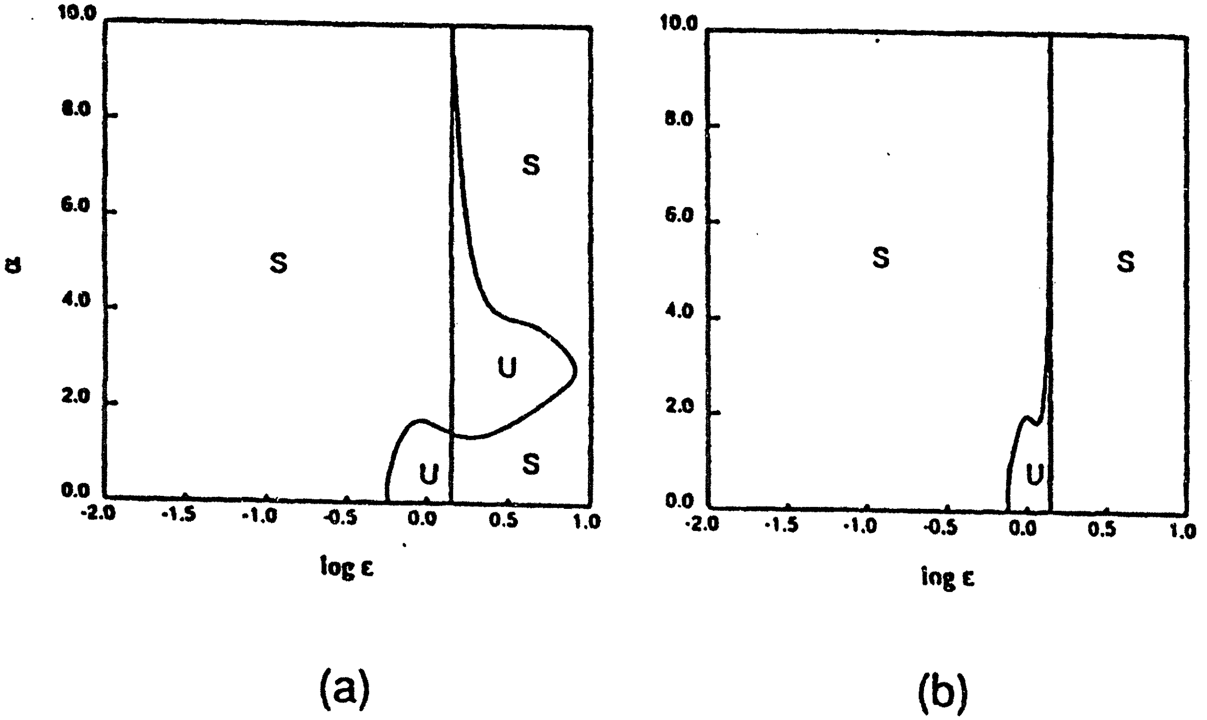

Figure 2.25 Neutral stability diagrams for Oldroyd-B fluids for $Re = 0.1$, $m = 2$, $r = 1$, $F = \Sigma = 0$. *a)* Oldroyd-B, $De_1 = 0.003$, $De_2 = 0.0003$, $\beta_1 = \beta_2 = 0.1$ and *c)* Oldroyd-B, $De_1 = 0.01$, $De_2 = 0.001$, $\beta_1 = \beta_2 = 0.1$; S denotes stable regions, U denotes unstable regions (from Su and Khomami 1992a).

$n > m^{1/2}$. The shear-thinning viscosity in the modified Oldroyd-B model led to complicated neutral stability diagrams in which at small depth ratios the flow was destabilized because of the decreased viscosity due to the high shear rate at the interface, and at intermediate depth ratios the stability was very sensitive to the Deborah and Reynolds numbers.

Although the analyses described above have shown that the interfacial stability depends on a wide range of parameters, few quantitative experimental studies have been conducted. The experiments of Wilson and Khomami using polymer melts provide a basis for comparison with the linear stability analyses, but no studies have been performed with polymer solutions. The composition of Boger fluids can be modified to study more easily the effects of elasticity on the interfacial instability.

Early experimental studies of the interfacial instability in polymer melts examined extruded products to determine if the interface was stable for a given set of operating conditions and materials, but did not attempt to determine growth rates or wavenumbers of the instabilities. Han and Shetty (1978) coextruded three- and five-layer films of low density polyethylene (LDPE) and polystyrene (PS) and of high density polyethylene (HDPE) and PS, and photographs of the extruded product showed an irregular structure in the plane of the flow direction and neutral direction (the x-z plane of figure 2.18), but the structure in the x-y plane was not shown. No instability was observed with the PS/HDPE system for any flow configuration, and this was attributed to the fact that the viscosities of the two materials were comparable over the range of conditions tested. However, the PS was much more viscous than the LDPE, and an instability was observed when PS formed the outer layers, but not when it was core, although the analysis of Anturkar *et al.* indicated that multilayer coextrusion of Newtonian fluids should be more unstable with the more viscous component as the core layer.

Schrenk *et al.* (1978) studied multilayer coextrusion using high impact PS and an acrylonitrile-butadiene-styrene (ABS) copolymer, and they attempted to show that the instability was related to a critical interfacial shear stress. They were able to study the interface shape by stopping the extruders, cooling the melt and then removing the polymer. Inspection of the product showed that for 'incipient instability' the interface was periodic in both the streamwise and neutral directions, and that higher flowrates led to 'severe instability', in which the wave crests in the streamwise direction had folded over and the structure was irregular in the neutral direction, as was found by Han and Shetty.

Twelve different polymer melts were used in 17 different two-fluid combinations by Han *et al.* (1984). Rheological data were coupled with calculations using a truncated power-law model to correlate the conditions for the onset of the instability with the interfacial conditions. Their results showed that there was not a critical interfacial shear stress for the onset, in contrast to the speculation of Schrenk *et al.* As Han and Shetty found for the multilayer coextrusion system, it was difficult to separate the effects of viscosity and elasticity stratification, since almost all of the unstable conditions corresponded to having the less elastic, more viscous fluid occupy more than half the channel. In only one case was the less elastic fluid also the less viscous, and this case was stable.

A more detailed series of experiments aimed at constructing a neutral stability diagram under a variety of experimental conditions was conducted by Wilson and Khomami (1992, 1993a, b; Khomami and Wilson 1995). Polypropylene (PP) and HDPE were coextruded through a metal die with four sets of optical windows along its length that allowed the interface to be viewed. Images of the flow were recorded at each window, and the images were analyzed to determine the growth or decay rates of disturbances to the interface. These disturbances were introduced with a controllable frequency and amplitude by periodically pulsing the flowrate of one of the polymers, thereby allowing the stability of a wide range of wavenumbers to be studied.

Experimental measures of the growth rate are shown in figure 2.26 as a function of the wavenumber based on the depth of PP (the more viscous and more elastic fluid), and growth rates as small as 0.0002 cm/cm could be resolved. Although a different range of wavenumbers was unstable for each depth ratio, the maximum growth rate always occurred near $\alpha = 1$. Theoretical results from a modified Oldroyd-B model (using a truncated power-law function for the viscosity) and the 'local-property' Oldroyd-B model using values of the viscosity and relaxation time based on the shear rate at the interface rather than the zero-shear-rate values predicted higher growth rates than observed experimentally. The modified Oldroyd-B model predicted a maximum growth rate near $\alpha = 1$, and although the 'local property' model gave better quantitative agreement in the range $0 \leq \alpha \leq 1$, it predicted a maximum growth rate for $\alpha = 3$ and high growth rates for wavenumbers up to $\alpha = 6$. The stability diagram for these experiments is shown in figure 2.27 along with the neutral stability curves from the modified Oldroyd-B model. The 'local property' model predicted the same critical depth ratio, but no stable region for large α and n. Although neither model could capture the shear-thinning of the normal stresses, they both were able to predict at least qualitatively the critical conditions.

Experiments in a converging channel led to a more stable flow, since the smaller channel height produced higher shear rates, and because the viscosity of the PP decreased more sharply with increasing shear rate, the effective viscosity ratio decreased. In contrast, experiments in a diverging channel resulted in a much more unstable flow.

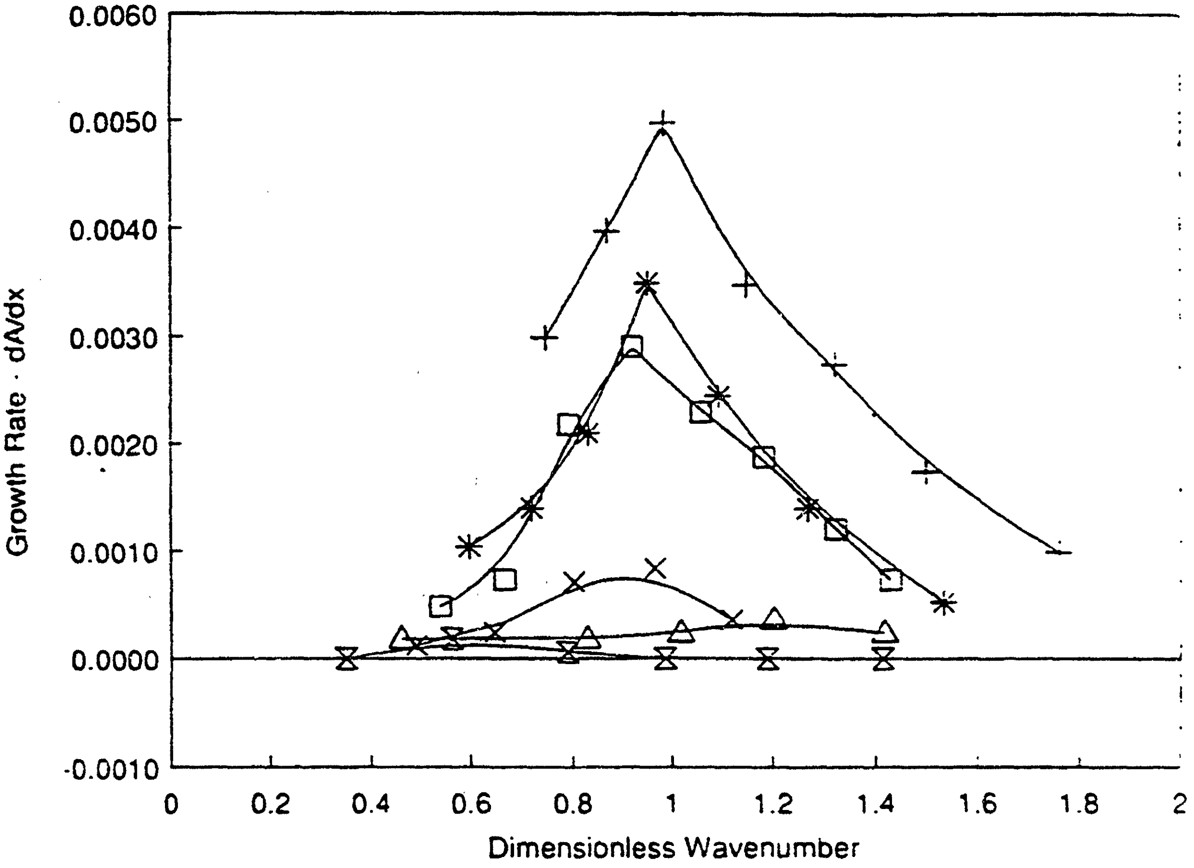

Figure 2.26 Experimental growth rates as a function of wavenumber for d_2/d_1 = 2.04 (+); 1.45 (∗); 1.09 (□); 0.88 (×); 0.69 (△) and 0.45 (⧖) (from Wilson and Khomami 1992).

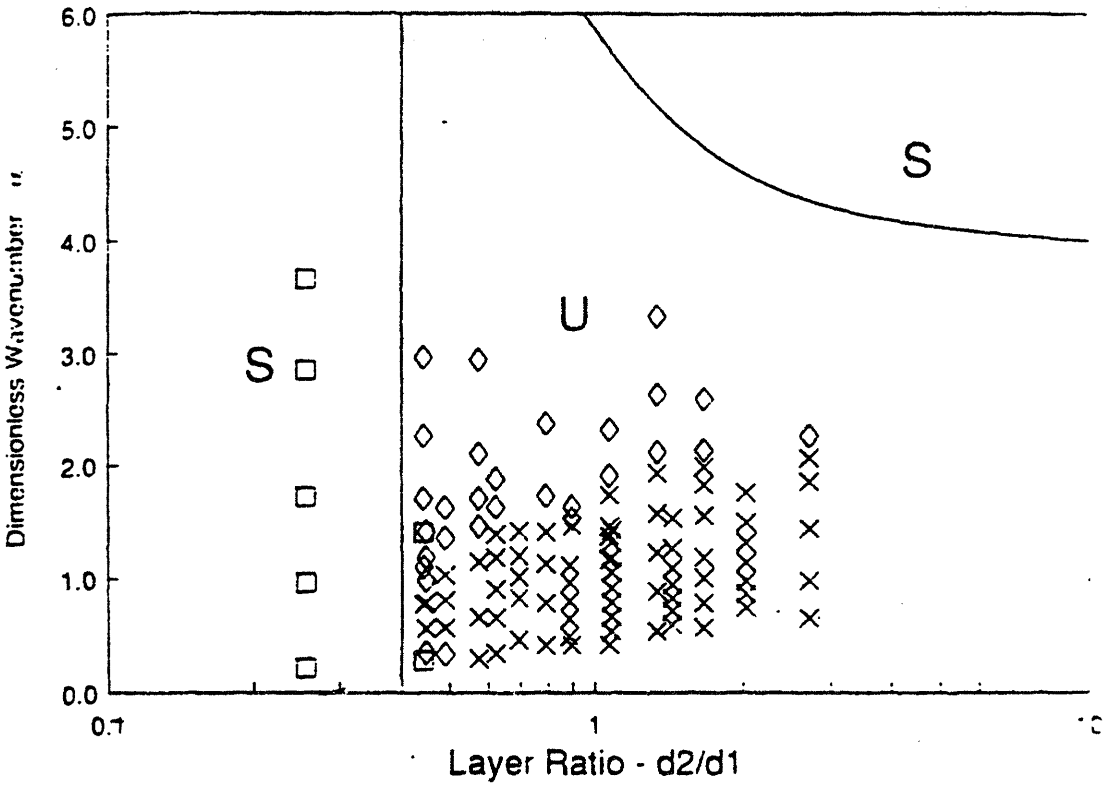

Figure 2.27 Neutral stability diagram for the modified Oldroyd-B diagram; S denotes stable regions, U denotes unstable regions. Experimental data are represented by (□) stable, (×) unstable and (◇) indeterminate (from Wilson and Khomami 1992).

The effects of elasticity on the instability were isolated by conducting experiments with the same interfacial viscosity ratio ($\eta_{PP}/\eta_{HDPE} = 4.8$) but different elasticity ratios. This was made possible by performing experiments at two different temperatures and adjusting the flowrates such that both the viscosity ratio and the depth ratio remained fixed, but the first normal stress difference ratio at the interface changed. The maximum growth rate was still found to be near $\alpha = 1$, but for the experiments with the greater elasticity ratio, the growth rate was higher and a broader range of wavenumbers was unstable. Experiments with larger amplitude disturbances were also conducted to show that subcritical bifurcations did not occur for this system, *i.e.*, linearly stable wavenumbers remained stable even for large initial disturbances. Instead, a supercritical bifurcation was observed in which linearly unstable disturbances that had grown to large amplitude did not remain sinusoidal but rather the wave crest bent back and eventually broke off due to the velocity difference across the height of the wave. Renardy (1995) presented a weakly nonlinear analysis of two UCM fluids for conditions qualitatively similar to those of the experiments of Wilson and Khomami, and showed that supercritical bifurcations occurred under most conditions, but that subcritical bifurcations were also possible, especially for longer wavelengths.

The effect of chemical compatibility was investigated by using linear low-density polyethylene (LLDPE) in place of PP for a series of experiments. The LLDPE has a slightly higher viscosity than PP and an almost identical first normal stress coefficient, but it was chemically compatible with the HDPE, so that interfacial diffusion and convective mixing were possible. The experimentally measured critical depth ratio was higher for this system even though the theory predicted a lower value, and smaller growth rates were observed for the LLDPE/HDPE system, whereas the viscosity and elasticity ratios would indicate that higher values should be observed. These differences were attributed to small-scale interfacial mixing, which would lower the effective viscosity ratio and remove energy from the disturbance.

Chapter 3

Experimental Method

This chapter describes the experimental system used to study the viscoelastic flow instabilities in three different types of flows. The fluids used in the experiments and the constitutive equations used to model their flow are discussed in §3.1, the flow geometries are described in §3.2, and the experimental techniques of laser Doppler velocimetry and image analysis are outlined in §§3.3-4.

3.1 Test Fluids

Although the flows to be studied in this thesis are complex and two- or three-dimensional, it is necessary first to understand how the fluids to be studied behave in simple, one-dimensional flows. Simple shear flows can provide information needed to determine the parameters of constitutive models, which can then be used in numerical simulations of complex flows. Although the parameters of nonlinear models can be determined from the shear-rate-dependence of the steady shear material properties, the same parameters also determine the elongational properties for many models. Obtaining reliable values of the elongational properties remains experimentally difficult, but as better measures become available, they can also be used to determine model parameters. Only by fully understanding the fluid rheology can meaningful comparison be made between numerical simulations and experimental results.

3.1.1 Rheological Methods

A summary of test flows used to determine material functions of non-Newtonian fluids can be found in Bird *et al.* (1987a). The flows most relevant to the work in this thesis are described here.

Steady Shear Flow

An example of steady shear flow is shown in figure 3.1, where fluid is placed between two plates, and the top plate moves with a constant velocity *V*. This establishes a

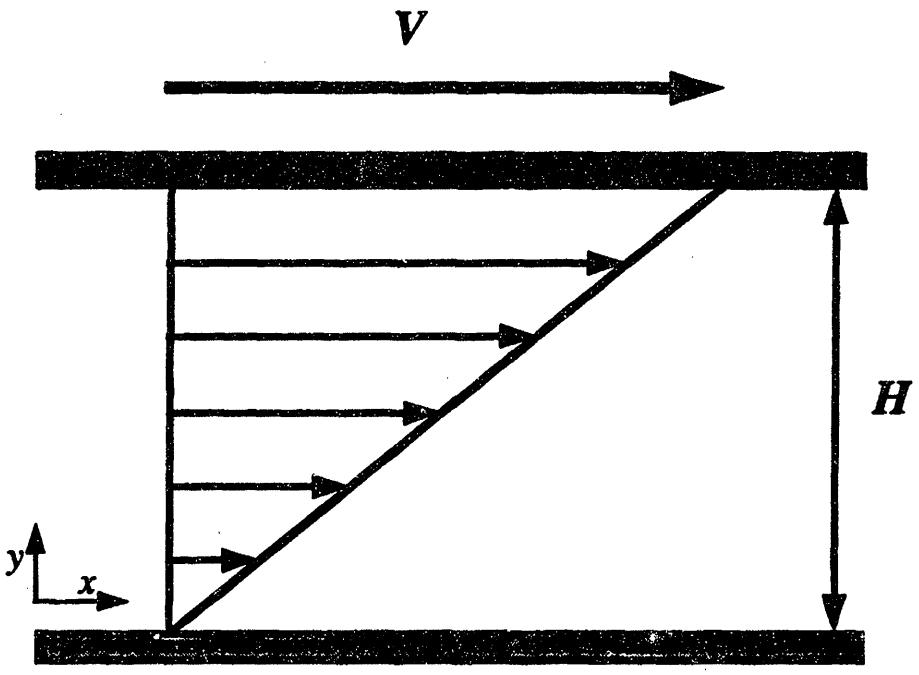

Figure 3.1 Shearing flow between parallel plates.

constant velocity gradient, $\dot{\gamma}_{yx} = V/H$, between the plates. The viscosity of a fluid, η, is defined by the shear stress exerted by the fluid divided by the applied shear rate:

$$\tau_{yx} = -\eta(\dot{\gamma})\dot{\gamma}_{yx}. \tag{3.1}$$

Newtonian fluids have a constant viscosity, μ, while for non-Newtonian fluids the viscosity will in general be a function of the shear rate.

For viscoelastic fluids is steady shear flow, the first and second normal stress coefficients, Ψ_1 and Ψ_2, are defined in terms of the normal stress differences N_1 and N_2 as

$$N_1 = \tau_{xx} - \tau_{yy} = -\Psi_1(\dot{\gamma})\dot{\gamma}_{yx}^2 , \tag{3.2}$$

$$N_2 = \tau_{yy} - \tau_{zz} = -\Psi_2(\dot{\gamma})\dot{\gamma}_{yx}^2 . \tag{3.3}$$

Both Ψ_1 and Ψ_2 are identically zero for Newtonian fluids. Although Ψ_1 is easily obtainable, Ψ_2 is more difficult to measure experimentally. Ψ_2 is expected to be much smaller than Ψ_1 and of opposite sign, and has been found to be nearly zero for Boger fluids such as those used in this thesis (Magda *et al.* 1991).

Small-Amplitude Oscillatory Shear Flow

In this flow, V of figure 3.1 is equal to $V_0\cos\omega t$, and $\dot{\gamma}(t)$ is equal to $\dot{\gamma}^0\cos\omega t$, where $\dot{\gamma}^0 = V_0/H = \gamma^0\omega$ for strain γ^0. For small strains, the shear stress can be expressed in terms of its components in phase and out of phase with the shear rate as

$$\tau_{xy}(t) = -\eta'(\omega)\dot{\gamma}^0\cos\omega t - \eta''(\omega)\dot{\gamma}^0\sin\omega t , \tag{3.4}$$

where η' is the dynamic viscosity and relates to the viscous nature of the fluid, while η'' relates to the fluid's elasticity. For a Newtonian fluid, $\eta' = \mu$ and $\eta'' = 0$. These material parameters are related to the steady shear flow material parameters in the limit of low shear rate and frequency by

$$\lim_{\omega\to 0} \eta'(\omega) = \lim_{\dot{\gamma}\to 0} \eta(\dot{\gamma}) = \eta_0, \tag{3.5}$$

$$\lim_{\omega \to 0} \frac{2\eta''(\omega)}{\omega} = \lim_{\dot{\gamma} \to 0} \Psi_1(\dot{\gamma}) = \Psi_{1,0}, \tag{3.6}$$

Equation 3.4 can also be written in terms of the strain as

$$\tau_{\mathrm{xy}}(t) = -G'(\omega)\dot{\gamma}^0 \sin \omega t - G''(\omega)\dot{\gamma}^0 \cos \omega t, \tag{3.7}$$

where $G' = \eta''\omega$ is the storage modulus and $G'' = \eta'\omega$ is the loss modulus.

Shearfree Flows

The velocity field for shearfree flow as shown in figure 3.2 is

$$v_{\mathrm{x}} = -\frac{1}{2}\dot{\varepsilon}(1+\kappa)x, \tag{3.8}$$

$$v_{\mathrm{y}} = -\frac{1}{2}\dot{\varepsilon}(1-\kappa)y, \tag{3.9}$$

$$v_{\mathrm{z}} = \dot{\varepsilon}z, \tag{3.10}$$

where $0 \leq \kappa \leq 1$ and $\dot{\varepsilon}$ is the elongation rate. Three different limiting types of extensional flow are possible depending on κ and $\dot{\varepsilon}$:

uniaxial extension	$\kappa = 0,\ \dot{\varepsilon} > 0,$
biaxial extension	$\kappa = 0,\ \dot{\varepsilon} < 0,$
planar extension	$\kappa = 1.$

Two material functions can be defined for shearfree flows:

$$\tau_{\mathrm{zz}} - \tau_{\mathrm{xx}} = -\bar{\eta}_1(\dot{\varepsilon},\kappa)\dot{\varepsilon}, \tag{3.11}$$

$$\tau_{\mathrm{yy}} - \tau_{\mathrm{xx}} = -\bar{\eta}_2(\dot{\varepsilon},\kappa)\dot{\varepsilon}. \tag{3.12}$$

For $\kappa = 0$, $\bar{\eta}_2 = 0$, and for Newtonian fluids $\bar{\eta}_1(\dot{\varepsilon}, 0) = 3\mu$ and $\bar{\eta}_2(\dot{\varepsilon}, 1) = 4\mu$.

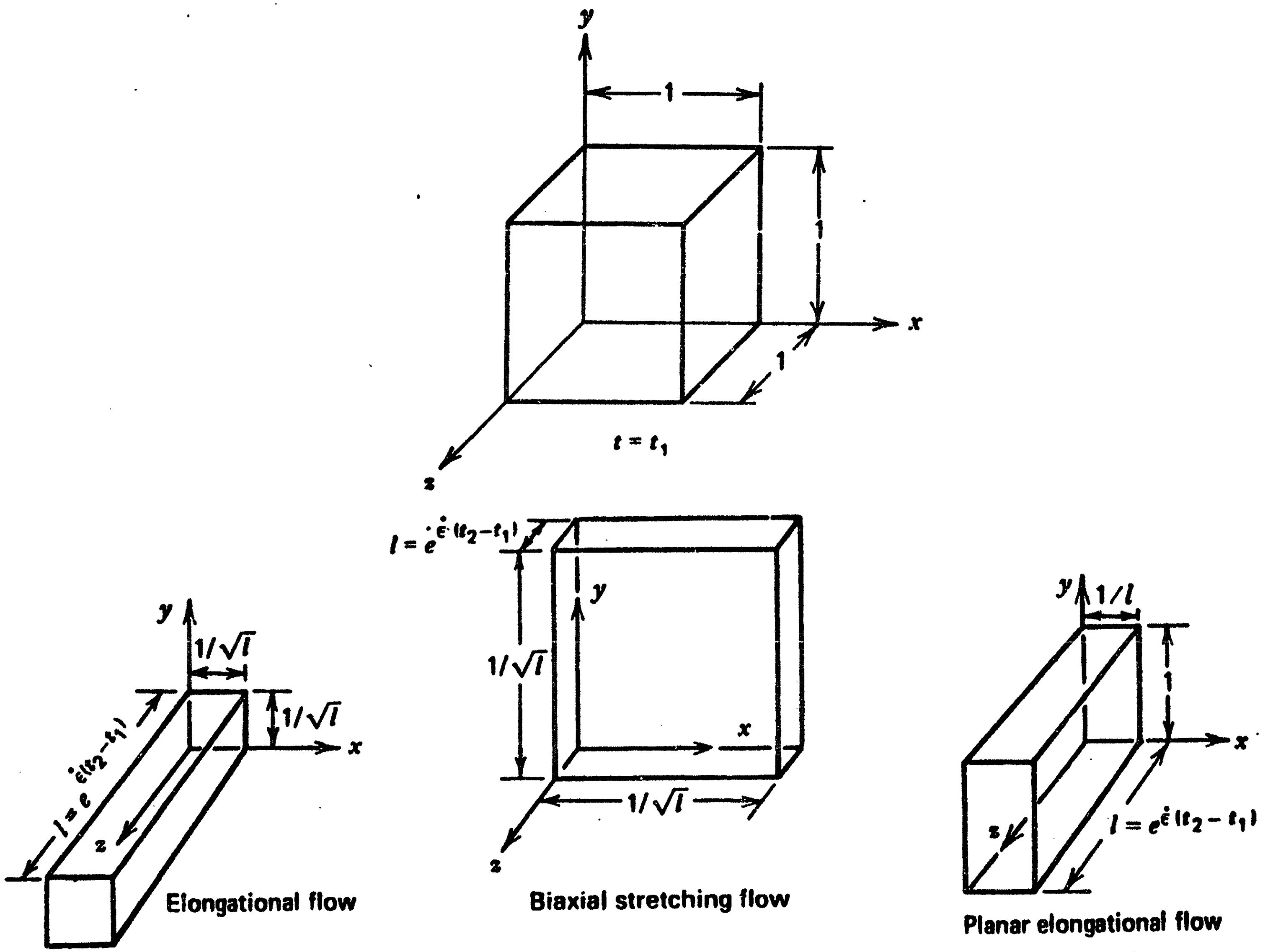

Figure 3.2 Deformation of a unit cube of material from time t_1 to t_2 ($t_2 > t_1$) in three kinds of shearfree flow (from Bird *et al.* 1987a).

Measurements of the steady shear (η, Ψ_1) and linear viscoelastic (η', η'') material properties can be obtained using a Rheometrics Mechanical Spectrometer (RMS-800). Fluid samples are placed either between two parallel coaxial circular plates or between a plate and an inverted cone, as shown in figure 2.1. The bottom plate is rotated and the torque and normal force exerted on the upper fixture are measured and used to calculate the material properties based on the test geometry (Bird *et al.* 1987a). The bottom plate can be rotated from $2\times10^{-6} \leq \Omega \leq 100$ rad/s for steady shear flow and $10^{-3} \leq \omega \leq 100$ rad/s for small-amplitude oscillatory shear flow. Two different transducers are used: the 'fluids transducer' measures torques up to 100 g·cm and normal forces up to 100 g, while the 'melts transducer' measures up to 2000 g·cm and 2000g. The minimum measurable value for each is about 0.1% of its full scale. A recirculating fluid bath allows the fluid temperature to be varied from -5 °C to 80 °C and controlled within ± 0.1 °C. An oven/dewar combination can be used with the melts transducer to extend the temperature range to $-150\ ^\circ\mathrm{C} \leq T \leq 500\ ^\circ\mathrm{C}$ with an accuracy of ± 2 °C.

Difficulties in obtaining purely extensional flows have limited the availability of reliable extensional viscosity data. For a discussion of the different experimental systems used to attempt to measure shearfree material functions, see the special issue of *The Journal of Non-Newtonian Fluid Mechanics*, **35** (1990). An alternative approach was taken by Quinzani (1991), who combined flow induced birefringence measurements of stress and laser Doppler velocimetry measurements of velocity along the centerplane of a 4:1 planar contraction to yield the transient planar extensional viscosity, which could be used to determine the parameters for different constitutive equations. Elongational viscosity data is desirable for obtaining appropriate model parameters for analysis of flows with strong extensional components, such as the stagnation flows discussed in §5.

3.1.2 Fluid Rheology

Four different viscoelastic test fluids were used for the experiments described in §§4-6. Each consisted of a small amount of a high molecular weight polyisobutylene (PIB) (Exxon Vistanex L-120, MW ~ 1.8×10^6 g/mol) in a highly viscous Newtonian solvent. These 'Boger fluids' (Boger 1977/78) were designed to have a viscosity that remains nearly constant over a large range of shear rates, and yet be highly elastic. The fluids are prepared by first dissolving the PIB in tetradecane (C14) and then mixing the PIB/C14 with a low molecular weight polybutene (PB) (Amoco H100, MW ~ 900 g/mol or Amoco H300, MW ~1300 g/mol). By varying the relative amounts of the three components, it is possible to create fluids with a wide range of relaxation times and solvent viscosity ratios.

The composition and zero-shear-rate viscometric properties (η_0, $\Psi_{1,0}$) of each fluid are given in Table 3.1. Also shown are the solvent viscosity ratio $\beta = \eta_s/\eta_0$ and the relaxation time for the Oldroyd-B model, $\lambda_1 = \Psi_{1,0}/2\eta_p$, where $\eta_p = \eta_0 - \eta_s$ is the polymeric contribution to the viscosity. A shear-rate-dependent mean relaxation time of the fluid can also be defined in terms of the steady shear properties as $\lambda(\dot{\gamma}) = \Psi_1(\dot{\gamma})/2\eta(\dot{\gamma})$. The value of this relaxation time decreases with increasing shear rate, and in the limit of small shear rates it is equal to the value obtained from the upper convected Maxwell model. Two Newtonian fluids were also used for studying the interfacial instability. The first of these was the H100 PB, with a viscosity of 25 Pa·s, and the other was 2.7 wt% C14 in H100 PB, with a viscosity of 13.7 Pa·s.

	0.31% PIB (*1*)	0.31% PIB (2)	0.50% PIB	0.20% PIB
% C14	4.83	4.83	9.50	3.80
PB	H100	H100	H300	H300
η_0 [Pa·s]	13.76	13.45	22.7	48.1
η_s [Pa·s]	8.12	9.22	13.2	40.1
$\Psi_{1,0}$ [Pa·s^2]	8.96	2.52	22.6	19.8
λ_1 [s]	0.794	0.30	1.19	1.24
β	0.59	0.67	0.58	0.84

Table 3.1 Viscometric properties of polyisobutylene (PIB) test fluids used in the experiments of §§4-6.

The 0.31 wt% PIB fluid labeled (*1*) is the same fluid that has been thoroughly characterized by Quinzani *et al.* (1990) and was used for the rotating flow and superposed flow experiments of §§4 and 6. A much larger volume was also used for the experiments for flow past a cylinder of McKinley *et al.* (1993), but a test of the fluid rheology following those experiments showed that the first normal stress coefficient had decreased by a factor of five from the values reported in Quinzani *et al.*, presumably due to mechanical degradation. No measurable decrease was found in the viscosity, which is not surprising since the viscosity is dominated by the low molecular weight solvent. The 0.31 wt% fluid labeled (*2*) was then prepared for use in the stagnation flow experiments of §5, and its original rheology was similar to that of the 0.31 wt% PIB (*1*) fluid, but after a small number of passes through the flow system, a similar decrease in Ψ_1 was found, and subsequent measurements of the rheology showed that no further changes occurred over the course of the experiments. Figure 3.3 shows the viscometric properties of the 0.31 wt% PIB (2) fluid. The material properties were measured at temperatures of 9 °C $\leq T \leq$ 41 °C, and are shifted to a reference temperature of 25 °C by means of time-temperature superposition (Ferry 1980). The temperature dependence is described by an Arrhenius equation with a flow activation energy of $\Delta H = 61.7$ kJ. A change of 1 °C in the fluid temperature results in an 8% change in the fluid viscosity and relaxation time, and it is therefore crucial to monitor carefully the ambient temperature and adjust the material functions appropriately. All experimental results are corrected to a reference temperature of 25 °C. The viscosity has a zero-shear-rate value of $\eta_0 = 13.45$ Pa·s and remains nearly constant over four decades of shear rate due to the high solvent viscosity. The zero-shear-rate value of the first normal stress coefficient is $\Psi_{1,0} = 2.52$ Pa·s^2, and at higher shear rates Ψ_1 exhibits a complex shear-thinning behavior. No measurements have been made of the second normal stress coefficient, but studies by Magda *et al.* (1991) indicate that for PIB Boger fluids, $\Psi_2 \approx 0$. The 0.31 wt% PIB (*1*) fluid has been thoroughly characterized by Quinzani *et al.*, and the solid curve in figure 3.3 is a fit to its original rheology. Measurements by Tirtaatmadja and Sridhar (1993) show that for the 0.31 wt% fluid (*1*) (fluid A in their work), the uniaxial extensional viscosity is approximately $\bar{\eta} = 2000\eta_0$. The material properties of the 0.2 wt% PIB and 0.5 wt% PIB fluid are shown in figures 3.4 and 3.5, respectively. For dilute, or semi-dilute solutions such as these Boger fluids, the longest relaxation time depends on the concentration and molecular weight of the polymeric solute, the polymer-solvent thermodynamic interactions and the viscosity of the solvent that the chains are dissolved in (Ferry 1980). Since the same polyisobutylene is used in all of the fluids and the chemical composition of the surrounding solvent is essentially unchanged (in all cases the solvent is essentially *athermal*; Flory 1953), the lower concentration of the polymer in the 0.20 wt% fluid is outweighed by the significantly higher solvent viscosity of the H300 polybutene, resulting in a larger first normal stress coefficient and a longer fluid relaxation time. The higher PIB concentration of the 0.5 wt% fluid is partially offset by the lower solvent viscosity.

3.1.3 Constitutive Equations

One of the primary aims of the field of non-Newtonian fluid mechanics is to describe the effects of elasticity in complex flows. The experimental results of §§4-6 show that elasticity can cause flow instabilities, and efforts to model the effects of elasticity,

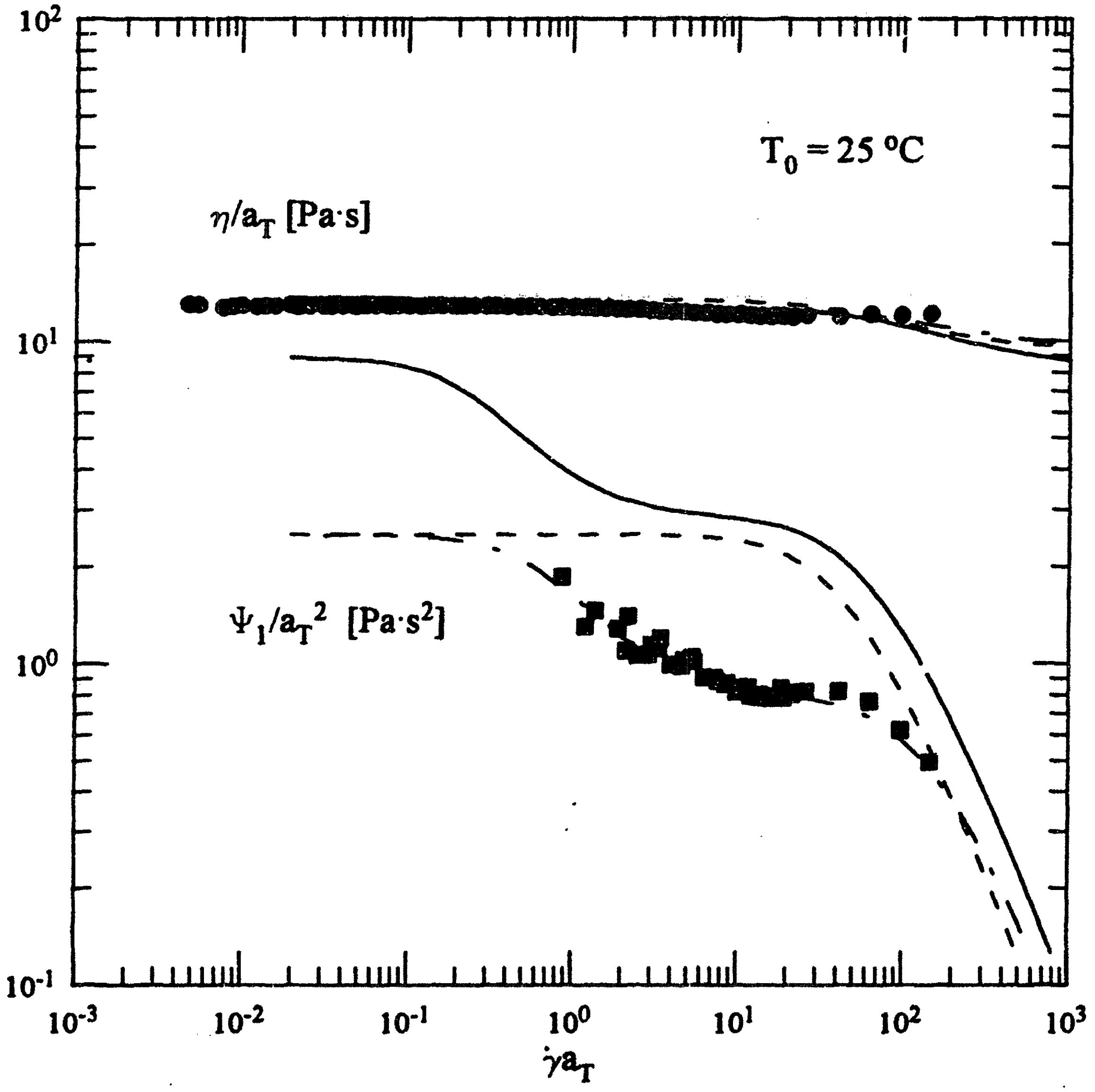

Figure 3.3 Master curves for the viscometric properties of the 0.31 wt% (*2*) test fluid at 25 °C: (●) viscosity η (Pa·s) and (■) first normal stress coefficient Ψ_1 (Pa·s^2). The dashed (- - -) curve is the prediction of the Giesekus model with $\alpha = 10^{-3}$ and the (- · -) curve is the prediction of a four-mode Giesekus model using the parameters of Table 3.2. The solid curve is the fit to the rheology of the 0.31 wt% (*1*) test fluid.

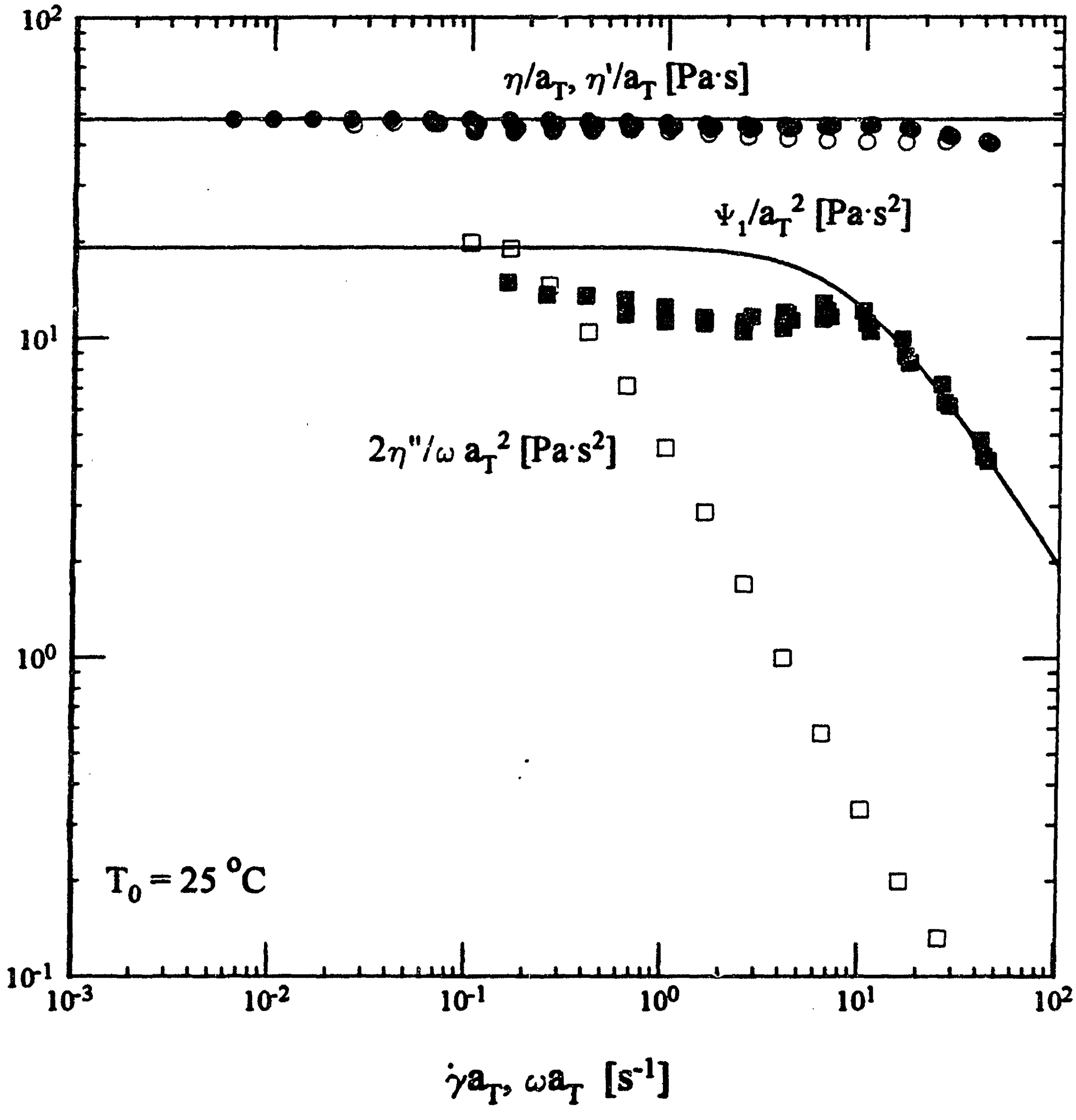

Figure 3.4 Master curves for the viscometric properties of the 0.20 wt% test fluid at 25 °C: (●) viscosity η (Pa·s), (■) first normal stress coefficient Ψ_1 (Pa·s^2), (○) dynamic viscosity η' (Pa·s) and (□) $2\eta''/\omega$ (Pa·s^2). The solid curve is the prediction of the Chilcott-Rallison model with $L = 20$.

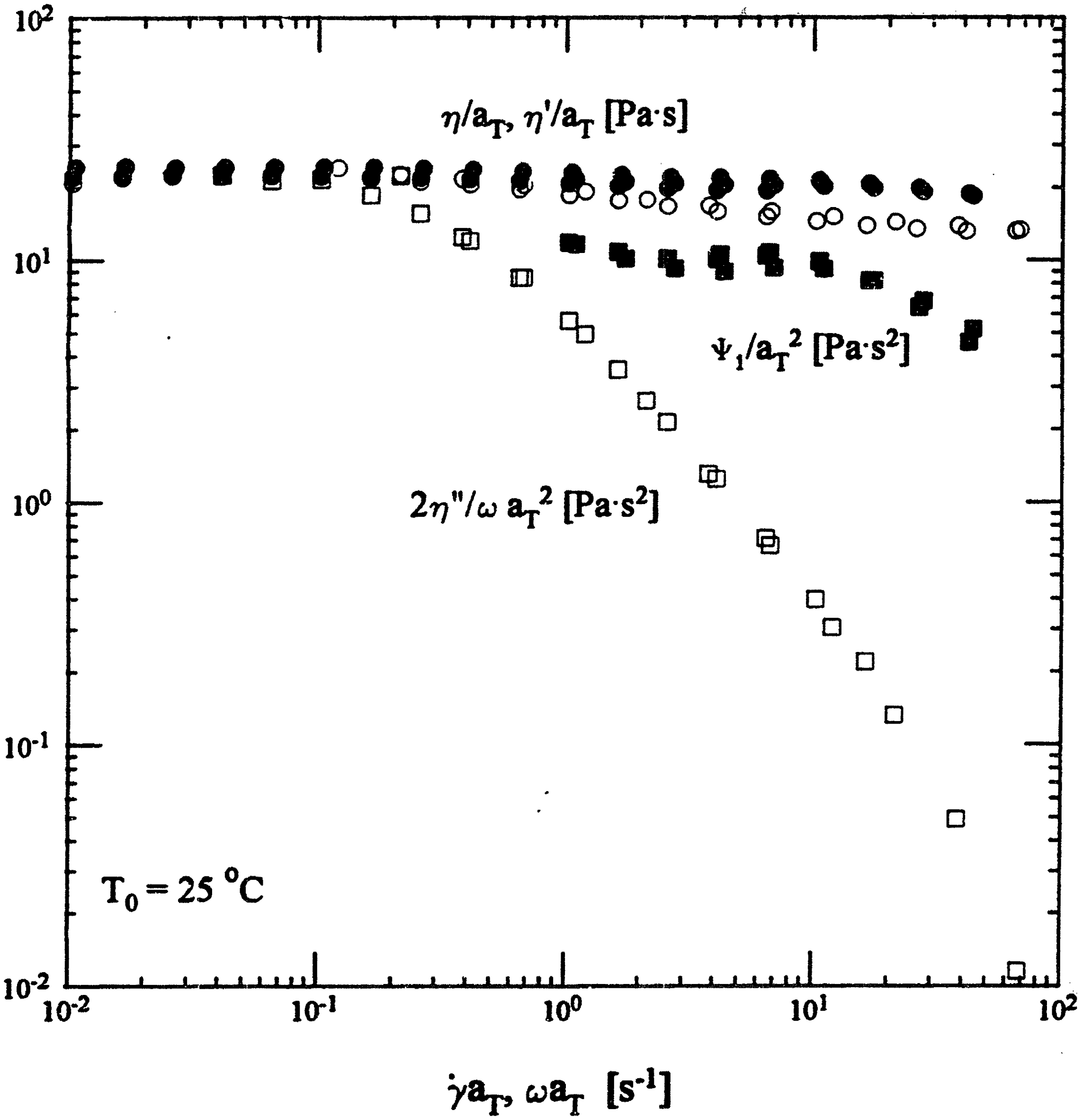

Figure 3.5 Master curves for the viscometric properties of the 0.50 wt% test fluid at 25 °C: (●) viscosity η (Pa·s), (■) first normal stress coefficient Ψ_1 (Pa·s^2), (○) dynamic viscosity η' (Pa·s) and (□) $2\eta''/\omega$ (Pa·s^2).

either by means of large-scale finite element simulations or through linear stability analysis require a constitutive equation to relate the flow kinematics to the polymeric stress. A comparison between the experiments and calculations serves as a test of the ability of the constitutive equation to capture the relevant physics of the flow. This section describes the four constitutive equations used to model the experimental results, and also gives the model parameters for the fluids discussed in §3.1.2.

Maxwell

The linear viscoelastic data obtained from small-amplitude oscillatory shear flow can be fit using the Maxwell model:

$$\tau + \lambda \frac{\partial}{\partial t} \tau = -\eta \dot{\gamma}, \tag{3.13}$$

where τ is the stress tensor, $\dot{\gamma}$ $\left[= \nabla v + (\nabla v)^T\right]$ is the rate-of-strain tensor and λ is the relaxation time. The dashed curve in figure 3.6 is the solution of equation 3.13 for the 0.31 wt% (*2*) fluid using the values of η = 13.45 Pa·s and $\lambda = \Psi_{1,0}/2\eta_0 = 0.094$ s. Because of the broad molecular weight distribution of the PIB molecules, and the fact that even a monodisperse polymer has many relaxation timescales, equation 3.13 fails to yield a quantitative fit of the linear viscoelastic data. The effects of multiple timescales can be incorporated by considering a multimode model

$$\tau(t) = \sum_{k=1}^{n} \tau_k(t), \tag{3.14}$$

where each of the τ_k follows equation 3.13. The values of $\{\eta_k, \lambda_k\}$ are obtained by fitting the data of figure 3.6 using the Levenberg-Marquardt nonlinear regression method (Press *et al.* 1985). Using the values of $\{\eta_k, \lambda_k\}$ given in Table 3.2 results in the quantitative fit shown in figure 3.6 as a solid curve.

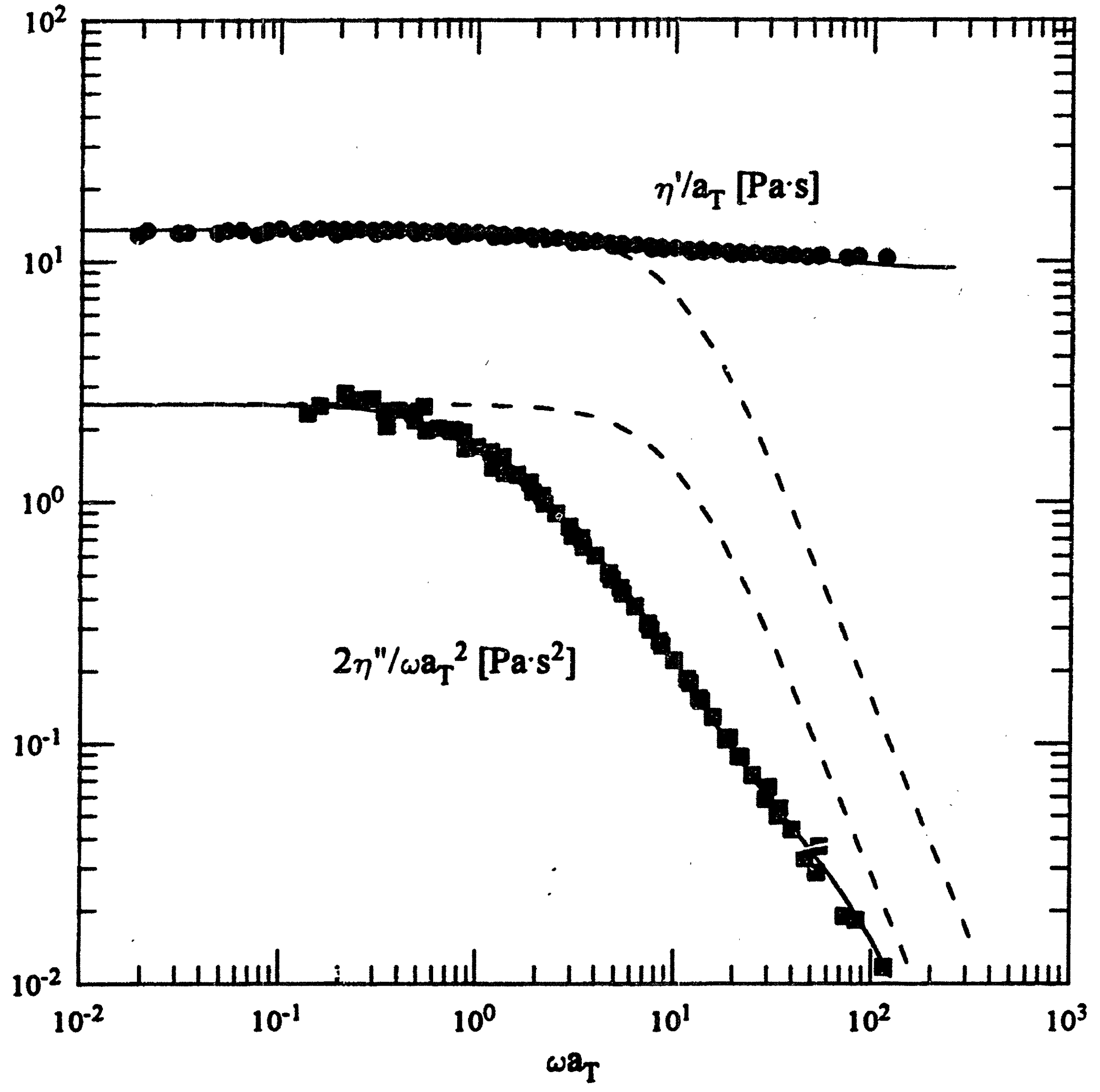

Figure 3.6 Master curves for the linear viscoelastic properties of the 0.31 wt% (*2*) test fluid at 25 °C: (●) dynamic viscosity η' (Pa·s) and (■) $2\eta''/\omega$ (Pa·s^2). The dashed (- - -) curve is the prediction of a single-mode Maxwell model, and the solid (——) curve is the prediction of a four-mode Maxwell model using the parameters of Table 3.2.

mode	η_k [Pa·s]	λ_k [s]	α_k
1	0.86	1.00	0.5
2	1.66	0.21	0.0002
3	0.40	0.08	0.001
4	1.31	0.014	0.5
solvent	9.22		

Table 3.2 Linear viscoelastic spectrum for the 0.31 wt% (*2*) fluid. Also given are the mobility parameters for the Giesekus model.

Oldroyd-B

The linear Maxwell model is limited to flows with small displacement gradients, but it can be modified to be applicable to more general flows by replacing the time derivative of the stress with its convected derivative $\tau_{(1)}$, which is defined as

$$\tau_{(1)} = \frac{\partial \tau}{\partial t} + v \cdot \nabla \tau - \left[(\nabla v)^T \cdot \tau - \tau \cdot (\nabla v) \right] . \tag{3.15}$$

The addition of a solvent viscosity η_s to the model results in the Oldroyd-B model (Oldroyd 1950)

$$\tau + \lambda_1 \tau_{(1)} = -\eta_0 \left(\dot{\gamma} + \lambda_2 \dot{\gamma}_{(1)} \right), \tag{3.16}$$

where λ_2 (= $\lambda_1 \beta$) is the retardation time, where β is the solvent viscosity ratio η_s/η_0 This model can also be obtained from a molecular theory that considers infinitely extensible Hookean dumbbells in a Newtonian solvent of viscosity η_s. The model predicts a constant viscosity and constant first normal stress coefficient and a second normal stress coefficient Ψ_2 of zero. The extensional viscosity becomes infinite at a strain rate of $\lambda_1 \dot{\varepsilon}$ = 0.5.

Chilcott-Rallison

In this constitutive model, the molecules are considered to be a dilute solution of noninteracting dumbbells with dimensionless concentration c, dissolved in a Newtonian solvent of viscosity η_s. The two beads of the dumbbell are connected by a nonlinear elastic spring with a finite maximum extensibility L, which represents the ratio of the fully extended length of the dumbbell to its r.m.s. length at equilibrium. By eliminating the second rank tensor describing the configuration of the dumbbells from the original equations of Chilcott and Rallison, the constitutive equation for the polymeric contribution to the stress τ_p can be written simply as

$$\tau_p + \lambda_1 \left(\frac{\tau_p}{f} \right)_{(1)} = -\eta_p \dot{\gamma}, \tag{3.17}$$

where $f \equiv \left(L^2 - \frac{\lambda_1}{\eta_p} tr(\tau_p) \right) / (L^2 - 3)$ is the nonlinear spring modulus. The solvent is Newtonian with constitutive equation $\tau_s = -\eta_s \dot{\gamma}$, and the total stress tensor is given by the linear combination $\tau = \tau_s + \tau_p$.

In the limit $L \to \infty$, the dumbbells become infinitely extensible and equation 3.17 simplifies to the Upper-Convected Maxwell model; the constitutive equation for the total stress tensor τ is then equivalent to the Oldroyd-B model. However, for finite values of L, the model predicts the onset of shear-thinning in the first normal stress coefficient beyond dimensionless shear rates of $\lambda_1 \dot{\gamma} \equiv L^2 / \sqrt{8(L^2 - 3)}$ with an asymptotic decrease at high shear rates which scales as $\Psi_1(\dot{\gamma}) \sim \dot{\gamma}^{-1}$. The viscosity of the model remains constant with a value $\eta_0 \equiv \eta_s + \eta_p$ and the polymeric contribution to the viscosity depends on the concentration of dumbbells as $\eta_p \equiv \eta_s c$. Like other dilute solution dumbbell models, the Chilcott-Rallison model predicts a zero value of the second normal stress coefficient Ψ_2 at all shear rates.

This model predicts a finite extensional viscosity, with a Trouton ratio $\bar{\eta}/\eta_p$ that scales as L^2. In the absence of measurements of the extensional viscosity, the value of L has been chosen to capture the shear-thinning behavior of $\Psi_1(\dot{\gamma})$ observed experimentally at high shear rates. This criterion yields values of $L = 20$ for the 0.20 wt% fluid, as shown by the solid curve in figure 3.4. The value of L for the 0.31 wt% (*1*) fluid based on $\Psi_1(\dot{\gamma})$ has previously been found to be $L = 12$ (McKinley *et al.* 1993). The measurements of Tirtaatmadja and Sridhar suggest that the Trouton ratio of this PIB Boger fluid in a homogeneous uniaxial extensional deformation is in the range 2–3×10^3. Using these measurements to determine the extensibility parameter suggests significantly larger values of $L \approx 50$. This important difference in the appropriate value of the model parameter L is discussed further in §5.

Giesekus

The Giesekus model (Giesekus 1982) also provides a bounded extensional viscosity, and shear-thinning of both the viscosity and normal stress coefficient. Anisotropic hydrodynamic drag is incorporated through the addition of a term of the form $\{\tau_p \cdot \tau_p\}$:

$$\tau_p + \lambda_1 \tau_{p(1)} - \alpha \frac{\lambda_1}{\eta_p}\{\tau_p \cdot \tau_p\} = -\eta_p \dot{\gamma}, \qquad (3.18)$$

where α is the mobility factor. For $\alpha = 0$, the Oldroyd-B model is recovered. The viscosity is predicted to shear-thin as $\dot{\gamma}^{-1}$ at high shear rates, although the addition of a solvent viscosity ensures a physically realistic value of $d|\tau_{12}|/d\dot{\gamma} > 0$. The first normal stress coefficient shear thins as $\dot{\gamma}^{-1.5}$ at high shear rates, and $\Psi_{2,0} = -\alpha \Psi_{1,0}/2$. The fit of this model to the 0.31 wt% PIB (2) fluid is shown in figure 3.3 for both a single-mode fit using $\alpha = 0.001$, and for a four-mode fit using the parameters given in Table 3.2. This model also provides a bounded extensional viscosity at high strain rates that depends on the same model parameter that governs the normal stress coefficient, in this case $\bar{\eta} = 2\eta_0/\alpha$. The extensional viscosity data of Tirtaatmadja and Sridhar therefore also predicts a values of $\alpha \approx 0.001$, in contrast to the Chilcott-Rallison model, for which markedly different values of the model parameter are obtained from the shear and extensional data.

3.2 Flow Geometries

3.2.1 Rotational Flows

All of the experimental measurements were conducted in the apparatus shown schematically in figure 3.7. A cylindrical coordinate system $(\hat{r},\theta,\hat{z})$ is defined with origin at the center of the upper, rotating disk. The plate separation H and the rotation rate Ω are chosen to define characteristic length and time scales; all variables are then dimensionless unless explicitly identified with carets. The Deborah number is defined based on the rotation rate as $De_0 = \lambda_1\Omega$, and the Weissenberg number is based on the shear rate, $We = \lambda\dot{\gamma}_R$, where $\dot{\gamma}_R = \Omega R/H$. The base of the test cell consisted of a smooth, polished plexiglass sheet supported by four threaded rods which could be independently adjusted to ensure that the plexiglass sheet was parallel to the upper disk. The position of the upper disk was controlled using a two-axis lathe mount attached to the rigid frame of the geometry, and the separation of the upper disk and the bottom plate was measured to within ±1 μm using a digital micrometer. Special care was taken to ensure that the upper and lower disks were parallel to within ± 0.1°. The radius of the upper disk was held constant at $R = 40.0$ mm, and gaps of $H = 2.00$ mm and $H = 3.50$ mm were used in the experiments. The choice of plate separations is experimentally constrained, since, for very small separations, it becomes difficult to resolve the spatial structure of the secondary flow that develops in the narrow gap, and for very large plate separations, gravity overcomes the wetting forces which pin the fluid at the edge of the disks, and the sample runs out of the rheometer.

Fluid samples were placed between the disk and the transparent lower plate, and excess fluid beyond the edge of the disk was carefully removed to leave a smooth, approximately cylindrical meniscus at the edge of the disks. According to the analysis of Olagunju (1994) and the material properties of the fluids given in §3.1.1, the maximum surface deflection is only expected to deviate by a maximum of ± 0.10 mm from a right cylinder and inertial secondary flows of von Kármán form can be completely ignored. The steady torsional flow was driven by rotating the upper disk, which was attached to the spindle of a high-torque d.c. gearmotor (Electrocraft E586). The angular rotation rate Ω of the motor was accurately measured by a tachometer and was incremented in small steps (typically $\delta\Omega = 0.52$ rad/s), until the onset of the instability was observed.

The flow was illuminated and visualized from a mirror placed below the plexiglass base at an angle of 45°. Two fiber-optic light sources were positioned to illuminate the

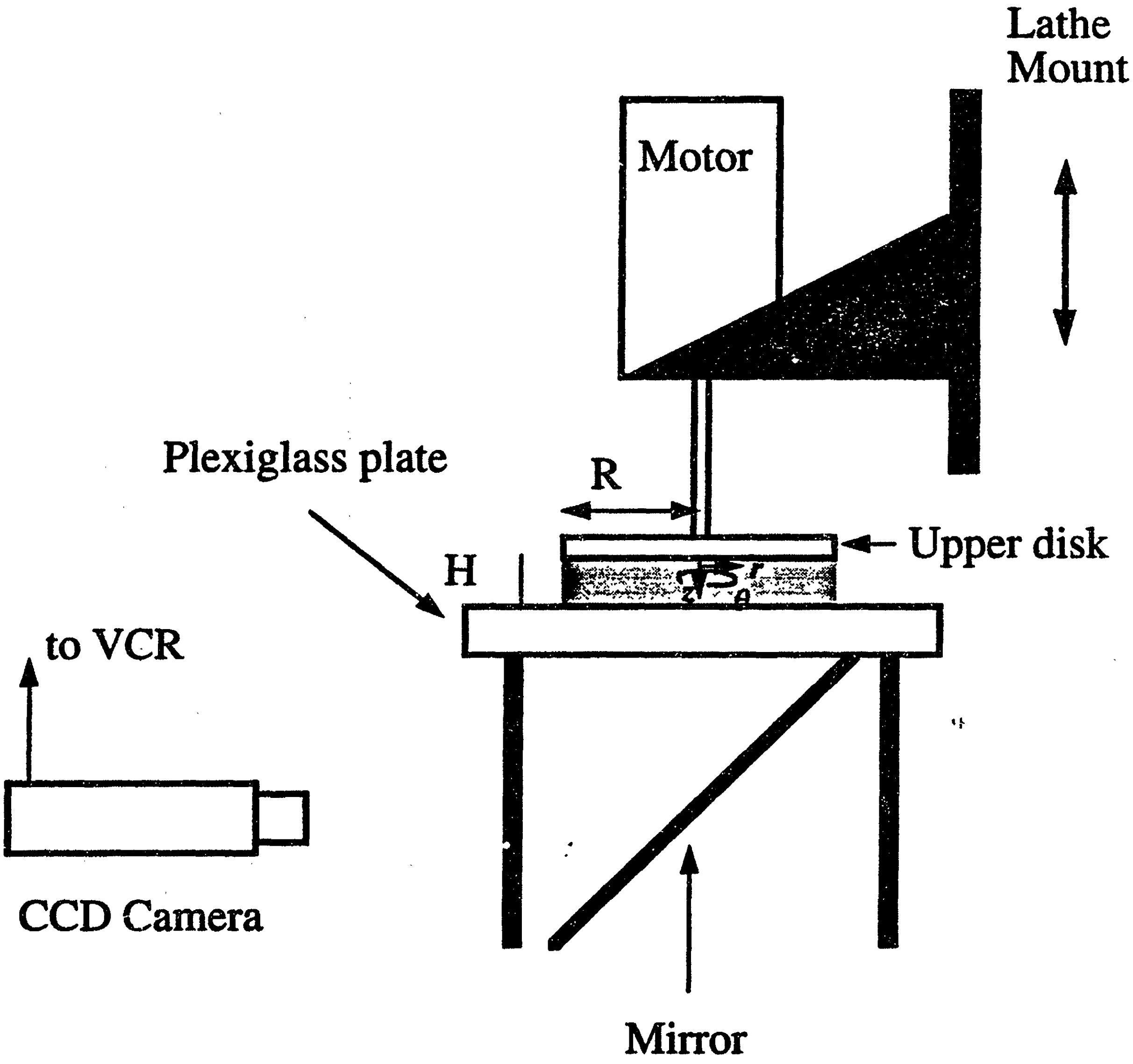

Figure 3.7 Schematic digram of the parallel plate geometry.

entire region between the disk and the plate as uniformly as possible, and trace quantities of small plate-like mica particles (Kalliroscope Corp., Groton, MA.) were uniformly dispersed into the test fluids in order to increase the visibility of the secondary flow.

Images of the flow were recorded using a high-resolution monochrome CCD camera (COHU 4910) and a Super-VHS video recorder (Panasonic AG1960). Since the analog gain of the CCD camera is linear, spatial and temporal variations in the intensity of the reflected light by the mica flakes are faithfully recorded as gray-scale variations in the video-images. In §3.4, it is explained how these fluctuations can be used to calculate the wavelength and wavespeed of the elastic instability that develops above a critical rotation rate, or Deborah number. Individual images (480 × 480 pixels) of the entire cross-sectional area of the disk were digitized from each frame of the videotape using an 8-bit frame-grabber (DIPIX P360), yielding a spatial resolution of ~ 0.18 mm/pixel. Although flow cells can be readily distinguished visually in the fluid sample and also in the recorded images, a series of image-processing operations were subsequently performed to enhance the visibility of the cells. First, spatial nonuniformities in background light intensity were corrected for by a pixel-by-pixel division of gray-scale values using a pre-recorded reference image of the steady flow, as suggested by Russ (1992). The random high-frequency fluctuations in pixel intensity then were smoothed using a low-pass filter with a 5 pixel × 5 pixel kernel. Finally, the gray-scale histograms of the images were expanded by simultaneously adjusting the contrast and brightness in order to give the best visual definition of the cells. These processed images were analyzed to determine the wavenumber, spiral number and wavespeed for each run as described below.

The geometric configuration of the cone-and-plate device is shown schematically in figure 2.1(*b*), with the origin of a spherical coordinate system ($\hat{r}$, θ, ϕ) located at the apex of the cone. In this work the lower plate is held fixed while the conical fixture is rotated at a constant angular velocity Ω. A set of conical fixtures with a constant radius of $R = 25$ mm and precisely machined cone angles of $\theta_0 = 4°$, $6°$, $10°$ and $15°$ were used in the experiments. The lower plate consisted of a smooth, polished plexiglass sheet carefully aligned to be perpendicular to the axis of rotation. In order to prevent frictional contact between the apex of the cone and plate, the tip of each cone was truncated to leave a gap of 50 μm at the center of the device. The rotation rate Ω is used to define a characteristic time scale for the flow, and the homogeneous shear rate in the gap is given by $\dot{\gamma} \equiv \Omega / \theta_0$ for the base flow. In these experiments, the maximum rotation rates attained are approximately $\Omega_{max} \sim 10$ rad/s corresponding to a maximum shear-rate in the 4° cone of $\dot{\gamma}_{max} \sim 150\ s^{-1}$.

3.2.2 Stagnation Flows

The flow geometry used for the experiments is shown schematically in figure 2.6. The origin of the coordinate system is located at the center of the cylinder, with the x-axis along the cylinder axis, the y-axis normal to the channel walls and the z-axis in the flow direction. The internal dimensions of the channel are width $\Delta x = 76.1$ mm, height $\Delta y = 12.7$ mm and length $\Delta z = 279.0$ mm, which allows the flow to become fully developed before reaching the cylinder and provides a large downstream region in which to study the instability. The channel is constructed of plexiglass in order to match closely the refractive index of the test fluid. Although the ratio of the width of the channel to its height is only 6:1, a two-dimensional velocity profile is obtained over the central 80% of the channel, and all measurements are restricted to this region.

The relative importance of the shearing flow in the gap between the cylinder and the channel wall and the extensional flow downstream of the cylinder is examined by using cylinders with a wide range of radii in this channel. Nine cylinders of radius R, 0.31 mm $\leq R \leq 5.32$ mm are used to obtain aspect ratios of $0.05 \leq R/H \leq 0.84$, where H is the half-height of the channel. Cylinders with $0.17 \leq R/H \leq 0.84$ are machined from aluminum with ends of $R = 3.18$ mm to fit in holes in the side panels of the flow cell. These holes are precisely positioned in the center of the panels to within ± 0.025 mm to ensure a symmetric base flow. The smallest cylinders of $R/H = 0.05$ and 0.10 are stainless steel wires that are welded to a support brace to prevent deflection by the flow.

The importance of the upstream flow conditions is investigated by replacing the cylinder with a planar divider. This consists of a flat plate of height $2R_{\text{div}}$ for $z < 0$ and a radius of curvature R_{div} for $z > 0$. The parabolic velocity profile across the entire channel for flow past a cylinder is therefore replaced by a parabolic velocity profile between the divider and the channel wall on both sides for $z < 0$, while for $z > 0$ both geometries are the same. Dividers are used with R_{div}/H of 0.23, 0.50 and 0.75. A tapered divider was also used in order to remove the curvature of the cylinder or divider while retaining a stagnation plane. The total included angle of the divider was 4°, and its minimum width was 0.2 mm.

Axisymmetric stagnation flows were also studied by using a rod with a rounded end mounted in the center of a circular plexiglass tube. The radius of the tube was $R_{\text{tube}} = 1.27$ cm, and the radii of the cylinders were $R_{\text{rod}} = 0.64$ and 0.32 cm. The end of each rod was rounded with a radius of curvature equal to R_{rod}. The rods were held in place by a disk mounted across the plexiglass tube. Holes in the disk for $R_{\text{rod}} < r < R_{\text{tube}}$ allowed the fluid to pass through, and a distance of 15 cm from the disk to the rounded end assures fully developed flow. These rods could be inserted in the flow system to study either the upstream or downstream stagnation point.

Two different timescales can be defined for the flow past a cylinder. Downstream of the rear stagnation the velocity increases from zero to the freestream value over a distance that scales with the cylinder radius, yielding $\mathcal{T}_1 = R/v_{z,\max}$, where $v_{z,\max}$ is the centerline streamwise velocity of the fully developed flow. A second timescale can be defined base on a typical shear rate in the gap between the cylinder and the channel wall, $\mathcal{T}_2 = (H - R)^2/Hv_{z,\max}$. Two dimensionless measures of the elastic effects are defined as

$$De = \lambda(\dot{\gamma})v_{z,\max}/R \tag{3.19}$$

and

$$We = \lambda(\dot{\gamma})v_{z,\max}H/(H-R)^2, \tag{3.20}$$

where *De* is the Deborah number and *We* is the Weissenberg number. Inertial effects are measured in terms of the Reynolds number,

$$Re = 2\rho v_{z,\max}R/\eta(\dot{\gamma}). \tag{3.21}$$

The maximum Reynolds number in any experiment is 0.02.

A schematic diagram of the fluid circulation system is shown in figure 3.8. Fluid from a high density polyethylene (HDPE) collection tank is pumped to a 40 gallon galvanized steel tank. The pump (Moyno, Model 2L8) is a positive displacement pump which operates under low shear conditions to prevent polymer degradation. Fluid from the tank flows to the geometry under nitrogen pressure. The flowrate can be controlled by changing the nitrogen pressure and pump setting and by adjusting valves in the system. The maximum flowrate is about 8 l/min. PVC tubing is used throughout the system, since it is resistant to the tetradecane (C14) used as a solvent.

3.2.3 Superposed Plane Poiseuille Flow

The stability of the interface between two fluids flowing through a rectangular channel was studied in the geometry shown schematically in figure 3.9. The flow cell was constructed of plexiglass in order to permit the interface to be viewed at any position along the length of the channel, rather than from a limited number of viewing ports in a metal geometry. The channel's height is 3.54 mm, its width is 40 mm, which ensures a two-dimensional base flow throughout the central portion of the channel, and its length is 300

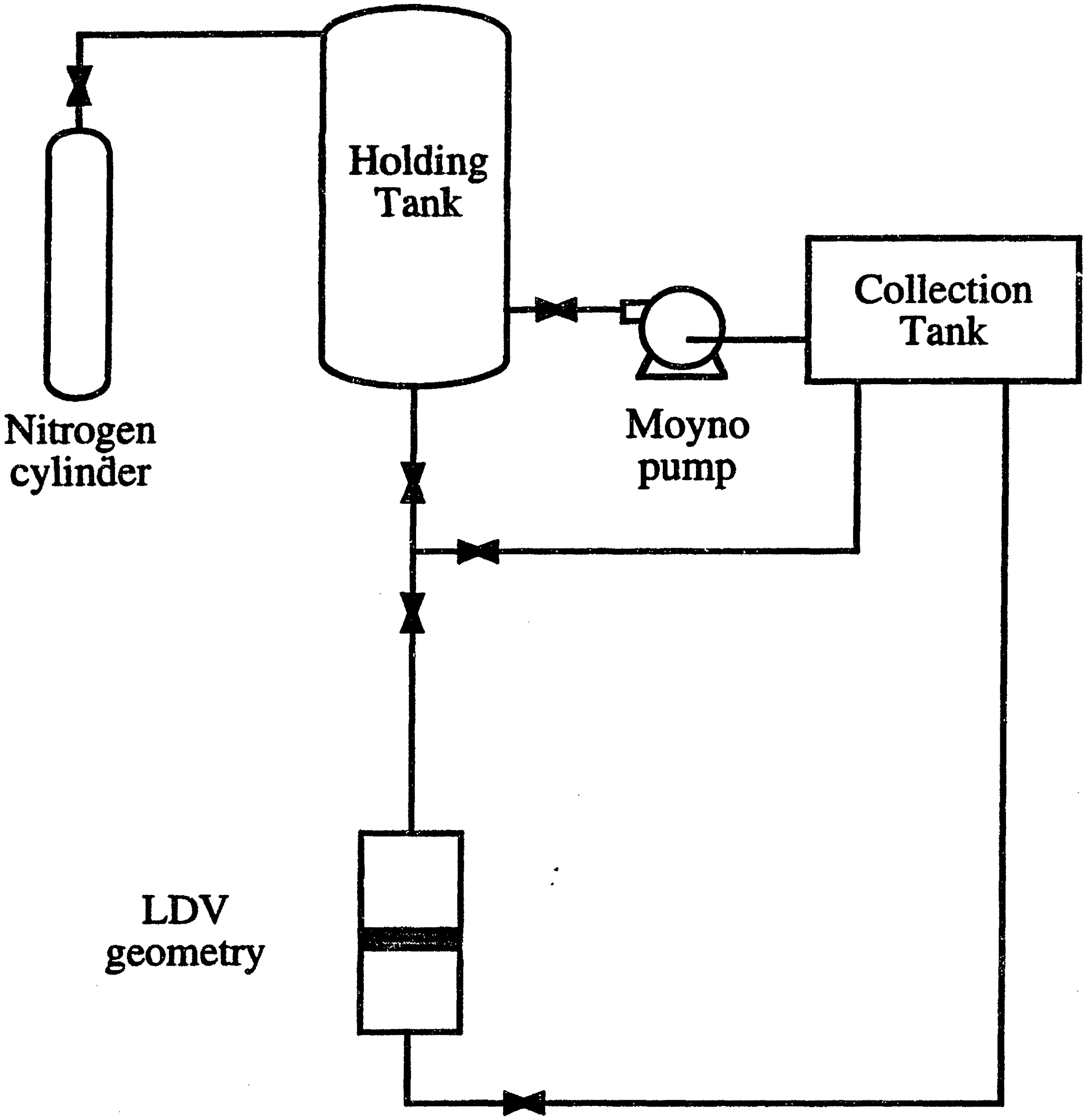

Figure 3.8 Schematic diagram of the fluid circulation system.

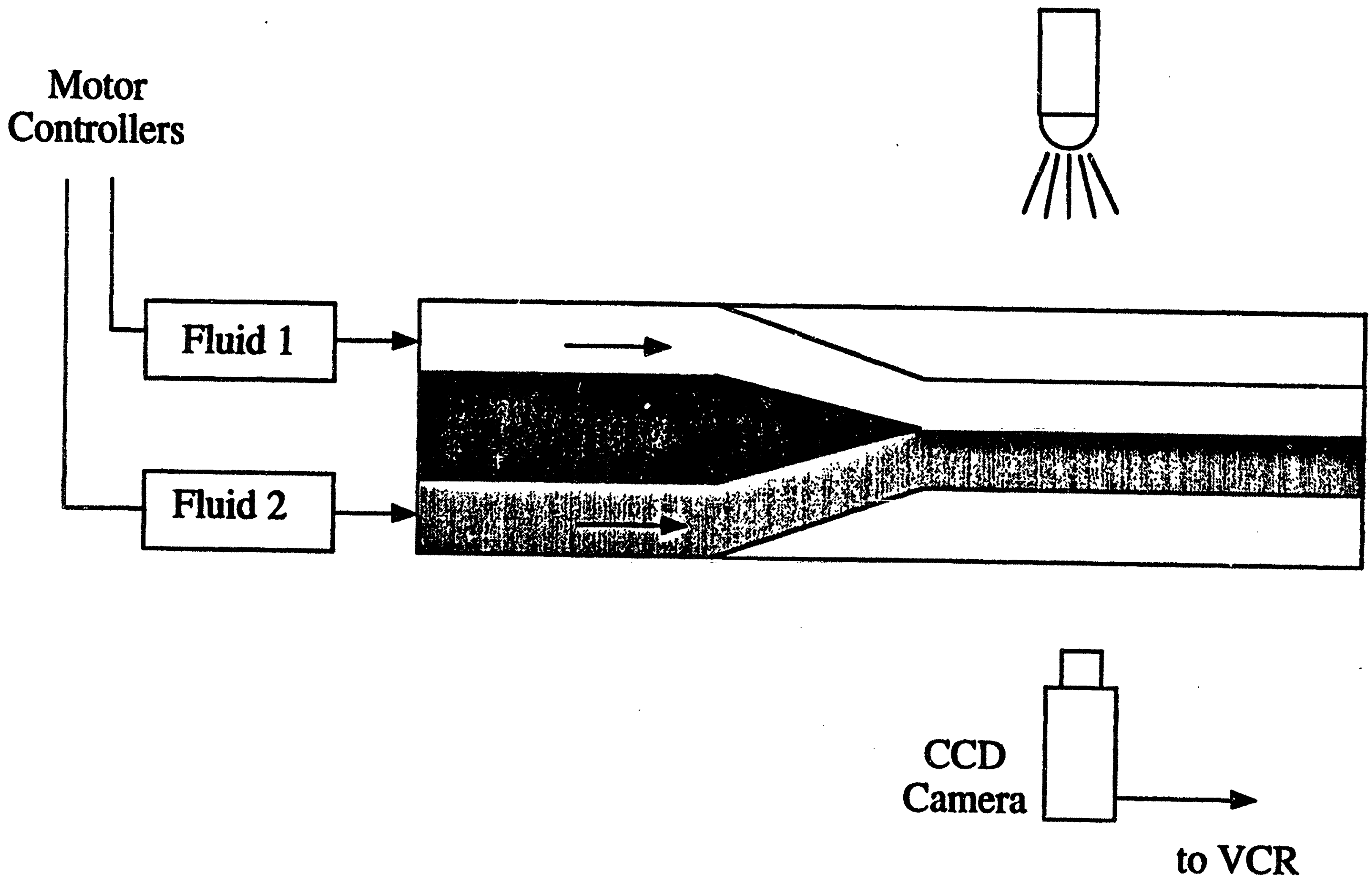

Figure 3.9 Schematic diagram of the experimental system for superposed plan Poiseuille flow.

mm, which allows the amplitude of interfacial disturbances to be determined over a large distance to determine their growth or decay rate.

Two fluids are pumped independently and are initially separated by a vane to establish a fully-developed upstream flow. Each fluid is driven from a cylindrical cartridge (Semco, C20) by a linear-drive stepper motor (Anaheim Automation, 23A102). Typical flowrates range from 0.005 to 0.1 cm^3/s, which correspond to displacements of the motor of 1.5×10^{-4} to 0.003 cm/s. This resolution can be obtained by using a microstepping controller (Anaheim Automation, DPMS256) which allows for step sizes as small as 2.5×10^{-6} cm. Furthermore, the flowrate of one of the fluids can be sinusoidally varied in order to introduce a disturbance of known frequency into the flow.

As discussed in §2.3, one of the important parameters governing the stability of the interface is the depth ratio of the two fluids. Because all of the fluids used for these experiments have viscosities that are nearly independent of the shear rate, the solution to the equations of motion for a Newtonian fluid is used to calculate the depth ratio and interfacial velocity for a given viscosity ratio and set of flowrates. The Deborah number is then $De = \lambda_1 u_{\mathrm{int}}/d_1$, where λ_1 and d_1 are the time constant and depth of the more elastic fluid and u_{int} is the interfacial velocity.

The center of the flow cell is illuminated by a fiber optic light source, and images of the flow are recorded using a high-resolution CCD camera (COHU, 4910) and a S-VHS VCR (Panasonic, AG-1970P). An organic dye is added to one of the fluids to increase the amount of scattered light and enhance the contrast at the interface between the two fluids. The image of the flow was magnified to yield a spatial resolution of ~0.01 mm/pixel.

3.3 Laser Doppler Velocimetry

Laser Doppler velocimetry (LDV) is a noninvasive means of accurately measuring velocities on very small length scales and rapid time scales. Depending on the signal processing used in conjunction with the optical components, either steady-state or time-dependent velocities can be measured. LDV has found many applications in fluid mechanics since various configurations allow for velocity measurements between 10 μm/s to Mach 8. Many of these possibilities have been described by Durst *et al.* (1981), and the important features of the system that will be used in this work are discussed below.

Velocities are measured using LDV by detecting and analyzing the light scattered by particles in a flowing fluid. As a particle passes through a laser beam, it will scatter light in all directions which is shifted in frequency by an amount that is directly proportional to its velocity. Since the amount of the shift to be measured (typically ~ 10^4 Hz for the velocities measured in this work) is small compared to that of the incident beams (~ 6 x 10^{14} Hz) the scattered light is heterodyned, or combined, with scattered light from another incident beam of the same wavelength. A signal can then be obtained with a frequency which is the frequency difference between the two scattered beams. This heterodyned light is then collected by a photomultiplier, and the shifted frequency is determined.

The principle of laser Doppler velocimetry can be understood in terms of a simple fringe model. When the beams intersect, constructive and destructive interference establishes a diffraction pattern of alternately light and dark fringes. If a particle in the fluid passes through the fringes, it will scatter light in all directions. The shift in frequency of the scattered light (f_s) can be thought of as the reciprocal of the time taken for the particle to pass from one bright fringe to the next. The fringe spacing is

$$d_f = \frac{\lambda}{2\sin\alpha}, \tag{3.22}$$

where λ is the wavelength of the light, α is the half-angle between the incident beams, and d_f is 1.2 μm in this system. The particle velocity is therefore

$$v = \frac{d_f}{f_s^{-1}} = \frac{\lambda f_s}{2\sin\alpha}, \tag{3.23}$$

where v is the component of velocity in the plane of the intersecting beams and normal to the bisector of the beams.

A two-color laser Doppler velocimetry system (TSI 9100-12) is used in a back-scatter configuration to provide accurate, noninvasive measurements the streamwise (v_z) and neutral direction (v_x) components of the velocity. The light source is a 4 Watt Argon-ion laser (Lexel, Model 95-4), and two separate wavelengths are used: green ($\lambda = 514.5$ nm) and blue (488 nm). Each color is split into two beams and passed through a series of optics to focus all four beams at a single point, and each pair of beams independently measures a separate component of the velocity. In the backscatter configuration the scattered light is collected along the same optical train that is used for the incident beams. The scattered light of each color passes through a filter and is collected by a photomultiplier, which produces an analog signal that is directly proportional to the intensity of the incident light. The measuring volume formed by intersecting beams is an ellipsoid of approximately 20 μm × 20 μm × 80 μm, while the radius of the smallest cylinder is 310 μm. Figure 3.10 schematically shows the optics of the LDV system and fringes of the measuring volume for a pair of beams. The entire optical train is mounted on a computer-controlled, three-dimensional translating table (TSI, Model 9500) which allows for pointwise velocity measurements at any position within the flow cell, or for velocity scans throughout the flow cell. Steady, pointwise measurements are obtained when Doppler-shifted light scattered by particles in the fluid is collected by the photomultiplier, and the signal from the photomultiplier is sent to a dual-channel, fast Fourier spectrum analyzer (Nicolet, Model 660B). The frequency spectrum of the 'Doppler burst' caused by a particle passing through the measuring volume is calculated, and about 50 spectra are averaged to obtain a velocity measurement at a position. Steady velocity measurements can be obtained in the range 0.04 - 400 cm/s with an accuracy of ± 1%.

Time-dependent velocity measurements of velocities in the range 0.1 - 1000 cm/s can also be made by using frequency trackers (DISA, Model 55N20/21) with an accuracy of ± 2%. The trackers lock onto the Doppler frequency and follow its evolution in time. Use of the LDV system in this manner requires a high rate of data, because the tracker will 'drop out' if it is unable to follow the frequency continuously. Spatially-varying velocities are recorded by using the frequency trackers to follow the Doppler frequency in time as the measuring volume is translated through the flow cell.

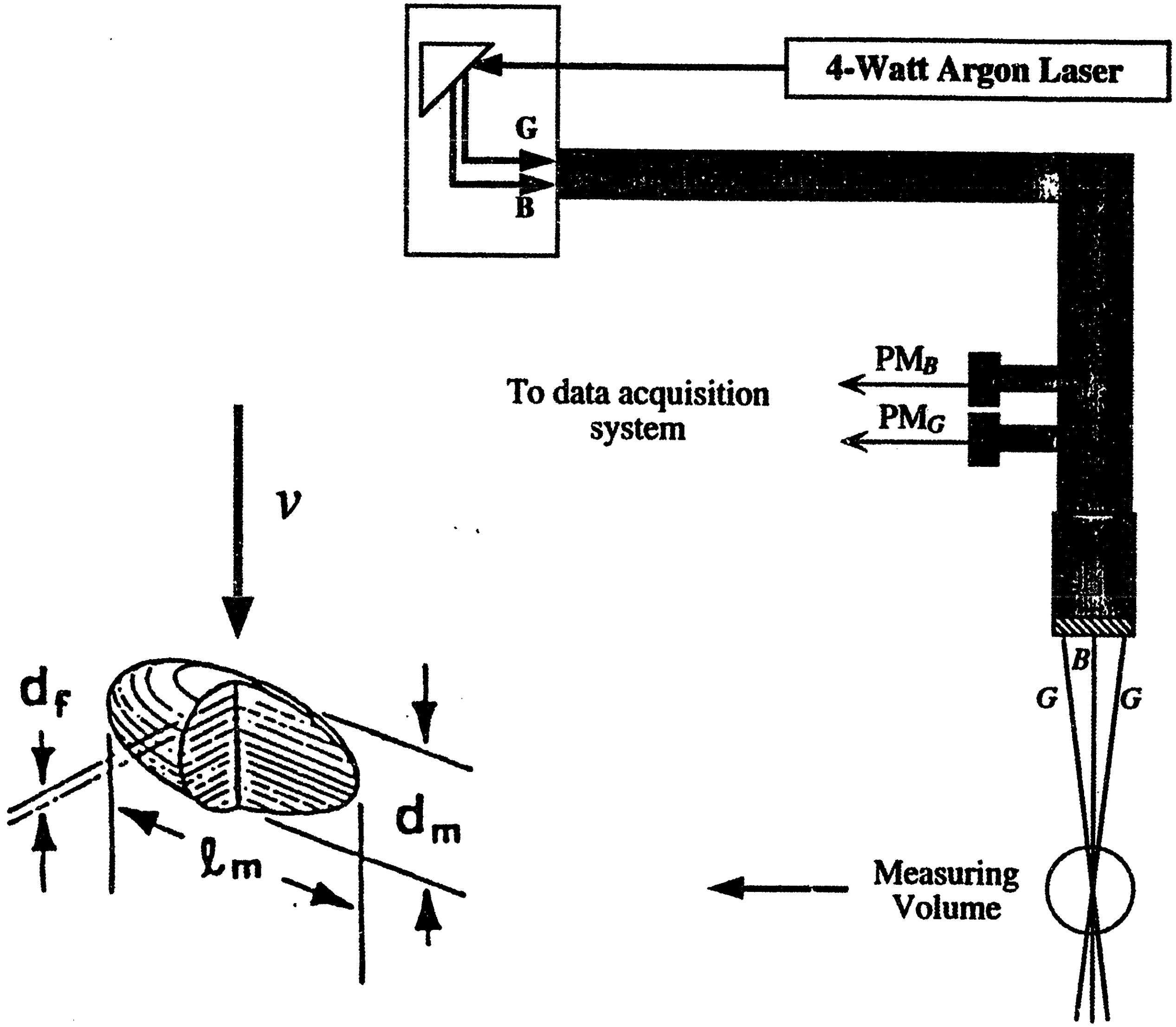

Figure 3.10 Schematic diagram of the LDV system and the measuring volume.

3.4 Image Analysis

3.4.1 Rotational Flows

The video-imaging system has been used to make quantitative measurements of the spatial and temporal evolution of the secondary flow that develops in the fluid sample above a critical rotation rate. In order to compare the experimental observations with the results of the linear stability calculations, it is first necessary to understand the relationship between the dimensionless parameters α, m and σ describing the form of the normal mode perturbations considered in the numerical analysis and the experimental quantities that are actually observable through the transparent base of the rheometer. The experimental work used a classical flow visualization technique (*cf.* Merzkirch 1987) based on the addition of anisotropic seeding particles to the viscoelastic test fluid which align with the local direction of the creeping flow between the plates. In a steady two-dimensional flow, the locally-averaged intensity of the reflected light is spatially uniform; however, following the onset of a hydrodynamic instability, spatial and/or temporal variations in the intensity of the reflected light at each point develop and can be used to infer the structure of the developing secondary flow.

Since the observations are limited to two-dimensional images in the r-θ plane of the test cell, the intensity of the reflected light $I(r, \theta, t)$ at any image coordinates (r, θ) fixed with respect to the center of the stationary base represents an integrated average of the reflections from seed particles moving through that point but distributed over a range of depths z in the fluid. If the observed flow instability is of the normal mode form, then the gray-scale intensity of any pixel in the image obtained from the CCD array is expected to vary as

$$I(r,\theta,t) \propto \overline{f(z)}\, e^{i\alpha r + im\theta + \sigma t}, \tag{3.24}$$

where $\overline{f(z)}$ indicates an undetermined weighted z-average of the spatial form of the disturbance to the base flow.

If a pixel is selected in a digitized, two-dimensional image with a maximum intensity I_{max} and points of constant intensity are tracked across the image, then the locus of these points at any instant in time will be given by

$$dI = 0 = i\alpha\, dr + im\, d\theta. \tag{3.25}$$

Or by integrating once as

$$r = -\frac{m}{\alpha}(\theta + \theta_0), \tag{3.26}$$

where θ_0 sets the radial location R_0 of the starting point with respect to the (arbitrary) definition of the line given by $\theta = 0$.

The spatial locations of the recirculating vortices in the secondary flow given by equation 3.26 are thus described by *Archimedean Spirals* (Davis 1993) and the winding number of the spiral curves is given by m/α. The radial wavenumber α is only meaningfully defined for positive real numbers and azimuthal periodicity requires that m takes integer values only. If $m > 0$ then the curves spiral inwards towards the origin with increasing θ; if $m < 0$ then the curves spiral outwards. The local *spiral angle* ε may be conveniently defined from equation 3.25 as

$$\tan\varepsilon = \frac{-dr}{r d\theta} = \frac{+(m/r)}{\alpha} \tag{3.27}$$

and can be interpreted as the ratio of the azimuthal wavenumber (m/r) at any given radius to the radial wavenumber α.

Sample curves are illustrated in figure 3.11 for a fixed value of radial wavenumber α and increasing values of azimuthal wavenumber $m = 0$, 1 and 2. In each case, the azimuthal coordinate θ is defined from the abscissa $y = 0$ and increases in the clockwise direction. For nonaxisymmetric disturbances ($m > 0$), note that although azimuthal periodicity at a fixed radius requires $f(\theta) = f(\theta + 2\pi)$, the locus of each line corresponding to the maximum intensity of a secondary vortex is given parametrically in terms of $0 < \theta < R\alpha/m$. It also should be noted that by following the locus of a single spiral curve it is not possible to determine the values of m and α unambiguously, but only the quotient m/α. The parameter m is determined independently, however, by noting that it indicates the integer number of intertwined, non-intersecting curves that cross a circumferential arc at every radius r.

Video-imaging measurements of variations in the intensity of the reflected light are combined with these equations to determine the parameters describing the spatial form of the instability. The temporal evolution of the secondary flow is quantified by making a sequence of such observations at successive time intervals of 1/30th second. Profiles of gray scale intensity as a function of radial position are presented in §4 and the peaks in the profile are identified as local maxima in the magnitude of the secondary flow. Profiles at a fixed azimuthal position for a sequence of elapsed times show that the instability consists of radially-periodic vortices which travel outwards across the disk. The radial wavenumber α

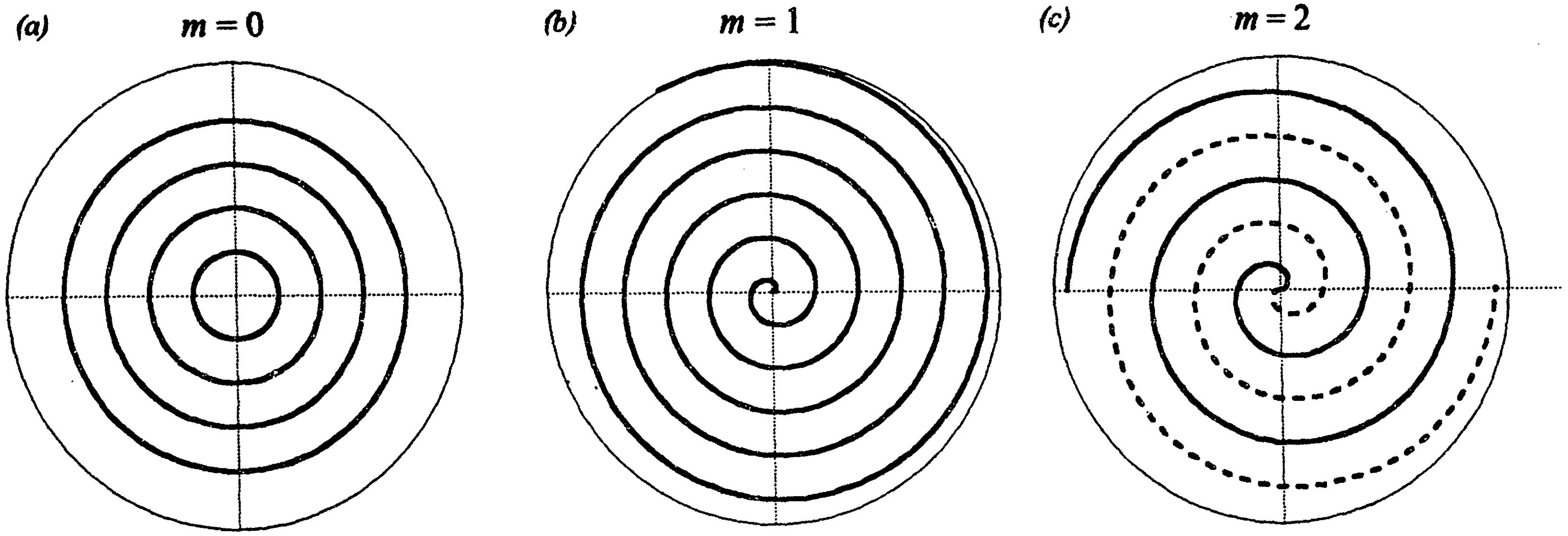

Figure 3.11 Archimedian spirals of the form given by equation 3.26: (*a*) axisymmetric mode, $m = 0$; (*b*) nonaxisymmetric mode, $m = 1$; (*c*) nested nonaxisymmetric spirals, $m = 2$. The radial wavenumber α of the spiral is the same in each case.

can be calculated from either the Fourier spectrum of a single radial profile $I(r)$, or from the average of all observed peak-to-peak distances at different angular positions. The wavespeed, $c \equiv \mathrm{Im}(\sigma)/\alpha$, of the secondary flow is determined by measuring the position of the center of each vortex at successive time intervals. Linear regression using equation 3.26 of a series of radial intensity profiles at different azimuthal angles θ in an image makes it possible to determine if the secondary flow is axisymmetric or three-dimensional. Information describing the temporal structure of the elastic instability at a single fixed point in space might be obtained from a time-series of LDV measurements (*cf.* McKinley *et al.* 1991b); however, such observations fail to yield the global spatial form of the instability at any instant in time, so this approach has not been pursued here.

The image analysis for the instability in the cone-and-plate geometry follows a similar approach, but the interpretation of the intensity profiles must be modified due to the altered spiral structure. The roll cells in the cone-and-plate geometry are wound into a well-defined spiral structure with a characteristic logarithmic radial spacing across the disks. This section defines the normal mode decomposition used to describe infinitesimal perturbations of this form and show that the two-dimensional planform of this representation has the form of self-similar *Bernoulli Spiral curves*.

The nonlocal spatial form of the secondary motion that is observed in the experiments, coupled with the lack of a characteristic length scale in the gap between the rotating cone and stationary plate suggests the use of a coordinate transformation to simplify the governing equations. A transformed radial coordinate, ξ, is defined by:

$$\xi \equiv \ln(\hat{r}/R_0), \tag{3.28}$$

where $\hat{r}$ is the dimensional radial coordinate in a $(\hat{r}, \theta, \phi)$ spherical polar coordinate system and R_0 is an arbitrary reference length scale, for example the finite radius of the experimental geometry.

When expressed in this dimensionless transformed radial coordinate, the experimental measurements of the separation between adjacent roll cells become equally-spaced and the secondary motion can be represented by *Archimedean Spirals* as for the parallel-plate elastic instability. In transformed coordinates, the disturbances considered for any dimensionless variable f in the linear stability analysis are then represented in the form

$$f(\xi,\theta,\phi,t) = F(\theta)e^{i\alpha_\xi \xi + im\phi + \sigma t}, \tag{3.29}$$

where α_ξ is the dimensionless wavenumber in the *transformed* radial coordinate, m is an integer indicating the periodicity in the azimuthal direction, σ is the dimensionless complex growth rate of the disturbance scaled with Ω^{-1}, and the complex amplitude function $F(\theta)$ satisfies the boundary conditions of the disturbance equations on the upper and lower fixtures.

Illumination of the fluid sample and observation of the reflected light results in a time-series of two-dimensional video-images in the $(\hat{r},\phi)$ plane. If the disturbance kinematics are of the form given by equation 3.29 then the intensity I of the images will vary as

$$I(\hat{r},\phi,t) \sim I_0 e^{i\alpha_\xi \ln(\hat{r}/R_0)+im\phi+\sigma t}, \tag{3.30}$$

where I_0 represents an (unknown) depth average of the reflected light from the fluid sample at each radial position.

Selecting a point in a single video-image corresponding to a maximum intensity in the secondary motion and following the location of this recirculating vortex in the $(\hat{r},\phi)$ plane yields a locus of points given by

$$dI \equiv \left(\frac{\partial I}{\partial \hat{r}}\right)d\hat{r} + \left(\frac{\partial I}{\partial \phi}\right)d\phi = 0 = \frac{\alpha_\xi}{\hat{r}}d\hat{r} + m\,d\phi. \tag{3.31}$$

Rearranging and integrating this expression results in a spiral curve $R(\phi)$ defined parametrically by

$$R(\phi) = R_0 e^{-(\alpha_\xi/m)\phi}. \tag{3.32}$$

where $-\infty \leq \phi \leq \infty$ and R_0 is an integration constant corresponding to the (arbitrary) radial location at which the spiral curve passes through the point $\phi = 0$.

The single curve defined by equation 3.32 is known as a *Bernoulli spiral*, and the constant factor $(-\alpha_\xi/m)$ is often defined as a winding number n. Unlike the Archimedean spirals observed for the parallel-plate geometry, there is no well-defined length scale in the radial direction. A rotation of the coordinate system by a factor ϕ_0 is equivalent to a scaling of the radial coordinate by a factor $s \equiv e^{n\phi_0}$, and this curve is a self-similar or fractal object (Peitgen *et al.* 1993). Figure 3.12 by shows the maxima in the disturbance kinematics for a fixed value of the wavenumber α_ξ and different values of the azimuthal wavenumber m.

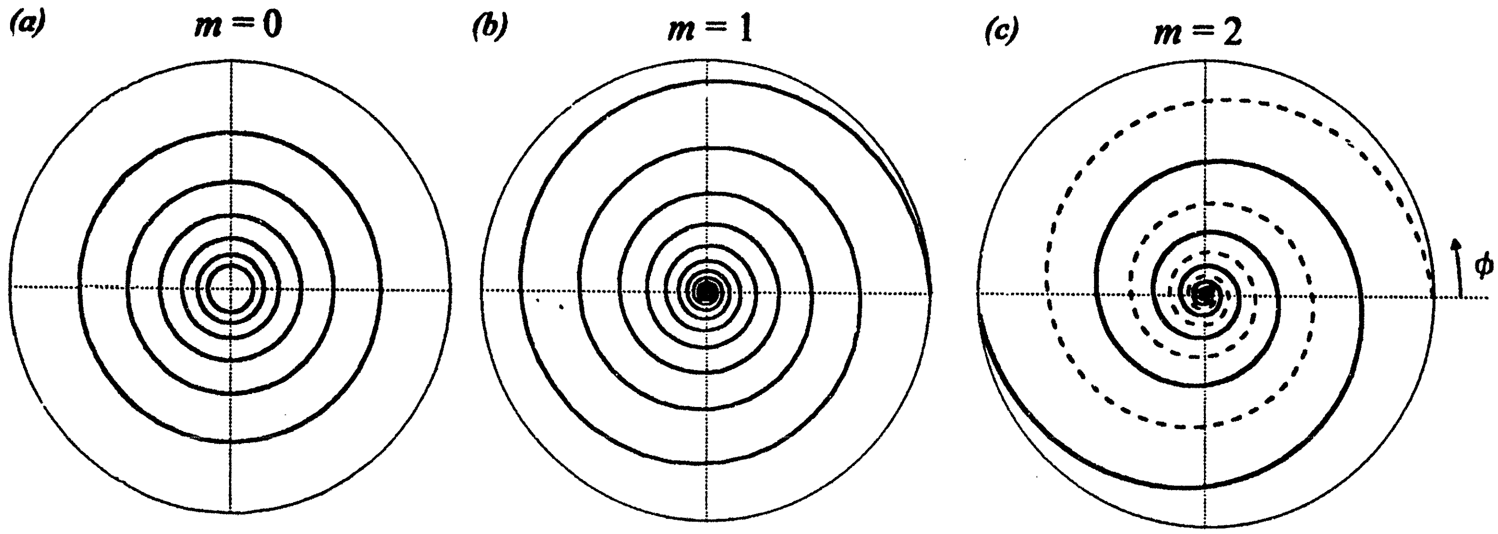

Figure 3.12 Logarithmic spirals of the form given by equation 3.31: *(a)* axisymmetric mode, $m = 0$; *(b)* non-axisymmetric mode, $m = 1$; (c) nested non-axisymmetric spirals, $m = 2$. The wavenumber α_ξ of the spiral in the transformed radial coordinate is the same in each case.

Both of the wavenumbers (m and α_ξ) describing the disturbance can be determined from experimental measurements of the gray-scale intensity $I(\hat{r},\phi)$. Measurements of the radial locations (R_i) of successive peak intensities taken radially outwards across the disk at any fixed value of the azimuthal coordinate ϕ are related by a geometric series (*cf.* equation 3.30):

$$\frac{R_{i+1}}{R_i} = e^{2\pi/\alpha_\xi} \tag{3.33}$$

Non-zero values of the parameter $|m|$ correspond to the integer number of intertwined non-intersecting spiral curves; for $m = 0$ the disturbance corresponds to axisymmetric toroidal vortices with a logarithmic radial spacing. The wavespeed of the disturbance is determined by following the spatial translation of the spiral cells such that $\mathrm{D}I/\mathrm{D}\hat{t} = 0$. The dimensional radial wavespeed $\hat{c}_r$ of the cellular disturbance is thus calculated from equation 3.30 to vary linearly across the disk as

$$c_\xi \equiv \frac{\hat{c}_r}{\hat{r}\Omega} = -\frac{\mathrm{Im}(\sigma)}{\alpha_\xi} \tag{3.34}$$

and the direction of propagation is determined from the sign of the imaginary part of the eigenvalue σ.

3.4.2 Superposed Plane Poiseuille Flow

In order to quantify the amplitude and wavenumber of the interfacial disturbances, a series of image processing operations must be applied to the images obtained as described in §3.2.3. For the magnification used, each frame of the videotape shows a region of the channel ~6 mm long and its entire height. However, the wavelengths of the instabilities studied here are typically 6 to 30 mm long, so a composite image of the flow is formed in order to compress the scale in the flow direction. A framegrabber (Scion, LG-3) was used to extract a single vertical line of pixels from images at rates from two to five frames per second, depending on the amount of compression needed to study a given wavelength. The compressed image shows the flow past a single point over a sufficiently long time so that the time series of the interface position contains enough periods of the disturbance to allow its wavenumber to be accurately determined by an FFT.

In order to obtain the position of the interface, the images must be processed to demarcate sharply the regions of the two fluids. All image processing was performed using the Concept V.i image analysis library (Graftek) in the LabVIEW programming system (National Instruments). The contrast between the two fluids was first increased by altering the histogram of the gray scale values of the pixels such that gray scale values over a selected interval were redistributed over the full range of 0 to 255. The interval was chosen such that the contrast within the region corresponding to each fluid was decreased, while the contrast between the two fluids was increased. After there was a clear contrast between the two regions, the image was transformed to a binary image to aid with further processing. A series of opening and closing operations were performed on the binary image to eliminate isolated pixels without affecting the shape or position of the interface. A Prewitt filter, a high-pass filter which highlights variations of intensity along the horizontal and vertical axes, was used to locate the position of the interface. A curve of the detected interface position can then be drawn on the original image to allow for a visual verification that the image processing operations did not alter the interface. The series of points corresponding to the interface position can then be used to determine the amplitude and wavenumber of the disturbances.

Chapter 4

Rotational Flow Instabilities

The elastic flow instabilities in the torsional flows between parallel plates and between a cone and a plate are studied by using a digital imaging system in order to determine the spatial and temporal characteristics of the instabilities. The effects of changing the flow geometry and fluid rheology are investigated for each case, and the results are compared with the predictions of a linear stability analysis.

4.1 Parallel Plate Geometry

Experimental observations are presented which allow the determination of the spatial and temporal characteristics of the purely elastic torsional flow instability between parallel plates. The consequences of the flow instability on the total torque and thrust exerted by the fluid on the plate are demonstrated in §4.1.1, and the limitations of the data that can be obtained from such spatially-averaged measurements are summarized. A detailed analysis of the spatial and temporal evolution of the flow instability in the 0.31 wt% Boger fluid for a fixed geometric aspect ratio of $R/H = 20$ is presented in §4.1.2, and the spiral parameters describing the local form of the nonaxisymmetric disturbance are determined. The effects of changing fluid rheology and aspect ratio on the instability are shown in §4.1.3. Observations of a second flow transition that develops at later times from well-defined spiral vortices of a single spiral number to a complex nonlinear state composed of nonaxisymmetric disturbances with a spectrum of radial wavelengths are described in §4.1.4.

4.1.1 Dynamic Torque and Normal Force Measurements

Previous measurements of the onset of the torsional flow instability typically have been limited to dynamic measurements of the total torque $\mathcal{T}$ and the total thrust, or normal force, $\mathcal{F}$ exerted on the stationary upper disk of a commercial parallel-plate rheometer as the lower disk is rotated at various speeds (Magda and Larson 1988; Steiert and Wolff 1990; McKinley *et al.* 1991a). Typical results are presented in figure 4.1 for the apparent first normal stress difference, $N_{1a}(t) = 4\mathcal{F}(t)/\pi R^2$ measured in the 0.20 wt% PIB Boger fluid during the start-up of steady shear flow in a Rheometrics RMS-800 Mechanical

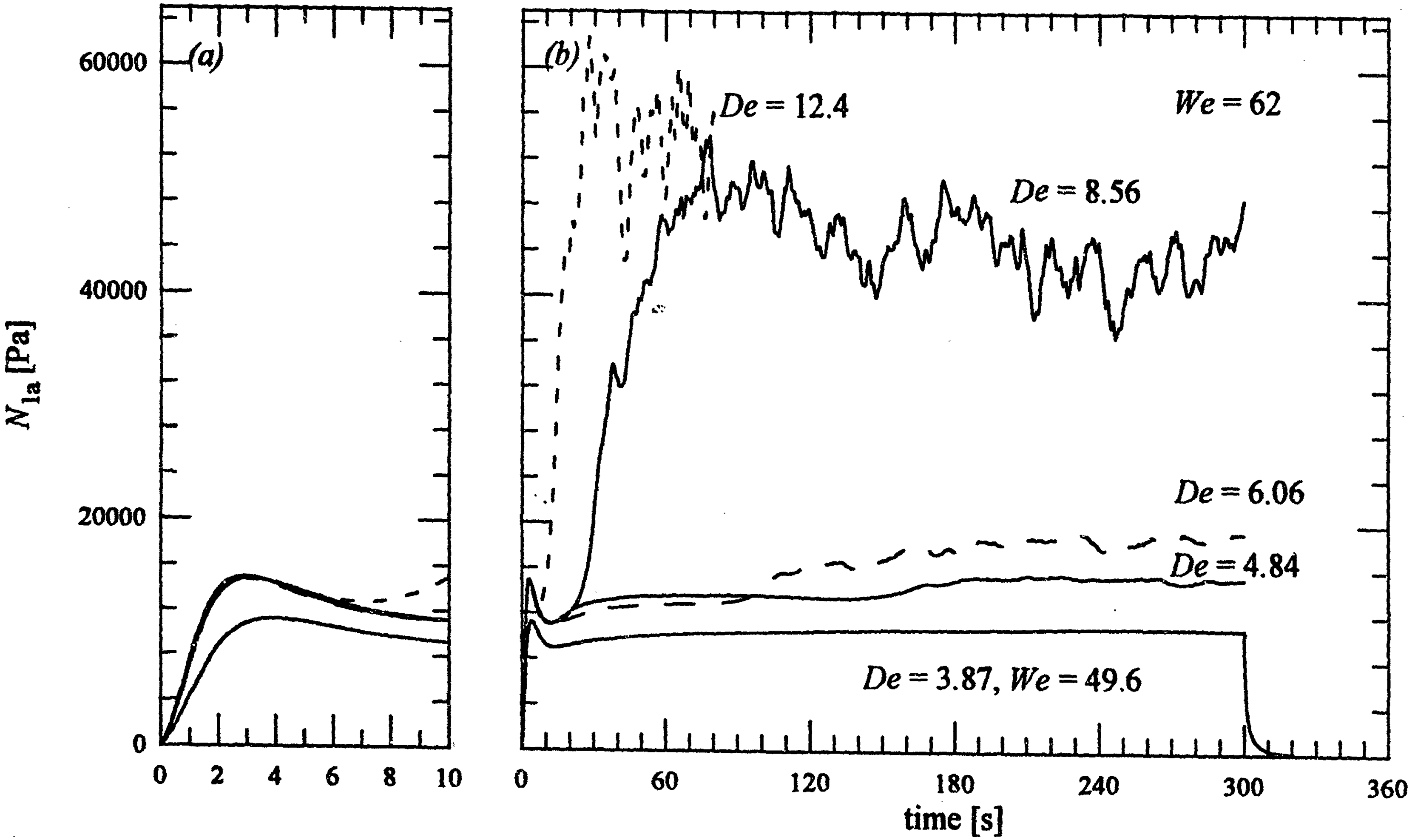

Figure 4.1 Transient response of the apparent first normal stress difference of the 0.20 wt% PIB fluid in a parallel plate rheometer: (*a*) initial overshoot and (*b*) growth of the instability as a function of Deborah number for a constant Weissenberg number *We*.

Spectrometer. The sensitive dependence of the instability on the angular rotation rate Ω between the plates is clearly observed. In each experiment, a fresh fluid sample is used, the rotation rate is increased, and the aspect ratio *R/H* between the plates is decreased proportionately, such that the rim shear-rate and thus the Weissenberg number of the flow remains fixed. At short times, N_{1a} grows quadratically, passes through a local maximum and then decreases towards a steady asymptotic value, as shown in figure 4.1(*a*). The initial transients superpose for all experiments performed at the same shear rate (or Weissenberg number), regardless of the rotation rate or Deborah number of the flow, as expected from the fundamental rheological premise that the material properties of a simple fluid are a unique function of the local (in a Lagrangian sense) deformation rate. For low values of the rotation rate, the first normal stress difference smoothly asymptotes to the expected steady-state value and subsequently remains constant at all future times. However, as the rotation rate is increased beyond a critical value of $\Omega_{\text{crit}} = 3.90$ rad/s, the normal stress exhibits a rapid increase above the expected steady-state value to a final time-dependent state. These complex aperiodic fluctuations correspond to the onset and nonlinear evolution of a nonaxisymmetric secondary flow between the plates, as shown in §4.1.2. The magnitude of this transient increase in the normal stress N_{1a} becomes larger, and the induction time for onset of the instability becomes progressively shorter as the rotation rate and Deborah number are increased. Similar behavior is observed in the torque exerted by the fluid on the plate. In McKinley *et al.* (1991a) a series of such measurements were used to show that the initial growth in the stresses is exponential in time, that there is hysteresis in the flow and thus that the instability is subcritical in rotation rate. However, because the measured thrust and torque correspond to integrated values of the actual stresses acting on the plate at each point, it is not possible to deduce information about the spatial form of the instability.

4.1.2 Nonaxisymmetric Disturbances of Spiral Form

A series of observations depicting the evolution of the kinematics in the torsional flow were made using the 0.31 wt% fluid with a fixed plate separation of $H = 2.00$ mm, corresponding to an aspect ratio of $R/H = 20$. The series of gray-scale images shown in figure 4.2 were obtained using the video-imaging system described in §3.3 and depict the spatial and temporal evolution of the flow *at a fixed rotation rate* as it progresses from the stable base flow *(a)*, through a well-defined spatially-periodic spiral structure *(b-d)* before ultimately developing into a nonlinear state with many modes present *(e-f)*. A steady rotational flow is initially established between the plates at a rotation rate below the critical

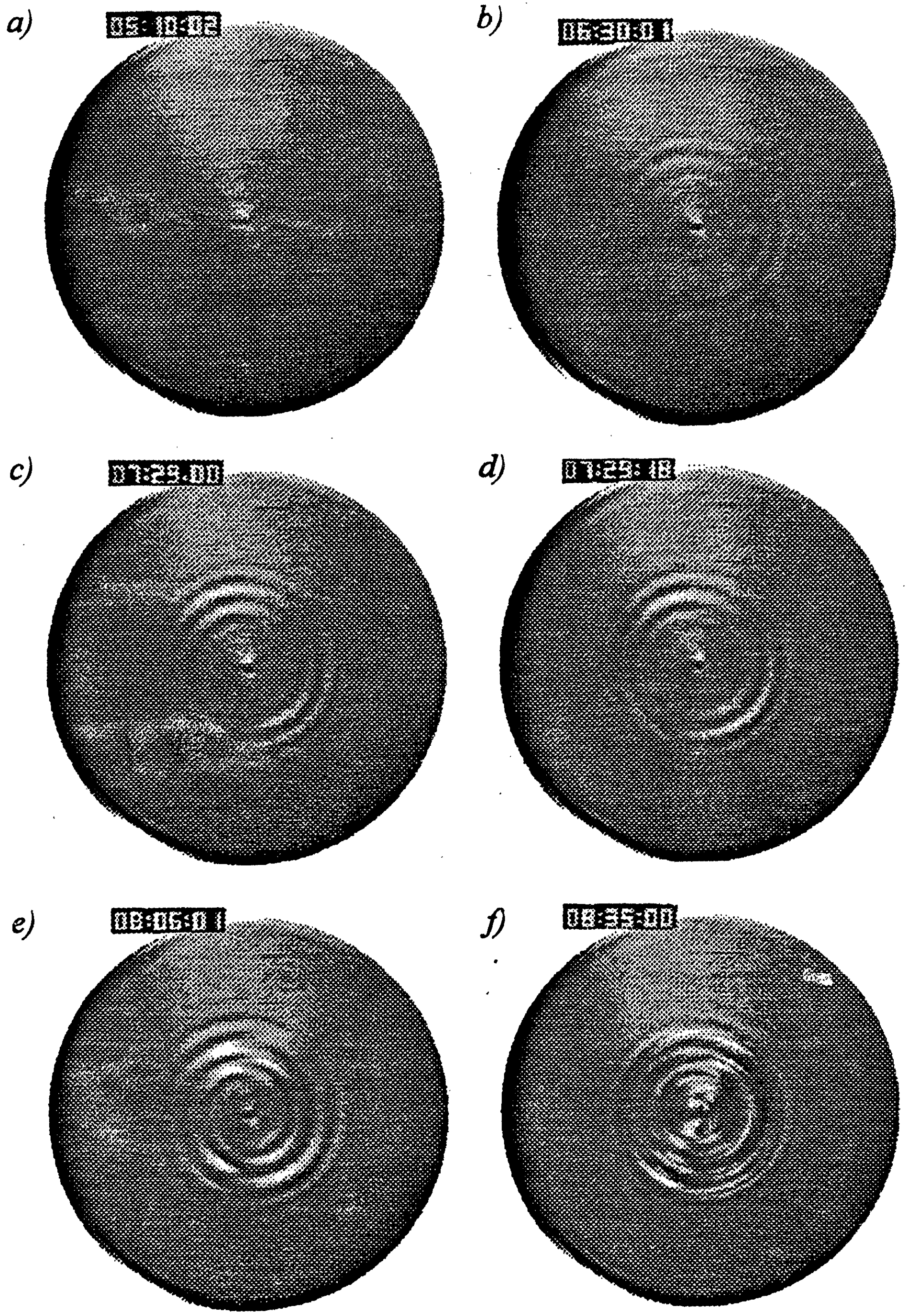

Figure 4.2 Onset and growth of the purely elastic instability observed in the torsional flow of the 0.31 wt% PIB fluid between coaxial parallel disks with $R/H = 20$: (*a*) flow appears stable shortly after the Deborah number is increased to $De_0 = 5.99$ at $\hat{t} = 5{:}00{:}00$ (min:sec:frame); (*b*) after an induction time of 90 s, the spatial structure of the secondary flow becomes visible; (*c*-*d*) outward traveling nonaxisymmetric secondary flow consisting of a single spiral vortex; (*e*) nonlinear mode interaction; (*f*) ultimate fully nonlinear state.

value Ω_{crit} and the flow is observed for 5 minutes or more to ensure that it is stable; this corresponds to the intensity of the light reflected by the seed particles being uniform across the disk. At time $\hat{t}$ = 5:00:00 (min:sec:frame), the rotation rate is incremented to a slightly supercritical value, corresponding to $De_0 = 5.99$. The flow field shown in figure 4.2*(a)* is already unstable, and measurements of the torque and normal force on the disks indicate that the initially small changes in the stresses arising from the secondary flow are growing exponentially. After 90 seconds, the secondary flow has grown in intensity sufficiently that a faint spiral structure can be discerned in figure 4.2*(b)* near the center of the disk. The strength of the secondary flow continues to increase; and after another 60 seconds, a well-defined spiral secondary flow is clearly visible in figure 4.2(*c*). Direct observation of the videotape clearly shows that these spiral vortices travel steadily outwards across the disk but remain confined to a narrow annular ring. The secondary flow structure shown in figure 4.2*(d)* was observed 0.60 s (18 video frames) after figure 4.2(*c*), at which time the vortices have moved outward by about one-half of their wavelength. Quantitative measurements of the wavelength, wavespeed and azimuthal structure characterizing this instability are presented below. At longer times nonlinear interactions become important, and the periodic spatial structure of the secondary flow begins to become less well-defined, as shown in figure 4.2(*e*). Dynamic measurements indicate that the increases in the forces exerted on the plates due to the secondary flow begin to saturate at this time. Ultimately, the secondary flow becomes highly nonlinear with a wide spectrum of spatial structures present, as shown in figure 4.2(*f*). This nonaxisymmetric time-dependent flow will persist until either the torsional motion is completely stopped, or the rotation rate is reduced below a second, lower critical value for return to the steady state torsional flow. Some evidence of polymer degradation is observed after long periods in the unstable state, as discussed by McKinley *et al.* (1991a).

In order to quantify the secondary flow, it is necessary to enhance the visibility of the structures observed in the sequences of video images, such as those shown in figure 4.2. Typical raw and postprocessed images are presented in figure 4.3 after application of the image processing operations described in §3.4. Correcting for the nonuniform background illumination increases the azimuthal visibility of the cellular structure around the entire disk, while adjusting the brightness and contrast expands the histogram of gray-scale values present to yield enhanced visual definition of the cells. However, as is clear from an examination of figures 4.3*(a)* and (*b*), these operations do not compromise the fidelity of the spatial variation in the secondary flow structure.

A Cartesian coordinate system is superimposed on the digitized images of the secondary flow with its origin at the center of the disk, as shown in figure 4.3, and the

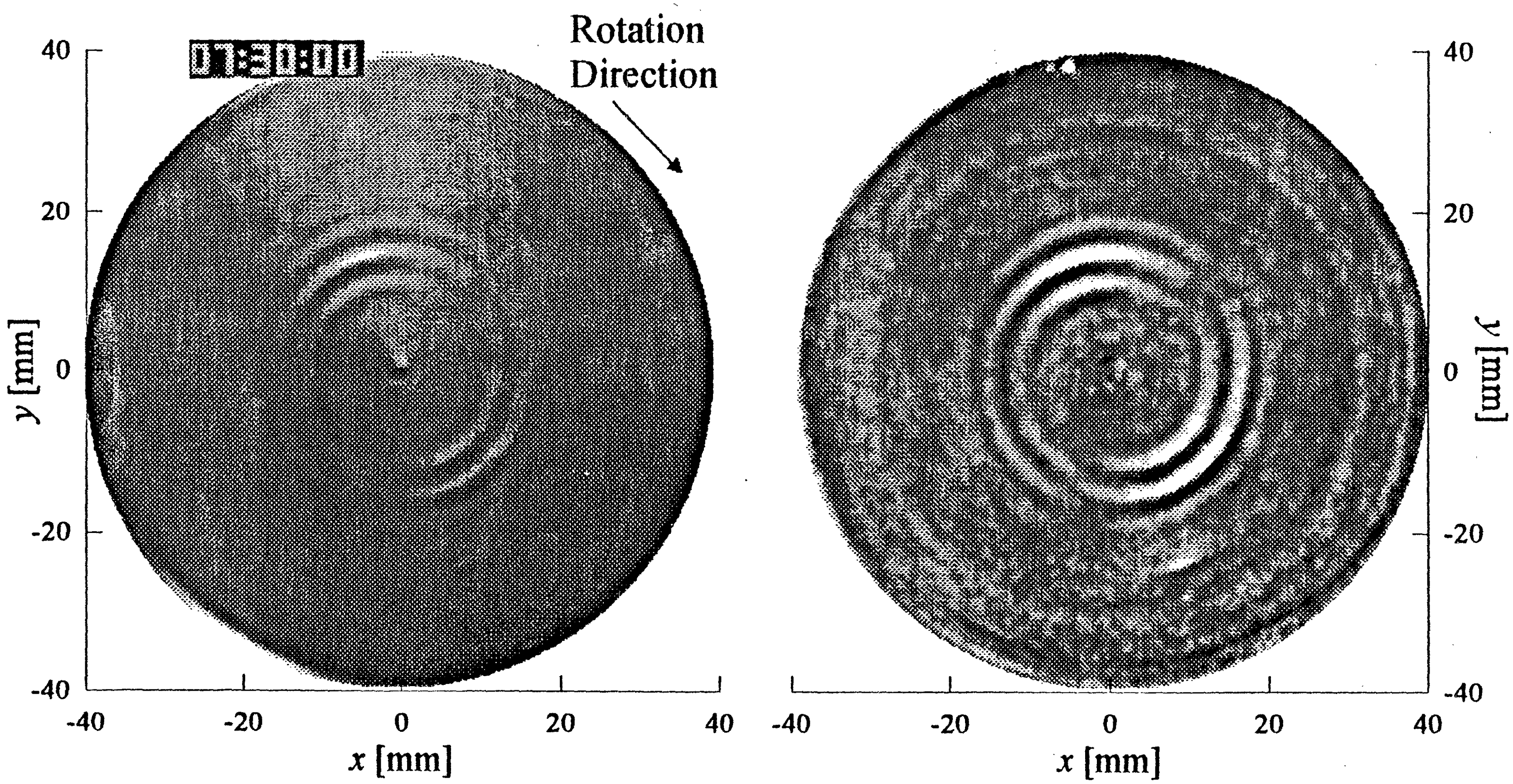

Figure 4.3 (*a*) Raw image of the flow instability and (*b*) enhanced image showing the spiral structure of secondary flow. $De_0 = 5.99$, $Re = 0.032$.

cylindrical coordinate system required for definition of the spiral disturbance forms discussed in §3.4 is located with the line $\theta = 0$ aligned along the positive x-axis, and angles increasing in the direction of rotation of the upper plate. For all the experimental results presented here, θ increases in the *clockwise* direction. The radial structure of the instability is determined by measuring gray-scale variations in the intensity of the light reflected by the seeding particles in the flow along any radial line passing through the origin, as demonstrated in figure 4.4*(a)* for the radial line corresponding to $\theta = -1.00$ rad. In this profile and all others presented in this work, the negative radial coordinates indicated on the abscissa indicate distances along the radial line given by extending $\theta \rightarrow \theta + \pi$ rad.

The radial wavelength of the secondary flow can be calculated from such profiles in a number of ways. A Fourier transform of the intensity profile yields the power spectrum shown in figure 4.4*(b)* and the radial wavelength is determined as $\hat{\lambda}_r = 3.57 \pm 0.12$ mm, corresponding to a dimensionless radial wavenumber of $\alpha = 3.52 \pm 0.12$. Alternatively, the radial separation between each pair of adjacent peaks in the intensity profile is calculated as a function of the angular position as shown in figure 4.4*(c)*. From such measurements, the radial wavelength is found to be almost constant at different azimuthal positions with an average value and standard deviation determined from figure 4.4*(c)* as $\hat{\lambda}_r = 3.66 \pm 0.53$ mm.

The temporal evolution of the flow is determined unambiguously from a sequence of radial intensity profiles along a line of constant θ, as shown in figure 4.5 for the same angular position of $\theta = -1.00$ rad. The elapsed times given in figure 4.5 are the same as those in figure 4.2, and the intensity of each profile has been vertically offset for clarity. These profiles clearly show the traveling-wave structure of the secondary flow. At any given instant in time, the disturbance appears radially periodic and the intensity of the secondary flow passes through a maximum with increasing $\hat{r}$. The center of each vortex moves radially outward with time; the growth and ultimate decay of the disturbance can be followed by following the location of a particular crest as a function of time. The smallest dimensionless radius at which an intensity peak can be detected is denoted as R_1^*, and the largest radius at which the peaks are still distinguishable is denoted as R_2^*. Although the experimentally observed secondary flow consists of spiral vortices which propagate radially outwards, it should be noted that they do not initiate at the center of the disks nor do they travel completely out to the edge of the fixtures. Rather, the vortices start at a finite radius, grow and then decay to zero amplitude at some second larger radial position, and are only visible for radial positions in the range 4.2 mm $< \hat{r} <$ 23.2 mm, corresponding to dimensionless positions of $2.1 < r < 11.6$. This is in sharp contrast to the predictions of the linear stability analysis for an Oldroyd-B fluid, which predicts that the torsional flow is

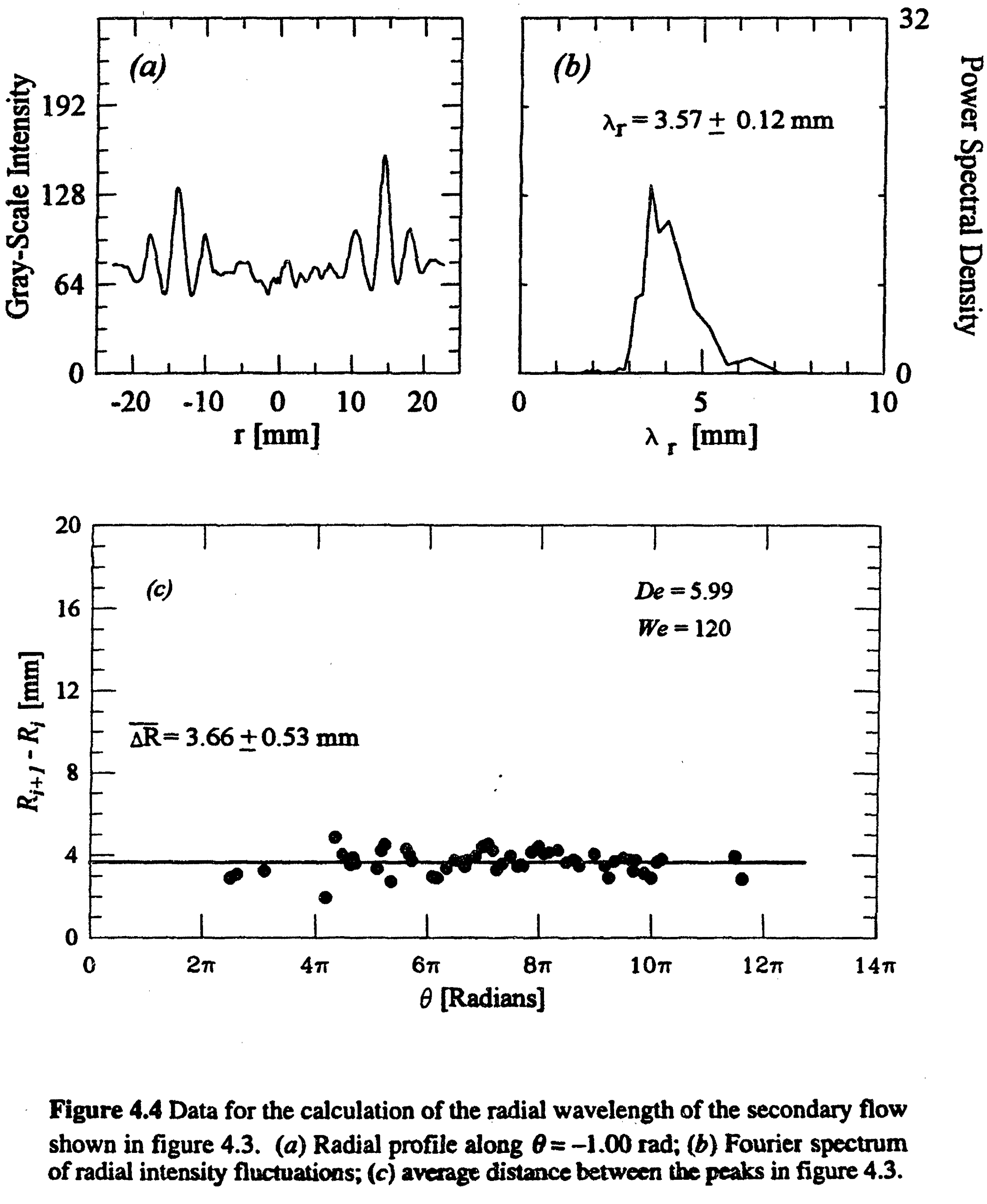

Figure 4.4 Data for the calculation of the radial wavelength of the secondary flow shown in figure 4.3. (*a*) Radial profile along $\theta = -1.00$ rad; (*b*) Fourier spectrum of radial intensity fluctuations; (*c*) average distance between the peaks in figure 4.3.

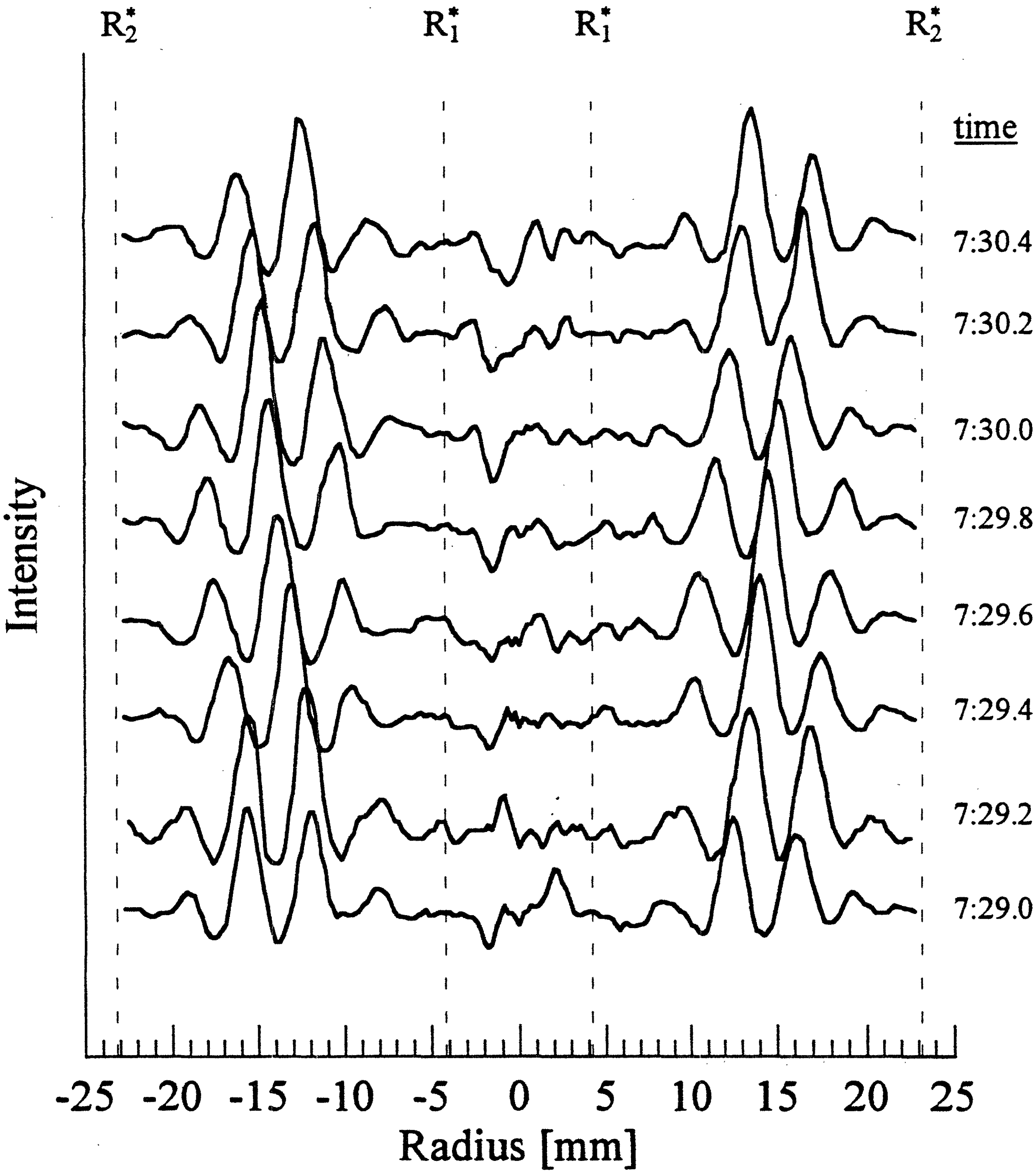

Figure 4.5 Temporal evolution of radial intensity profiles along a fixed line of $\theta = -1.00$ rad. The scale is vertically offset for each profile to show the movement of the cells. The line $\theta = 0$ is along the line $y = 0, x > 0$ in figure 4.3. The time scale is indicated in min:seconds.

linearly unstable to spiral disturbances of the same form as observed here for *all* radii greater than a single critical radius $R^* = R^*_{\mathrm{crit}}$. These disturbances subsequently decay beyond a second critical radius due to shear-thinning of the first normal stress difference, which reduces the relative importance of the elastic effects in the flow. The irregular fluctuations in the baseline intensity near the center of the disk are caused by an imperfect match between the background reference image and each successive image of the instability. These fluctuations are present even between successive images of the uniform base flow at subcritical rotation rates and typically arise because of small inhomogeneities in the flow, such as minute air bubbles, which are difficult to eliminate and which migrate to the region of low shear near the center of the disks.

The radial position of each successive peak in the intensity profiles shown in figure 4.5 is determined for each time step, and is replotted in figure 4.6 as a function of time. Linear regression through each series of points yields the wavespeed of the instability. The radial component of the wavespeed is determined as $\hat{c}_r = 3.18 \pm 0.27$ mm/s, equivalent to a dimensionless value of $c_r = 0.23 \pm 0.02$.

It is immediately apparent from figure 4.4*(a)* that the secondary flow is nonaxisymmetric, because the peaks in the intensity profiles are located at different radial positions on either side of the origin. However, from closer consideration of equation 3.26 and figure 3.11, it is clear that this single profile can only be used to determine that the disturbance, if of spiral form, does not correspond to an even value of the integer spiral number m. In order to determine precisely the nonaxisymmetric structure of the instability, similar measurements of the radial structure are required across the disk at different angular positions. As previously noted, the spiral number m only appears in equation 3.26 in the product m/α. Analysis of the data proceeds by selecting a trial value of m, and combining this with an initial guess for the value of α taken from the independent measurements shown in figure 4.3. Linear regression of the experimental data with equation 3.26 then yields best fit values of α^{-1} and θ_0 for a given value of m. Selection of the Archimedean spiral which most closely describes the overall spatial form of the flow is then based on the data regression which results in the highest correlation coefficient. For the flow of the 0.31 wt% fluid between parallel plates with an aspect ratio of $R/H = 20$, the spatial structure of the secondary flow is best described by an outwardly-traveling spiral of positive angle ($m = 1$) with a dimensionless radial wavenumber $\alpha = 3.64$. Figure 4.7(a) shows the positions of the intensity maxima of the digitized image superimposed on a raw image of the secondary flow. Figure 4.7(b) shows the same data as figure 4.7(a), but with the spiral curve representing the instability 'unwrapped' in the θ-direction to demonstrate more clearly how well this form of the disturbance can describe the experimentally observed

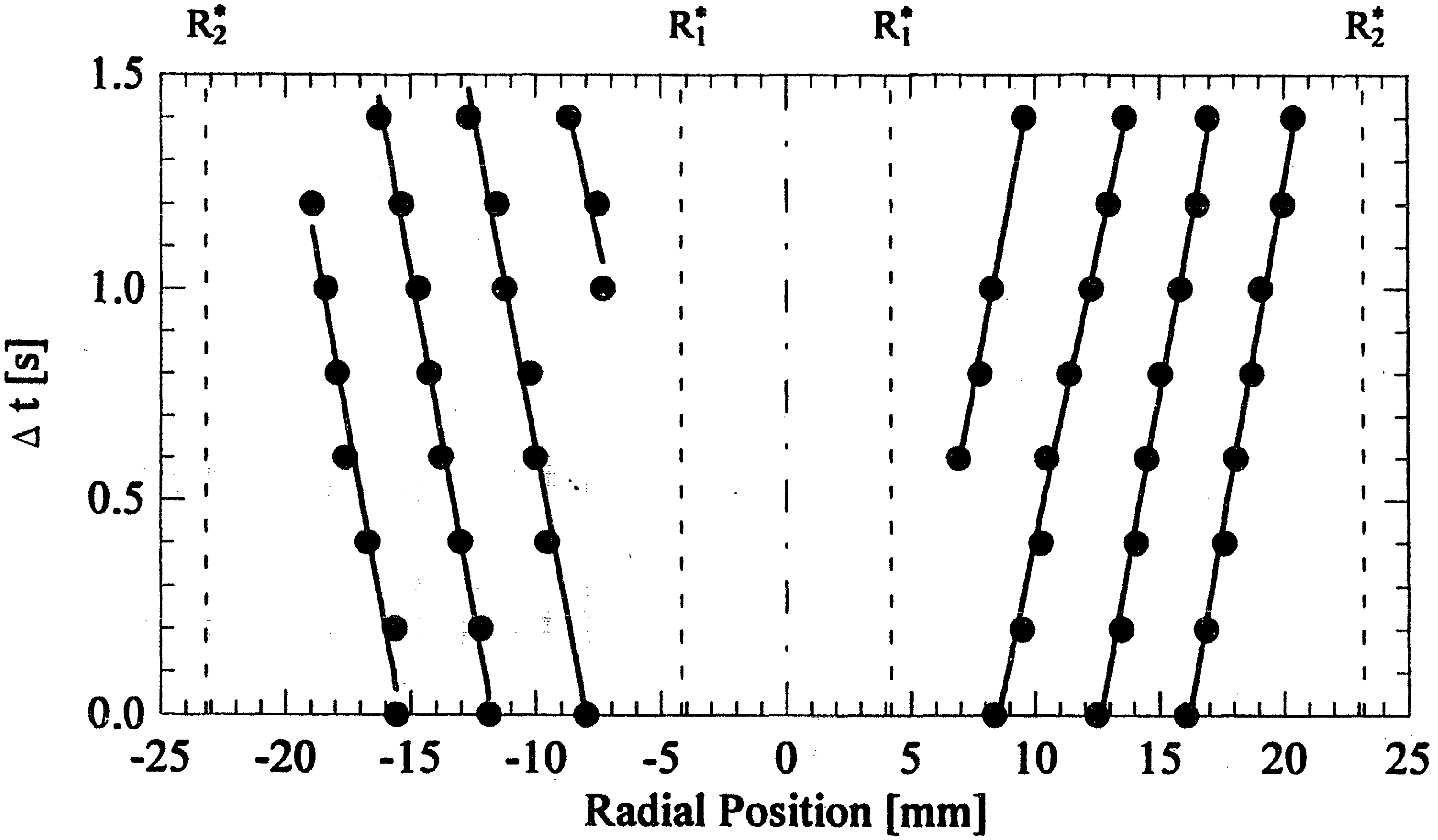

Figure 4.6 Positions of the peaks measured from the profiles of figure 4.5 as a function of elapsed time. The wavespeed is calculated as 3.18 ± 0.27 mm/s.

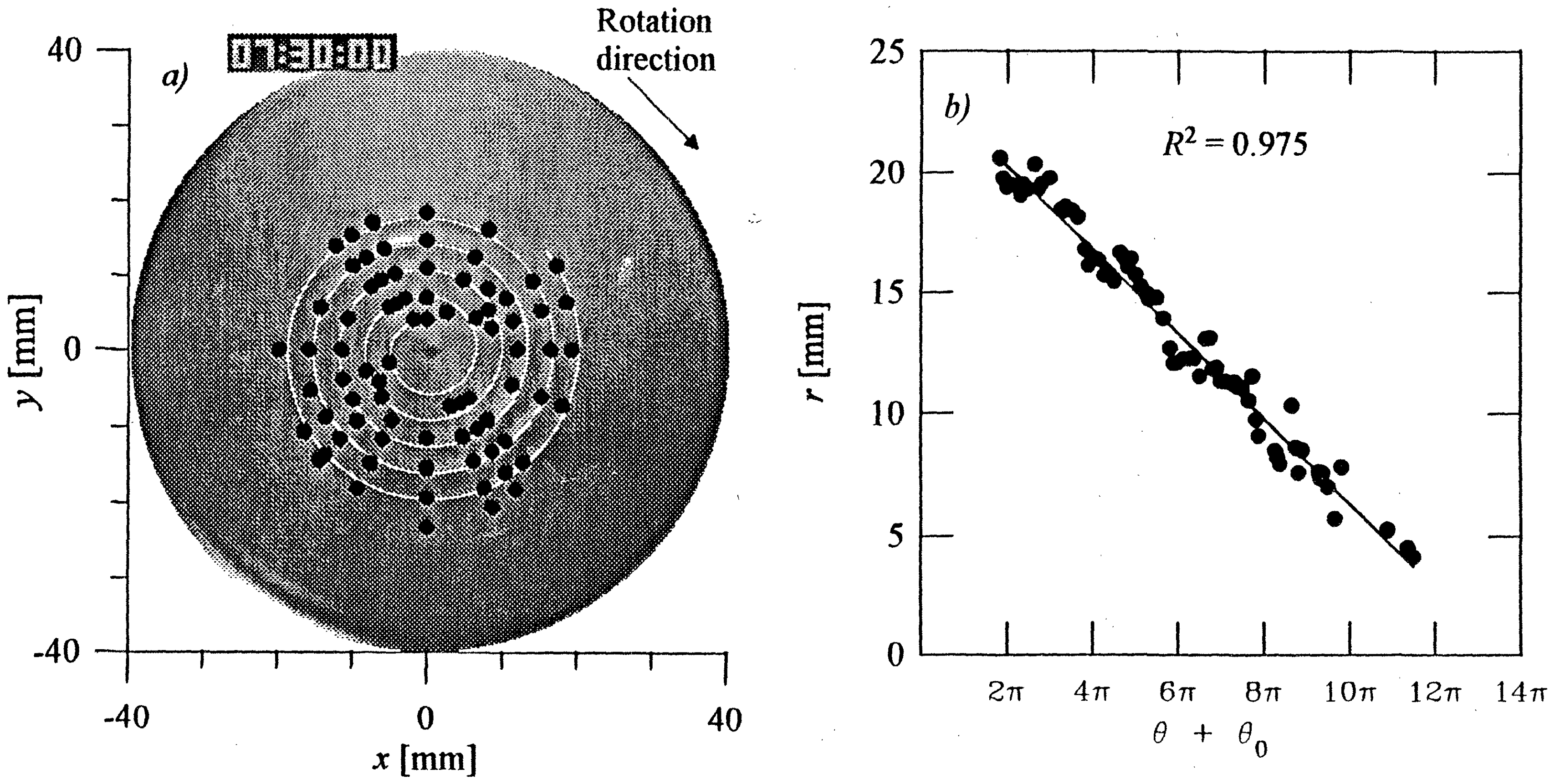

Figure 4.7 (*a*) Positions of the peaks determined from intensity profiles at different azimuthal positions superimposed on a video image of the flow. (*b*) Positions of the peaks with the best fit of equation 3.26 to these positions with $m = 1$, $\hat{\alpha} = 1.80\ \text{mm}^{-1}$ and $\theta_0 = 0.435$ rad.

nonaxisymmetric flow. For $m > 1$, there would be m different curves corresponding to m intertwined spiral vortices, each offset by an angular displacement of $2\pi/m$.

The quantitative values of the wavespeed, wavelength and azimuthal structure of the instability also compare well with the linear stability analysis of Öztekin and Brown (1993). If the apparent relaxation time of the fluid is evaluated at the local shear rate of $\dot{\gamma} = 16\ \mathrm{s}^{-1}$ corresponding to the onset radius R_1^*, then the local shear-rate-dependent Deborah number is $De(\dot{\gamma}) \approx 2.8$. At this Deborah number, the most unstable mode is predicted by Öztekin and Brown to be a nonaxisymmetric disturbance with $m = 1$, a wavespeed of $c_r = 0.24$ and a wavenumber $\alpha = 3.13$.

4.1.3 Effect of Aspect Ratio and Fluid Rheology

The linear stability analysis of Öztekin and Brown for the Oldroyd-B fluid indicated that the spatial form of the instability scaled with the gap separation H between the parallel plates and that the loci of the neutral stability curves were sensitive functions of the dimensionless solvent viscosity ratio β. Sets of experiments similar to those described in §4.1.2 have been performed for the two different PIB Boger fluids described in §3.2 by using two different representative aspect ratios. The results from these experiments are summarized in Table 4.1. The two fluids are differentiated in Table 4.1 and the subsequent text by their respective values of the solvent viscosity ratio, which are $\beta = 0.59$ for the fluid containing 0.31 wt% PIB, and $\beta = 0.84$ for the 0.20 wt% fluid.

β	R/H	$De_{0\mathrm{crit}}$	$\dot{\gamma}_R$ [s^{-1}]	$\hat{\lambda}_r$ [mm]	R_1^*	R_2^*	α	c_r	m
0.59	20.0	5.99	151	3.45	2.1	11.6	3.64	0.23	1
0.59	11.4	6.35	91	5.94	3.3	11.2	3.70	0.23	0
0.84	20.0	5.85	94	3.06	1.1	8.8	4.11	0.21	2
0.84	11.4	6.18	57	5.46	2.7	9.5	4.03	0.21	1

Table 4.1 Critical conditions for the onset of the rotational flow instability for two different viscoelastic PIB/PB/C14 test fluids.

In each fluid, enlarging the separation between the plates and decreasing the aspect ratio R/H results in a small increase in the critical Deborah number required for onset of the elastic instability. However, for the smaller aspect ratio of $R/H = 11.4$, the shear rate at the edge of the disk, and thus the Weissenberg number at the onset of the flow instability, is actually lower. This is in good agreement with the earlier experimental and theoretical findings. For a larger gap, the local shear rate at any radial position across the plates at onset is lower and shear-thinning effects are less important. Consequently, the spatial extent of the secondary flow extends almost completely out to the edge of the disks. The dimensional wavelength and wavespeed both increase as the gap is increased; however, the dimensionless wavenumber α (scaled with the gap H) remains almost unchanged, as expected from the analysis of Öztekin and Brown. The wavespeed also scales well with gap size, and is in excellent agreement with the value predicted for the Oldroyd-B model with the shear-rate-dependent relaxation time.

For the $\beta = 0.59$ fluid, an axisymmetric instability consisting of concentric vortices which travel radially outwards across the disk is observed for an aspect ratio of $R/H = 11.4$. Although Öztekin and Brown predict that the $m = 1$ mode should still be the most unstable mode at these conditions, the spacing in the stability curves for different m is very small, and the $m = 0$ mode is just slightly more stable at this De. The linear stability analysis yields neutral stability curves along which the temporal growth rate of the instability is zero and does not predict which finite amplitude states will be observed at supercritical conditions. Such results must be found from a nonlinear analysis.

The Deborah number at the onset of the instability appears to increase slightly in the second experiment, but in fact both values are overpredictions of the true critical Deborah number. Very long induction times of greater than 1000 s are common for onset of the elastic instability very close to the critical rotation rate (Jackson *et al.* 1984; Magda and Larson 1988; McKinley *et al.* 1991a). However, to perform such experiments requires careful isolation of the apparatus from external perturbations, and effects such as viscous heating in the fluid, or long term temperature fluctuations in the laboratory. In these experiments observation times at each rotation rate have been limited to ~300 s and after a given De_0 was determined to be stable for this period of time, the motor speed was increased in steps of $\delta\Omega = 0.52$ rad/s, which corresponds to finite increments in De_0 of 0.42 and 0.65 for the $\beta = 0.59$ and $\beta = 0.84$ fluids, respectively.

The predicted onset radius for the $\beta = 0.59$ fluid at $De_0 = 6.0$ is $R_1^* = 2.2$, which is in good agreement with the experimental results. The value of R_1^* is defined as the radius at which the instability begins to grow; however, because only cells that have already grown to a finite amplitude large enough to produce a discernible peak in the radial intensity profiles (see figure 4.5) can be detected, the values of R_1^* in Table 4.1 will necessarily tend to overpredict the true onset radius.

The most important difference between the experimental results and the predictions of Öztekin and Brown (1993) is that the Oldroyd-B model predicts that the flow should be unstable for all dimensionless radii greater than R_1^*, whereas there is an experimentally observed position R_2^* beyond which the flow remains stable. Although the critical radius R_1^* for onset of the instability is predicted well for $De_0 = 6$, the analysis using the Oldroyd-B model predicts that the critical radius *increases monotonically* as the rotation rate is decreased. There should therefore be a larger value of R^* at which a secondary flow is observed experimentally for Deborah numbers smaller than $De_0 = 6$. As long as the value of the critical dimensionless radius R_1^* is less than the finite aspect ratio R/H of the experimental apparatus, the instability should be observed from R_1^* outwards to the edge of the disk, and as De_0 is increased, the region of unsteady flow should move inwards. For example, for $De_0 \sim 1$, the analysis for the Oldroyd-B model with $\beta = 0.59$ predicts that the flow will be unstable with $m = 3$ at $R_1^* = 19$, whereas for $De_0 \sim 3$, $m = 1$ is the most unstable mode for all dimensionless radii $R^* \geq 2.2$. In contrast, experiments show that the flow remains stable at all radii across the disk for all rotation rates below the critical rotation rate corresponding to $De_0 = 6.35$, when the cells form between R_1^* and R_2^*. As shown in §4.3.2, this qualitative inconsistency with the linear analysis can be alleviated by considering a more realistic constitutive equation that includes shear-thinning of the first normal stress coefficient.

Furthermore, the linear stability analysis predicts that multiple spiral modes should be present in the secondary flow, whereas it is clear from the observations that only a single mode is observed at short times. For $De(\dot{\gamma}) = 3$, the $m = 1$ mode is predicted to be most unstable in the sense that it has the smallest critical radius of $R_1^* = 2.2$. However, the modes with $m = 0$ and $m = 2$ are both unstable at the slightly larger radius of $R_1^* = 2.7$. The neutral stability curves yield no information about the temporal growth rates of the different modes, or the amplitudes of the disturbances, and therefore no means of determining which mode should be selected in an experiment.

For the $\beta = 0.84$ fluid, the onset of the instability was again observed at $De_0 \approx 6$ for both aspect ratios, and the shear-rate-dependent Deborah number based on the shear rate at R_1^* was $De(\dot{\gamma}) \approx 3$, as observed for the $\beta = 0.59$ fluid. The analysis for the Oldroyd-B model predicts that for a given De_0, the critical radius R_1^* should be greater for the $\beta = 0.84$ fluid, whereas the observed value of R_1^* is slightly smaller for the $\beta = 0.84$ fluid than for the $\beta = 0.59$ fluid. The instability again extended across only a portion of the disk, and R_2^* was found to decrease for the $\beta = 0.84$ fluid.

The secondary flow for the $\beta = 0.84$ fluid between parallel plates with an aspect ratio of $R/H = 20$ was observed to have the form of two nested non-intersecting spirals, as shown in figure 4.8, whereas for $R/H = 11.4$ a secondary flow with $m = 1$ was observed.

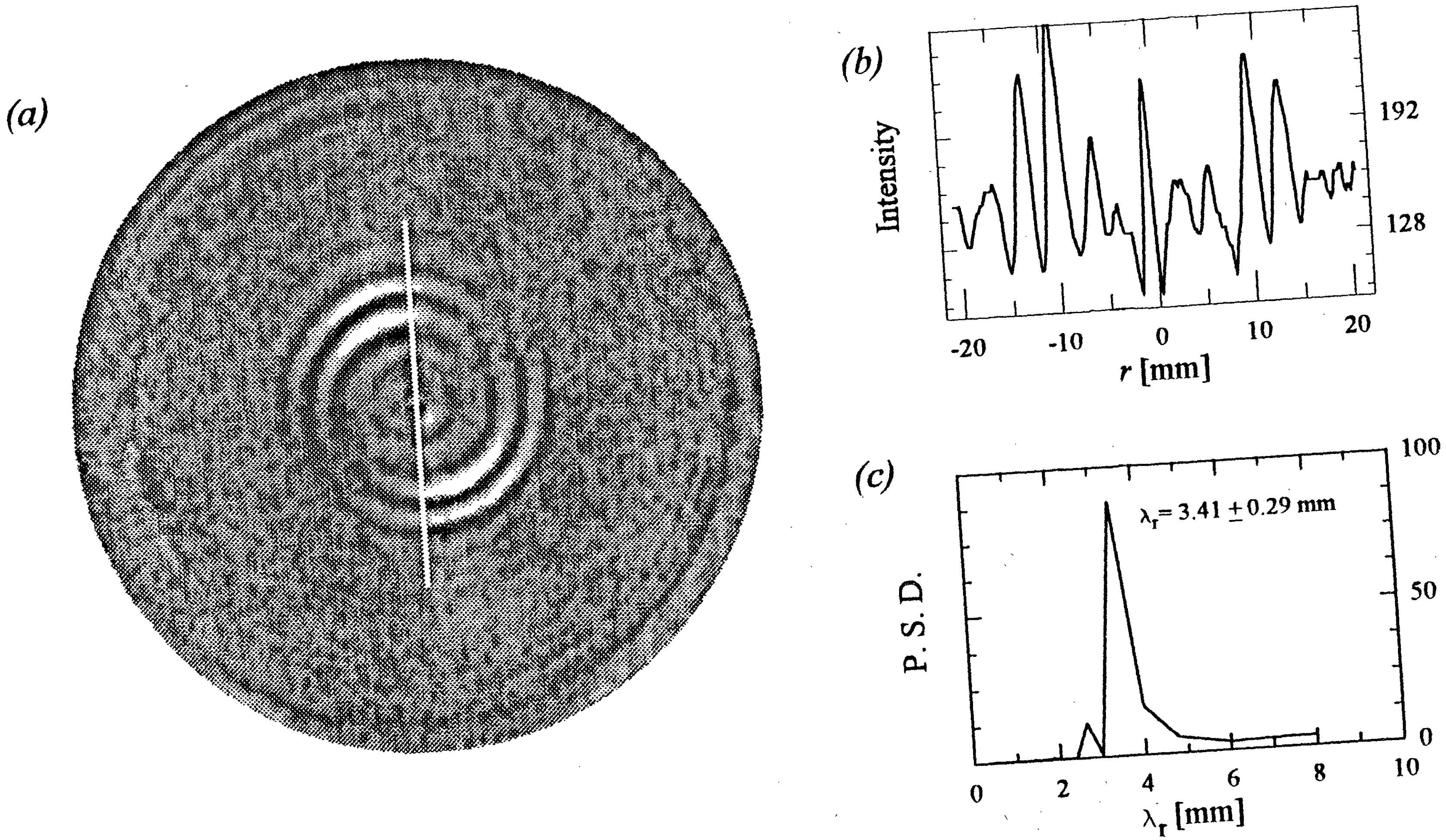

Figure 4.8 Secondary flow (*a*) for a fluid with viscosity ratio $\beta = 0.84$ and aspect ratio $R/H = 20$ at flow conditions $De_0 = 5.85$ and $Re = 0.007$ shows two nested spiral vortices, $m = 2$. Calculation of the wavelength of the disturbance along the line $\theta = +1.57$ rad (*b-c*) gives $\hat{\lambda}_r = 3.41 \pm 0.29$ mm.

Öztekin and Brown predict that the axisymmetric mode should be the most unstable for $\beta = 0.84$ and $De_0 = 6$, although $m = 1$ and $m = 2$ are the next most unstable modes. The wavenumber and wavespeed both scale with the gap size, with the wavenumber increasing and the wavespeed decreasing relative to the $\beta = 0.59$ fluid.

Experiments spanning a wider range of aspect ratios (R/H) and solvent viscosity ratios (β) are desirable; however, the range of parameters experimentally attainable are constrained by a number of physical considerations. For disks with a given radius R, larger aspect ratios correspond to vortices of a smaller wavelength which are difficult to resolve spatially. Furthermore, for very small gap separations, the region of unsteady flow given by dimensionless radii in the range $R^*_{1\text{crit}} \leq R^* \leq R^*_{2\text{crit}}$ would physically correspond to a very narrow annular ring close to the center of the disk. The elastic instability will still be present, but the contribution of the secondary flow to integrated measurements of the torque and normal force on the plates will be negligible. On the other hand, for larger gap separations the surface tension of the fluid is insufficient to overcome centrifugal and gravitational body forces and the sample will be flung out of the gap between the plates. The range of viscosity ratios η_s/η_0 physically realizable with Boger fluids also is limited. If the polymer concentration is increased in order to increase the relative contribution of η_p then the polymer solution crosses over from the dilute to the entangled regime, and stabilizing effects such as a nonzero value of the second normal stress coefficient Ψ_2 and pronounced shear-thinning in the viscosity become dominant. This typically constrains the solvent contribution to be greater than $\beta \geq 0.50$. Reducing the polymeric contribution to the viscosity below $\eta_p \approx 0.1\eta_0$ leads experimentally to very dilute nonentangled solutions with short relaxation times, and the numerical stability calculations show that larger values of β result in increasing stabilization of the base circumferential flow. It thus becomes difficult experimentally to achieve sufficiently high rotation rates and/or Deborah numbers to observe this torsional flow instability.

4.1.4 Onset of Nonlinear Interactions

The results presented in §§4.1.2-3 are for times shortly after the onset of the instability when the secondary flow consists only of a single spiral vortex which intensifies as it travels across the disks. At longer times, the temporal measurements of normal force shown in figure 4.1, and the video-images of the spatial form of the secondary flow shown in figure 4.2 indicate that the subcritical instability eventually saturates as slower growing modes become increasingly important and the flow enters a complex aperiodic state far from the base torsional flow. The beginnings of this transition can be seen in figure 4.9, which shows results from the experiments with $\beta = 0.84$ and $R/H = 11.4$. The critical De_0 was exceeded at $\hat{t} = 16{:}00$ min, and figures 4.9(*a-c*) show that initially a single spiral with $m = 1$ and $\hat{\lambda}_r = 5.27$ mm is present which intensifies with time and travels radially outwards across the entire disk. However, at longer times this single spiral begins to split at intermediate radial positions, as shown in figures 4.9(*d-f*). A single well-defined spatial wavelength is still discernible, but it is now much shorter than the single mode spiral structures present in the linearly unstable regime, and the characteristic wavenumber has approximately doubled to $\alpha = 6.49$. The primary mode is clearly still in evidence at other radial locations. Similar nonlinear mode interactions are observed for both fluids and all aspect ratios examined. An example of the final unsteady flow reached at long times is shown in figure 4.10, for the $\beta = 0.59$ fluid and $R/H = 11.4$. The initial spiral mode was axisymmetric with $m = 0$ and a single well-defined radial wavelength of $\hat{\lambda}_r = 5.94$ mm, and the steady torsional base flow remained stable for all radii less than $\hat{r} = 14.7$ mm. As the Fourier spectrum in figure 4.10(*c*) shows, the secondary flow can no longer be characterized by a single wavelength. Although considerable power remains in disturbances with wavelengths close to $\hat{\lambda}_r = 6$ mm, shorter wavelength modes also are present. Close examination of the videotape and images such as figure 4.10(*a*) reveals the presence of both positive angle ($m > 0$) and negative angle ($m < 0$) spirals with a wide range of radial wavelengths. These negative angle spirals have negative wavespeeds and move radially inward until the nonlinear time-dependent secondary flow extends across the entire disk.

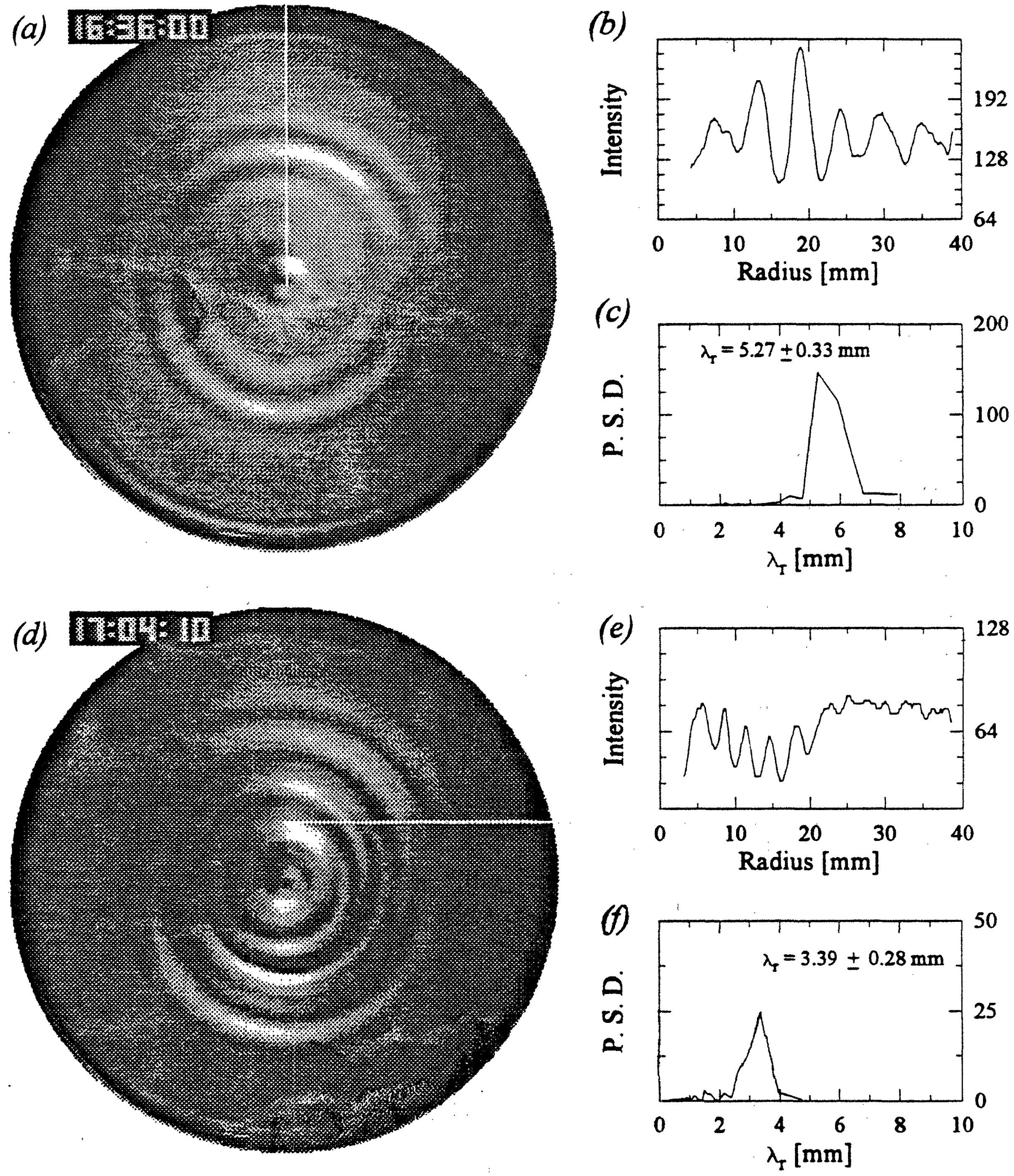

Figure 4.9 Transition to nonlinear state for $\beta = 0.84$ and $R/H = 11.4$ at flow condition $De_0 = 6.18$ and $Re = 0.009$: (*a-c*) initial secondary flow has the form of a single spiral vortex with radial wavelength $\hat{\lambda}_r = 5.27$ mm; (*d-f*) as the instability saturates, the cellular structure splits and the wavelength reduces to $\hat{\lambda}_r = 3.39$ mm.

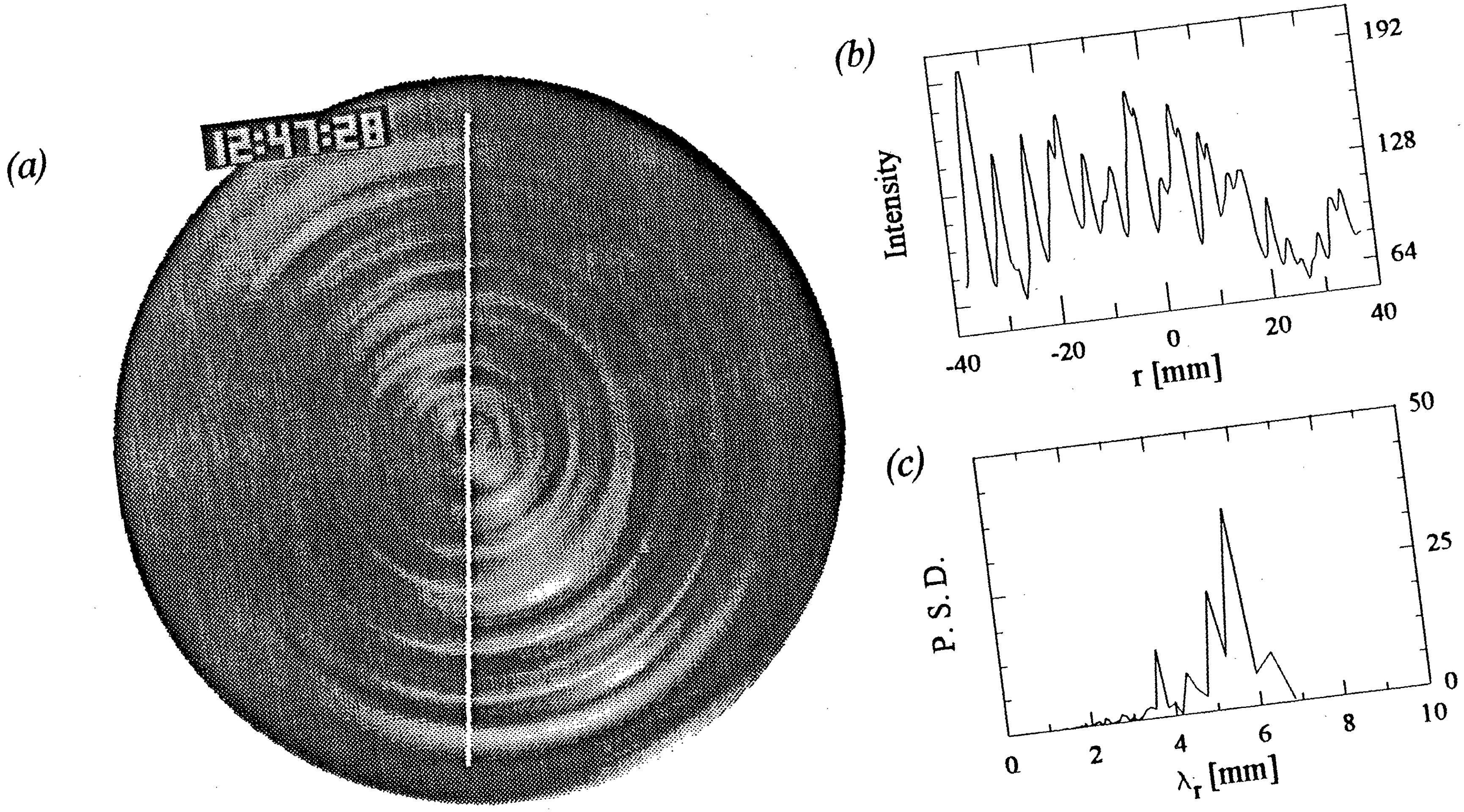

Figure 4.10 Fully nonlinear flow state for $\beta = 0.59$ and $R/H = 11.4$ with multiple modes and wavelengths present after 48 seconds shearing at $De_0 = 6.35$ and $Re = 0.075$. At short times the flow exhibited a single axisymmetric disturbance with $m = 0$ and $\hat{\lambda}_r = 5.94$ mm.

4.2 Cone-and-Plate Geometry

Experimental observations are presented that illustrate the procedure by which the spatial and temporal characteristics of the purely elastic cone-and-plate instability are determined. A detailed analysis of the spatial and temporal evolution of the flow instability in the 0.31 wt% Boger fluid for a cone angle of $\theta_0 = 10^\circ$ is presented in §4.2.1, and the parameters of the spiral that describes the global form of the non-axisymmetric disturbance are determined. The effects on the flow instability of systematically varying the cone angle are demonstrated in §4.2.2. Finally, the effects of changing fluid rheology are discussed in §4.2.3.

4.2.1 Spiral Instability

The series of gray-scale images shown in figure 4.11 depict the spatial and temporal evolution of the flow for the 0.31 wt% PIB Boger fluid and a conical fixture with $\theta_0 = 10^\circ$. A steady torsional flow is initially established between the cone and plate at a rotation rate below the critical value Ω_{crit} and this flow is observed for 5 minutes or longer to ensure that it remains stable. Note that even in the steady base flow, the intensity of the light reflected by the seed particles in the fluid is not radially uniform across the disk. This is because the depth of the fluid sample reflecting the incident light increases radially outwards from the apex of the cone which is located at the center of each image. The Deborah number was then incremented to a supercritical value of $De_0 = 5.28$ by increasing the rotation rate of the conical fixture at the time indicated by 21:00:00 (min:sec:frame) in figure 4.11. Although the flow is already unstable in figure 4.11(*a*), the amplitude of the secondary flow is too small to be observed because of the slow temporal growth rate of the disturbance near the critical conditions. Seventy-five seconds later, the secondary flow shown in figure 4.11(*b*) has grown sufficiently to be observed as a bright spiral vortex. Direct observation of successive frames on the videotape reveal that this spiral vortex slowly translates inwards towards the apex of the cone. The instability continues to grow in intensity, and it is clear from figure 4.11(*c*) that there is a single spiral that fills the entire region between the cone and plate. Eventually nonlinear interactions become important, as shown in figure 4.11(*d*), and there is no longer a single clearly-defined spatial structure to the flow. However, in contrast with observations of the fine-scale turbulent motion observed following onset of inertial instabilities between a cone and plate (Sdougos *et al.* 1984), it is clear that these elastically-driven disturbances continue to

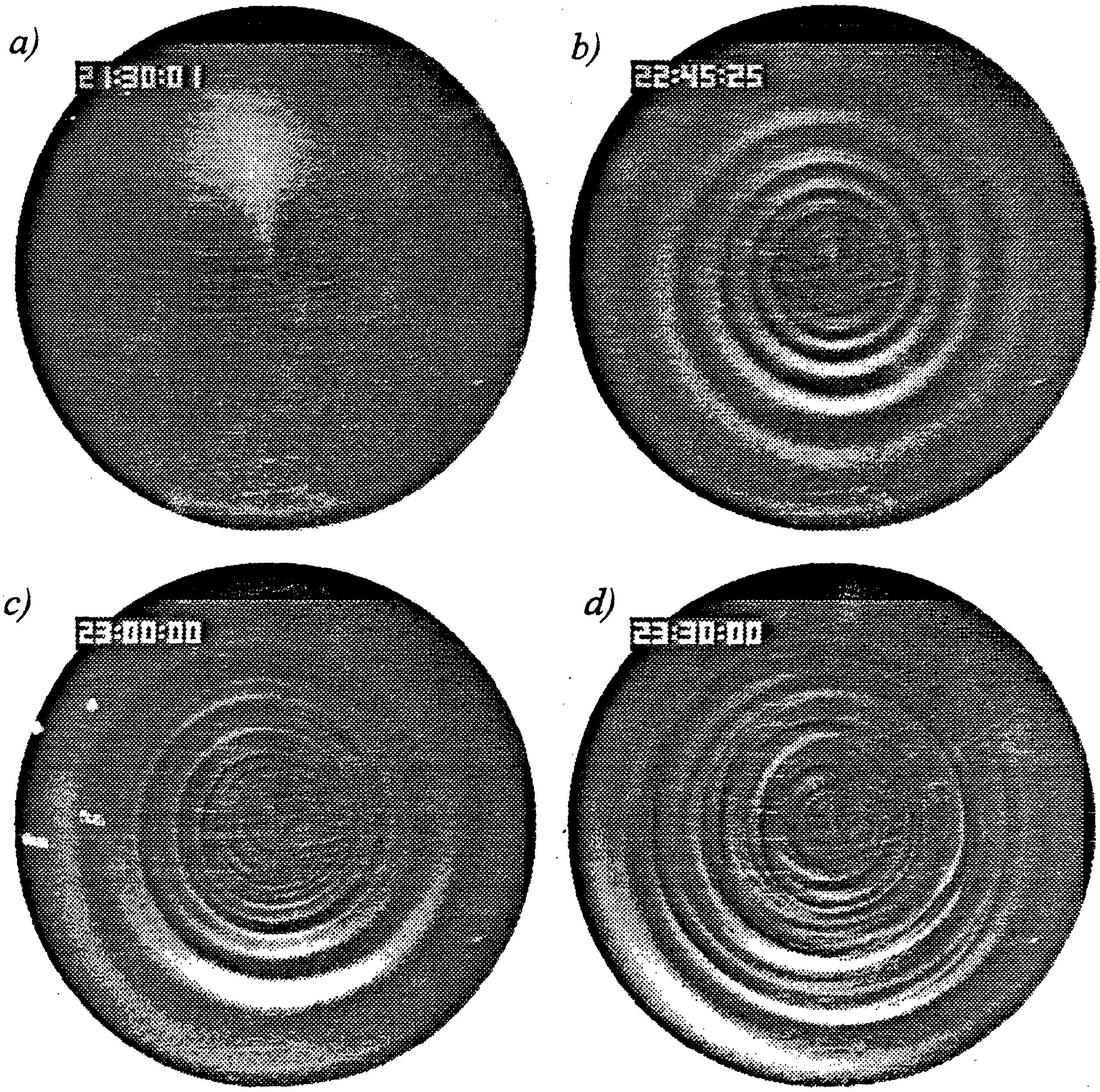

Figure 4.11 Onset and growth of the purely elastic instability observed in the torsional flow of the 0.31 wt% PIB fluid in a cone-and-plate geometry with $\theta_0 = 10^\circ$: *(a)* flow appears stable shortly after the Deborah number is increased to a supercritical value $De_0 = 5.28$ at time $\hat{t} = 21{:}00{:}00$ (min:sec:frame); *(b)* 75 sec later the secondary flow becomes visible; *(c)* inward traveling non-axisymmetric flow consisting of a single logarithmic spiral vortex; *(d)* ultimate fully nonlinear state. Note that the direction of rotation of the upper conical fixture in this and all subsequent figures is counterclockwise.

propagate throughout the entire fluid sample and are composed of cellular structures with a wide spectrum of spatial wavenumber. This non-axisymmetric time-dependent flow will persist indefinitely, until either the rotational motion is completely stopped, or the rotation rate is reduced below a second, *lower* critical value for return to the steady two-dimensional torsional flow. This hysteresis is characteristic of a subcritical bifurcation and has been documented clearly in the previous measurements of Magda and Larson (1988) and McKinley *et al.* (1991).

Of course, the complex three-dimensional time-dependent flow that ultimately develops at long times (cf. Fig 4.11*d*) cannot be described by a linearized stability analysis. However, such a linear analysis can describe the initial growth of infinitesimal disturbances in the fluid at short times and the slow transient evolution of the flow away from the steady base motion following a small, carefully-controlled increase in the rotation rate beyond the critical value Ω_{crit}.

In order to quantify the structure of the instability, the individual gray-scale images are processed as described in §3.4 to enhance the visibility of the secondary flow. The time-dependent evolution of the gray-scale intensity along a fixed radial line passing through the origin is shown in figure 4.12. Each profile is taken from a different video-image evenly spaced at 0.2 sec (6 video frames) apart and the profiles are offset vertically for clarity. Negative radial coordinates on the abscissa indicate distances along the diametric line given by extending $\phi \rightarrow \phi + \pi$ rad. This series of profiles clearly shows that the recirculation moves slowly inward, and that the instability fills the entire gap, in sharp contrast to the Archimedean spiral instability in the parallel plate geometry, which only filled an annular region between the disks. As discussed in §4.1, the limited extent of the elastic instability in the parallel plate geometry results from shear-thinning in the normal stresses at the higher shear rates near the outer edge of the disk. By contrast, the homogeneous base flow in the cone-and-plate geometry results in a shear rate that is uniform throughout the sample. The intensity, the distance between successive maxima of the line profiles, and the size of each cell increases with radius, as shown in figure 4.12. The smaller cell size near the center of the geometry coupled with the fact that there are fewer seed particles to reflect light in the narrow gap makes it difficult to resolve maxima at radii of less than about $\hat{r} \leq 4$ mm ($0.16R$).

From the form of the logarithmic similarity transform, we expect the magnitude of the radial component of the wavespeed, $\hat{c}_r$, to increase linearly with radius (*cf.* equation 3.34). Although the profiles of figure 4.12 clearly show that the spiral travels radially inwards, it is difficult to quantitatively measure $\hat{c}_r$ from these profiles. The radial positions of each maximum can be found at each time step, but any estimates of the wavespeed

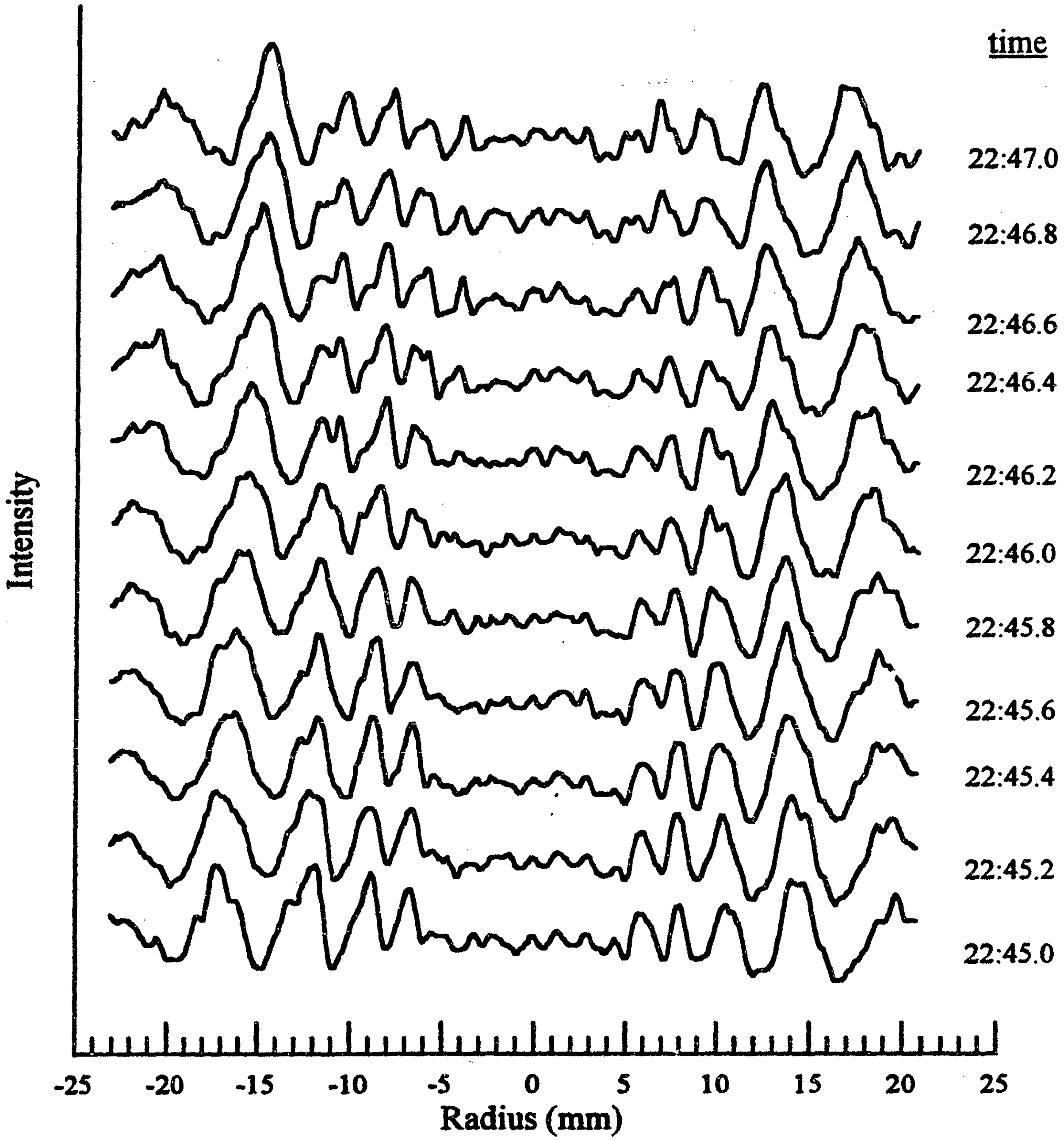

Figure 4.12 Temporal evolution of radial intensity profiles along a fixed line of $\phi = \pi/2$ rad. The azimuthal origin $\phi = 0$ is indicated in figure 3.12, and ϕ increases in the counterclockwise direction. The ordinate is vertically offset for each profile to show the translation of the cells, and the time scale is shown in (min:sec) to correspond to the images shown in figure 4.11.

require assuming that $\hat{c}_r$ is constant over some interval $\Delta\hat{t}$. A more direct approach is to calculate the wavespeed in transformed coordinates (ξ, θ, ϕ), since the dimensionless wavespeed c_ξ is constant. The displacement of the ξ-location of each peak with dimensionless time t is shown in figure 4.13. From such plots, the dimensionless wavespeed of the elastic spiral instability in a 10° cone-and-plate geometry was calculated to be $c_\xi = -0.0107 \pm 0.0030$.

A sequence of radial profiles similar to those in figure 4.12 were also obtained at different angular positions, at a fixed time, in order to study the azimuthal structure of the instability. The wavenumber of the spiral varies linearly with radial position in physical ($\hat{r}$, θ, ϕ) space, but is a constant in the transformed (ξ, θ, ϕ) coordinates. Without any additional knowledge of the spatial structure of the flow, α_ξ is determined from the geometric series of the radial locations of successive peaks using equation 3.33. The plot of the dimensionless ratio R_{i+1}/R_i shown in figure 4.14(*a*) gives an average value of $R_{i+1}/R_i = 1.345$, corresponding to a dimensionless wavenumber of $\alpha_\xi = 21.2$. The value of m describing the non-axisymmetric structure of the flow instability often can be determined in experiments directly by inspection of images such as figure 4.11, but for higher mode numbers a more robust regression technique is necessary. In the (ξ, θ, ϕ) domain the spiral is of Archimedean form, so a linear regression of the experimental data analogous to those reported in §4.1 yields the best fit values of α_ξ and ϕ_0 for a given choice of m. Selection of the Archimedean spiral which most closely describes the overall spatial form of the secondary motion is based on the linear regression which results in the highest correlation coefficient. For the elastic instability shown in figures 4.11–13, $m = -1$, where modes $m < 0$ indicate 'negative angle spirals' which spiral radially *outwards* as ϕ increases (*cf.* equation 3.32). The ability of this spiral form to describe accurately the experimental data is demonstrated in figure 4.3(*b*), where regression of the (ξ, ϕ) coordinates of each peak R_i to equation 3.32 yields a single curve. For $|m| > 1$, there would be $|m|$ different curves corresponding to $|m|$ intertwined spiral vortices each offset by an angular displacement of $2\pi/m$. The slope of this single line gives the winding number n of the spiral defined in equation 3.32 as $n = 0.047$, in good agreement with the values of m and α_ξ independently determined above.

The data in figure 4.14(*b*) can be viewed as the spiral structure of the elastic cone-and-plate instability in (ξ, θ, ϕ) coordinates when 'unwrapped' in the ϕ-direction. This description is contrasted directly to the original video-imaging observations in figure 4.15, where the best fit line from figure 4.14(*b*) has been transformed back into ($\hat{r}$, θ, ϕ) coordinates and juxtaposed directly with a raw image of the secondary flow structure. It is

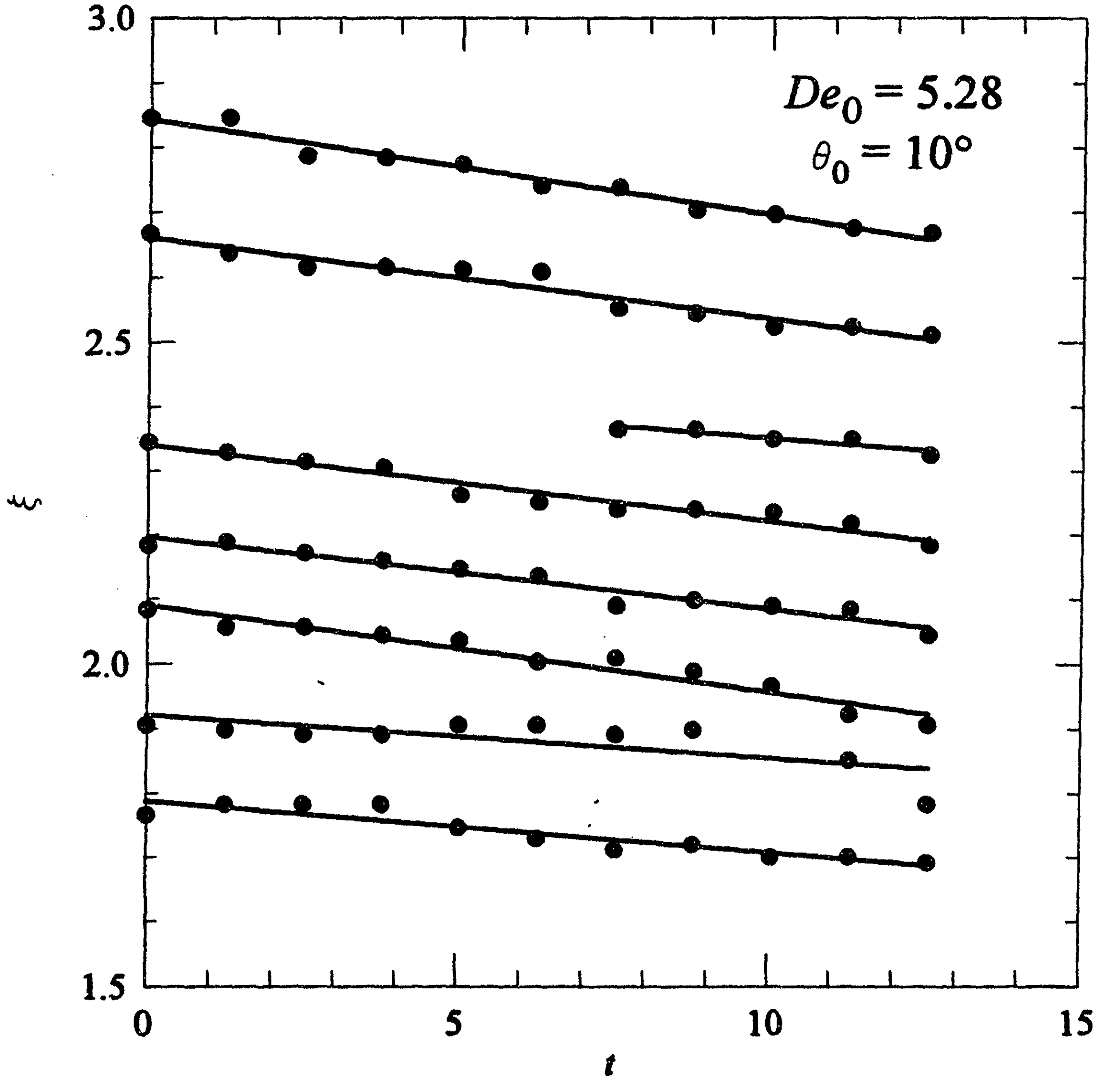

Figure 4.13 Positions of the peaks measured from the intensity profiles of figure 4.12 in the transformed domain (ξ, θ, ϕ) as a function of dimensionless time. The wavespeed is calculated to be $c_\xi = -0.0107 \pm 0.0030$.

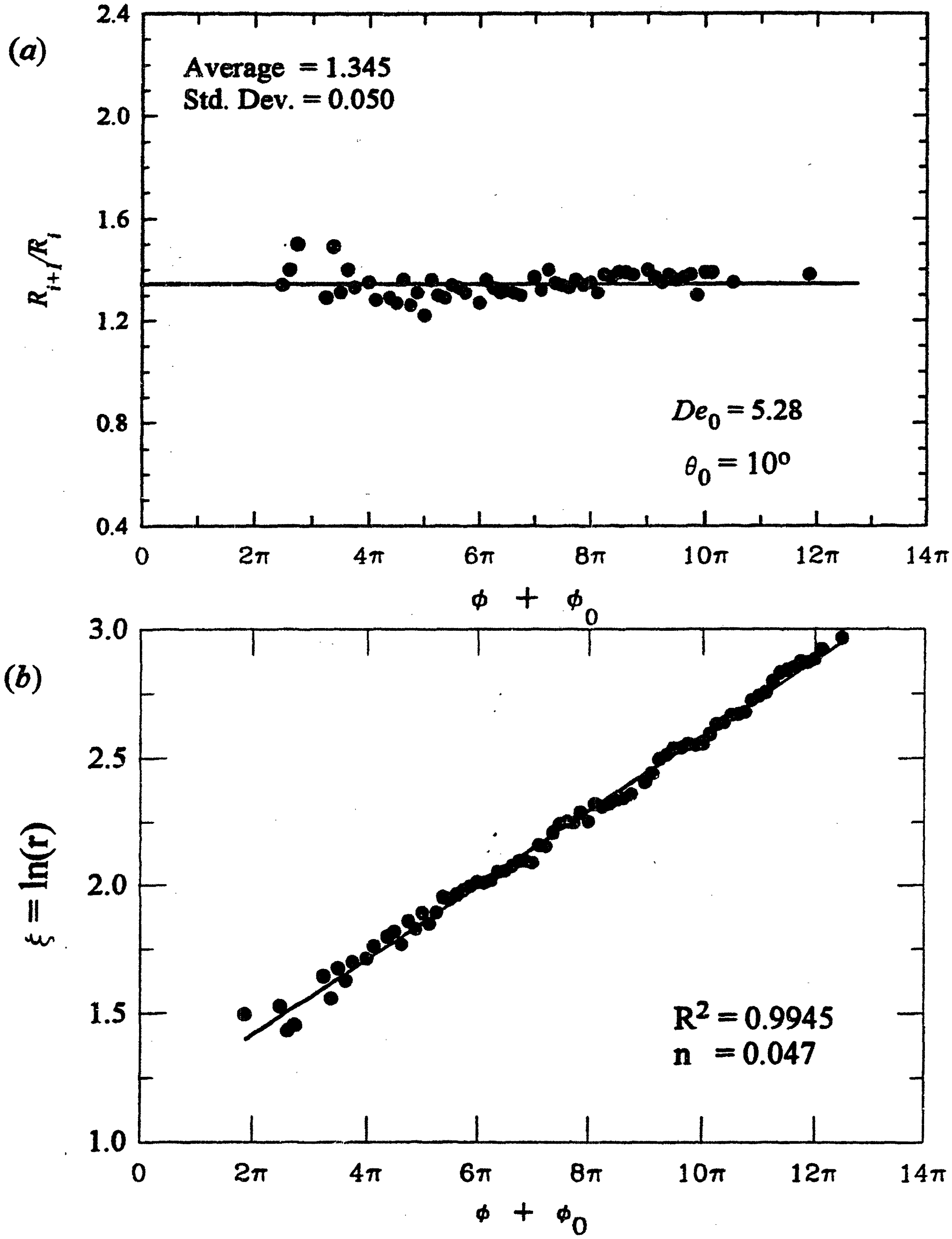

Figure 4.14 Determination of the spatial structure of the secondary flow. *(a)* Ratio of the values of the radial positions of successive peaks (R_i, R_{i+1}). The wavenumber is calculated as $\alpha_\xi = 21.2$. *(b)* ξ-positions of the peaks as a function of azimuthal position lie on a single curve with $n = 0.047$.

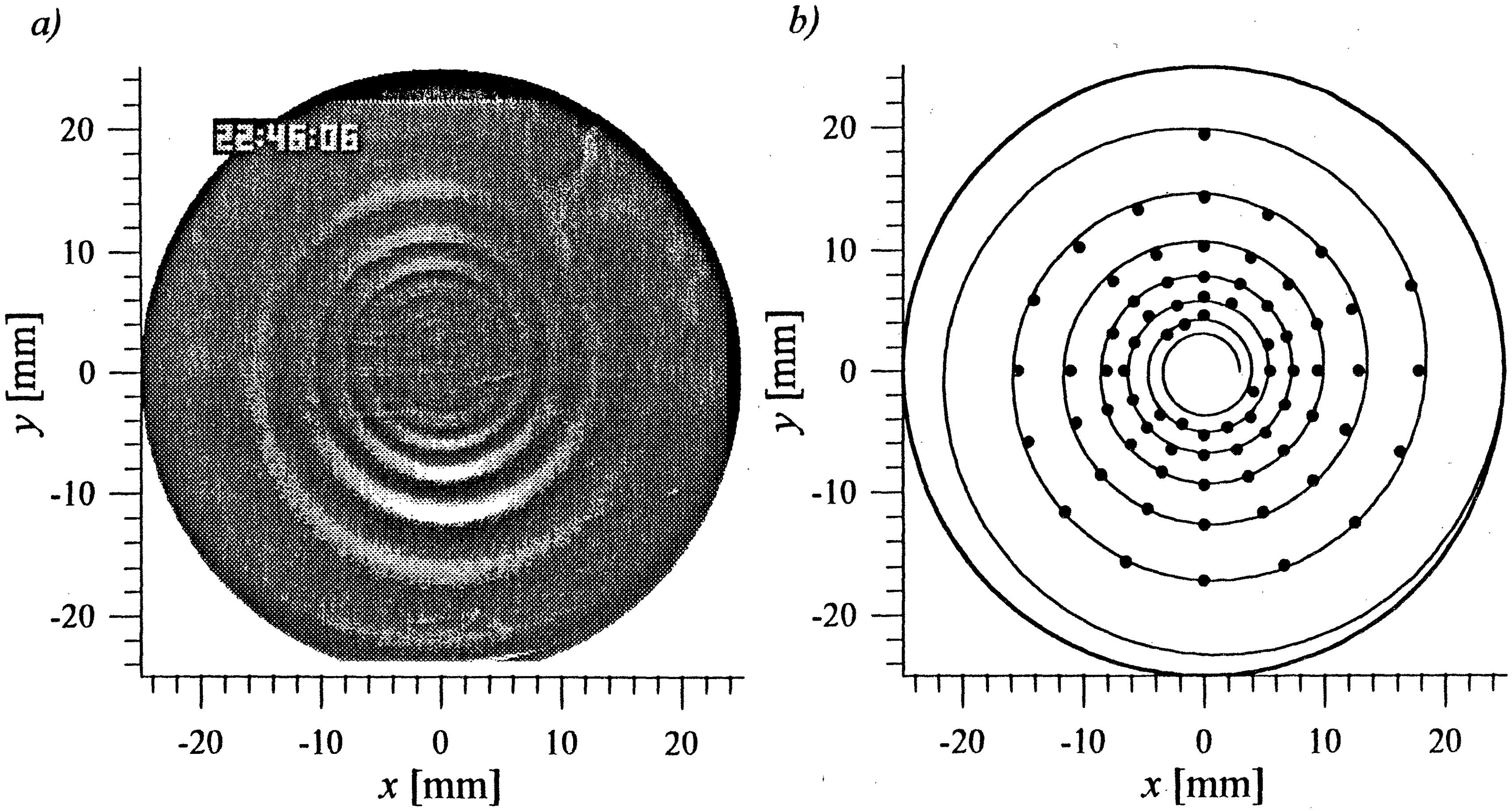

Figure 4.15 *(a)* Raw video image of the flow instability observed at $De_0 = 5.28$ and $\theta_0 = 10^\circ$; *(b)* locations of peaks obtained from processed image and the best fit of equation 3.32 to these positions with $m = -1$, $\alpha_\xi = 21.2$ and $\phi_0 = -1.12$ rad.

clear that a single Bernoulli spiral provides an excellent description of the elastic cone-and-plate instability.

4.2.2 Variation with Cone Angle θ_0

Similar experimental measurements to those described above have also been conducted using conical fixtures with cone angles of 4°, 6° and 15° with the 0.31 wt % PIB Boger fluid, and are summarized in Table 4.2. Quantitative comparisons of the experimental data with linear stability calculations are presented in §4.3. In general, the observations show that as the cone angle is increased, the critical Deborah number $De_{0\text{crit}}$ increases and the transformed radial wavenumber α_ξ of the disturbance decreases. In addition to this trend, the azimuthal mode number of the most unstable non-axisymmetric disturbance is also found to increase as the cone angle decreased. In the 6° cone-and-plate geometry a logarithmic spiral instability with $m = -3$ is observed very close to the critical onset conditions. The three intertwined branches of this spiral instability are shown in figure 4.16 superimposed on an image of the flow at $De_0 = 4.95$. The wavenumber in this geometry is determined to increase to $\alpha_\xi = 30.4$ and the dimensionless wavespeed decreases slightly from the value determined in the 10° geometry to $c_\xi = -0.0128$. This increase in the azimuthal wavenumber at lower cone angles is consistent with the linear stability calculations discussed in §4.3.

For the largest conical fixture ($\theta_0 = 15°$), gravitational body forces overcame the surface tension in the large gap at the outer edge of the cone, and observations of the static fluid meniscus shape showed that fluid only bridged the region between the fixtures out to a reduced radius of $R \sim 13$ mm. For this large cone angle, the base flow is not expected to be purely azimuthal (Walters and Waters 1968, Olagunju 1993); however, no radial recirculation was discernible from flow visualization. Despite these experimental nonidealities, as the Deborah number is incremented to a critical value of $De_0 = 6.32$, a negative angle spiral instability with $m = -1$ is still observed in the fluid sample. The wavenumber is determined to be $\alpha_\xi = 16.0$ and the wavespeed is reduced to a value of $c_\xi = -9.0 \times 10^{-4}$.

These variations in the critical conditions for onset of the instability with cone angle are not unexpected and can be at least qualitatively explained by a stability analysis for the quasilinear Oldroyd-B constitutive model. However, the most striking observation is that for a cone angle of 4°, no elastic instability was observed at any rotation rate up to the maximum obtainable Deborah number of $De_0 = 8.31$ ($Re = 0.42$). The possibility that this apparent lack of instability resulted simply from insufficient seeding in the thin fluid sample

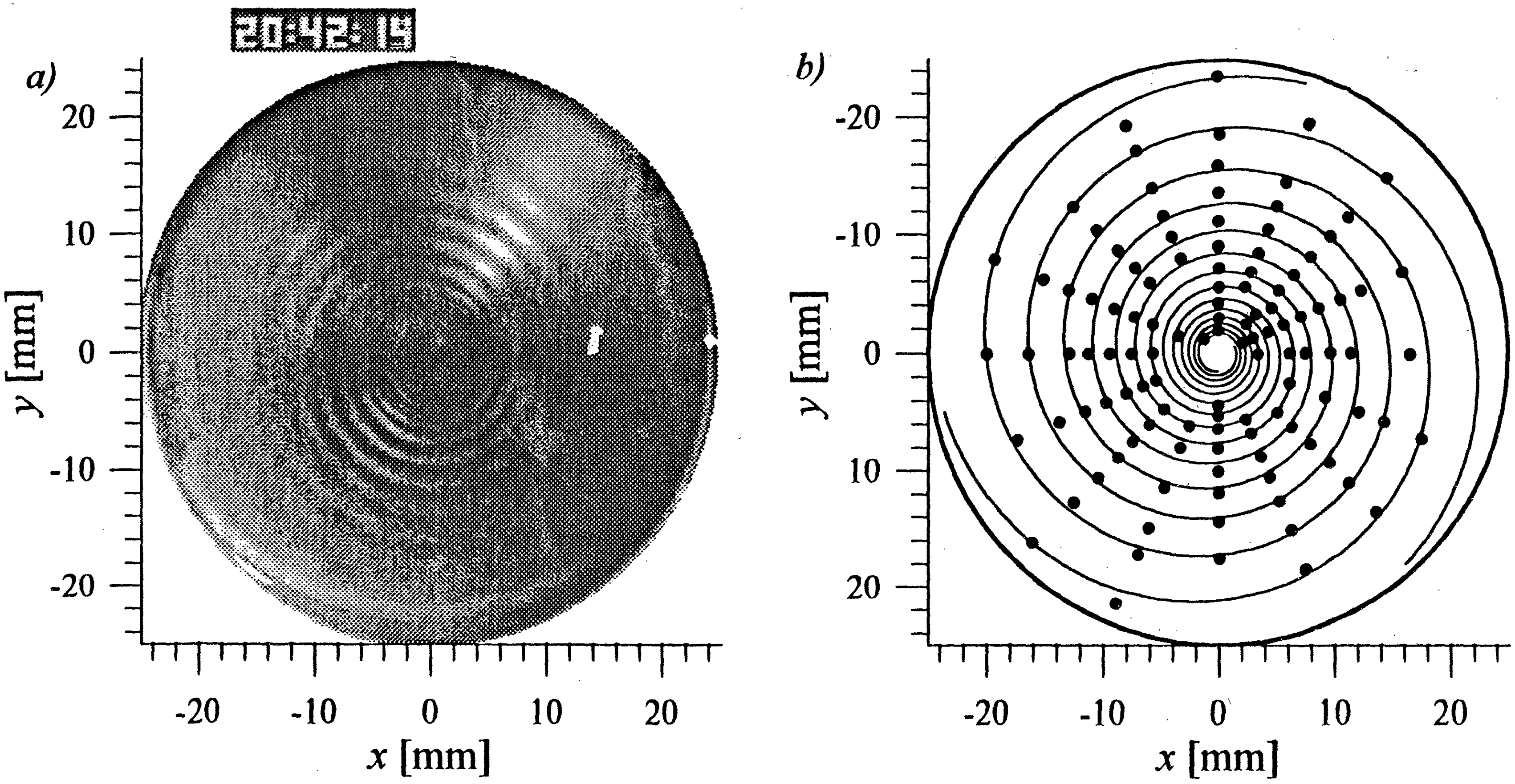

Figure 4.16 *(a)* Raw image of the flow instability at flow conditions of $De_0 = 4.95$ in the 6° cone-and-plate geometry. *(b)* Locations of peaks obtained from processed image (●) and the best fit of equation 3.32 to these positions with $m = -3$, $\alpha_\xi = 30.4$ and $\phi_0 = -0.25$ rad.

to reveal the secondary motion was eliminated by performing careful supplementary experiments in a conventional rheometer (Rheometrics RMS-800). No time-dependent variations in either the total torque or the normal force exerted on the fixtures was detected over the same range of De_0. As discussed in §4.3, the complete elimination of this elastic instability cannot be explained using the quasilinear Oldroyd-B model which actually predicts that the critical Deborah number should *decrease* monotonically as the cone angle decreases. However, the restabilization of the base flow is explained by incorporating a constitutive equation that predicts a shear-rate-dependent first normal stress coefficient into the analysis. By decreasing the cone angle of the geometry the shear rate $\dot{\gamma} = \Omega / \theta_0$ experienced by the fluid sample is increased at any value of the rotation rate. Since the apparent relaxation time $\lambda_1(\dot{\gamma})$ of the test fluids decreases with increasing shear rate, §4.3 shows that the increasing relative importance of viscous effects for small cone angles may ultimately restabilize the base viscometric motion at all rotation rates.

4.2.3 Effect of Fluid Rheology

In order to explore the sensitivity of the spiral instability to small modifications in the fluid rheology, tests were also conducted in each conical fixture with samples of the 0.20 wt% PIB/PB-H300/C14 Boger fluid. For completeness, the wavenumbers and wavespeeds for each of the experimental conditions explored in this work are shown in Table 4.2.

Fluid	θ_0	De_0	α_ξ	c_ξ	m
0.31% PIB	4°	—	—	—	—
($\beta = 0.59$)	6°	4.95	30.3	−0.0128	−3
	10°	5.28	21.2	−0.0107	−1
	15°	6.32	16.0	−0.0009	−1
0.20% PIB	4°	—	—	—	—
($\beta = 0.84$)	6°	7.60	45.0	−0.0001	0
	10°	5.87	16.6	−0.0147	−1

Table 4.2 Summary of the variations in the Deborah number, wavenumber, wavespeed and azimuthal mode number at onset of the elastic instability observed experimentally in two elastic Boger fluids over a range of cone angles.

In the 0.20 wt% elastic fluid, spiral instabilities only could be observed for the 6° and 10° cones. In the 10° cone a single inward traveling spiral ($m = -1$) was again observed, with a wavenumber slightly lower than that calculated in the 0.31 wt% fluid. However, for the 6° cone the instability had the form of nearly stationary axisymmetric cells, which were poorly defined and hard to resolve with the imaging system. Although it is dangerous to infer trends from only two data points, the progressive increase in the dimensionless wavenumber $\alpha\xi$ of the spiral instability for the 0.20 wt% fluid appears similar to that discussed in detail above for the 0.31 wt% fluid. Increasing the solvent viscosity ratio also appears to shift consistently the elastic instability to higher Deborah numbers.

Section 4.3 shows that most of the these variations in the spatio-temporal characteristics of the instability can be explained by linear stability analysis of the Oldroyd-B model. Somewhat more puzzling for the 0.20 wt% fluid data shown in Table 4.2 is the apparent reversal in the trend of progressively decreasing values of the critical Deborah number with smaller cone angles. Section 4.3 shows that this trend can be explained, at least qualitatively, by considering the stability of a nonlinear constitutive model.

4.3 Comparison with Linear Stability Analysis

In conjunction with the experimental studies discussed in §§4.1-2, a linear stability analysis of the spiral instabilities was also conducted by A. Öztekin. Details of the analyses can be found in Byars *et al.* (1994) and McKinley *et al.* (1995), and the major conclusions are briefly outlined here.

4.3.1 Linear Stability Analysis

Parallel Plate Geometry

The linear stability analysis for the parallel plate geometry of Öztekin and Brown (1993) for the Oldroyd-B model was extended to the Chilcott-Rallison model in order to incorporate the effects of a shear-thinning first normal stress coefficient. The analysis was restricted to radially localized disturbances of the velocity, stress and pressure that could be written in the normal mode form $A(z)e^{i\alpha r+im\theta+\sigma t}$, where α is the radial wavenumber, m is the azimuthal wavenumber, σ is the temporal growth rate and $A(z)$ is an amplitude function that satisfies the boundary conditions on the upper and lower plates. Calculations were performed for Deborah numbers and dumbbell extensibilities $0 \leq De_0 \leq 8$ and $10 \leq L \leq \infty$, respectively, for axisymmetric and positive angle spirals.

The neutral stability curves $R^*=R^*(\alpha)$ computed for axisymmetric ($m = 0$) and nonaxisymmetric ($m = 1$) disturbances for $\beta = 0.59$ and several values of the dumbbell extensibility L are shown in figure 4.17 for $De_0 = 1$ and $De_0 = 5$. The solid curve in each plot represents the neutral stability curve $R^*=R^*(\alpha)$ for the Oldroyd-B limit, $L \to \infty$. For the Oldroyd-B model, there is a critical value $R^*=R^*_{\text{crit}}(\alpha_{\text{crit}})$ at each Deborah number that corresponds to the minimum in the neutral stability curve $R^*=R^*(\alpha)$. For $R^* < R^*_{\text{crit}}(\alpha_{\text{crit}})$ the viscometric flow is stable for all values of the radial wavenumber α, whereas for any $R^* > R^*_{\text{crit}}(\alpha_{\text{crit}})$ the flow is unstable to disturbances in some range of α, as previously shown by Öztekin and Brown (1993). The shape of the neutral stability curves for the nonlinear Chilcott-Rallison model is fundamentally different. These neutral stability curves form closed loops; as a result, there is a finite range of radii $R^*_{1\text{crit}}(\alpha_{1\text{crit}}) < R^* < R^*_{2\text{crit}}(\alpha_{2\text{crit}})$ for which the viscometric base flow is unstable. For all radii outside this range, i.e. $R^* < R^*_{1\text{crit}}(\alpha_{1\text{crit}})$ *and* $R^* > R^*_{2\text{crit}}(\alpha_{2\text{crit}})$, the steady flow is stable. The values $R^*_{1\text{crit}}$ and $R^*_{2\text{crit}}$ are, respectively, the minimum and maximum of the neutral stability curves $R^*=R^*(\alpha)$. As L decreases and shear-thinning of $\Psi_1(\dot{\gamma})$

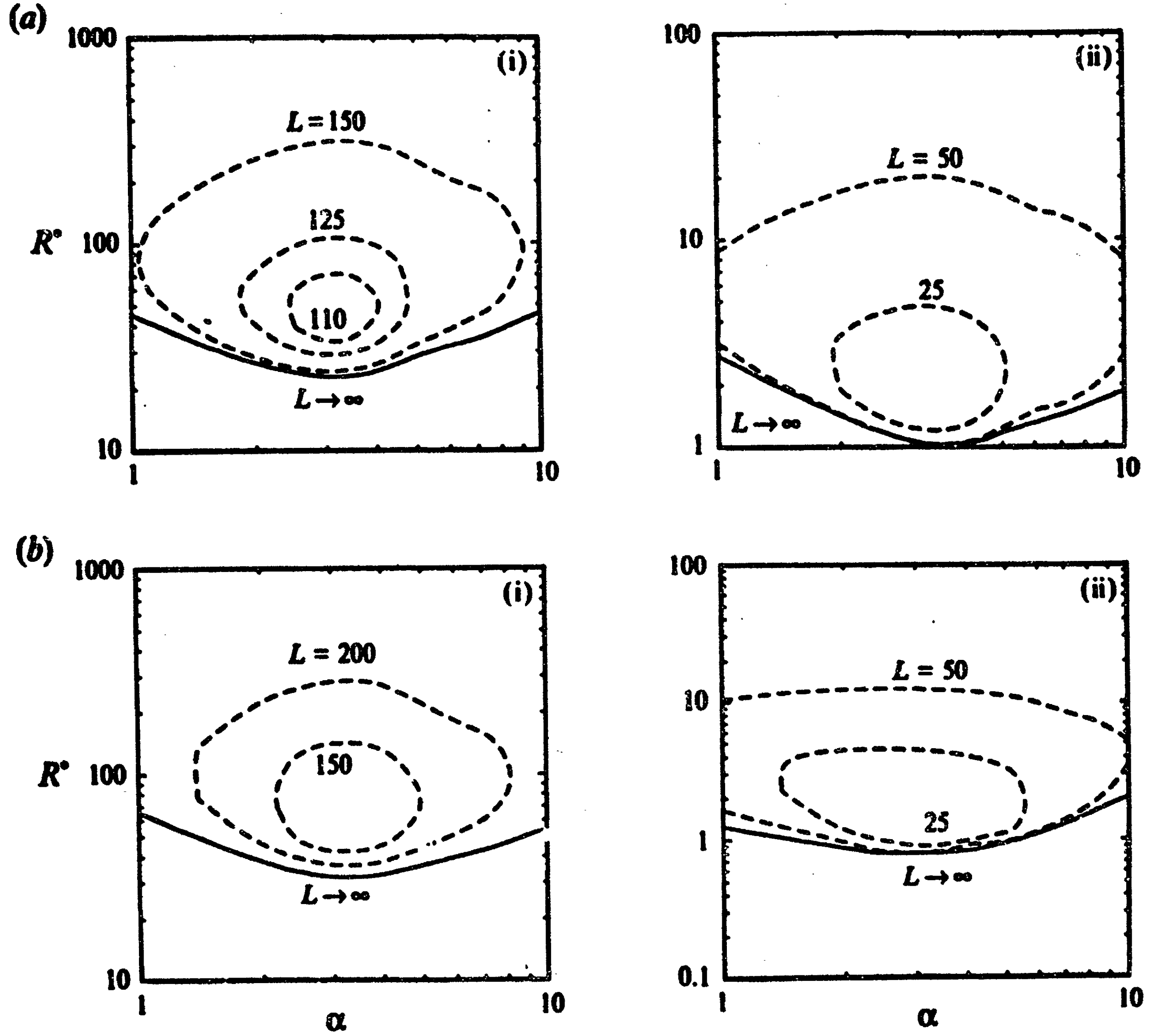

Figure 4.17 The neutral stability curves $R^*\!=\!R^*(\alpha,m)$ computed for the Chilcott-Rallison model with $\beta = 0.59$ and various values of L for (*a*) axisymmetric ($m = 0$) and (*b*) $m = 1$ nonaxisymmetric disturbances with Deborah numbers of (i) $De_0 = 1$ and (ii) $De_0 = 5$.

becomes increasingly important, the unstable region contained by R^* becomes smaller and ultimately disappears completely below a critical value of L. Monotonically increasing De_0 reduces the critical radii $R^* = R^*_{\rm crit}(\alpha_{\rm crit})$ for all curves, but also decreases the critical value of the extensibility L for which the flow is stable everywhere to both axisymmetric and nonaxisymmetric disturbances. The critical value of the radial wavenumber changes little with De_0. The most dangerous radial wavenumbers for the onset $(\alpha_{1\rm crit})$ and for disappearance $(\alpha_{2\rm crit})$ of the instability remain close to about $\alpha \approx 3$ for both axisymmetric and nonaxisymmetric disturbances; this wavenumber corresponds to disturbances with a wavelength of approximately twice the gap spacing.

Finite extensibility has only a small stabilizing effect on the value of $R^*_{1\rm crit}$ compared to the value obtained for the Oldroyd-B model. For low shear rates, the Chilcott-Rallison model predicts quadratic growth in the basic state values of hoop stress $\hat{S}_{0\theta\theta}$. However, for dimensionless shear rates exceeding $De_0 R^* \geq L^2 / \sqrt{8(L^2 - 3)}$ shear-thinning in the normal stress becomes appreciable and the neutral curves in figure 4.17 deviate significantly from the Oldroyd-B limit. Ultimately, for $R^* > R^*_{2\rm crit}(\alpha_{2\rm crit})$ the shear-thinning reduces the gradient in the normal stress to the extent that the viscometric motion is restabilized.

For all values of the viscosity ratio β, the value of $De_{0\rm crit}$ increases and the range of radii where the base flow is unstable shrinks as L is decreased and the shear-rate-dependence of the first normal stress coefficient becomes increasingly important. Note also that the predictions of the critical radii for the onset of instability $R^*_{1\rm crit}$ are very similar for both the Oldroyd-B and the Chilcott-Rallison models and that the critical value of $R^*_{2\rm crit}$ predicted by the Chilcott-Rallison fluid for any value of L has a weak dependence on De_0, as shown in figure 4.18. These features of the neutral stability diagram can be explained better by plots of the *apparent Deborah number* $De \equiv De_0 / f_0$ as a function of dimensionless radius, which asymptotes to zero for all values of De_0 and any finite value of L due to shear-thinning in the first normal stress coefficient. For $L = 50$, the difference in the apparent Deborah number for $3 \leq De_0 \leq 8$ is very small for radii beyond $R^* \approx 20$. This is consistent with the linear stability analysis for this fluid, which predicts the value of $R^*_{2\rm crit}(\alpha_{2\rm crit}) \cong 20$, approximately independent of De_0. However, for much smaller values of R^* the shear-thinning of the normal stress is small and the apparent Deborah number is not reduced significantly below the zero-shear-rate value of De_0. Therefore, the differences between the predictions of $R^*_{1\rm crit}$ for the Oldroyd-B and the Chilcott-Rallison models are small; this is seen in figure 4.18.

The results in figure 4.18(b) show that no instability should be expected below a critical Deborah number $De_0 \approx 6$, for a fluid described by $\beta = 0.59$ and $L \approx 15$. Beyond this Deborah number disturbances are expected to be radially localized to a thin annular

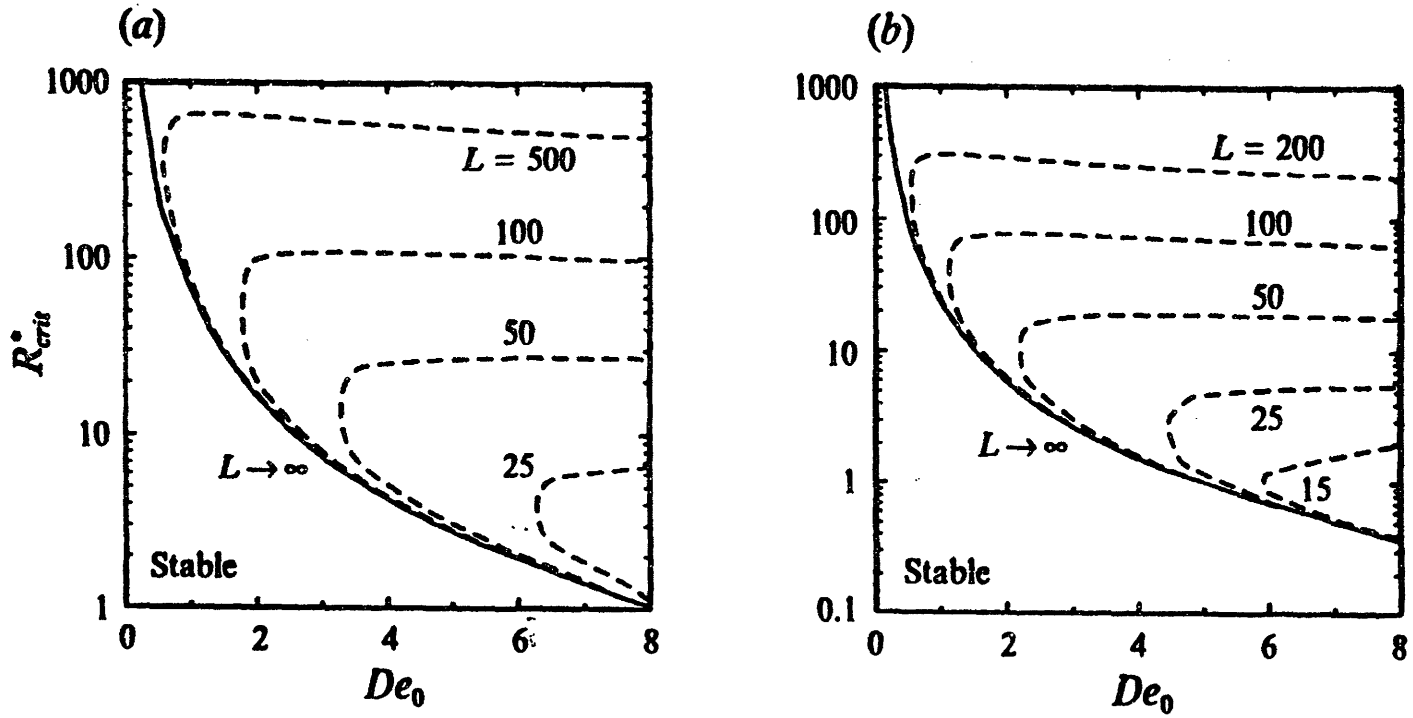

Figure 4.18 The critical radius R^*_{crit} for the onset of the axisymmetric instability as a function of De_0 for a viscosity ratios of (a) $\beta = 0.90$ and (b) $\beta = 0.59$.

ring. This prediction is in good qualitative agreement with the experimental results shown in Table 4.1. A more detailed comparison between the linear stability calculations and observations is discussed in §4.3.2.

Cone-and-Plate Geometry

The analysis for the cone-and-plate geometry follows a similar procedure, except that it is written in the transformed coordinate system (ξ, ϕ) and is therefore not restricted to radially localized disturbances.

The neutral stability curves $R^{*}(\alpha_{\xi}) \equiv 1/\theta_0(\alpha_{\xi})$ for axisymmetric disturbances ($m = 0$) of the Chilcott-Rallison model with a solvent viscosity ratio of $\beta = 0.59$ are shown in figure 4.19 for a range of representative values of the extensibility parameter L. The solid curve in each plot represents the neutral stability curves in the Oldroyd-B fluid limit ($L \to \infty$). The characteristics of the neutral stability curves for the Chilcott-Rallison model are very different; the locus of neutrally stable points (*i.e.* where $\Re\mathrm{e}(\sigma) = 0$) forms a closed loop, and hence the viscometric base motion is only unstable for a finite range of cone angles $\theta_{0\mathrm{crit}_1}\left(\alpha_{\xi\mathrm{crit}_1}\right) > \theta_0 > \theta_{0\mathrm{crit}_2}\left(\alpha_{\xi\mathrm{crit}_2}\right)$ at each value of the extensibility parameter L. The values of $R^{*}_{\mathrm{crit}_1} \equiv 1/\theta_{0\mathrm{crit}_1}$ and $R^{*}_{\mathrm{crit}_2} \equiv 1/\theta_{0\mathrm{crit}_2}$ are, respectively, the minimum and maximum of each neutral stability curve. As L decreases and the nonlinearity in the FENE spring increases, shear-thinning in the elastic hoop stresses becomes increasingly important and the unstable region becomes progressively smaller until it eventually disappears completely below a critical value of the extensibility L. It can be seen from comparisons of figures 4.19*(a-b)* that increasing the Deborah number increases the destabilizing elastic stresses and a smaller critical value of L is required to restabilize the base flow over all values of cone angle.

Stability diagrams for axisymmetric and non-axisymmetric disturbances to the Chilcott-Rallison model are determined by calculating the critical cone angles at which the base flow is destabilized for each value of De_0 and L. The results of such calculations are shown in figure 4.20. In the Oldroyd-B limit ($L \to \infty$), a finite value of the critical cone angle is predicted for any non-zero value of the Deborah number. For large cone angles (and therefore small shear rates) the stability curves of the Chilcott-Rallison model closely follow the Oldroyd-B stability loci. However, the curves diverge as the critical cone-angle decreases and shear-thinning effects in the fluid become increasingly important. For finite values of the extensibility L there exists a critical value of the Deborah number (corresponding to the turning point in each of the curves plotted in figure 4.20) below

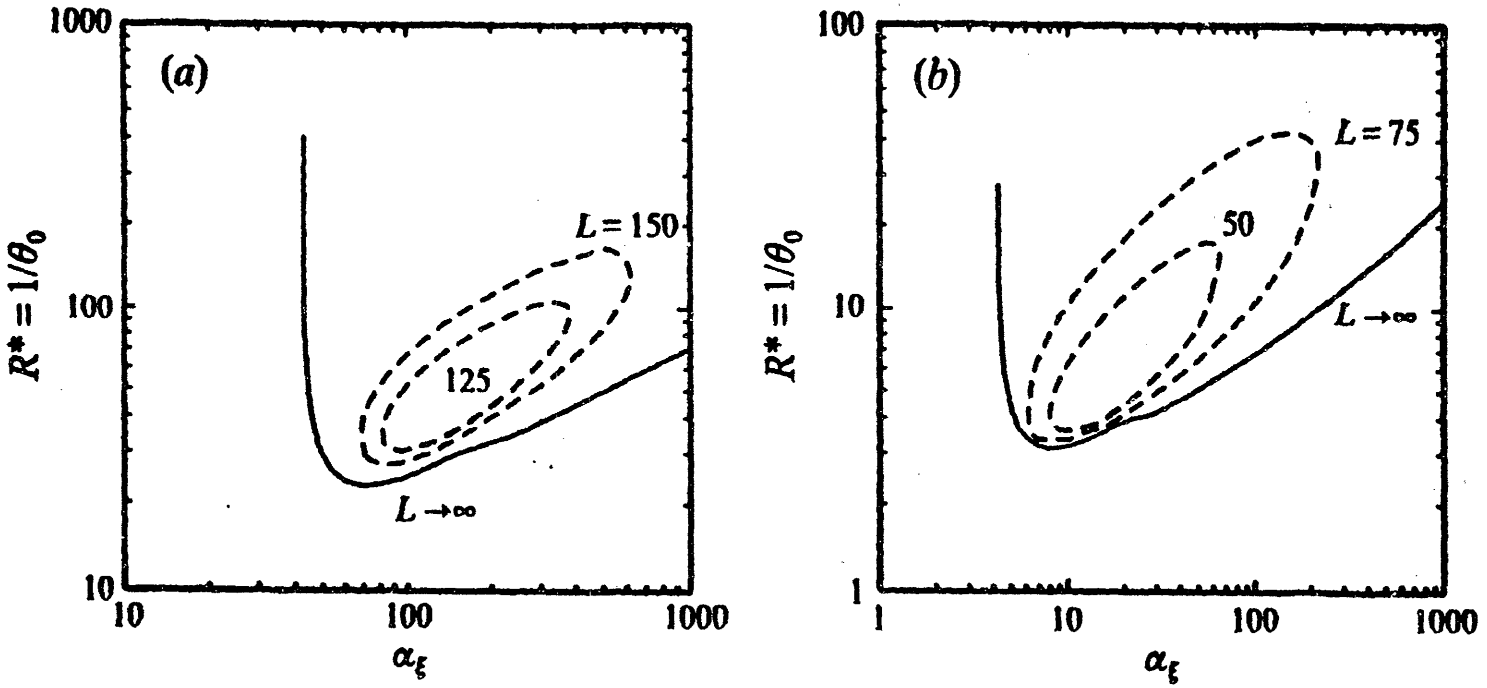

Figure 4.19 Neutral stability curves for axisymmetric disturbances to the Chilcott-Rallison model with $\beta = 0.59$ and for various values of the dumbbell extensibility parameter L at (a) $De_0 = 1$, (b) $De_0 = 3$.

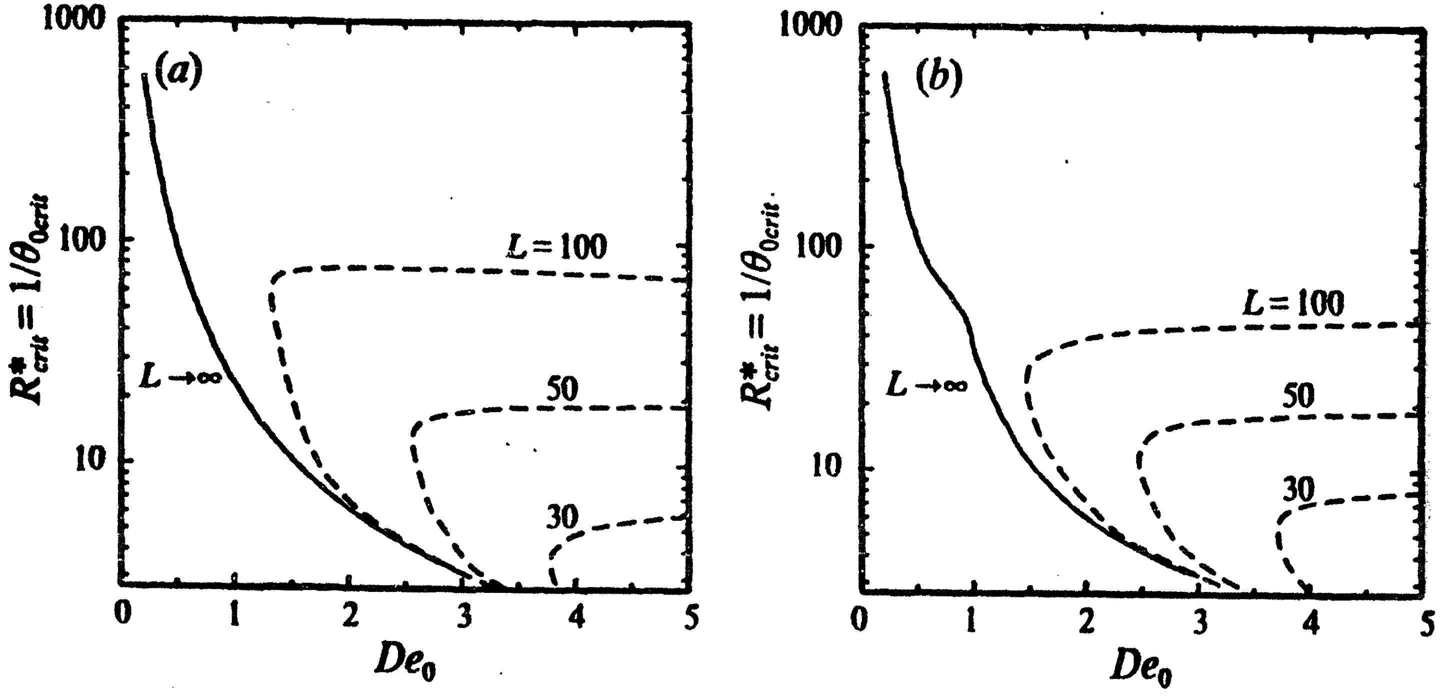

Figure 4.20 Stability diagrams for onset of logarithmic spiral disturbances in the Chilcott-Rallison model ($\beta = 0.59$) with spiral mode (a) $m = 0$, (b) $m = -2$.

which the base flow is stable *for all cone angles.* For $De_0 > De_{0\text{crit}}$, the base flow is unstable over the finite range of cone angles $\theta_{0\text{crit}_1} > \theta_0 > \theta_{0\text{crit}_2}$, but at lower values of the Deborah number, the base torsional motion between a plate and a cone of any angle is stable to all axisymmetric and non-axisymmetric disturbances of spiral form. Of course, this is subject to the important caveat that the purely azimuthal base flow is a valid approximate solution to the inertialess equations of motion. This requires that $\theta_0 < 10°$ (0.173 rad), or equivalently $R^* > 5.7$.

The value of $De_{0\text{crit}}$ increases and the range of unstable cone angles shrinks for both the axisymmetric and non-axisymmetric disturbances as the extensibility L is decreased. At large Deborah numbers the variation in the upper stability boundary $R^*_{\text{crit}_2} \equiv 1/\theta_{0\text{crit}_2}$ with De_0 is weak for all values of L and m, since the rate of shear-thinning in the normal stresses asymptotically approaches $\dot{\gamma}^{-1}$. Increasing the Deborah number thus results in almost no change in the destabilizing elastic stresses predicted by the Chilcott-Rallison model.

4.3.2 Comparison of Experiments and Linear Stability Analysis

Parallel Plate Geometry

The evolution of the disturbances and the shape of the neutral stability diagrams predicted by the linear stability analysis of the nonlinear Chilcott-Rallison model are consistent with the experimental observations. Most importantly, it shows that for a given solvent viscosity ratio β and finite dumbbell extensibility L in the Chilcott-Rallison model, the elastic flow instability is limited to an annular ring near the center of the disks. The instability develops at the critical radius $R^* = R^*_{1\text{crit}}(\alpha_{1\text{crit}})$ and the secondary motion propagates radially outward as traveling spiral waves when the Deborah number exceeds the critical Deborah number for the onset of instability. This disturbance flow dies out at a second, larger critical radius $R^* = R^*_{2\text{crit}}(\alpha_{2\text{crit}})$ and the flow becomes laminar, steady and purely azimuthal again.

The agreement between experiment and theory for the prediction of the critical Deborah number is also greatly improved over the previous work of Öztekin and Brown (1993). In the limit $L \to \infty$ (corresponding to the quasilinear Oldroyd-B model), the present analysis for infinite disks predicts that the critical value of De_0 monotonically approaches zero, and the torsional flow is always unstable for any finite De_0 at large enough radii.

However, when the magnitude of shear-thinning in the first normal stress coefficient is increased by decreasing the extensibility parameter L, the positive spatial gradients in the normal stresses which provide the driving force of the elastic instability are decreased and the critical value of De_0 is increased. For quantitative comparison, the experimental values (with appropriate error bounds) and the prediction from the linear stability analysis for the critical Deborah number $De_0 = De_{0crit}(L)$ are shown in figure 4.21 for $\beta = 0.59$ and 0.84. The base flow remains stable everywhere for small values of De_0 for both values of β and all finite values of L. For a fixed viscosity ratio, the numerical value of the critical Deborah number is dependent on the exact value of the extensibility parameter L, which is determined experimentally from the best fit to the shear-rate-dependent first normal stress coefficient $\Psi_1(\dot{\gamma})$ of the PIB/PB/C14 elastic liquids. The steep slopes of the numerically calculated curves in figure 4.21 for $L \leq 50$ signify how sensitive the critical Deborah number De_{0crit} is to changes in this extensibility parameter. This parameter can only be determined approximately from the steady-shear-flow rheological data available, and only a single-mode model was used in the calculations, so some discrepancy between the data and computations in figure 4.21 is to be expected. In addition it should be noted that the experimental values of De_{0crit} determined from the growth of finite amplitude perturbations to the base flow underpredict the linear stability calculations, as expected for a flow instability with a subcritical bifurcation structure. Both the experimental observations and the numerical calculations shown in figure 4.21 also indicate that the degree of stabilization by shear-thinning in the first normal stress coefficient is stronger for the higher solvent viscosity ratio. Similar stabilizing effects were demonstrated by Larson *et al.* (1994) using the K-BKZ model, and physically arise from the increased damping of the disturbance energy that is obtained when the relative contribution of the Newtonian solvent viscosity is increased. Numerical calculation is not continued for Deborah numbers beyond $De_0 = 8$ because the critical onset radius of the disturbances becomes very small. Since the present analysis is restricted to radially localized disturbances, it becomes unreliable when the onset radius of the instabilities becomes too small.

The predictions from the linear stability analysis for the axisymmetric and the $m = 1$ and $m = 2$ spiral vortices show that the difference in the critical onset radii for these modes is very small for elastic fluids with $\beta = 0.59$ or $\beta = 0.84$ and for the most physically realistic values of the parameter L. It is therefore likely that both axisymmetric and nonaxisymmetric vortices will be observed simultaneously in experiments. In fact, both the current flow visualization experiments and previous observations by McKinley *et al.* (1991a) show the existence of several modes once the disturbances reach finite amplitude. Even close to the onset point of the instability, it is found that both the

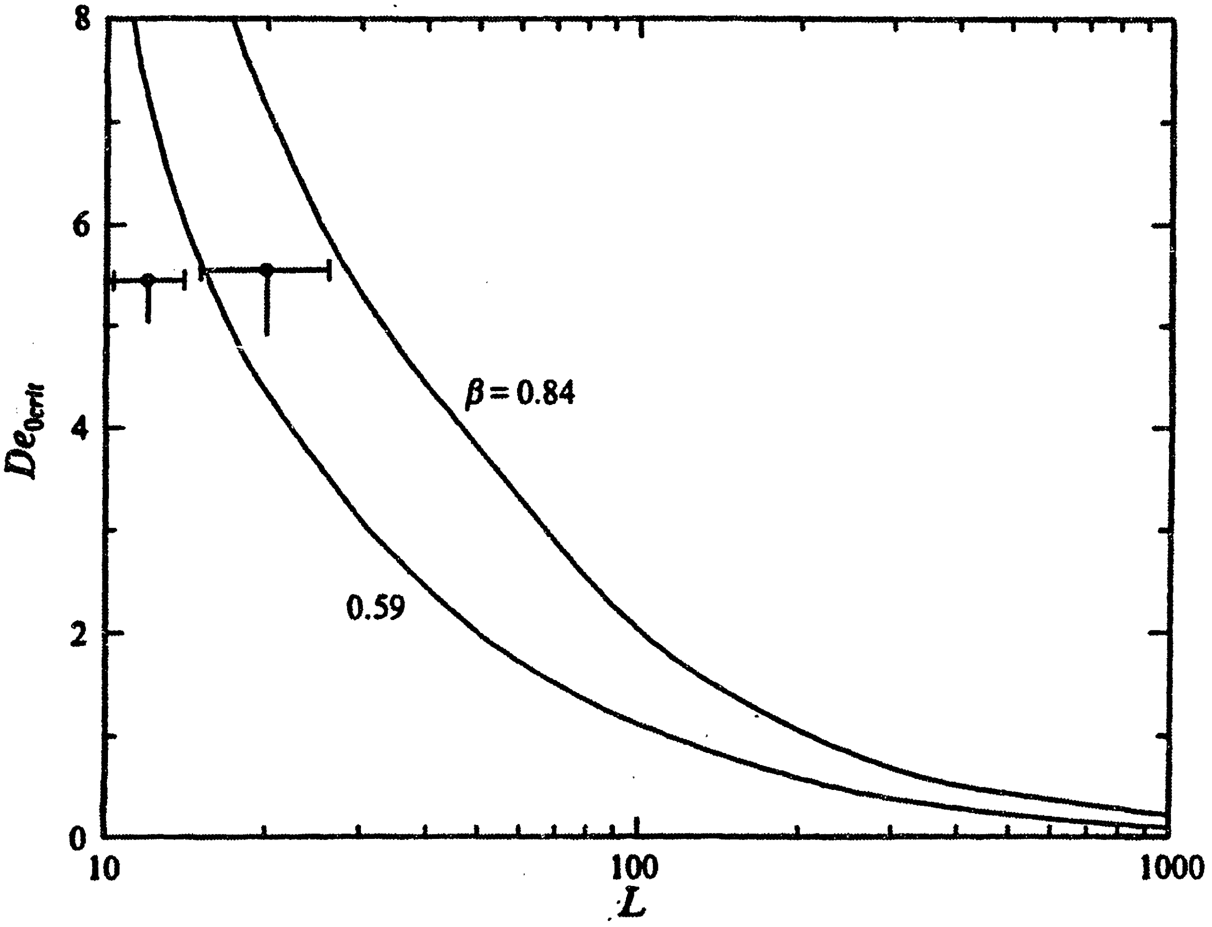

Figure 4.21 The critical Deborah number De_{0crit} as function of L for $\beta = 0.59$ and $\beta = 0.84$ predicted by experiments (●) and stability analysis (—) for the most dangerous instability mode.

axisymmetric ($m = 0$) and the nonaxisymmetric ($m = 1, m = 2$) spiral vortices can be observed in different experiments for slightly different values of the Deborah number, as indicated in Table 4.1. For a solvent viscosity ratio of $\beta = 0.59$, the linear stability analysis predicts the $m = 1$ nonaxisymmetric mode is *always* the most critical. However, for most values of the extensibility parameter L, the difference in the calculated onset radii of the axisymmetric and $m = 1$ and $m = 2$ spiral vortices are very small.

Both the axisymmetric and nonaxisymmetric spiral waves observed in the experiments correspond to vortices with dimensional radial spacing of approximately twice the gap between the plates, in good agreement with the calculations. The experimentally measured radial spacing between two bright regions at a constant value of θ corresponds to the wavelength $2\pi/\alpha$ shown in the normal mode representation of the disturbances (equation 3.26). A similar representation has been used for the flow of Newtonian fluids over a rotating disk to compare the predictions for spiral angle between experiments and calculations for the inertial instability, or Ekman spirals (Kobayashi *et al.* 1980; Malik 1986). Both the measured and the calculated wavenumbers of the axisymmetric and nonaxisymmetric disturbances exhibit a weak dependence on De_0 and β: the measured wavenumbers for different values of De_0 and β are $3.64 \leq \alpha \leq 4.11$, and the calculated wavenumbers vary in the range $3 \leq \alpha \leq 4$ for a broad range of De_0 and β. The wavenumbers from both the experiments and the analysis increase slightly as β increases.

The dimensionless radial wavespeed of the disturbances observed in the experiments remains approximately unchanged across the annular region of secondary flow, and is measured to be $c_r \approx 0.23$ for axisymmetric mode and spiral vortices in both PIB/PB/C14 Boger fluids, as shown in Table 4.1. The linear stability analysis for the axisymmetric mode ($m = 0$) predicts that the wavespeed of the disturbance depends on both the Deborah number and the radial location R^* being considered. For a fixed value of $De_0 = 5.5$, the radial wavespeed is approximately 0.08 when instability starts at $R^* = R^*_{1\text{crit}}(\alpha_{1\text{crit}})$ and is about 0.25 when disturbances decay again at $R^* = R^*_{2\text{crit}}(\alpha_{2\text{crit}})$. These values are relatively insensitive to the azimuthal form of the disturbance. For example, the calculated values of the critical wavespeed are 0.07 and 0.19 for spiral vortices with a winding number $m = 1$. The agreement between the experiments and the analysis is therefore good at larger radii. In fact, the comparison of the wavespeeds predicted by experiments and analysis for the Oldroyd-B model is equally good if the calculations are carried out at Deborah numbers based on the 'apparent relaxation time', $De = De(\dot{\gamma})$, evaluated at the local shear rate between the plates. The wavespeed of the axisymmetric instability for the Oldroyd-B fluid model with a solvent viscosity ratio

$\beta = 0.59$ is calculated to be $c_r = 0.18$ using a Deborah number corresponding to the local shear rate at $R^* = R^*_{1\text{crit}}(\alpha_{1\text{crit}}) = 3.5$ (Öztekin and Brown 1993).

The critical values of the radii $R^* = R^*_{1\text{crit}}(\alpha_{1\text{crit}})$ and $R^* = R^*_{2\text{crit}}(\alpha_{2\text{crit}})$ defining the annular region of the unsteady flow determined from the experiments and stability calculations are shown in figure 4.22(*a*) and (*b*) for solvent viscosity ratios of $\beta = 0.59$ and $\beta = 0.84$, respectively. The observations and the calculations with the Chilcott-Rallison constitutive model are in qualitative agreement. Both show that the axisymmetric and spiral vortices are confined to an annular region bounded by $R^*_{1\text{crit}}$ and $R^*_{2\text{crit}}$; however, the stability analysis consistently predicts lower values of these critical radii. Since the experimental observations of secondary motions are inherently finite in amplitude they are expected to result in an overestimation of R_1^*; similarly, outwardly-traveling disturbances of finite amplitude may be expected to decay more slowly than infinitesimal perturbations and the decay radius R_2^* will thus also be overestimated by the experiments. Closer comparison between theory and experiment requires nonlinear calculations of the finite amplitude states or the incorporation of a more complex constitutive model with a spectrum of time constants which better describes the steady and transient material functions of the elastic test fluids. The systematic differences between the experimental measurements and the numerical predictions also may result from considering only radially-localized disturbances. Since the disturbances are confined into a finite annular region for the Chilcott-Rallison model, the validity of this assumption is easier to justify than it is in the Oldroyd-B model for which the instabilities occur in an infinite domain. However, rigorous removal of this assumption requires consideration of the fully two-dimensional nonseparable eigenvalue problem in the (r, z) plane for each spiral mode.

Although the analysis predicts that the difference in the onset radius of the radially inward-traveling negative angle and outward-traveling positive angle spiral vortices is very small, only positive angle spirals are observed by flow visualization at the linear stage of the instability. This is probably due to the fact that negative angle spirals travel radially inwards to smaller radii where the analysis suggests the base flow is linearly stable to all disturbances of spiral form. Any small disturbances which can be represented in this form will therefore be damped so that their amplitudes are never large enough to be detected in the experiments. However, it is obvious from figures 4.2(*e*) and 4.2(*f*) that negative angle spiral vortices are observed in the nonlinear motions observed at longer times. These structures propagate radially inward toward the center of the disk and probably reflect back from the center. The nonlinear interactions between these reflected waves and other

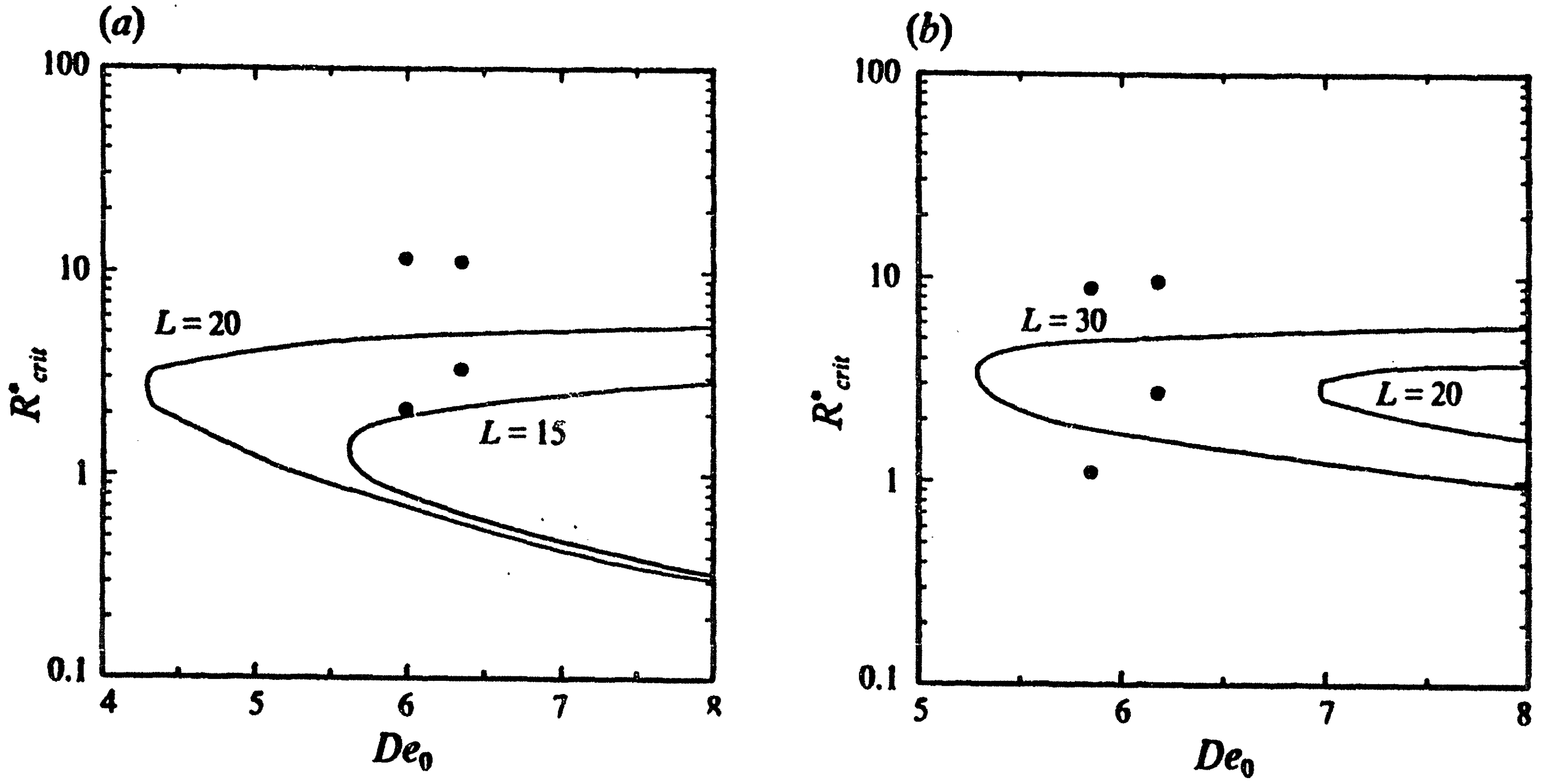

Figure 4.22 The critical onset radius $R^* = R^*_{crit}(\alpha_{crit})$ of the most dangerous mode as a function of De_0 predicted by experiments and stability analysis for the viscosity ratios of (*a*) $\beta = 0.59$ and (*b*) $\beta = 0.84$.

traveling waves make the flow too complicated to decompose into discrete disturbance modes.

Cone-and-Plate Geometry

The critical value of the wavenumbers $\alpha_\xi = \alpha_{\xi\text{crit}}(\theta_0)$ and $c_\xi = c_{\xi\text{crit}}(\theta_0)$ determined from experiments and predicted by linear stability analysis for the axisymmetric ($m = 0$) and non-axisymmetric disturbances with $m = -1, -2$ and -3 are shown in figure 4.23. As the cone angle decreases, the wavenumber steadily increases, and the experimental observations and numerical calculations for the critical wavenumber are in excellent quantitative agreement. Additionally, the calculations show that the values of the critical wavenumber of each mode are similar for all cone angles and also that these values become very large as the cone angle approaches zero. The measured and calculated values of the radial wavespeed of the disturbance also agree well for the smallest cone angle of $\theta_0 = 6°$; however, for larger cone angles the wavespeed of the logarithmic spirals observed in experiments is smaller than the predicted value for any mode. This discrepancy at larger cone angles might be expected since both our experimental and numerical assumptions of a purely azimuthal base flow become inaccurate for cone angles beyond $\theta_0 > 10°$. The linear stability analysis also predicts that the concentric waves ($m = 0$) travel faster than the non-axisymmetric $m = -1, -2$ and -3 logarithmic spirals and that the wavespeed of the recirculating vortices decreases as the cone angle is progressively reduced.

The Oldroyd-B model thus appears to provide an accurate description of the spatial form of the elastic instability in cone-and-plate flows. However, under the typical flow conditions attained at onset of these elastic instabilities, Boger fluids actually exhibit shear-rate-dependent material properties; most notably, the first normal stress coefficient $\Psi_1(\dot{\gamma})$ decreases monotonically as a function of increasing shear rate. Construction of an experimental stability diagram and quantitative comparison of critical flow conditions at the onset of the elastic instability therefore requires the definition of an appropriate relaxation time for the test fluid. The Oldroyd-B fluid model of course does not predict any shear-rate dependence in the viscometric properties; however, an *ad hoc* comparison between experiments and linear stability calculations can be effected by defining an 'apparent relaxation time' (McKinley *et al.* 1991; Larson *et al.* 1994) as $\lambda_1(\dot{\gamma}) \equiv \Psi_1(\dot{\gamma})/2[\eta(\dot{\gamma}) - \eta_s]$. In this fashion, the actual values of the viscosity and first normal stress coefficient for the fluid are used to construct a new, Oldroyd-like time constant locally at each value of the shear rate in the steady base state. This definition has the correct zero-shear-rate asymptote given in Table 3.1 and, because linear stability calculations are only concerned with

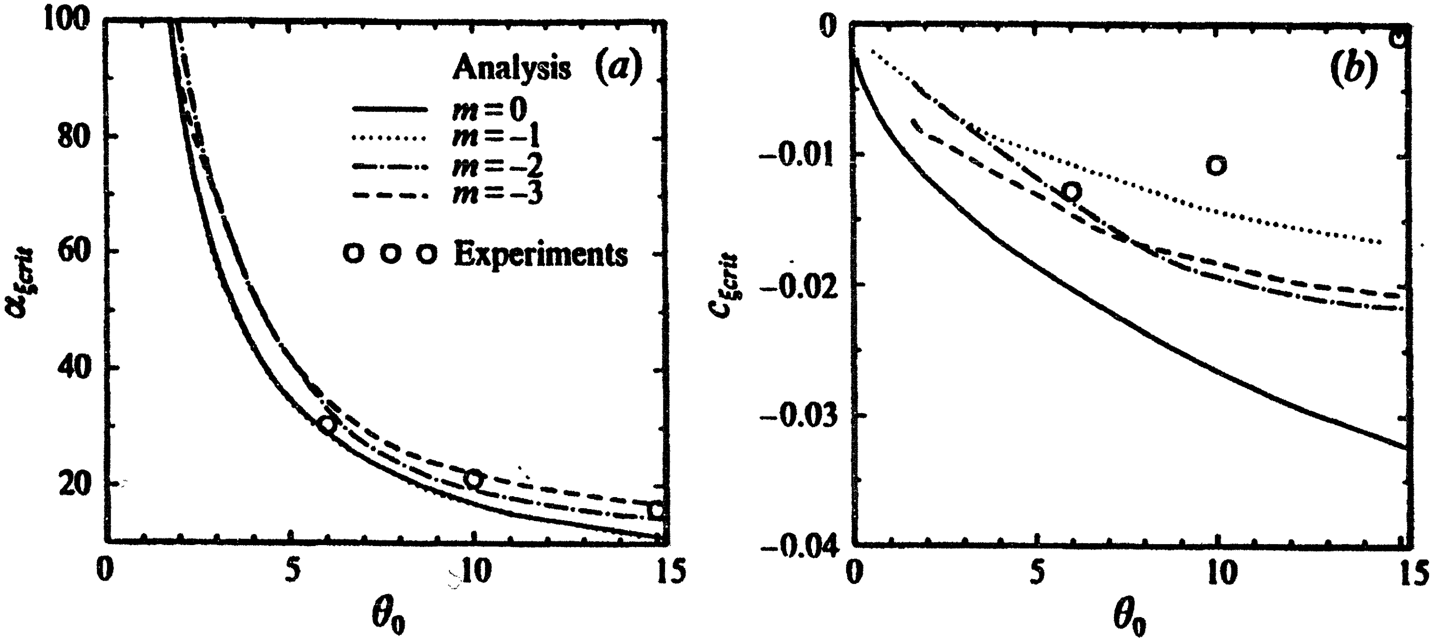

Figure 4.23 Comparison of experimental measurements and predictions from linear stability calculations with the Oldroyd-B model ($\beta = 0.59$) for *(a)* the dimensionless wavenumber α_ξ, and *(b)* the dimensionless wavespeed c_ξ.

infinitesimal perturbations about the base state, spatial variations in the apparent relaxation time may be expected to be very small at onset of stability.

A direct comparison of the experimentally-determined and numerically-predicted stability diagram for onset of the elastic spiral instability in cone-and-plate rheometers is presented in figure 4.24. The shear-rate-dependent relaxation time $\lambda_1(\dot{\gamma})$ is used to calculate an 'apparent critical Deborah number' $De_{\text{crit}}(\dot{\gamma}) \equiv \lambda_1(\dot{\gamma})\Omega_{\text{crit}}$ and an 'apparent critical Weissenberg number' $We_{\text{crit}}(\dot{\gamma}) \equiv [De(\dot{\gamma})/\theta_0]_{\text{crit}}$ for onset of instability in the Boger fluid, and these values are compared with linear stability calculations for the most unstable disturbance mode predicted using the Oldroyd-B model with $\beta = 0.59$. This critical Weissenberg number corresponds to either the critical dimensionless shear rate that must be achieved for onset of instability in a series of experiments with a fixed conical fixture, or alternatively to the critical cone angle for onset of instablity in linear stability calculations at a fixed Deborah number.

In addition to the observations with the 0.31 wt% PIB Boger fluid, the hollow circles in figure 4.24 indicate similar data extracted from the recent rheological studies of the 'M1' international test fluid (Hudson and Ferguson 1990; Laun and Hingmann 1990; Steiert and Wolff 1990). This is another polyisobutylene-based Boger fluid containing 0.244 wt% PIB in polybutene and kerosene, with a similar value of the solvent viscosity ratio $\beta_{\text{M1}} = 0.52$ (Laun and Hingmann 1990). In these earlier studies using cone-and-plate rheometers with cone angles in the range $1° \leq \theta_0 \leq 4°$ the flow instability was interpreted in terms of a 'critical shear stress' for structure formation. No information was given about the spatial and temporal characteristics of the instabilities observed in the 'M1' fluid; however, it appears likely that the instability is identical to the traveling logarithmic spiral vortices observed in the current investigation and is better interpreted in terms of a critical Deborah number. It is clear from figure 4.24 that the agreement between the experiments and theory for the prediction of onset of the elastic cone-and-plate instability is good for both our PIB/PB/C14 and the 'M1' Boger fluid.

In order to compare the experimental observations with linear stability calculations it is first necessary to choose an appropriate value of the dumbbell extensibility L. As discussed above in §3.1, this parameter is best ascertained from extensional viscosity measurements; however, in the absence of such data we resort to fitting the shear-rate-dependence of the first normal stress coefficient $\Psi_1(\dot{\gamma})$for the 0.31 wt% PIB Boger fluid. Nonlinear regression results in the best fit value of $L \approx 15$ given in Table 3.1. However, calculations with such a small value of L result in growth of spiral instabilities only at very large values of De_0. Recent birefringence measurements in extensional flows through packed beds (Evans *et al.* 1994) suggest that the molecular extensibility of the PIB

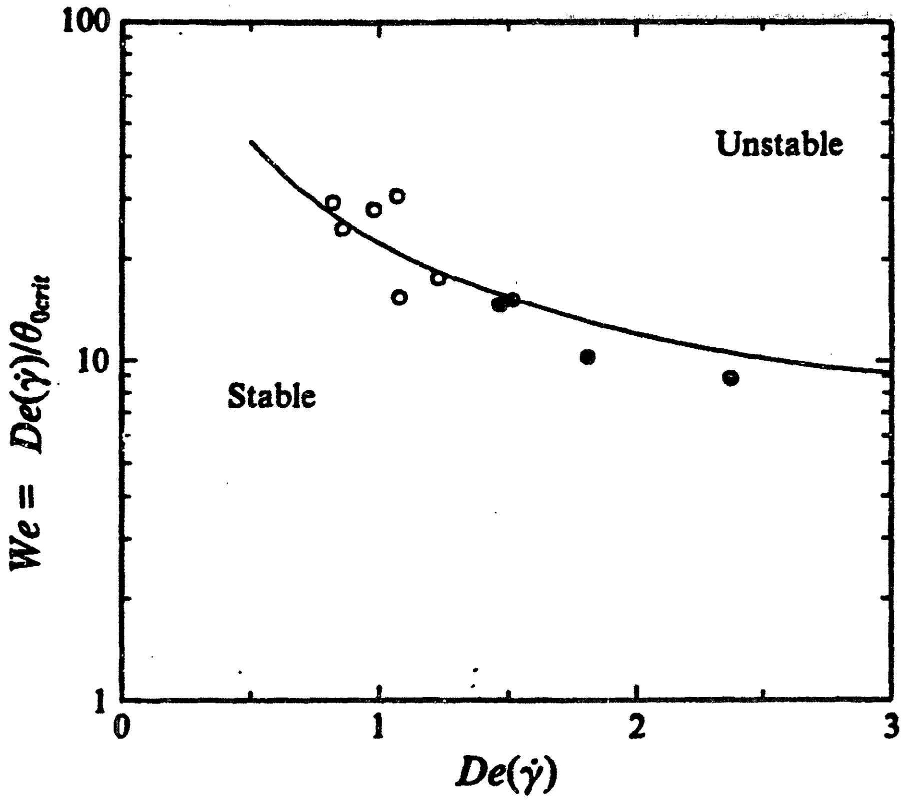

Figure 4.24 Stability diagram for the onset of the elastic instabilities in a cone-and-plate rheometer in terms of the shear-rate-dependent critical Weissenberg number; (●) present experiments with 0.31 wt% PIB/PB/C14 Boger fluid, (○) earlier experiments for M1 Boger fluid, (——) most unstable mode predicted by linear stability analysis with Oldroyd-B model ($\beta = 0.59$).

molecules in a Boger fluid is actually considerably larger than the value obtained from only considering the weak shear-rate-dependent variations in the viscometric properties, and values in the range $30 \leq L \leq 100$ are typically obtained for the extensibility of the dumbbells in the Chilcott-Rallison constitutive model. In the comparisons presented below, we find numerical stability calculations with values of $L = 30$ and $L = 50$ best describe the experimentally-measured critical conditions for the 0.31 wt% PIB and 0.20 wt% PIB fluid respectively. This discrepancy between experimental and numerical values of the nonlinear parameter L is to be expected considering the limitations inherent in describing a polydisperse semidilute polymer solution with a single mode FENE dumbbell model. A more accurate comparison of experimental observations with linear stability analysis for a multimode nonlinear viscoelastic constitutive equation has recently been presented by Öztekin *et al.* (1994).

A composite stability diagram for comparison of experimental observations and numerical calculations of the cone-and-plate instability in each fluid can be constructed in several ways. The numerically-determined critical cone angles for the most unstable azimuthal mode can be plotted as a function of the Deborah number De_0. However, for consistency with the earlier work of McKinley *et al.* (1991), and the previous comparison with the Oldroyd-B model (*cf.* figure 4.24) the stability diagram is presented here in terms of the critical Weissenberg number $We_{\text{crit}} \equiv \lambda_1 \Omega / \theta_{0\text{crit}}(\alpha_{\xi\text{crit}}, m_{\text{crit}})$ as a function of the zero-shear-rate Deborah number De_0, for the appropriate values of the solvent viscosity ratio, $\beta = 0.59$ and $\beta = 0.84$ respectively. In this parameter space, sets of experimental data points with a given conical fixture thus describe straight lines extending from the origin with slope $1/\theta_0$. Experimental measurements in each fluid corresponding to stable and unstable base flow are marked in figure 4.25 by open (○) and closed (●) circles, respectively. For comparison, the predictions from the linear stability analysis for the most dangerous azimuthal disturbances are also shown in figure 4.25 for both the Oldroyd-B limit ($L \rightarrow \infty$) and for the nonlinear Chilcott-Rallison model with a value of L that best fits the experimental data. For cone angles greater than 20°, a secondary flow consisting of a weak toroidal motion is present, and the assumption of a purely azimuthal base flow is no longer valid.

In contrast to the comparison presented previously in figure 4.24, there is no *ad hoc* adjustment in the relaxation time made here and each figure represents a direct comparison. The experiments in the 0.31 wt% PIB Boger fluid ($\beta = 0.59$) indicate that the critical Deborah number, below which no instability is seen, is $De_{0\text{crit}} \cong 4.25$ and also show that for small cone angles ($\theta_0 \leq 4°$) the base flow is stable for all values of rotation rate experimentally achievable in our experimental device. Also shown for completeness on this

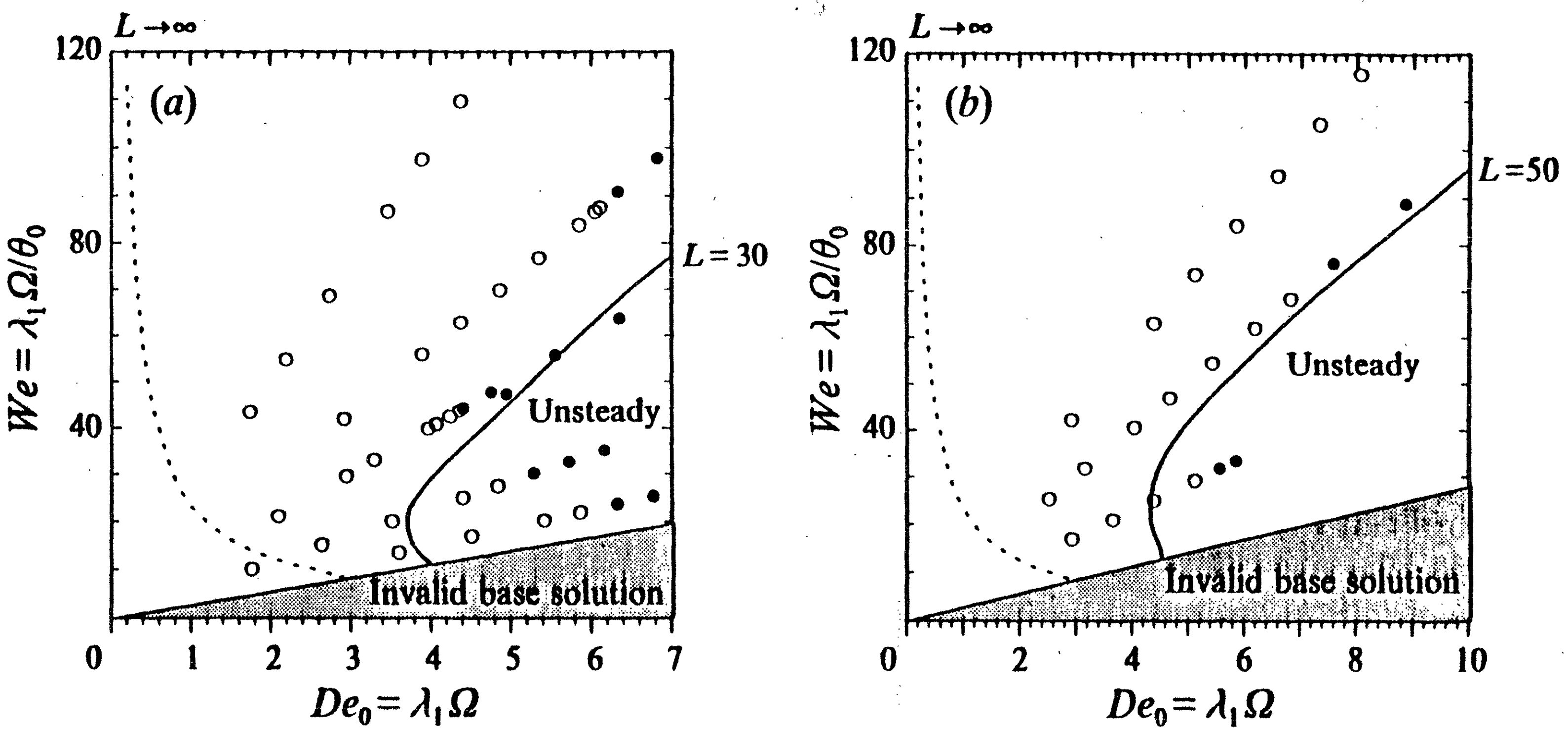

Figure 4.25 Comparison of experimentally-determined and numerically-calculated stability diagrams for onset of spiral instabilities between a cone and a plate in Boger fluids with solvent viscosity ratios of *(a)* $\beta = 0.59$, and *(b)* $\beta = 0.84$. In each figure symbols indicate experimental measurements of steady (○) or unsteady (●) base flow, dashed lines (– – –) indicate predictions of the Oldroyd-B model with appropriate value of β, and solid lines (——) indicate predictions of the Chilcott-Rallison model with indicated value of *L*.

figure are additional experimental measurements performed earlier in a standard rheometer (McKinley, 1991) using a conical fixture with $\theta_0 = 2.54°$ (0.04 rad). These observations are in sharp contrast to the predictions for the Oldroyd-B model, which is qualitatively incorrect and predicts $De_{0\text{crit}} \to 0$ for $We >> 1$. The experimental observations and the linear stability calculations for the Chilcott-Rallison FENE dumbbell model with $L = 30$ and $\beta = 0.59$ are not in quantitative agreement, however the general characteristics are correct. The predicted value of the critical Deborah number is $De_{0\text{crit}} \approx 3.75$ which is close to the value determined by experiments. The analysis also predicts that the viscometric flow is stable to all disturbances for all cone angles below about $\theta_0 \approx 4.7°$ (0.08 rad).

The stability diagram shown in figure 4.25*(b)* also provides an explanation for the initially puzzling observation discussed in §4.2 of a large increase in the critical Deborah number required for onset of instability in the experiments with the 0.20 wt% fluid in the 6° geometry. The increase in the solvent viscosity ratio, β, shifts the neutral stability curve for onset of spiral disturbances to higher Deborah numbers, and the locus of points in $We - De_0$ parameter space that are accessible with a 6° conical fixture now intersects the neutral stability curve in the region where shear-thinning effects in the normal stress result in increasing stabilization of the base azimuthal flow. A more extensive series of experiments with a large number of different conical fixtures would allow the experimental stability boundaries to be mapped out with even greater precision; however, it is clear that the nonlinear constitutive model is capable of describing the key features of the stability diagrams obtained in cone-and-plate experiments with Boger fluids.

The values of the FENE dumbbell extensibility parameters ($L = 30$, or $L = 50$) used in the comparisons for the 0.31 wt% and 0.20 wt% PIB Boger fluids respectively, were selected to provide the most reasonable description of the experimental stability data over the range of parameter space represented in figure 4.25. Such values agree well with estimates that can be deduced from recent uniaxial elongation studies with the 0.31 wt% PIB Boger fluid performed by Tirtaatmadja and Sridhar (1993). However, these values are *inconsistent* with the much smaller values of $L = 15$ or $L = 20$ independently obtained from regression to the steady shear flow rheological data. The most plausible explanation for this discrepancy lies in the poor approximation of the single mode constitutive models to the linear viscoelastic spectrum of the test fluids. Previous rheological studies of the viscometric properties of these Boger fluids clearly indicate a spectrum of relaxation times (Quinzani *et al.* 1990). Even in experiments with monodisperse polymer solutions, a large number of relaxation modes are available for microscopic deformation of the polymer chains and different macroscopic viscometric tests probe differently weighted averages of this relaxation spectrum (Larson *et al.* 1994). It should not be expected that a simple single-mode FENE dumbbell model can capture such phenomena even qualitatively. A detailed stability analysis with a multi-mode constitutive model might improve the quantitative comparison between theory and experiments; particularly since earlier rheological studies indicate different nonlinear coefficients (*e.g.* FENE extensibilities) are associated with different deformation modes (Quinzani *et al.* 1990).

This possibility has recently been investigated by considering the stability of torsional motion between a cone and a plate with four-mode formulations of the Oldroyd-B and Giesekus models. The results of this comparison are described by Öztekin *et al.* (1994) and show excellent agreement between analysis and experiment. They first showed that a single-mode Giesekus model provided qualitative agreement with the experiments that was comparable to the Chilcott-Rallison model. Figure 4.26 compares the critical value of the geometric parameter $R^* = 1/\theta_{0\mathrm{crit}}$ as a function of the Deborah number from the calculations with a value of $\alpha = 9\times10^{-4}$ (solid curve) with the expermental measurements for the 0.31 wt% PIB fluid (dashed curve). The linear stability analysis predicts both a critical Deborah number below which the flow is stable for all cone angles, and a range of cone angles for which the flow is unstable for $De > De_{\mathrm{crit}}$. However, the agreement with the experimental results is only qualitative; furthermore, the analysis predicted that axisymmetric disturbances ($m = 0$) were the most dangerous, whereas nonaxisymmetric disturbances ($m \neq 0$) were observed experimentally.

As with the analysis for the single-mode Chilcott-Rallison model, the critical Deborah number was underpredicted by the single-mode Giesekus model. This is a result of the fact that the models overpredict the value of the first normal stress coefficient at moderate rotation rates for the values of the nonlinear parameters (α or L) chosen. As shown by Quinzani *et al.* (1990), a four-mode Giesekus model can quantitatively describe the complex shear-thinning of the first normal stress coefficient, and the second mode of the model determines the plateau behavior at intermediate shear rates (*cf.* figures 3.3-5). However, it was shown that whereas neither the viscometric data of Quinzani *et al.* nor the transient elongational viscosity measurements of Tirtaatmadja and Sridhar (1993) were known with sufficient accuracy to distinguish between values of $\alpha_2 = 10^{-4}$ (as given by Quinzani *et al.*) and $\alpha_2 = 1.5\times10^{-4}$, the linear stability analysis was very sensitive to the value of α_2. Calculations with four-mode Oldroyd-B and Giesekus models both showed results similar to the single-mode Oldroyd-B and Chilcott-Rallison models for both the wavenumber α_ξ and the wavespeed c_ξ (see figure 4.23). However, the neutral stability diagram showed a strong dependence on α_2, and figure 4.27 shows that $\alpha_2 = 1.5\times10^{-4}$ provides excellent quantitative agreement with the experimental results.

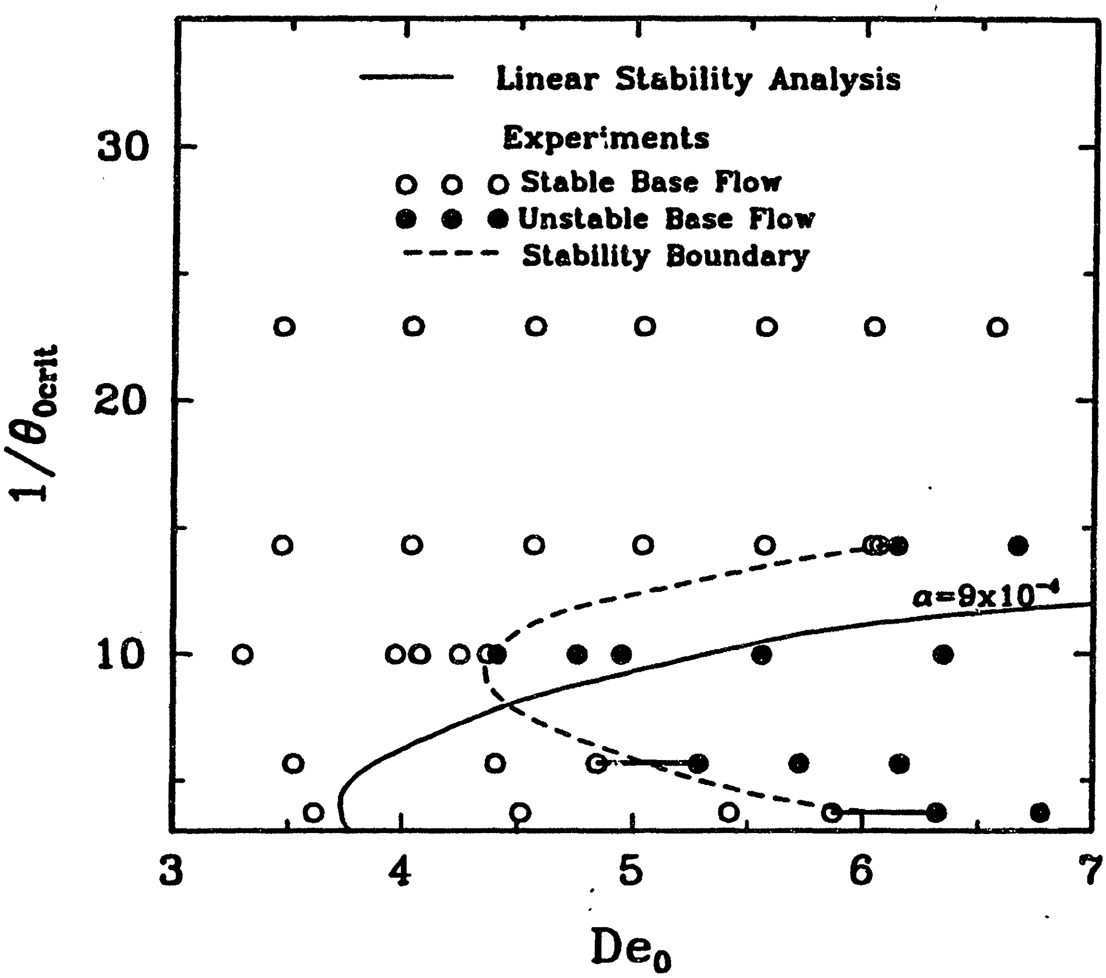

Figure 4.26 Comparison of experimentally-determined and numerically-calculated neutral stability curves for the onset of spiral instabilities between a cone and a plate for the 0.31 wt% Boger fluid. Symbols indicate experimental measurements of steady (○) or unsteady (●) base flow, the experimentally-determined stability curve (– – –) and the predictions of the single-mode Giesekus model with $\alpha = 9\times10^{-4}$ (——). Error bars on the experiments are shown as a heavy curve (from Öztekin *et al.* 1994).

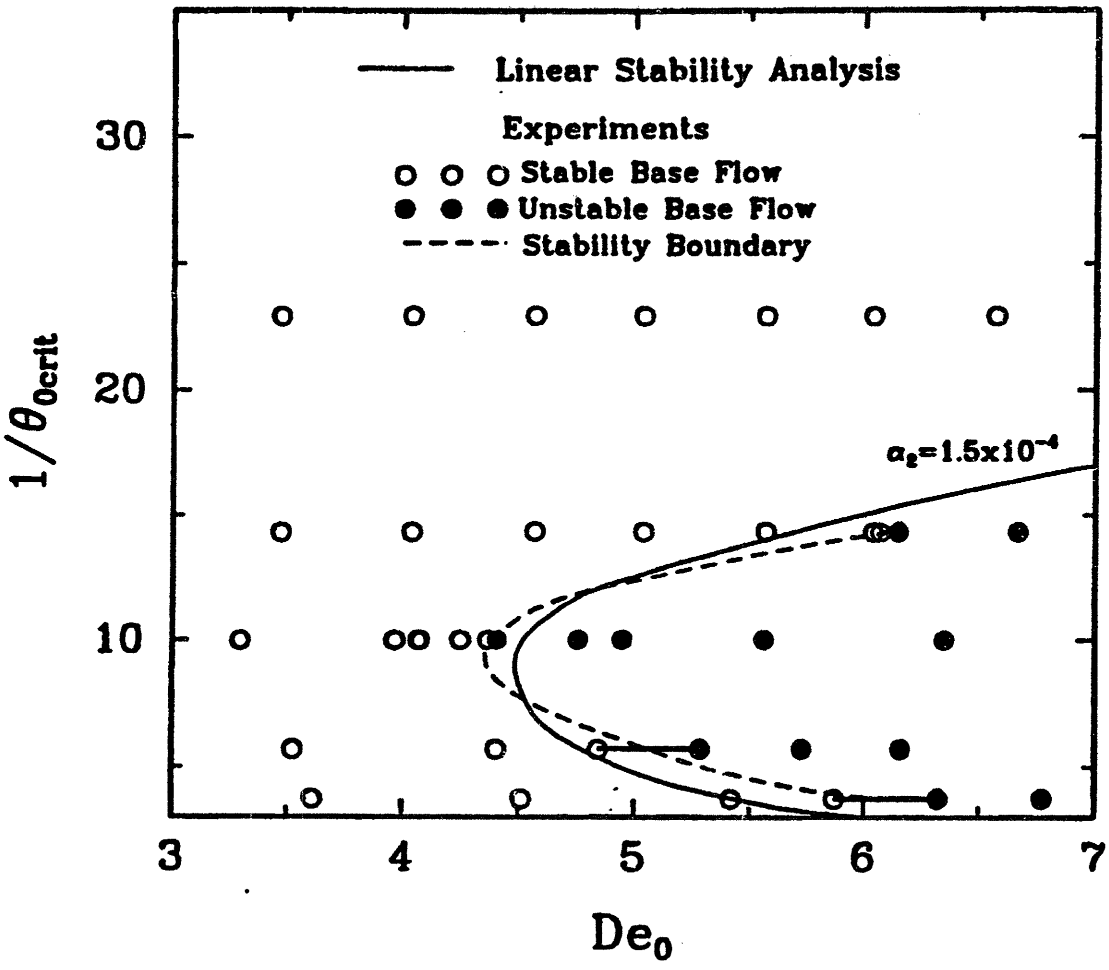

Figure 4.27 Comparison of experimentally-determined and numerically-calculated neutral stability curves for the onset of spiral instabilities. Symbols indicate experimental measurements of steady (○) or unsteady (●) base flow, the experimentally-determined stability curve (– – –) and the predictions of the four-mode Giesekus model with $\alpha_2 = 1.5\times10^{-4}$ (——). Error bars on the experiments are shown as a heavy curve (from Öztekin *et al.* 1994).

Connections between Parallel-Plate and Cone-and-Plate Instabilities

Although the spatial structures of the elastic instabilities presented for the viscoelastic flow between a cone and a plate are very different from those for the flow between coaxial parallel rotating disks, the numerous similarities between the base torsional motion in two geometries and the form of the disturbance equations (after coordinate transformation in the cone-and-plate or radial localization in the parallel-plate configuration) suggest that these two spiral instabilities should be closely related. In the limit $\theta_0 \to 0°$, the radial variation in the local gap between the cone and the plate $h(\hat{r}) = \hat{r}\theta_0$ is very weak. If localized displacements $\delta\hat{r}$ about an arbitrary radial position such as R_0 are considered, the logarithmic radial coordinate transformation (equation 3.28) can be linearized as $\xi = \ln(1 + \delta\hat{r} / R_0) \approx \delta\hat{r} / R_0$. Substituting this linearized transform coordinate into the disturbance kinematics described by equation 3.29, and defining the local gap between the two fixtures as $R_0\theta_0 \equiv H$, leads to

$$exp\left[i\alpha_\xi\xi + im\phi + \sigma t\right] \approx exp\left[i(\alpha_\xi\theta_0)(\delta\hat{r}/H) + im\phi + \sigma t\right] \tag{4.1}$$

By identifying the modified spatial wavenumber appearing in equation 4.1 as $\alpha_\xi\theta_0 \equiv \alpha_{PP}$, it becomes clear that this normal mode decomposition is equivalent to the form of the Archimedean spiral disturbances considered above. In the limit of small cone angles (*i.e.* $R^* \equiv 1/\theta_0 \to \infty$) we expect the dimensionless product $\alpha_\xi\theta_0$ constructed from the spatial wavenumber of the cone-and-plate disturbance to approach the dimensionless radial wavenumber α_{PP} of the parallel-plate disturbance that can obtained in the limit $R^* \equiv R/H \to \infty$ by linearizing the radial variations in the corresponding disturbance equations (Öztekin and Brown 1993). To verify this interconnection between the two elastic instabilities, figure 4.28*(a)* shows the appropriate critical wavenumbers for the onset of axisymmetric instabilities in each geometry as a function of Deborah number for the Oldroyd-B model with $\beta = 0.59$. For this quasi-linear model the critical value of the geometric parameter R^* in each geometry becomes infinite in the limit as $De_0 \to 0$. The calculations clearly show that although the dimensionless wavenumber α_ξ of the cone-and-plate disturbance becomes very large for small cone-angles (*cf.* figure 4.23) the product $\alpha_\xi\theta_0$ approaches the same asymptotic value (≈ 3.1) as the wavenumber α_{PP} calculated for the parallel-plate disturbance in the limit $De_0 \to 0$. A similar comparison could be drawn from the predictions of the Chilcott-Rallison model; however, for each geometric

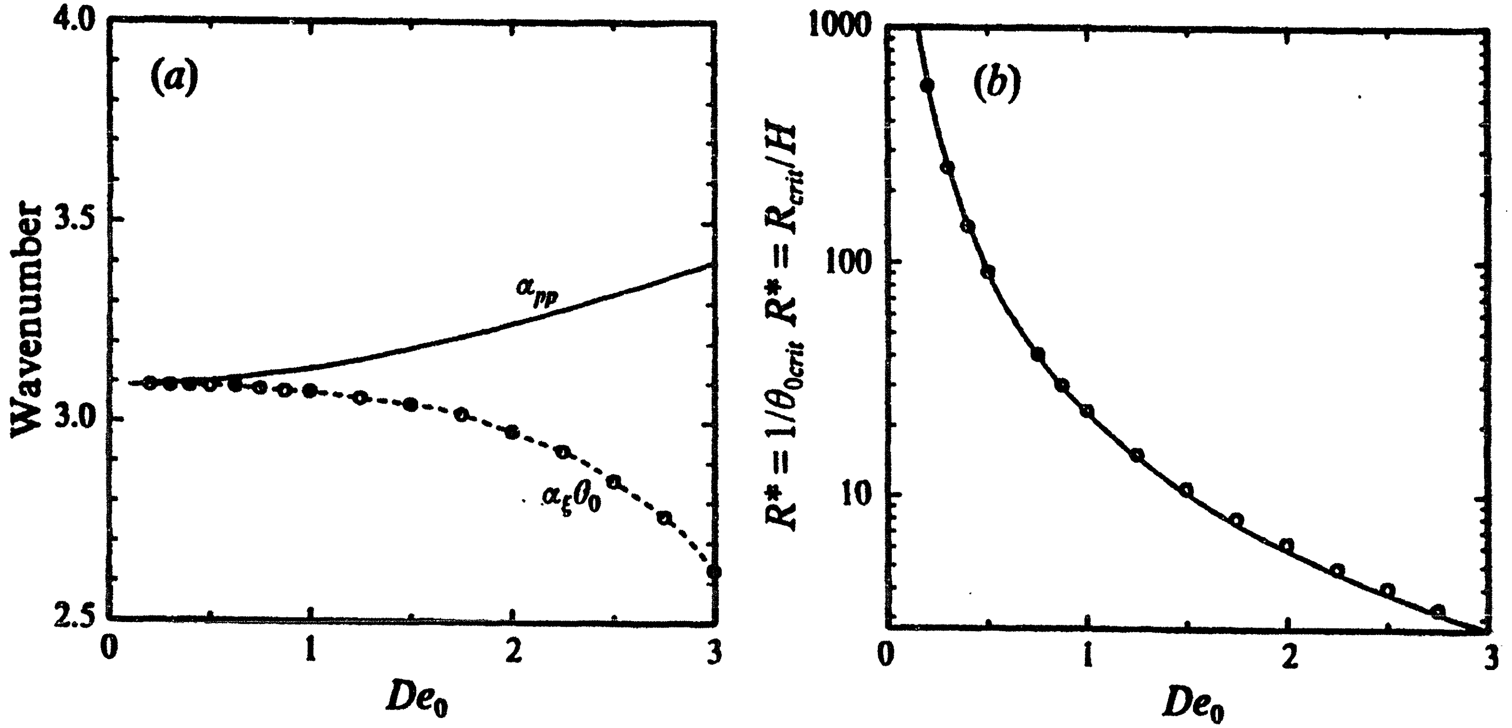

Figure 4.28 Connection between elastic instabilities in torsional motion between parallel rotating disks (Öztekin and Brown 1993) and between a cone and a plate: *(a)* The critical wavenumber (α_{pp}) of axisymmetric disturbances in the parallel plate (——), and the critical modified wavenumber $\alpha_\xi\theta_0$ in the cone and plate (- - -). *(b)* The critical geometric parameter R^*_{crit} for onset of axisymmetric disturbances in each geometry; (——) parallel plate, (O) cone-and-plate. All calculations are for the Oldroyd-B model with $\beta = 0.59$.

configuration the curves would terminate at a non-zero value of the Deborah number, corresponding to the appropriate value of $De_{0\mathrm{crit}}$ below which all disturbances of spiral form are restabilized by shear-thinning in the viscoelastic hoop stress.

Another connection between the linear stability predictions for the onset of elastic spiral instabilities in parallel-plate and cone-and-plate motions may be made by comparing the stability diagrams for the two geometries. The critical onset conditions for the axisymmetric disturbance modes for each geometry are plotted in figure 4.28*(b)* in terms of the appropriate critical geometric parameter, *i.e.* the critical radial location $R^* = \hat{r}_{\mathrm{crit}}/H$ in the parallel-plate geometry and the critical cone angle $R^* = 1/\theta_{0\mathrm{crit}}$ for the cone-and-plate geometry. Given the results in figure 4.28*(a)*, it is not surprising that the predictions of R^* for both geometries are similar to one part in 1000 as $De_0 \to 0$. However, it is very interesting that the values of R^* remain very close for Deborah numbers as large as $De_0 = 3$. These results serve to justify two critical approximations made in the cone-and-plate and parallel-plate analyses. One is the approximation applied to find the solution of viscometric base flow between a cone and a plate. The results shown here indicate that the onset of instability is not particularly sensitive to the approximate form of the solution for the purely azimuthal base flow. At $De_0 = 3$ the critical cone angle becomes as large as $15° - 20°$; however, the corresponding value of $R^* \equiv 1/\theta_0 \approx 3$ remains close to the value of $R^* \equiv \hat{r}_{\mathrm{crit}}/H$ for flow between parallel plates, in which the kinematics of the inertialess base flow are exact. Secondly, figure 4.28*(b)* shows that the critical conditions for onset of spiral instabilities in the parallel-plate configuration are insensitive to the approximation of localizing the disturbances. As described above, disturbances in the cone-and-plate geometry are not localized to any particular region, in contrast with the analysis for flow between parallel plates. The very close agreement in the values of the critical geometric parameters R^* for the onset of both instabilities over a wide range of Deborah numbers serves to justify the localized disturbance assumption first applied by Öztekin and Brown (1993).

Chapter 5

Stagnation Flow Instabilities

5.1 Flow Past a Cylinder Confined in a Channel

LDV measurements are used to characterize the viscoelastic wake instability for a wide range of cylinder radius to channel height ratios. Details of the onset conditions are first presented, then further information about the spatial structure of the instability is shown, and finally the effects of changing the upstream flow conditions are examined.

5.1.1 Onset of Three-dimensional Flow

The video-imaging experiments of McKinley *et al.* (1993) clearly demonstrate that the instability has the form of a cellular structure in the wake of the cylinder. Illumination of the centerplane of the flow cell shows periodically spaced bright bands that correspond to regions of higher streamwise velocity. Quantitative measures of the instability can be obtained by LDV scans along the axis of the cylinder, as shown in figure 5.1 for $R/H = 0.63$. Scans are shown of the streamwise velocity along the centerplane of the flow cell one-half cylinder radius downstream of the stagnation point, *i.e.* $\{x, 0, 1.5R\}$. Before the onset of the instability, the streamwise velocity, v_z, is uniform along the length of the cylinder and the flow is two-dimensional, whereas beyond the critical conditions it becomes periodic along the length of the cylinder. Careful measurements near the critical conditions show that for increments of $\Delta De = 0.01$ there is no hysteresis in the flow, and that this is a supercritical instability. These fluctuations in the streamwise velocity persist downstream for a distance of about four cylinder radii, beyond which the flow is again two-dimensional, as shown in figure 5.2.

Although the instability persists only four radii downstream, full-field birefringence measurements show that molecules are highly oriented by the stagnation flow and remain oriented over fifteen radii downstream of the cylinder. Figure 5.3 shows a series of images of the birefringence in the wake of the cylinder for $R/H = 0.5$ for increasing De. Polarizers with their axes of polarization crossed at 90° to one another are placed at each end of the flow cell, and the images view the length of the flow cell in the direction of the cylinder axis. In the absence of flow, no light should pass through the second polarizer. However,

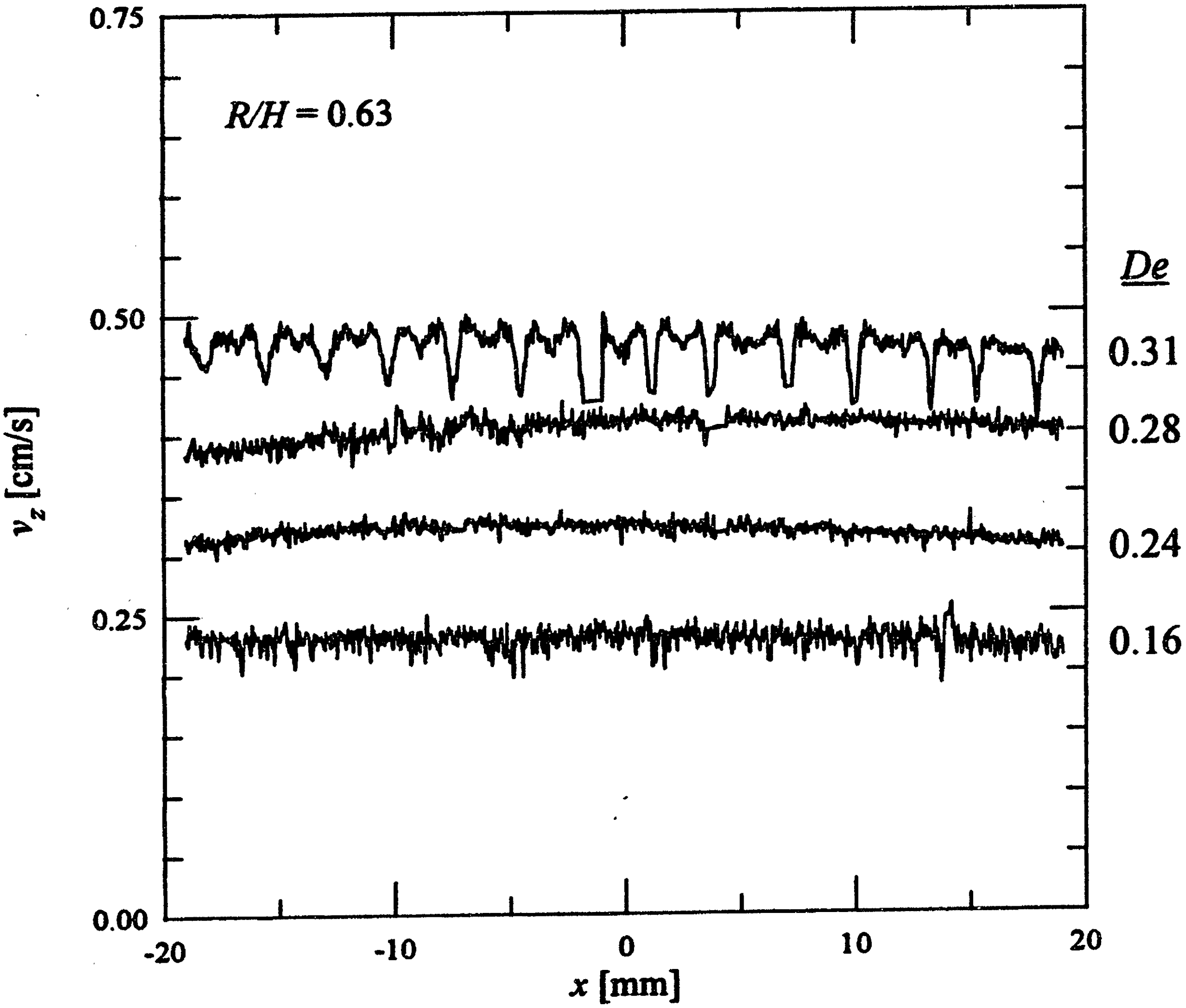

Figure 5.1 Axial profiles of the streamwise velocity v_z for $R/H = 0.63$ across the channel at $(y/R, z/R) = (0, 1.5)$ as the Deborah number is increased from $De = 0.16$ to $De = 0.31$.

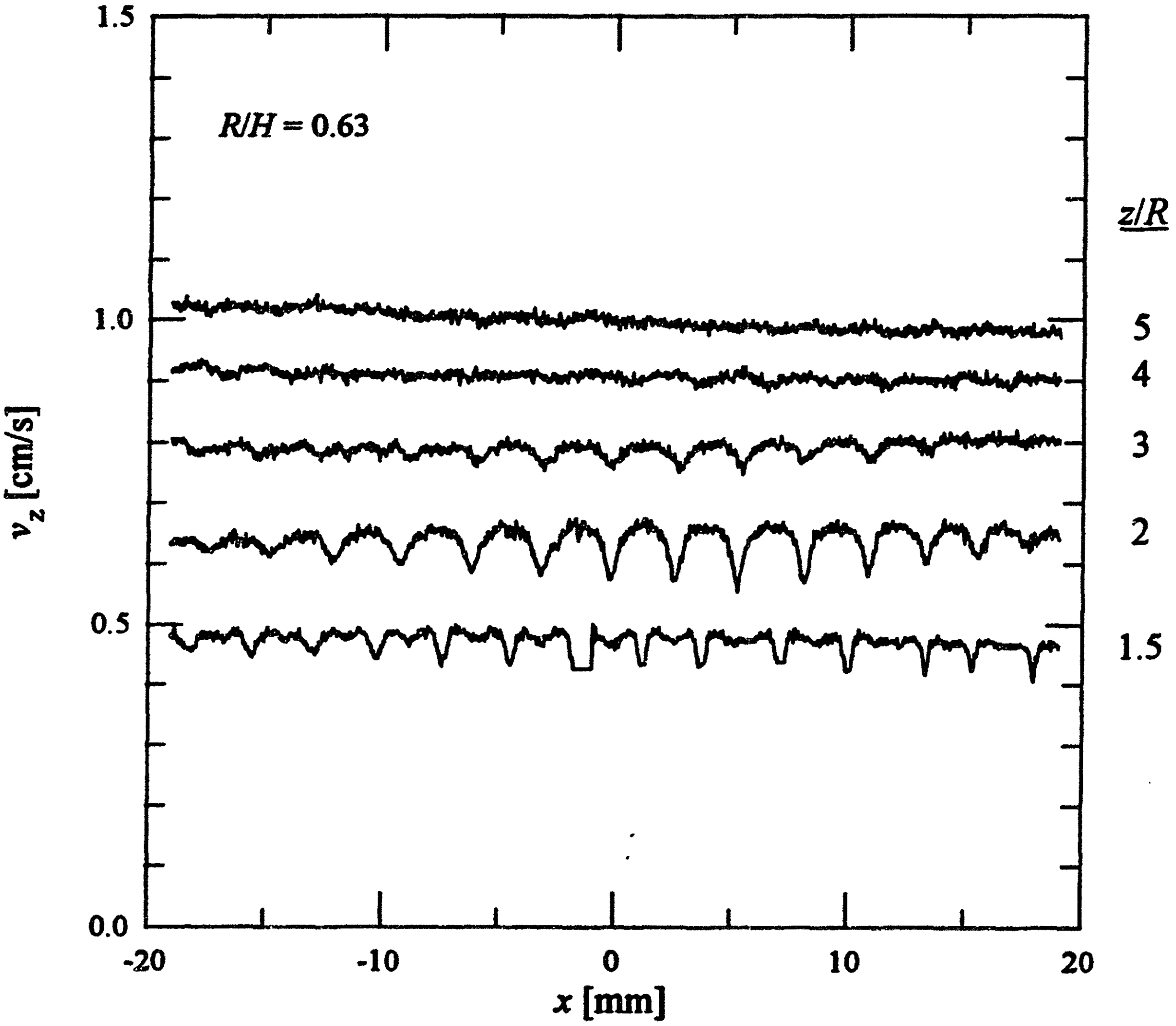

Figure 5.2 Axial profiles of the streamwise velocity for $R/H = 0.63$ and $De = 0.31$ at $y/R = 0$ and increasing z/R.

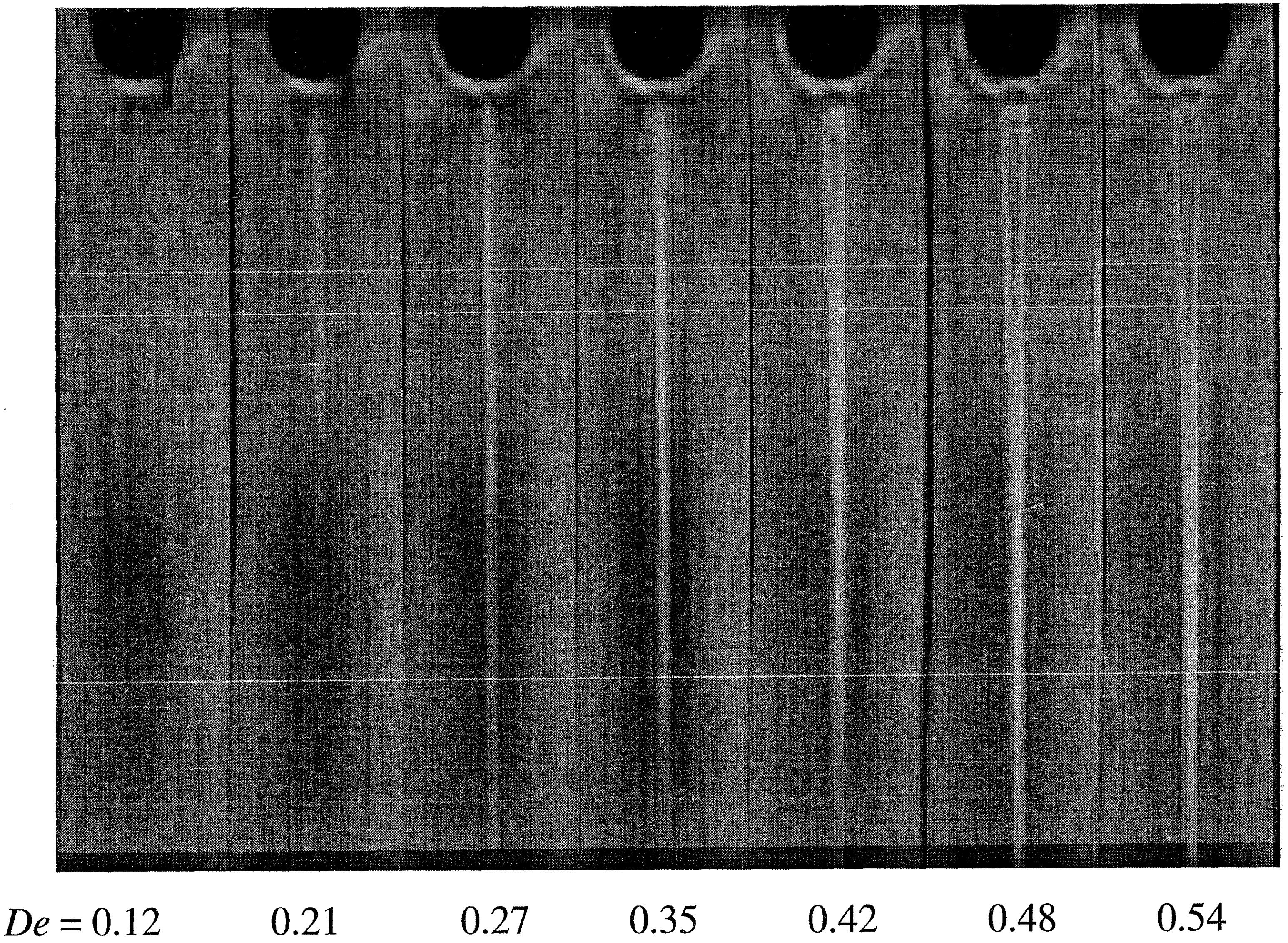

Figure 5.3 Birefringent strand in the wake of the cylinder for $R/H = 0.50$ and $0.12 \leq De \leq 0.54$. Flow is from top to bottom.

as De is increased, the flow aligns polymer molecules in the stagnation region, which rotate the polarization of the light, resulting in the bright region (the 'birefringent strand') along the centerplane for $De \geq 0.21$. For this aspect ratio $De_{\text{crit}} = 0.31$, indicating that the presence of a birefringent strand region cannot be used as a criterion for flow stability, although it does serve as an indicator of the extent of the extension-dominated region of the flow. The birefringent strand extends over 15 radii downstream for $De \geq 0.35$, whereas the instability is only observed within four radii of the downstream stagnation point.

The birefringent strand grows in thickness, downstream extent and brightness as the Deborah number is increased. The birefringence observed in these images is the integrated effect along the entire width of the flow cell (76 mm), and attempts at observing the cellular structure of the instability normal to the cylinder axis by full-field birefringence were unsuccessful due to the narrow birefringent region (~2 mm). Furthermore, flow induced birefringence measurements were made impractical by difficulties with measuring the birefringence of three-component Boger fluids and the high residual stresses of the plexiglass flow cell walls. Because flow induced birefringence measurements depend on the flow field along the entire beam path, they could only be used for the two-dimensional flow before the onset of the instability, and would not provide any further information about the structure of the instability.

The critical conditions expressed as both De_{crit} and We_{crit} for $0.05 \leq R/H \leq 0.84$ are shown in figure 5.4, along with the data from McKinley *et al.* Both fluids show the same onset conditions, but neither De_{crit} nor We_{crit} approaches an asymptotic limit for the aspect ratios for which they would be expected to predominate. For small R/H, the cylinder is well removed from the effects of the channel walls, and the cylinder radius becomes the relevant length scale. However, De_{crit}, which is based on R, does not approach a constant value for small R/H, but instead increases as $(R/H)^{-0.4}$ for small R/H. The scaling for De_{crit} assumes that $\langle v_z \rangle / R$ is a characteristic strain rate downstream of the cylinder. However, finite element simulations of Newtonian flow past a cylinder in a channel (Liu 1995) show that the streamwise velocity is shifted further downstream for smaller values of R/H, such that the velocity recovers to its freestream value over a distance much larger than R for small R/H. An alternative definition of the Deborah number is $De^* = \lambda \dot{\varepsilon}_{\max}$, where $\dot{\varepsilon}_{\max}$ is the maximum strain rate, which occurs at $z/R \sim 1.7$ for a Newtonian fluid. However, $\dot{\varepsilon}_{\max}$ increases linearly with increasing R/H, so rescaling De based on $\dot{\varepsilon}_{\max}$ also fails to provide an asymptotic limit at small R/H since De^* *decreases* for decreasing R/H. The shearing flow in the gap between the cylinder and the channel wall becomes important for large R/H, but We_{crit} continues to increase for large R/H. Purely elastic instabilities have been observed in other flows with shearing along curved streamlines (Larson *et al.* 1990;

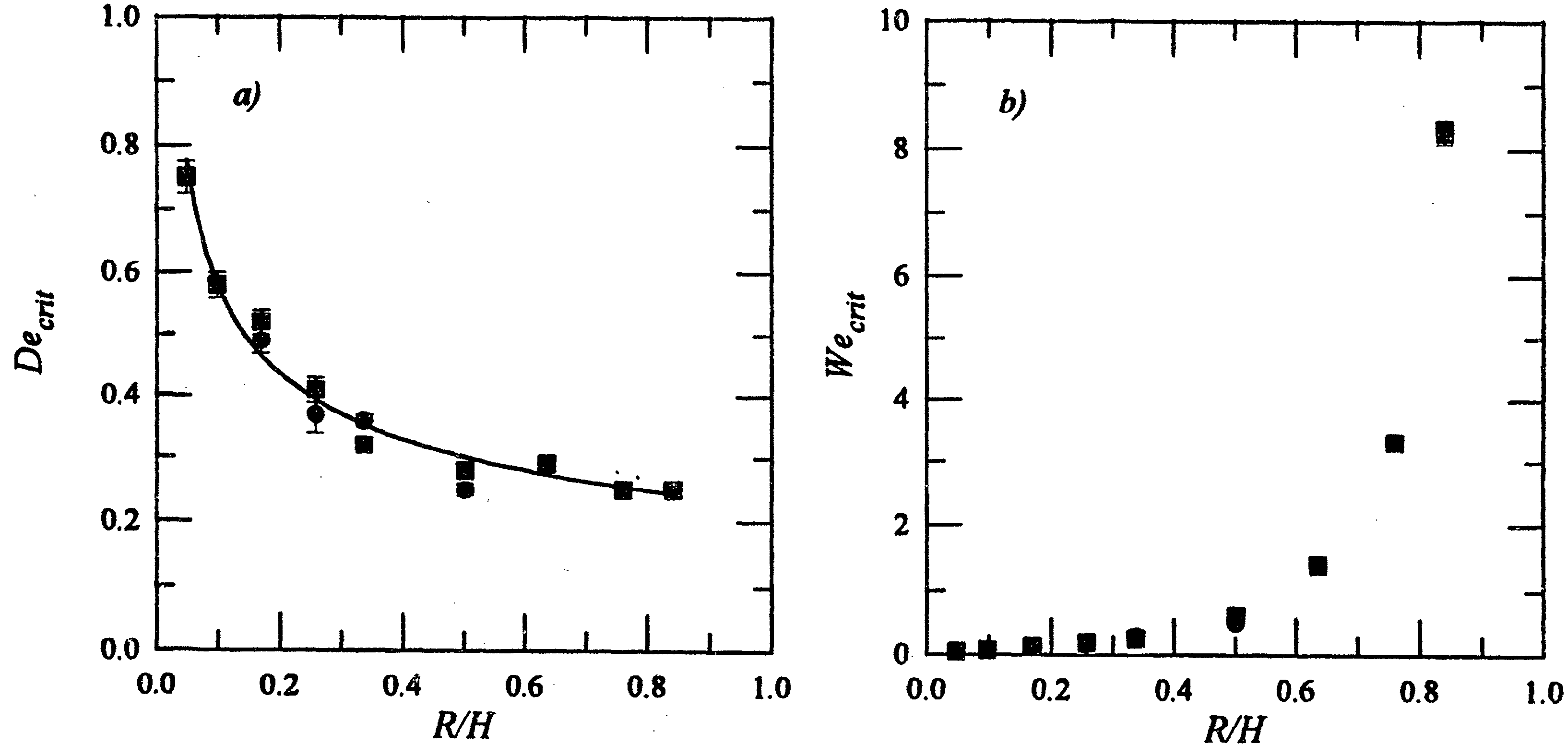

Figure 5.4 Critical conditions in terms of *(a)* the Deborah number and *(b)* the Weissenberg number for the onset of three-dimensional flow as a functions of aspect ratio *R/H*.

Joo and Shaqfeh 1992; Byars *et al.* 1994; McKinley *et al.* 1995), but for this flow We_{crit} increases dramatically as R/H increases. Although neither De_{crit} nor We_{crit} as scaled here shows an asymptotic limit, it should be noted that De_{crit} varies by only a factor of three over the entire range of aspect ratios investigated, while We_{crit} varies by more than a factor of 200, indicating that the instability scales primarily with the extensional flow in the wake of the cylinder.

It should also be noted that although the composition is identical, the fluid used for the current experiments is not the same fluid as used by McKinley *et al.* Rheological measurements conducted after the completion of their experiments showed that the first normal stress coefficient had decreased by a factor of five from the original value at all shear rates, whereas no detectable change was observed for the viscosity. Another batch of the same test fluid was prepared, and its rheological properties closely matched that given by McKinley *et al.* However, following a small number of passes through the flow system, the first normal stress coefficient of this fluid also decreased, presumably due to mechanical degradation. Careful monitoring of the fluid's rheology over the course of the experiments showed that no further decrease occurred. It is this lower value that is used throughout, and all comparisons to McKinley *et al.* are based on the final rheological properties of their fluid.

5.1.2 Spatial Structure of the Three-dimensional Flow

The periodic fluctuations of the streamwise velocity can be quantified by Fourier analysis to yield a spatial wavelength, λ_x of the instability. A fast Fourier transform (FFT) of the velocity profile produces a power spectrum as function of the spatial frequency, f_x (mm^{-1}), which can be inverted to give the power spectrum in terms of the spatial wavelength. Figure 5.5 shows a sample velocity profile for $R/H = 0.34$ and its power spectrum, which shows that the wavelength of the disturbance is 1.85 ± 0.09 mm. The wavelengths for all aspect ratios made dimensionless with both the cylinder radius and the gap width are shown in figure 5.6, along with the results from McKinley *et al.* The wavelengths reported are for conditions close to De_{crit}, although no variation in the wavelength is observed for higher De.

As is the case for the onset conditions, neither the cylinder radius nor the gap width seems to provide a satisfactory scaling. At intermediate values of the aspect ratio, the wavelength nearly equals the cylinder radius, but for the smallest values, where the cylinder radius is expected to be the only relevant physical dimension, the wavelength increases to twice the cylinder radius. Equally striking is the fact that the current measures

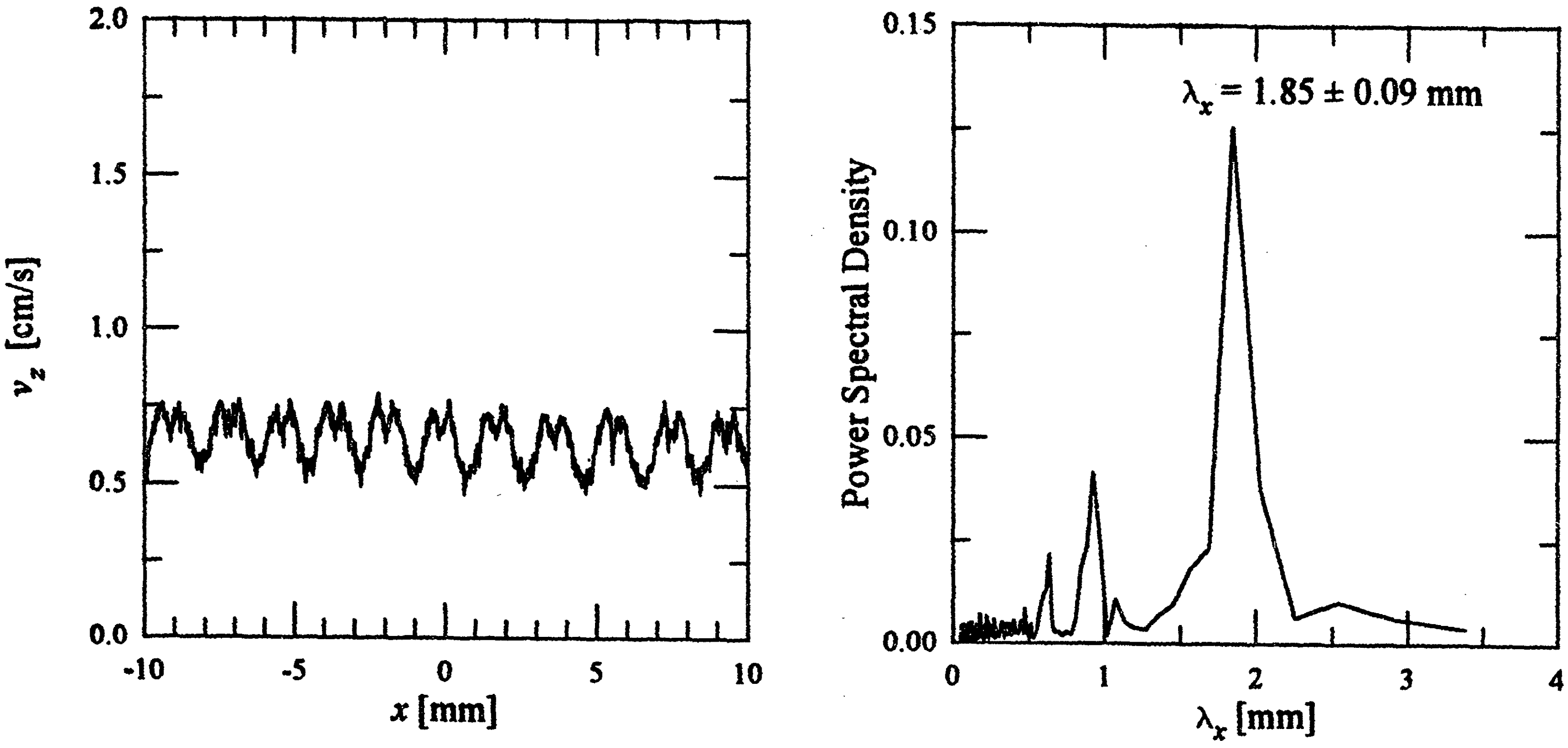

Figure 5.5 *(a)* Axial profile of the streamwise velocity for $R/H = 0.34$ at $z/R = 1.5$ and $De = 0.45$. *(b)* The FFT spectrum shows that the wavelength of the disturbance is $\lambda_x = 1.85 \pm 0.09$ mm.

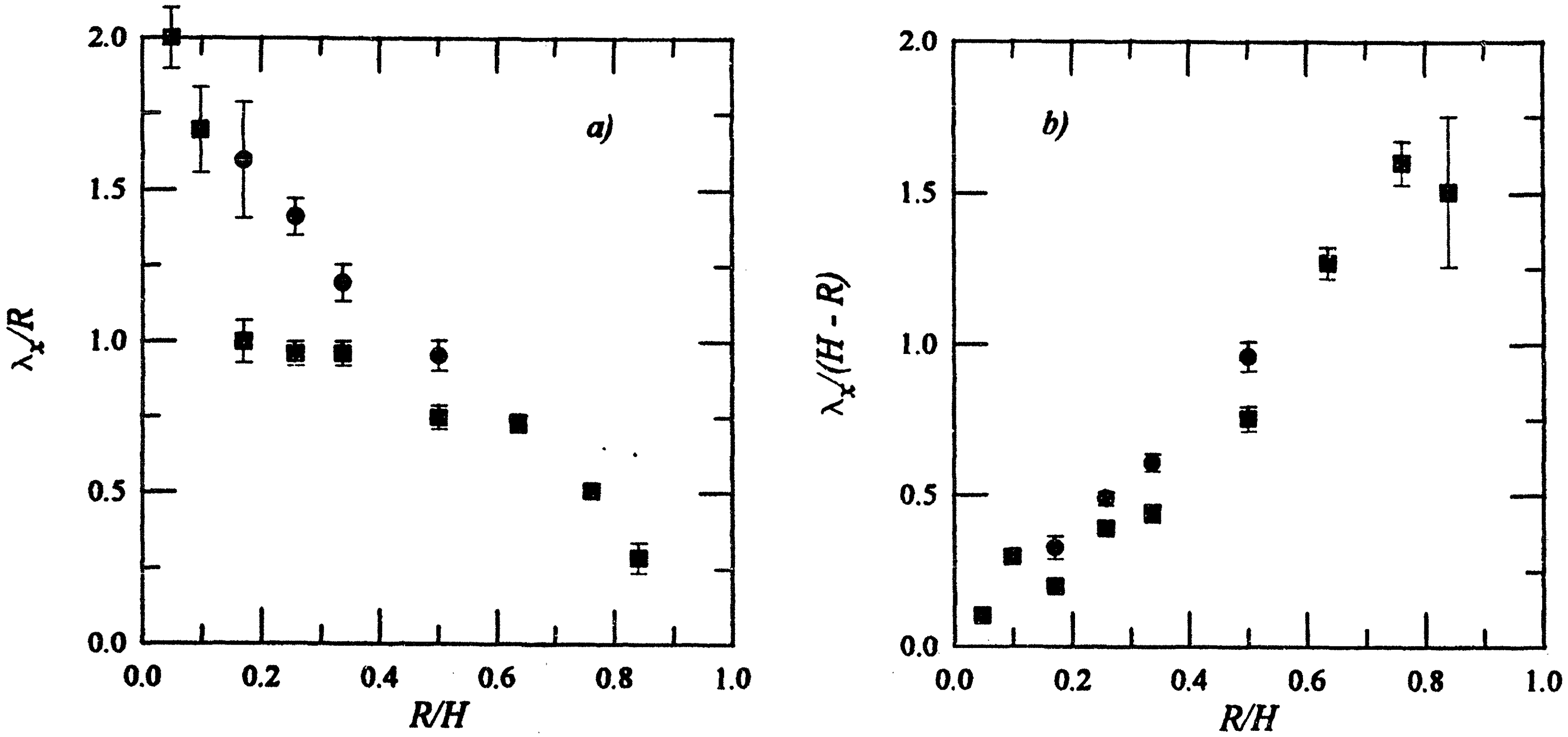

Figure 5.6 Wavelength of the fluctuations of the streamwise velocity, λ_x, scaled with *(a)* the cylinder radius, R and *(b)* the gap between the channel wall and the cylinder, H - R. Results are shown for (■) the current work and (●) from McKinley *et al.*

of the wavelength markedly differ from the previous measurements of McKinley *et al.* Instead of approaching a value of $\lambda_x/R = 1$, McKinley's values increase as the cylinder radius is decreased. Other than the slight differences in rheological properties mentioned above, the experimental system used for this work is identical to that of McKinley *et al.*, and the values of λ_x/R for the smallest aspect ratios and the two different values observed at intermediate aspect ratios suggest a weak wavelength selection mechanism for this instability. Linear stability analyses of other viscoelastic instabilities (Larson *et al.*; Joo and Shaqfeh 1992; Öztekin and Brown) have produced shallow neutral stability curves for the critical wavelength, and experimental measures have confirmed that multiple wavelengths are present above the critical conditions (Larson *et al.*; Joo and Shaqfeh 1994; Byars *et al.* 1994; McKinley *et al.* 1995). However, it should be noted that the discrepancy here is between sets of experiments with different fluids, and that for a given fluid only a single wavelength is observed up to $De \approx 2De_{\text{crit}}$.

In order to investigate the strength of the wavelength selection, a disturbance velocity with a wavelength equal to that observed by McKinley *et al.* is introduced by means of a cylinder with a sinusoidally varying radius. For the case of $R/H = 0.50$, McKinley reported a wavelength of $\lambda_x = 3.03 \pm 0.15$ mm, while for the same aspect ratio in the current work, $\lambda_x = 2.38 \pm 0.08$ mm. The maximum radius of the cylinder is 3.175 mm ($R_{\text{max}}/H = 0.50$), the minimum radius is $0.9R_{\text{max}}$, and the wavelength of the variations of the radius is 3.175 mm, as shown schematically in figure 5.7(*a*). Figures 5.7(*b-c*) show that below De_{crit} fluctuations in the streamwise velocity are introduced with the wavelength of the variation of the cylinder radius. However, beyond De_{crit}, the predominant wavelength is nearly equal to that measured for the circular cylinder, as shown in figure 5.8, indicating a strong preference for the selected wavelength.

In addition to its wavelength, the instability can be characterized in terms of its spatial extent. McKinley *et al.* showed that the instability extends along the centerplane of the geometry about four cylinder radii downstream of the rear stagnation point, and that it also can be observed slightly away from the centerplane. Measurements close to the cylinder show that the instability also exists along the cylinder *upstream* of the stagnation point. Figure 5.9(*a*) shows axial scans at a constant radius of $1.25R$ and different azimuthal positions for $R/H = 0.50$, where $\theta = 0°$ is along the z-axis. The angular extent of the instability increases linearly as the Deborah number is increased above De_{crit}. For the case shown in figure 5.9, $De - De_{\text{crit}} = 0.27$, and the instability extends 45° upstream of the stagnation point, while for higher $De - De_{\text{crit}}$ the instability has been observed as far as 60° upstream.

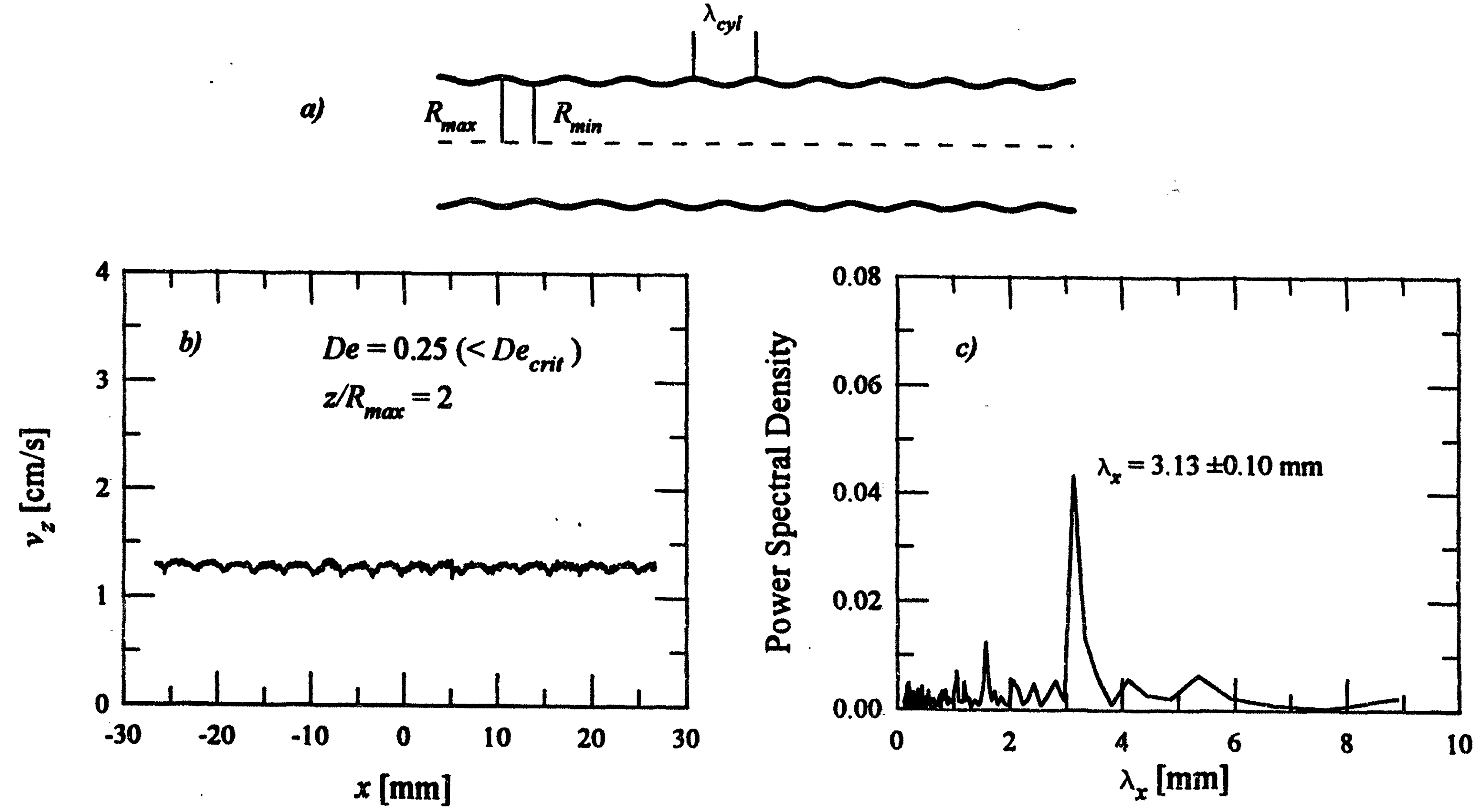

Figure 5.7 *(a)* Cylinder with sinusoidally-varying radius: $R_{max} = 3.18$ mm, $R_{min} = 2.86$ mm and $\lambda_{cyl} = 3.18$ mm. Below the critical Deborah number, *(b)* a disturbance velocity is introduced with *c)* $\lambda_x \approx \lambda_{cyl}$.

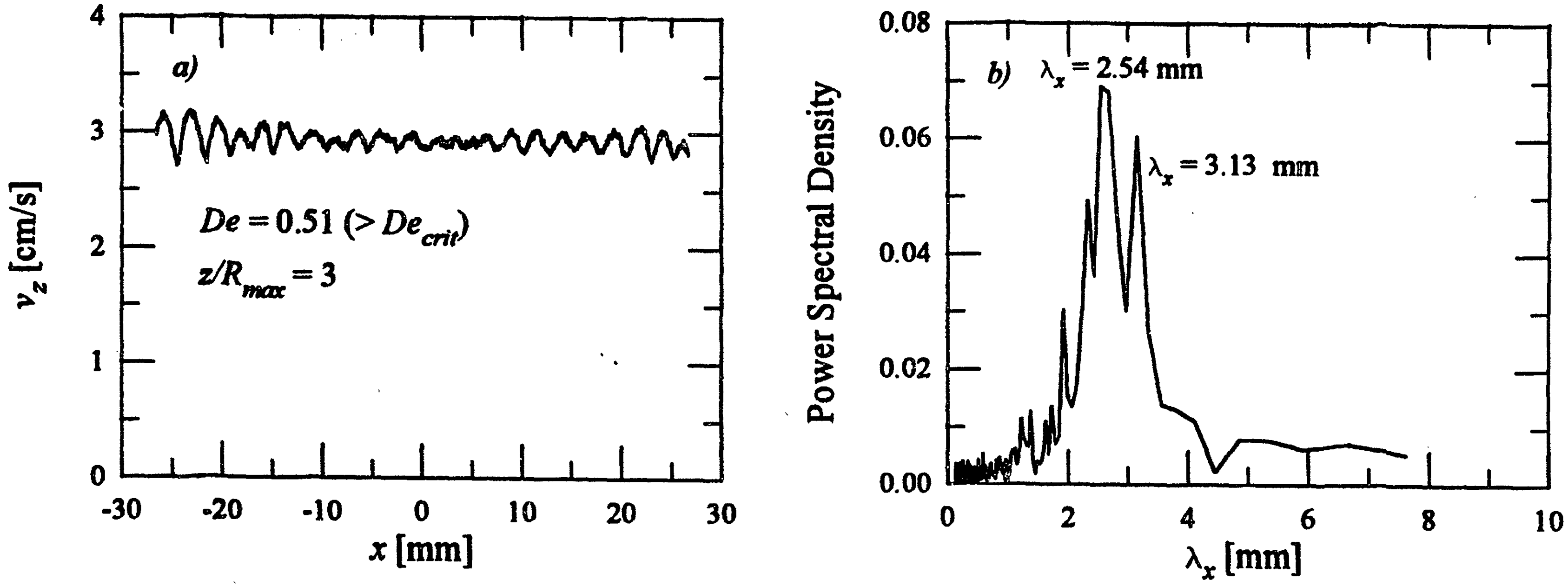

Figure 5.8 *(a)* Axial profile of the streamwise velocity for the cylinder with sinusoidally-varying radius above the critical Deborah number. *(b)* In addition to the wavelength introduced by the cylinder ($\lambda_x = 3.13$ mm), an additional wavelength is observed at $\lambda_x = 2.54$ mm.

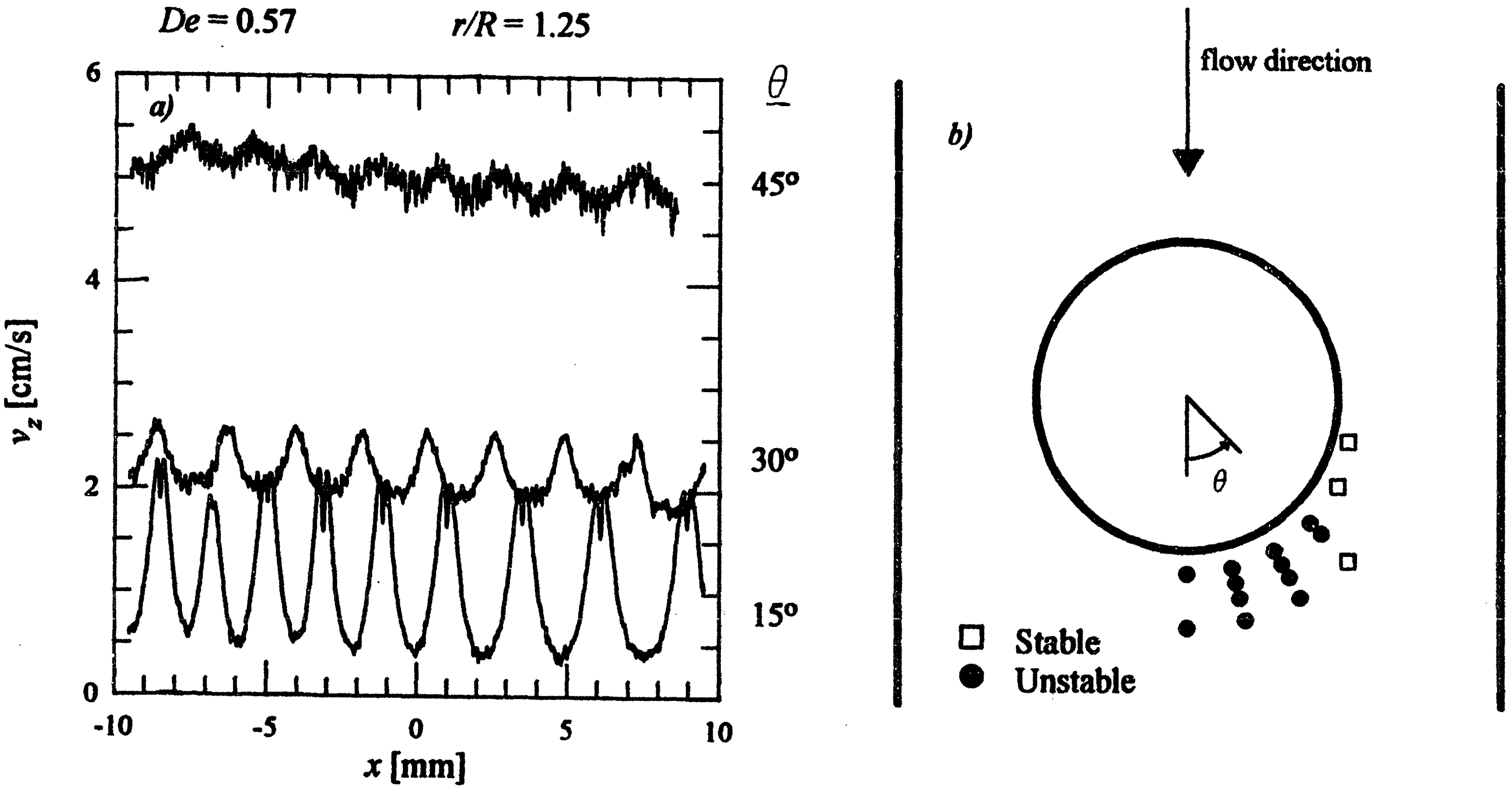

Figure 5.9 *(a)* Axial profiles of the streamwise velocity for $R/H = 0.50$ at azimuthal positions θ for $r/R = 1.25$. *(b)* Azimuthal extent of the instability for $R/H = 0.50$ and $De - De_{crit} = 0.27$. Results are shown for $r/R = 1.15, 1.25, 1.35$ and 1.50.

The angular extent of the instability can be understood in the framework of an extensionally-driven instability by considering velocity scans in the y-direction passing below the cylinder. Such scans are shown in figure 5.10 for $R/H = 0.34$ at positions of $z/R = 1.2$, 1.4, 1.6, 1.8 and 2.0. Close to the cylinder, the form of the velocity profiles deviates from Newtonian profiles in that the minimum velocity is not on the centerplane, but they are symmetric about the centerplane. However, measurements taken slightly above De_{crit} show that the instability breaks the flow symmetry. Figure 5.11 shows that not only is the local velocity maximum shifted off the centerplane, but also that the local minima now have different values. This asymmetry is related to the axial scans shown above by noting that the asymmetry about the centerplane has the same periodicity along the cylinder axis as the fluctuations in the streamwise velocity. Figure 5.12 shows two y-direction scans taken one-half radius apart along the length of the cylinder. In this distance, which corresponds to $\lambda_x/2$ for this aspect ratio, the asymmetry has reversed itself about the centerplane. A measurement of v_z taken along the length of the cylinder at, for example, $y/R= 0.25$ would therefore pass through a maximum value at $x/R = 0$ and a minimum at $x/R = 0.5$.

The y-dependence of the velocity field shown in figure 5.11 and its axial dependence shown in figure 5.12 also help to clarify the interpretation of axial scans along the centerplane near the cylinder, such as in figure 5.5, where $z/R = 1.5$. In the region where the y-direction profile has two local minima, the FFT of an axial profile near the centerline contains a secondary peak at $\lambda_x/2$ due to the contributions from the cells on both sides of the cylinder. Further downstream, the y-profile has a single minimum, and only a single wavelength at λ_x is observed for the axial scan, where λ_x is the same wavelength that is observed along the cylinder upstream of the stagnation point.

The interaction between the cells from opposite sides of the cylinder can be seen by considering simultaneous measures of the streamwise velocity v_z and the axial velocity v_x, as shown in figure 5.13 for $R/H = 0.34$, $z/R = 1.2$, $y/R = 0.2$ and $De = 0.69$. Each velocity component has a single wavelength, and the phase between the velocity components is such that the oscillations in the axial velocity reinforce the oscillations in the streamwise velocity. In figure 5.13, $v_x = 0$ at positions where $|v_z|$ is at its maximum, and $v_x > 0$ at positions where $dv_z/dx > 0$ and $v_x < 0$ where $dv_z/dx < 0$, thereby adding fluid to regions of higher streamwise velocity and causing the cells to grow. In contrast, McKinley *et al.* showed (see their figure 15) that at $z/R = 1.4$, $y/R = 0$, the wavelength for v_z was one-half that for v_x, and that v_z had a minimum where $|v_x|$ reached a maximum, so that fluid was removed from alternate cells and added to the neighboring cells, such that at $z/R = 2$, v_z displayed a single wavelength of λ_x (see figure 16 of McKinley *et al.*).

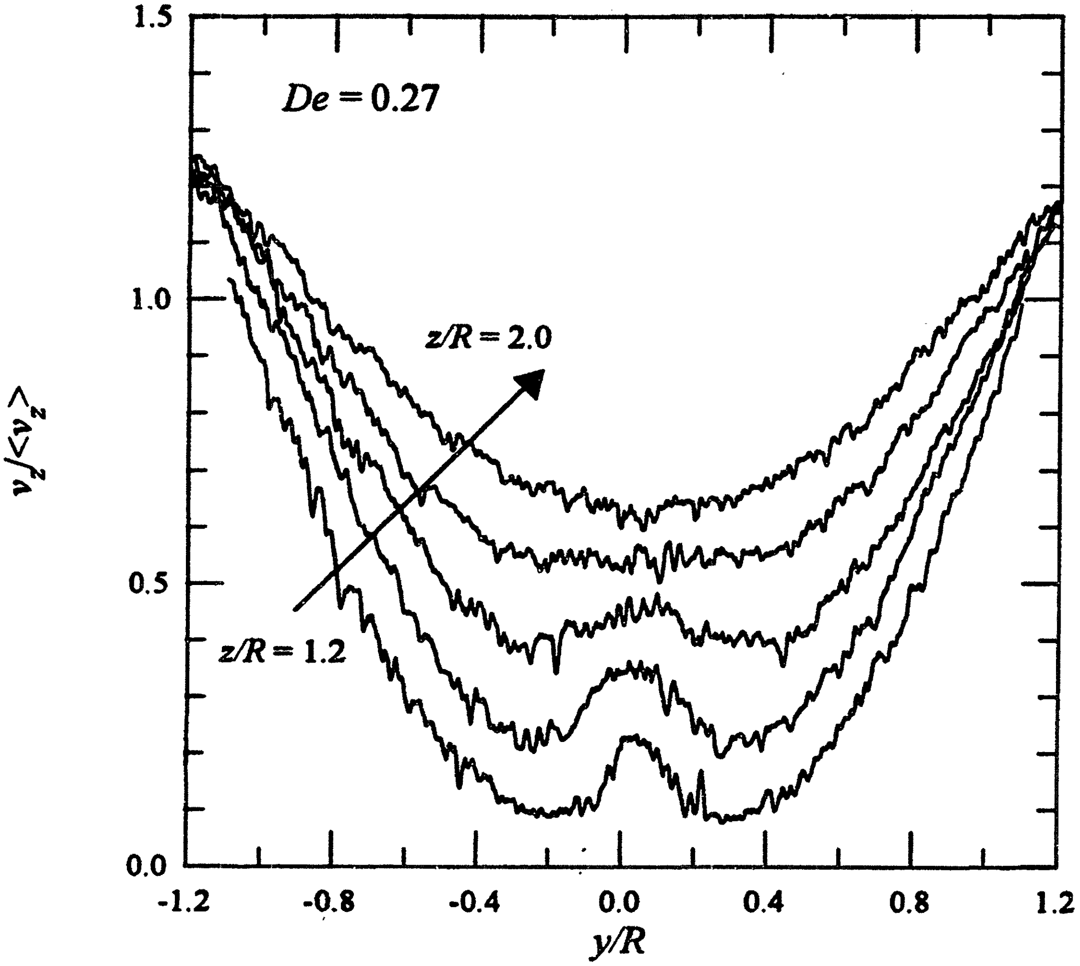

Figure 5.10 Transverse profiles of the streamwise velocity below the critical Deborah number for *R/H* = 0.34 at positions of *z/R* = 1.2, 1.4, 1.6, 1.8 and 2.0.

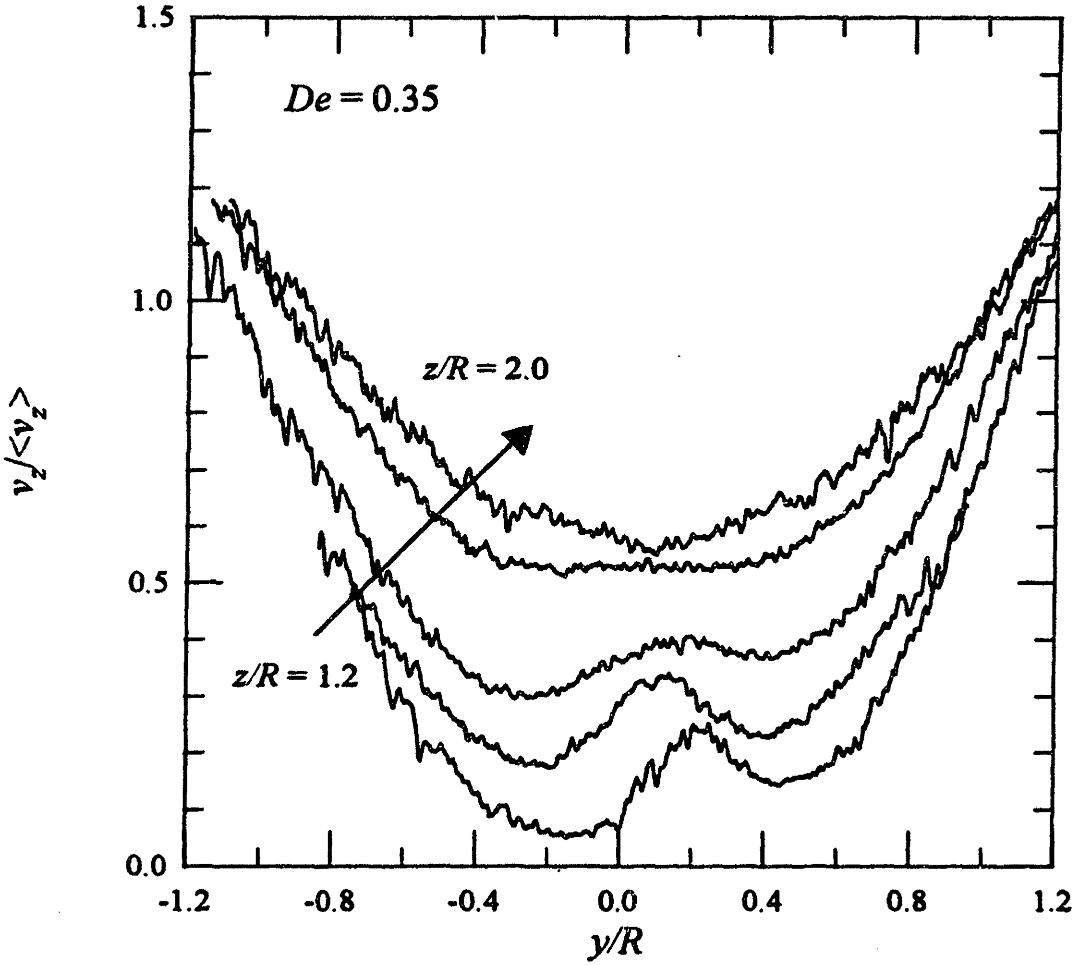

Figure 5.11 Transverse profiles of the streamwise velocity above the critical Deborah number for $R/H \approx 0.34$ at positions of $z/R = 1.2, 1.4, 1.6, 1.8$ and 2.0.

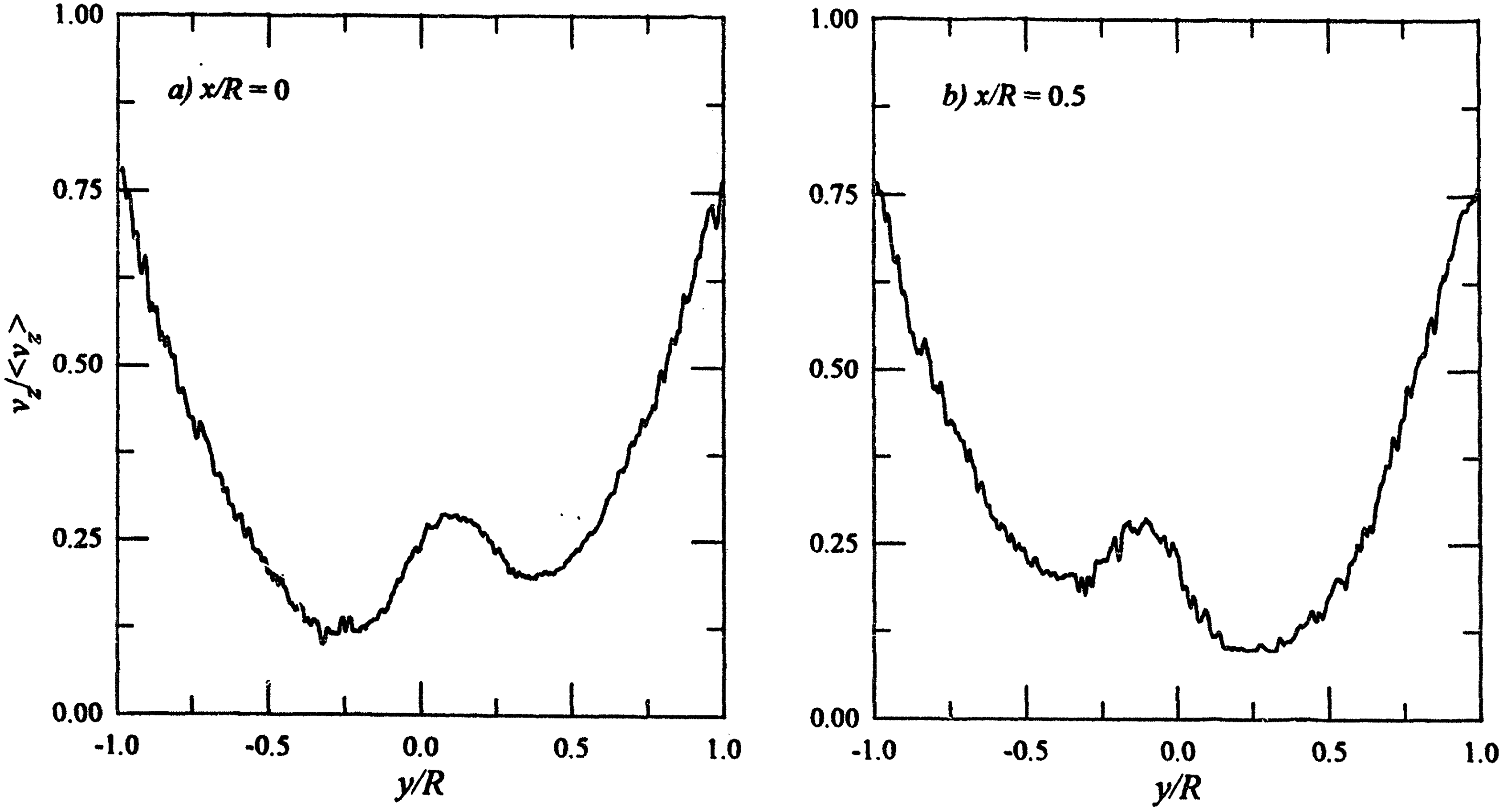

Figure 5.12 Transverse profiles of the streamwise velocity for *R/H* = 0.34, *z/R* = 1.3 and *De* = 0.41. *(a) x/R* = 0 and *(b) x/R* = 0.5.

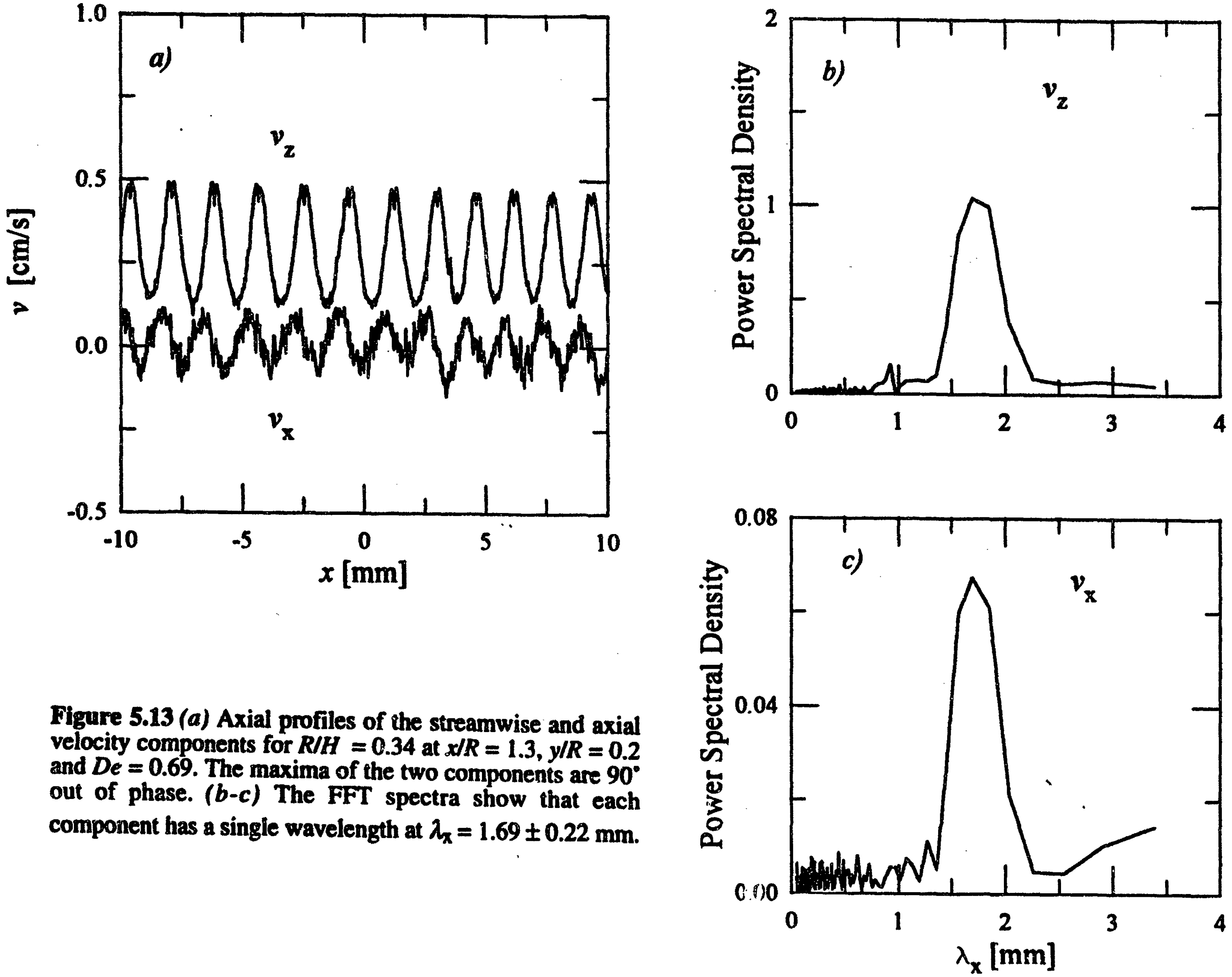

Figure 5.13 *(a)* Axial profiles of the streamwise and axial velocity components for $R/H = 0.34$ at $x/R = 1.3$, $y/R = 0.2$ and $De = 0.69$. The maxima of the two components are 90° out of phase. *(b-c)* The FFT spectra show that each component has a single wavelength at $\lambda_x = 1.69 \pm 0.22$ mm.

5.2 Effect of Stagnation Geometry

5.2.1 Planar Divider

Experiments are also conducted using a planar divider in place of the cylinder in order to determine the importance of the upstream flow conditions on the instability. The downstream stagnation point is still present, but the upstream stagnation point and the converging flow in the gap is replaced with a fully developed shear flow in the gap between the divider and the channel walls. The series of scans in figure 5.14 compare the fluctuations of the streamwise velocity for the cylinder and planar divider with $R_{\mathrm{div}}/H = 0.5$. The critical Deborah number is nearly identical for this radius, but the structure of the instability has changed slightly. The wavelength for the divider is shorter than that for the cylinder, and the amplitude and downstream extent of the instability both also decrease. The results for three dividers are compared to the previously shown results for the cylinder in figure 5.15, which shows that De_{crit} is the same as for the cylinder for R_{div}/H of 0.50 and 0.75 and much higher than for the cylinder for R_{div}/H of 0.23, and that the wavelength of the instability is much shorter than for the cylinder for all values of R_{div}/H.

The effect of upstream flow conditions is further examined by using a tapered divider with a total included angle of 4° and a minimum height at its tip of 0.2 mm, thereby eliminating any curvature effects present in the cylinder or planar divider geometries. Figure 5.16 shows velocity profiles along the centerplane for $De = 0.07$, 0.16, 0.22, 0.30, 0.37 and 0.42, where $De = \lambda(\dot{\gamma})\langle v_z \rangle / H$ for this geometry, since no characteristic length can be associated with the geometry. As with the cylinder and planar divider, there is a downstream shift of the velocity profile as De increases. However, scans along the neutral direction indicate that no equivalent instability is seen for this geometry, as shown in figure 5.17, although the interpretation of this result is made ambiguous by the flow geometry itself. As figure 5.4 shows for the cylinder, De_{crit} increases dramatically for small aspect ratios, although if the divider half-height at its minimum is assumed to be equivalent to a radius, the flow conditions shown in figure 5.17 should be well above the critical conditions, since its De would be 3.1, whereas De_{crit} for a cylinder of this size is 1.25. However, the results for the planar divider with $R_{\mathrm{div}}/H = 0.23$ show that the scaling for cylinders at small aspect ratios may not apply to other geometries. A more important consideration is that the downstream extent and amplitude of any disturbance velocity are also expected to scale with the equivalent radius. The instability for the cylinder with $R/H =$

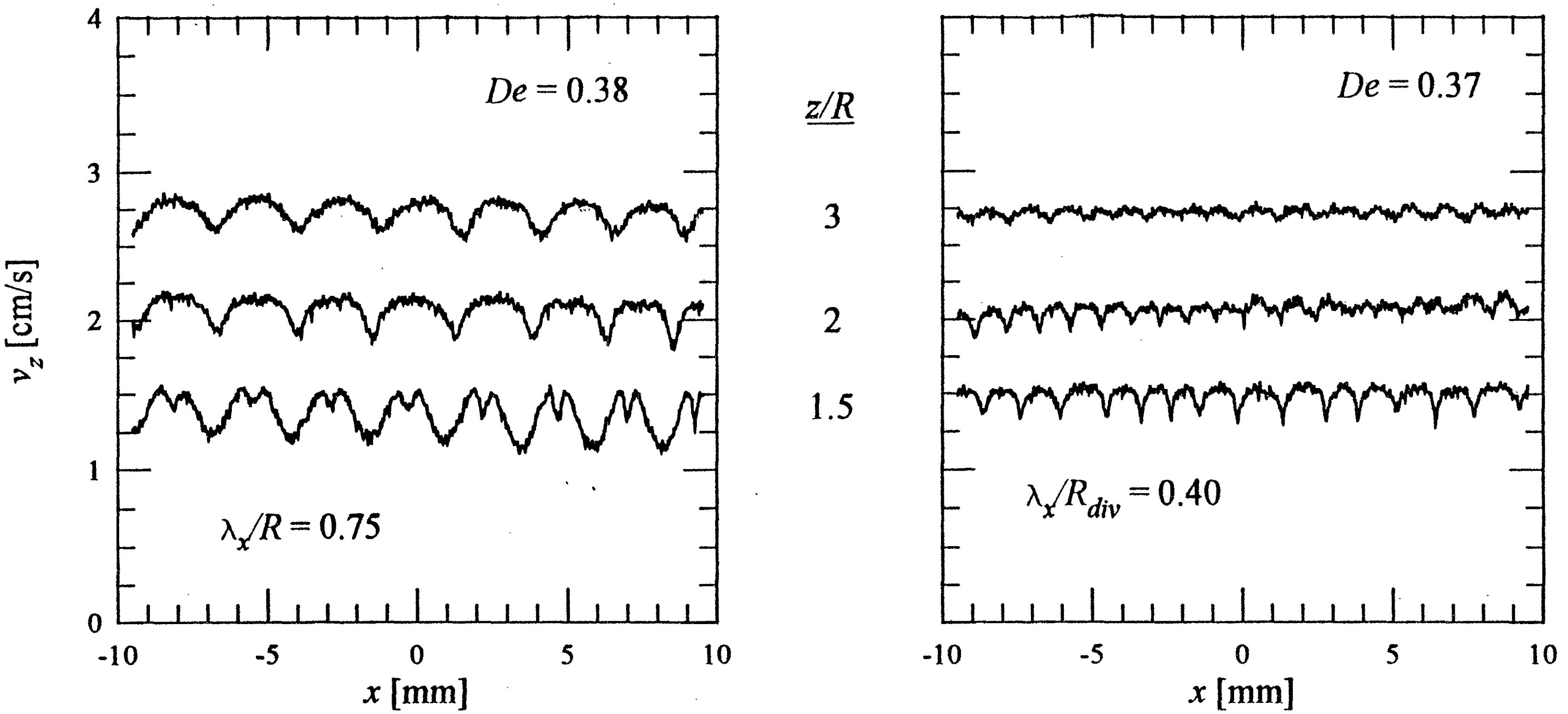

Figure 5.14 Axial profiles of the streamwise velocity at positions of z/R = 1.5, 2.0 and 3.0 for *(a)* cylinder with R/H = 0.50 and De = 0.38 and *(b)* planar divider with R_{div}/H = 0.50 and De = 0.37.

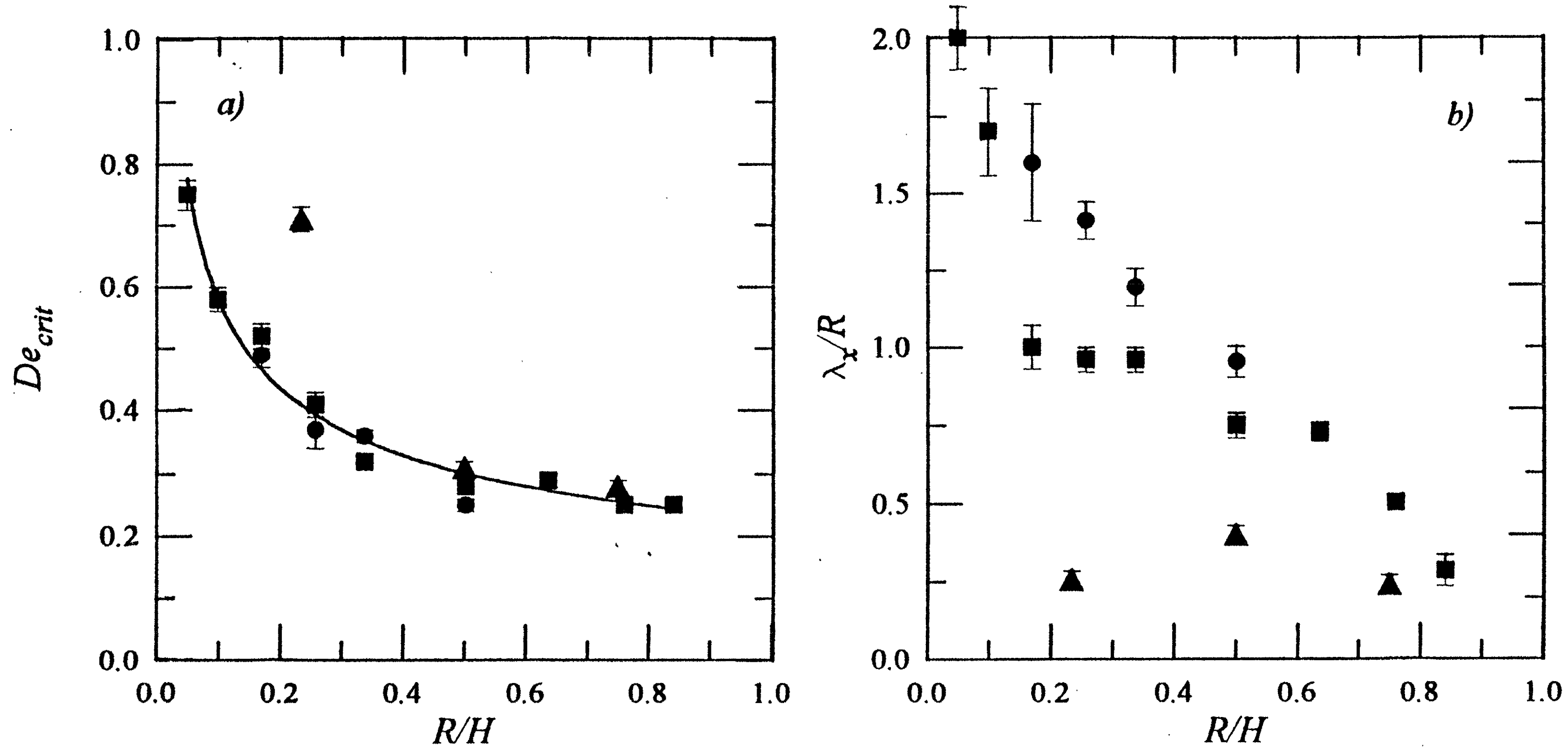

Figure 5.15 *(a)* Critical Deborah number and *(b)* wavelength λ_x/R_{div} for (▲) the planar divider. Also shown are the results for the cylinder in (■) the current work and (●) McKinley *et al.* .

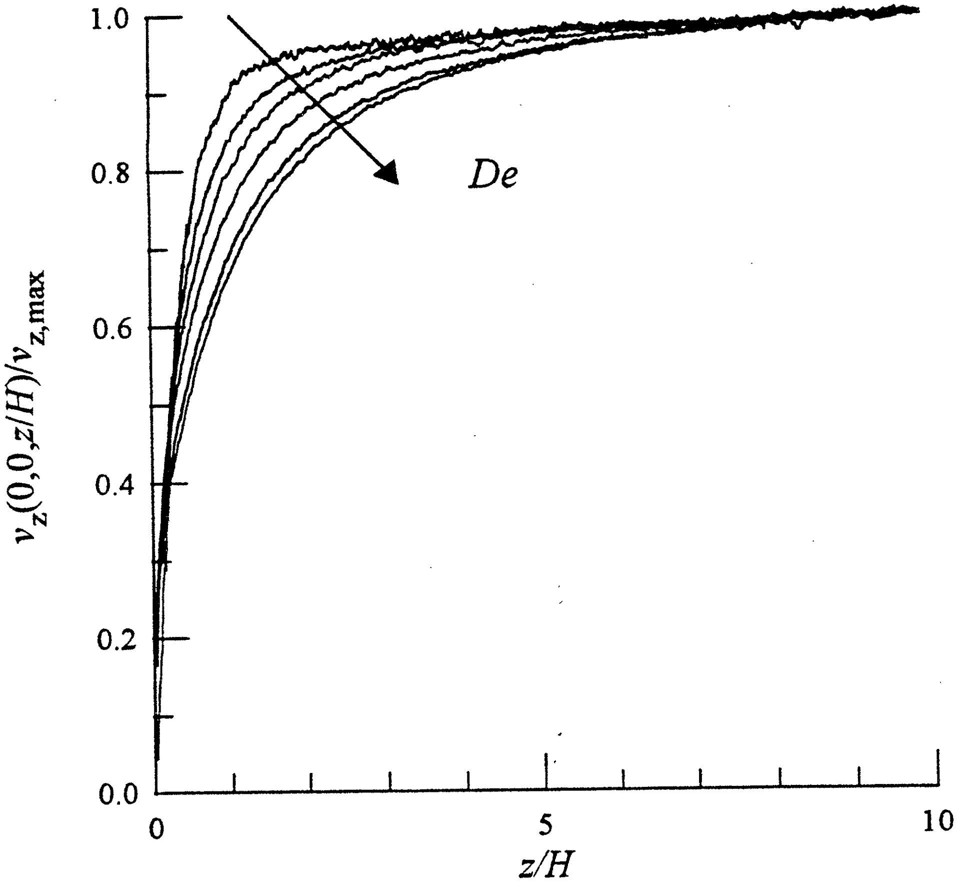

Figure 5.16 Streamwise profiles of the streamwise velocity along the centerplane of the tapered divider as a function of *De*.

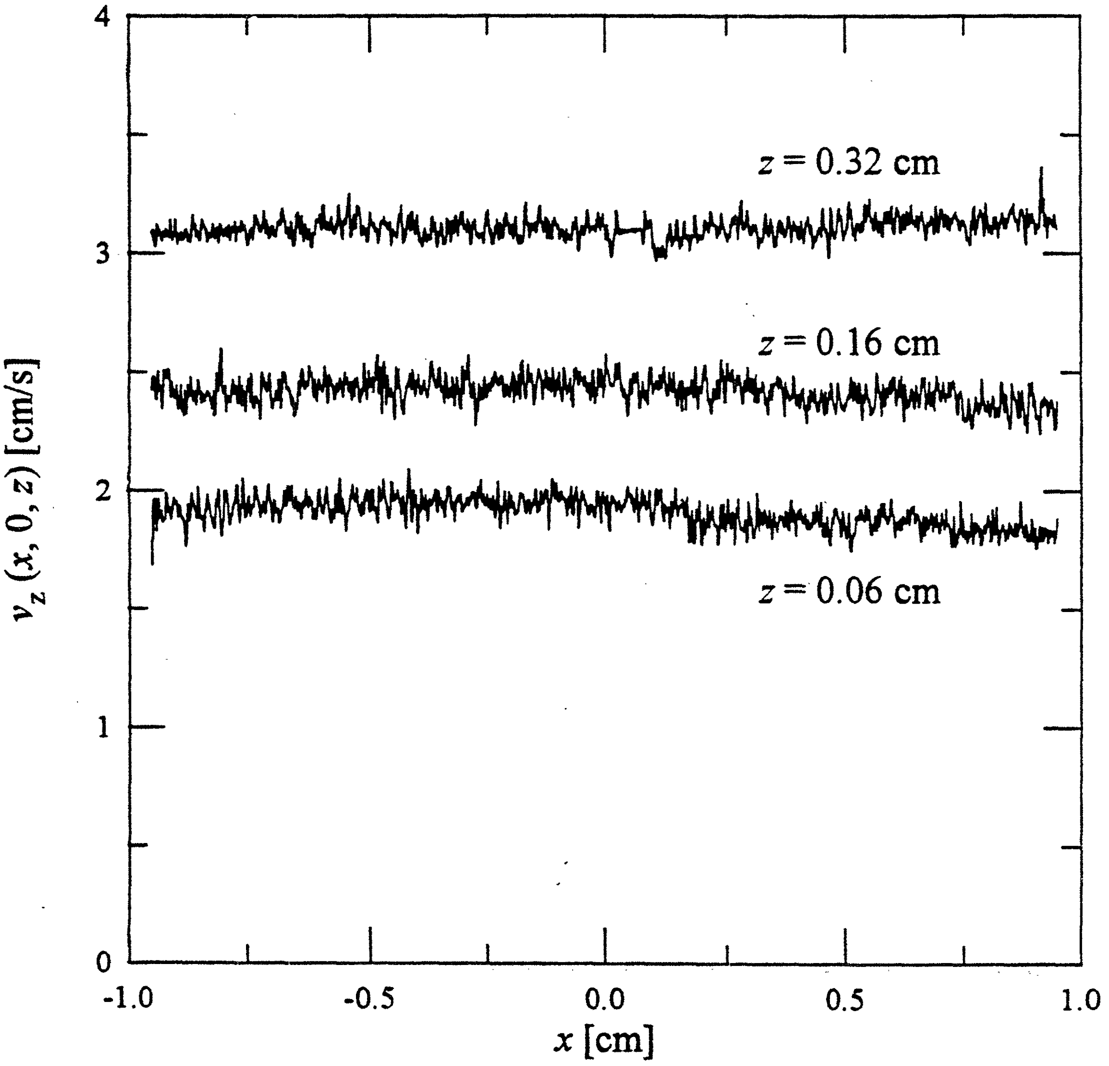

Figure 5.17 Axial profiles of the streamwise velocity for the tapered divider at $z = 0.06$, 0.16 and 0.32 cm and $De = 0.27$. No fundamental frequency can be determined from the profiles.

0.05 at $z/R = 2$ for $De - De_{crit} = 0.56$ had streamwise velocity fluctuations of ± 0.02 cm/s compared to a mean velocity of 0.15 cm/s. The closest measurements could be taken to this divider was 0.06 cm, which is equivalent to $z/H = 6$, and the velocity is already 2 cm/s. Any disturbance velocity would therefore be difficult to measure with this system, due to both the relatively large distance from the stagnation point and the high background velocity. The present flow system is not well-suited for creating a purely planar extensional flow, since, for example, if a divider with a flat end were used in place of a rounded end, a recirculation region would exist behind the stagnation point, rather than the desired extensional flow, as seen by Jones and Walters (1989) for flow past square obstacles.

5.2.2 Axisymmetric Stagnation Flow

The similarity between the instabilities observed for the cylinder and the planar divider suggests that the geometry of a rod with a rounded end provides a good model for investigating the stability of flow past a sphere. The difficulties involved with experiments with spheres falling through viscoelastic fluids can be avoided with this geometry since the rod is fixed in space and the fluid flows past it. Construction and operation of this system are also considerably simpler than with magnetic levitation of a sphere (Byars 1992).

The axial velocity along the centerline for $De = 0.06$, 0.16, 0.25, 0.48 and 0.70 is shown in figure 5.18 for $R_{rod}/R_{tube} = 0.25$. At higher Deborah numbers the velocity profiles are shifted further downstream, as has been observed for flow past a sphere. However, even at the maximum obtainable De of 0.70, no instability is seen in the wake, and no negative wake is observed. In this coordinate system, a negative wake would be indicated by $v_z/v_{z,max} > 1$. In contrast to the measurements of Bisgaard (1983) for a 1% PAA/glycerol solution (figure 2.16), the velocity recovers smoothly to its maximum for all De. Similar measurements are also obtained at radial positions of $r/R_{rod} = 0.2$, 0.4, 0.6 and 0.8. In each case, the velocity profiles are shifted downstream with increasing De, and the amount of the shift decreases for larger r/R_{rod}. The recovery to the fully-developed value is smooth for all cases.

Time-dependent measures of the axial velocity are also obtained for $De = 0.67$. Time series of the velocity are shown in figure 5.19 at a radial position of $r/R_{rod} = 1.2$ and angular positions of $\theta = 0°$, 22.5°, 45°, 67.5° and 90°, where θ is defined in a cylindrical coordinate system with its origin at the center of curvature of the rod and with $\theta = 0°$ along the axis of the tube. These scans indicate that the velocity is temporally steady at all positions about the rod.

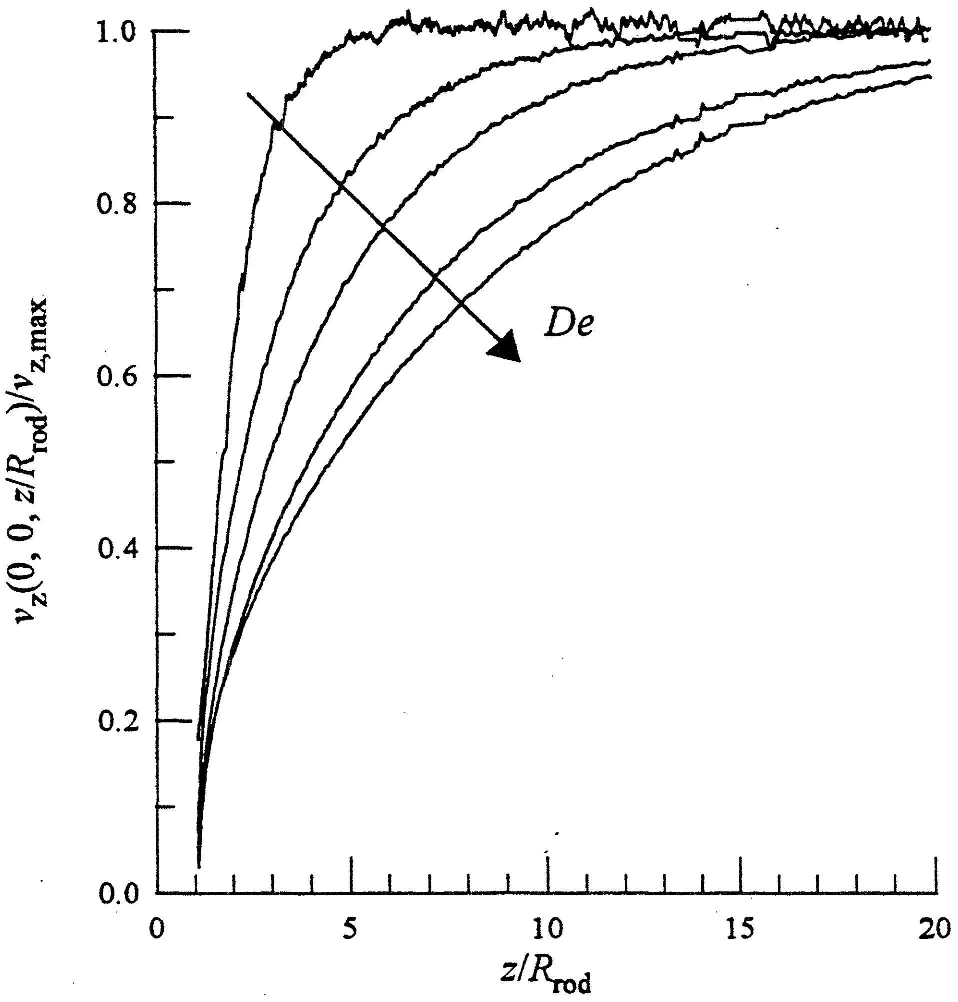

Figure 5.18 Streamwise profiles of the streamwise velocity along the centerline of the axisymmetric stagnation geometry for $R_{\mathrm{rod}}/R_{\mathrm{tube}} = 0.25$ as a function of *De*.

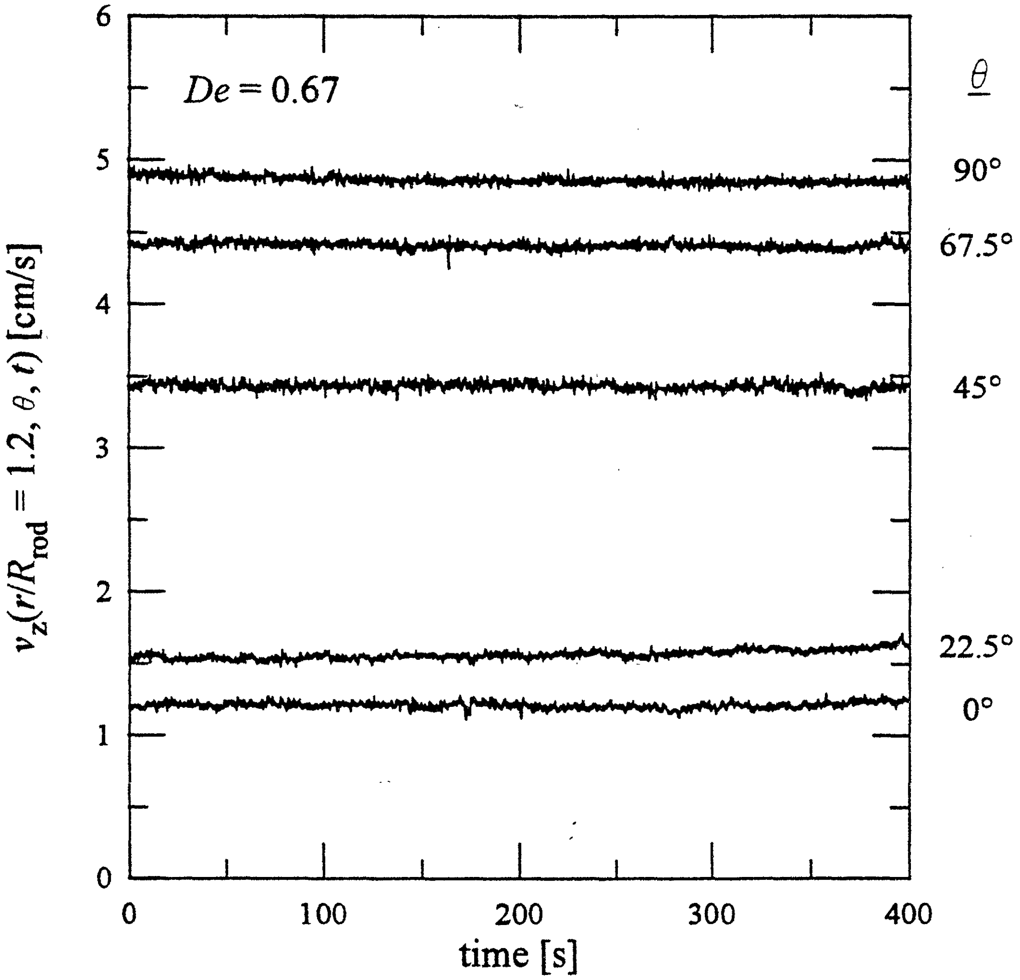

Figure 5.19 The streamwise velocity as a function of time at different azimuthal positions for the axisymmetric stagnation geometry with $R_{rod}/R_{tube} = 0.25$, *De* = and $r/R_{rod} = 1.2$.

Although these sets of measurements do not indicate a flow instability for flow past a sphere, it is difficult to prove conclusively that the flow is stable. However, it can be shown that the flow conditions in these experiments produce a strong extensional flow. Qualitative measures of the birefringence similar to those shown above for flow past a cylinder are shown in figure 5.20. At the highest Deborah numbers, a birefringent strand can be seen to extend over ten radii downstream. Because the amount of fluid passing through the stagnation region in the axisymmetric geometry is much less than for the cylinder, the birefringent strand is not expected to be as bright in this case even for equivalent molecular extensions.

A more quantitative estimate of the strength of the extensional flow can be obtained by using the experimental velocity profile and the FENE-P model (Bird *et al.* 1987b) to calculate the transient extension of molecules in the flow, $<Q^2/Q_0^2>$, which is the average of the extension of the dumbbells in the flow compared to their fully extended length, Q_0. At high strain rates, the Trouton ratio equals $2b$, so a value of $b = 1000$ is used based on the data of Tirtaatmadja and Sridhar. Polynomial fits of the experimental velocity profiles in figure 5.18 are differentiated to give the experimental strain rate profiles. For a stagnation flow, the velocity should initially increase quadratically with distance, but the LDV system cannot resolve velocities in this region for this flow. The resolution of the velocity profiles yields strain rate profiles which are reliable to within $0.05R_{\text{rod}}$ of the stagnation point. Due to limitations in the resolution of the velocity measurements near the stagnation point, an initial value of $<Q^2/Q_0^2>$ must be assumed at $r/R_{\text{rod}} = 1.05$, rather than considering a fully relaxed molecule at the stagnation point. Calculations using the Chilcott-Rallison model for flow past a cylinder show that $<Q^2/Q_0^2> = 0.05$ is a typical value at $z/R = 1.05$ for $L = 12$ and $De = O(1)$ (Liu 1995). Although a molecule that passes near the stagnation point may have a long residence time in the extensional flow, the strain rates close to the stagnation point are very low, and a large amount of extension is not expected for $z/R \leq 1.05$. Using this initial guess for this flow results in the $<Q^2/Q_0^2>$ profiles shown in figure 5.21 for the two highest Deborah numbers of figure 5.18. Figure 5.21(*a*) shows that for both Deborah numbers the molecules become highly extended within a short distance downstream of the stagnation point and then relax slowly as the strain rate decreases further downstream. If the value of $<Q^2/Q_0^2>$ at $r/R_{\text{rod}} = 1.05$ is taken to be 0.10, the maximum value of $<Q^2/Q_0^2>$ nearly reaches the fully-extended value for the maximum strain rate of 26 s^{-1}. The higher strain rates for $De = 0.70$ lead to higher maximum extension than for $De = 0.48$, but as figure 5.21(*b*) shows, the higher De flow only leads to greater extension for the first ~ 0.13 s and that both flows result in nearly equal extensions above 60% and in similar relaxation profiles. In light of the high extension already achieved for this flow and

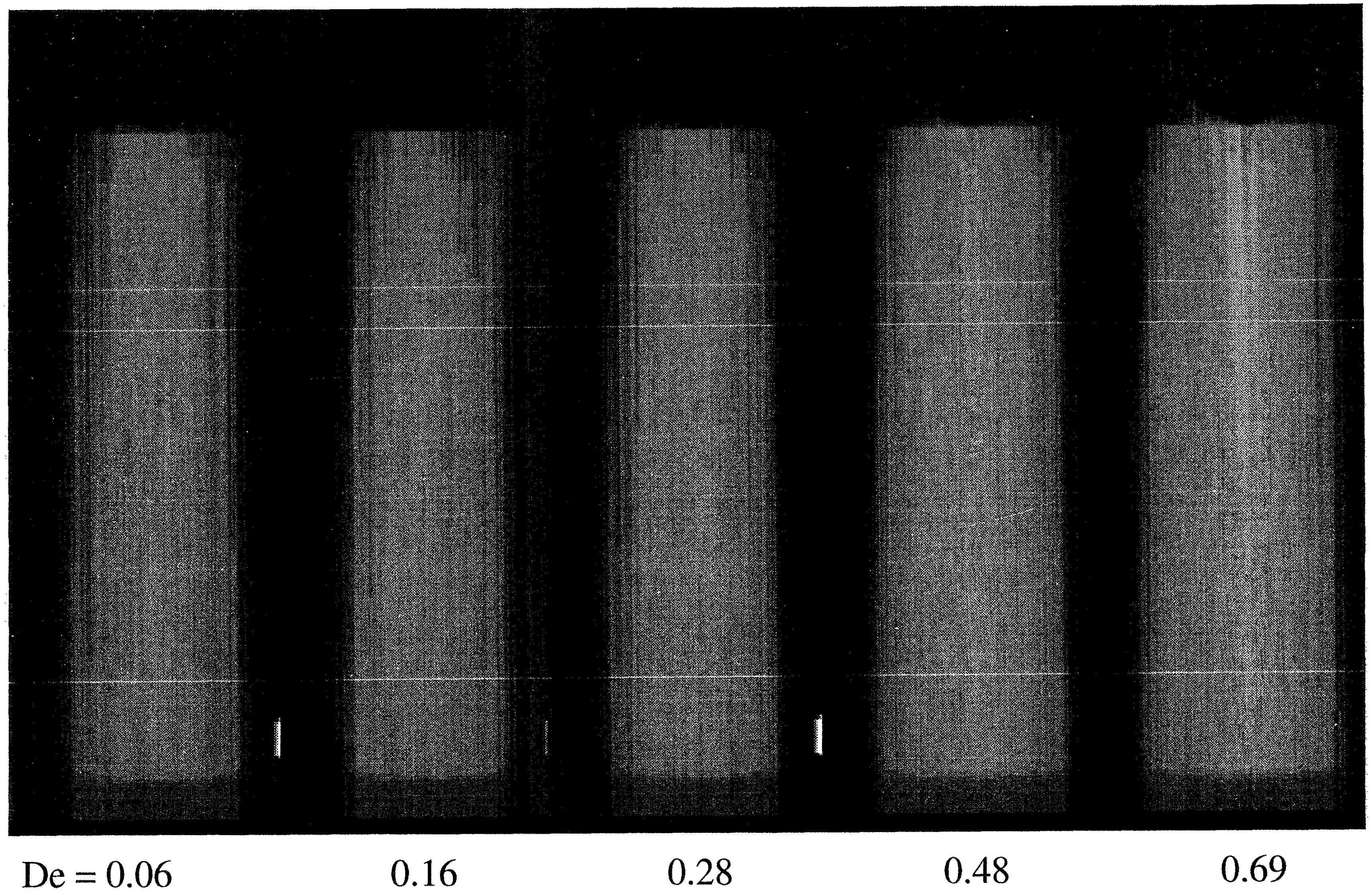

Figure 5.20 Birefringent strand in the wake of the axisymmetric stagnation geometry with $R_{\mathrm{rod}}/R_{\mathrm{tube}} = 0.26$ and $0.06 \le De \le 0.69$. Flow is from top to bottom.

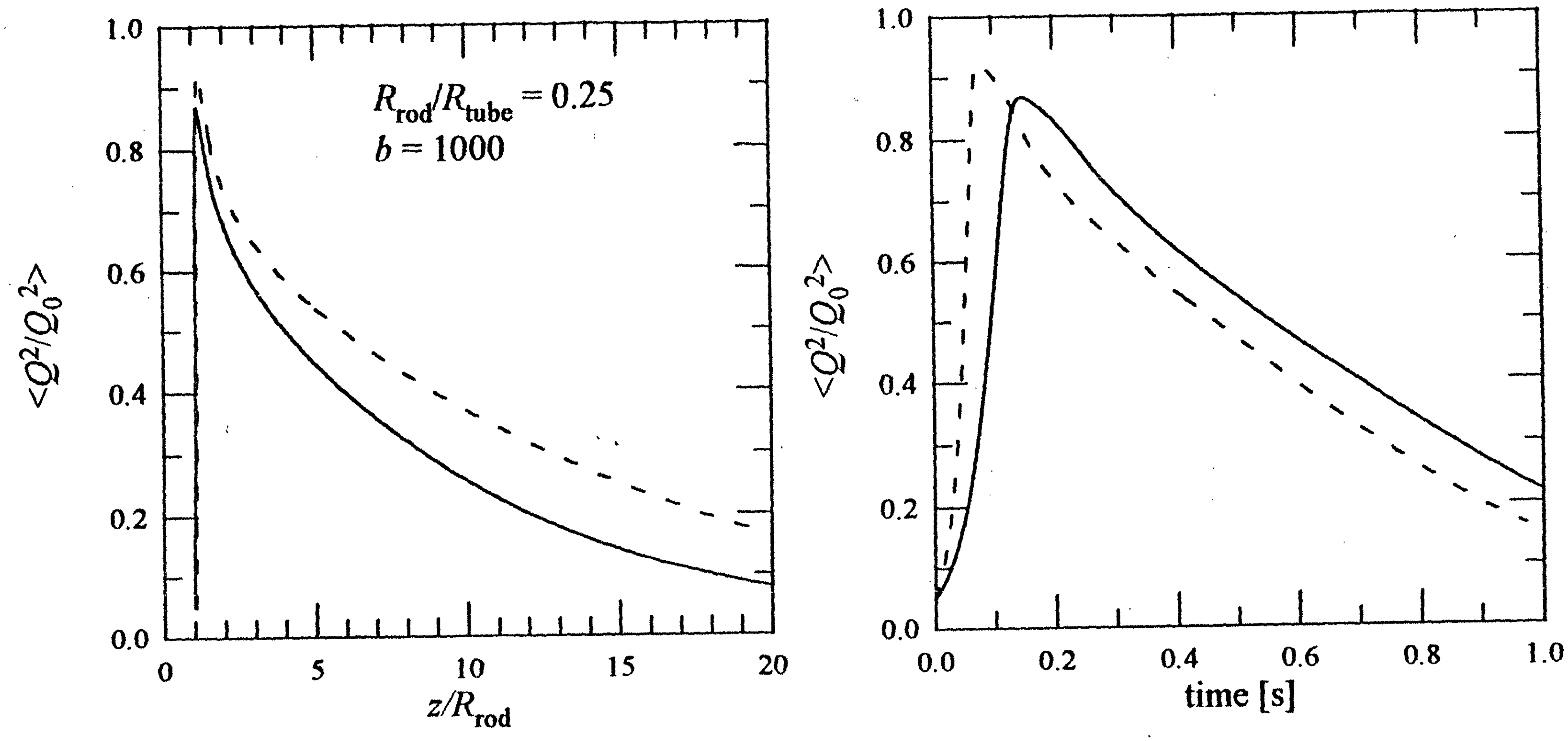

Figure 5.21 Molecular extension $<Q^2/Q_0{}^2>$ in the axisymmetric stagnation geometry at $De = 0.48$ and 0.70 as a function of *(a)* position and *(b)* time.

the small changes at increased De, it seems unlikely that a stronger extensional flow would lead to a qualitative change in the flow field resulting in a flow instability.

5.3 Comparison with Linear Stability Analysis

A linear stability analysis of viscoelastic flow past a cylinder was performed by Öztekin (Öztekin *et al.* 1995) in an attempt to predict the flow instability observed here. Although the analysis used a simplified flow geometry and a single-mode constitutive equation, it was able to capture the importance of the extensional flow downstream of the cylinder and predict the same dependence on the aspect ratio for the critical Deborah number and wavelength of the instability. The purpose of this section is to compare the experimental results of this thesis with this analysis.

The computational domain for the linear stability analysis is shown in figure 5.22, where instead of placing the cylinder in a channel, a uniform velocity has been imposed a distance R_w from the cylinder. The computational domain is limited to a narrow wedge about the centerline in order to calculate the base flow in a similarity form. This also allows the angle to be treated as a perturbation parameter for the disturbances, which can be written as

$$A(r,\theta,z,t) = \left[A_0(r) + A_1(r)\theta + A_2(r)\theta^2\right]e^{iaz+\sigma t} \tag{5.1}$$

where A is the amplitude of a disturbance in pressure or a component of the velocity or polymeric stress, a is the axial wavenumber of the disturbance and σ is its temporal growth rate.

The linear stability aspect ratio R/R_w was related to the experimental aspect ratio R/H by comparing the maximum strain rate and its downstream position as calculated from the linear stability analysis and finite element simulations of flow past a cylinder in a channel. For a Newtonian fluid, a given value of the aspect ratio gives the same result for both cases for $R/R_w = R/H \leq 0.1$, whereas for larger aspect ratios the similarity solution yields a higher value of the maximum strain rate. For the Oldroyd-B model with $\beta = 0.59$ and $R/R_w = R/H = 0.05$, the maximum strain rate agreed well for the two methods for $0.1 \leq De \leq 2.5$, but the maximum tensile stress and the position of the maximum strain rate showed only qualitative agreement.

Neutral stability curves of $De_{\text{crit}} = De_{\text{crit}}(a)$ for a single-mode Oldroyd-B model with $\beta = 0.59$ are shown in figure 5.23 for $0.025 \leq R/R_w \leq 0.1$. De_{crit} increases as R/R_w is decreased, and the critical dimensionless axial wavelength λ_x/R increases from 2.0 to 2.8

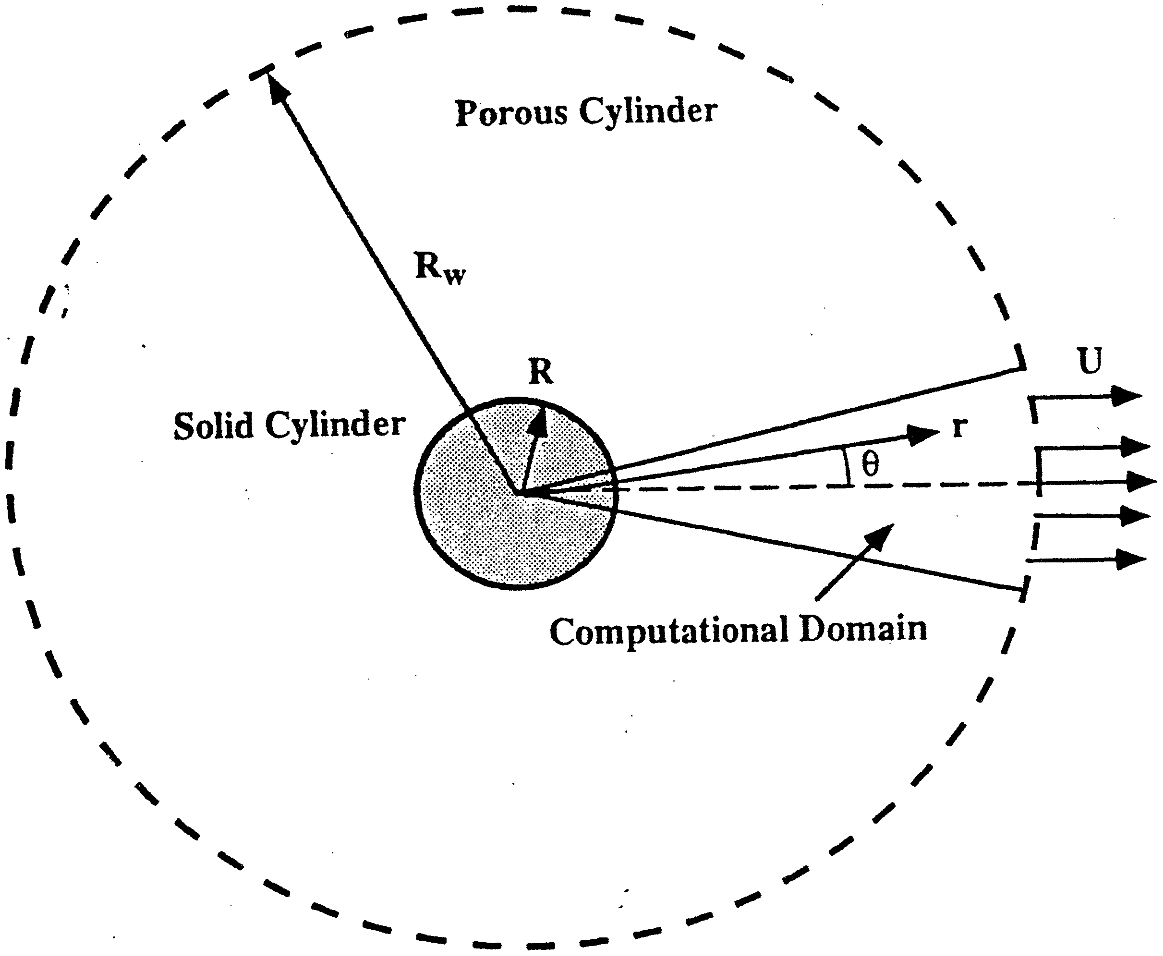

Figure 5.22 Scehmatic diagram of the computational domain used in the linear stability analysis. A polar coordinate system is defined with its origin at the center of the solid cylinder. A porous cylinder is placed at $r = R_W$.

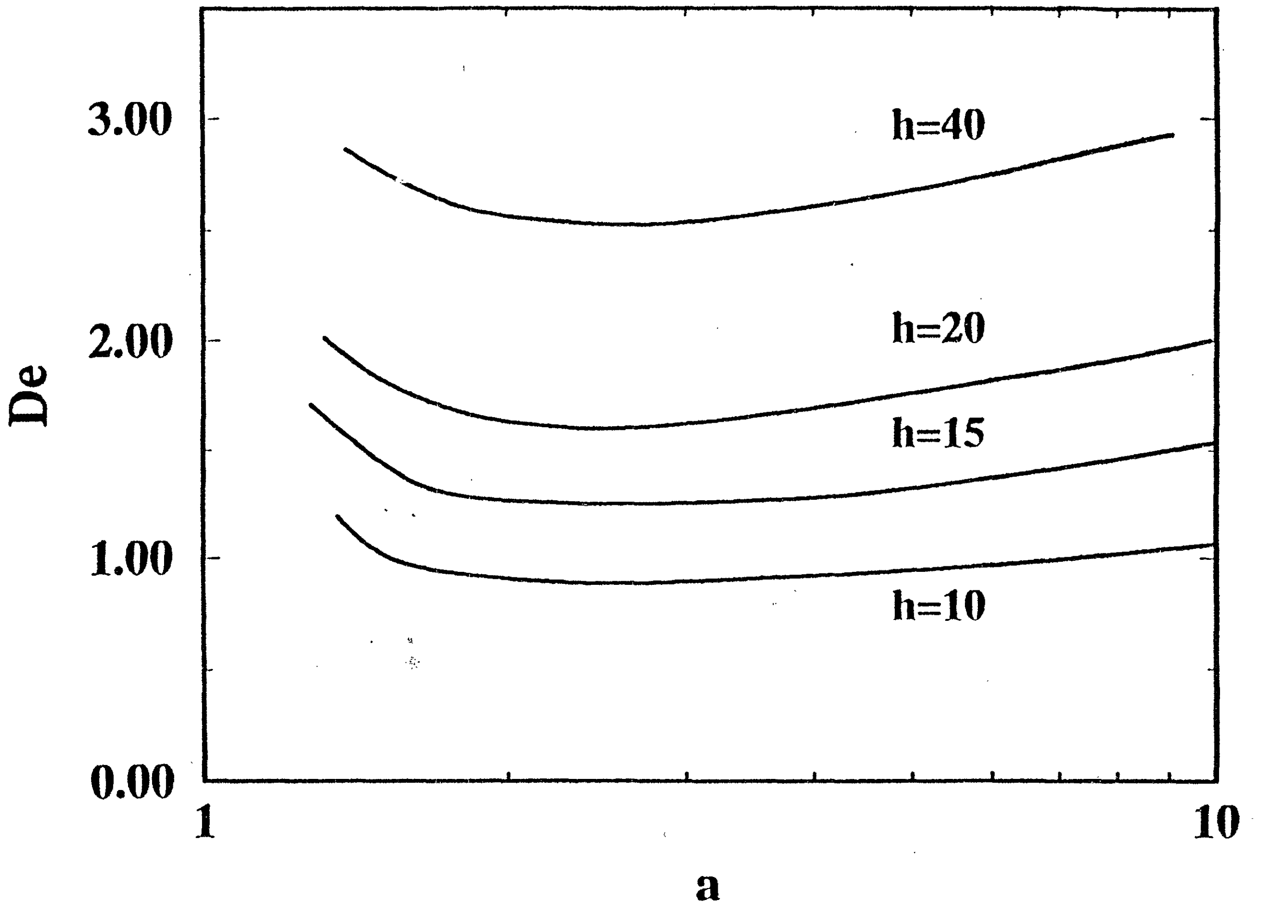

Figure 5.23 The neutral stability curves $De = De(a)$ computed for the Oldroyd-B model with $\beta = 0.59$ for values of $h \equiv H/R$.

as R/R_w is decreased for 0.1 to 0.025, although the neutral stability curves are very shallow. At onset, the wavespeed is zero, in agreement with the experimental observations. De_{crit} is nearly independent of the solvent viscosity ratio for $0.1 \leq \beta \leq 0.99$, but it approaches infinity in the Newtonian limit of $\beta = 1$. Calculations with a single-mode Giesekus model showed that De_{crit} and a_{crit} are nearly independent of the mobility parameter α for $\alpha \leq 0.01$, as seen in figure 5.24. The Oldroyd-B model is recovered for $\alpha = 0$. For a value of $\alpha = 0.001$ that most accurately characterizes the experimental fluid, De_{crit} for $R/R_w = 6.7$ increases from the Oldroyd-B value of 1.248 to 1.255, and the neutral stability curve remains shallow, although for large values of α (*e.g.* $\alpha = 0.05$) disturbances with $a < 2.26$ become stable for all values of De for which the base flow can be calculated.

The critical Deborah number and wavelength for the Oldroyd-B model and the Giesekus model with $\alpha = 0.001$ and $\beta = 0.59$ are compared to the experimentally measured values as functions of the aspect ratio in figures 5.25 and 5.26. For the value of $\alpha = 0.001$ that best describes the rheological properties of the test fluid, the predictions of the two models are nearly identical. The linear stability analysis predicts a much lower De_{crit} for all values of the aspect ratio, but shows a similar dependence with De_{crit} increasing sharply for small R/R_w. The predictions for the critical wavelength are in better quantitative agreement with the experimental results, with both the linear stability analysis and experimental results showing an increase in λ_x/R for small aspect ratios. The agreement is surprisingly good considering that even the Newtonian flow fields differ in the two geometries for $R/H > 0.1$ and that seven of the nine cylinders used in the experiments had aspect ratios greater than 0.1. Furthermore, although the critical wavelength agrees well with the experimental results, the theory predicts a shallow neutral stability curve, whereas very strong wavelength selection was found experimentally. The results indicate that both models can qualitatively describe the instability, but that the inclusion of a bounded extensional viscosity and shear-rate-dependent normal stress coefficient in the Giesekus model do not improve the quantitative comparison.

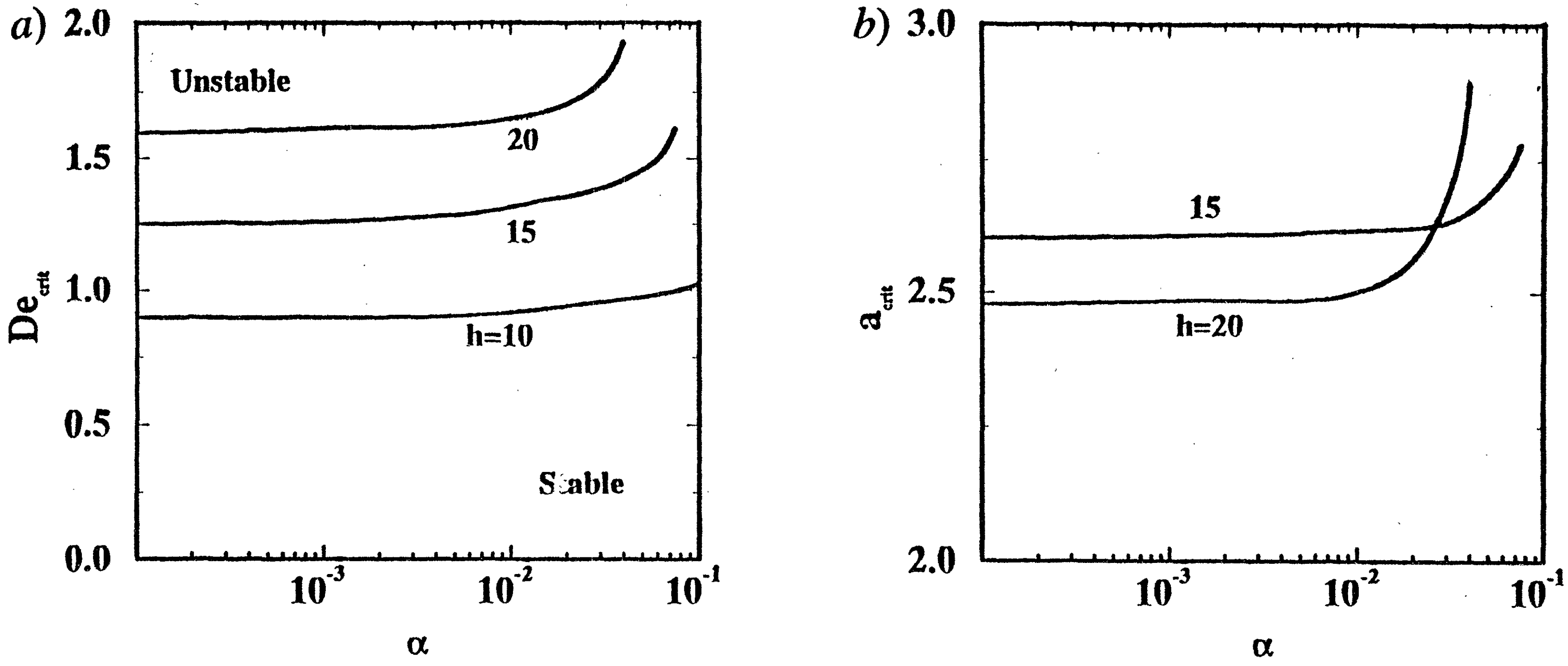

Figure 5.24 (*a*) The critical Deborah number De_{crit} and (*b*) wavenumber for the onset of the instability for the Giesekus model with $\beta = 0.59$ as functions of $h \equiv H/R$.

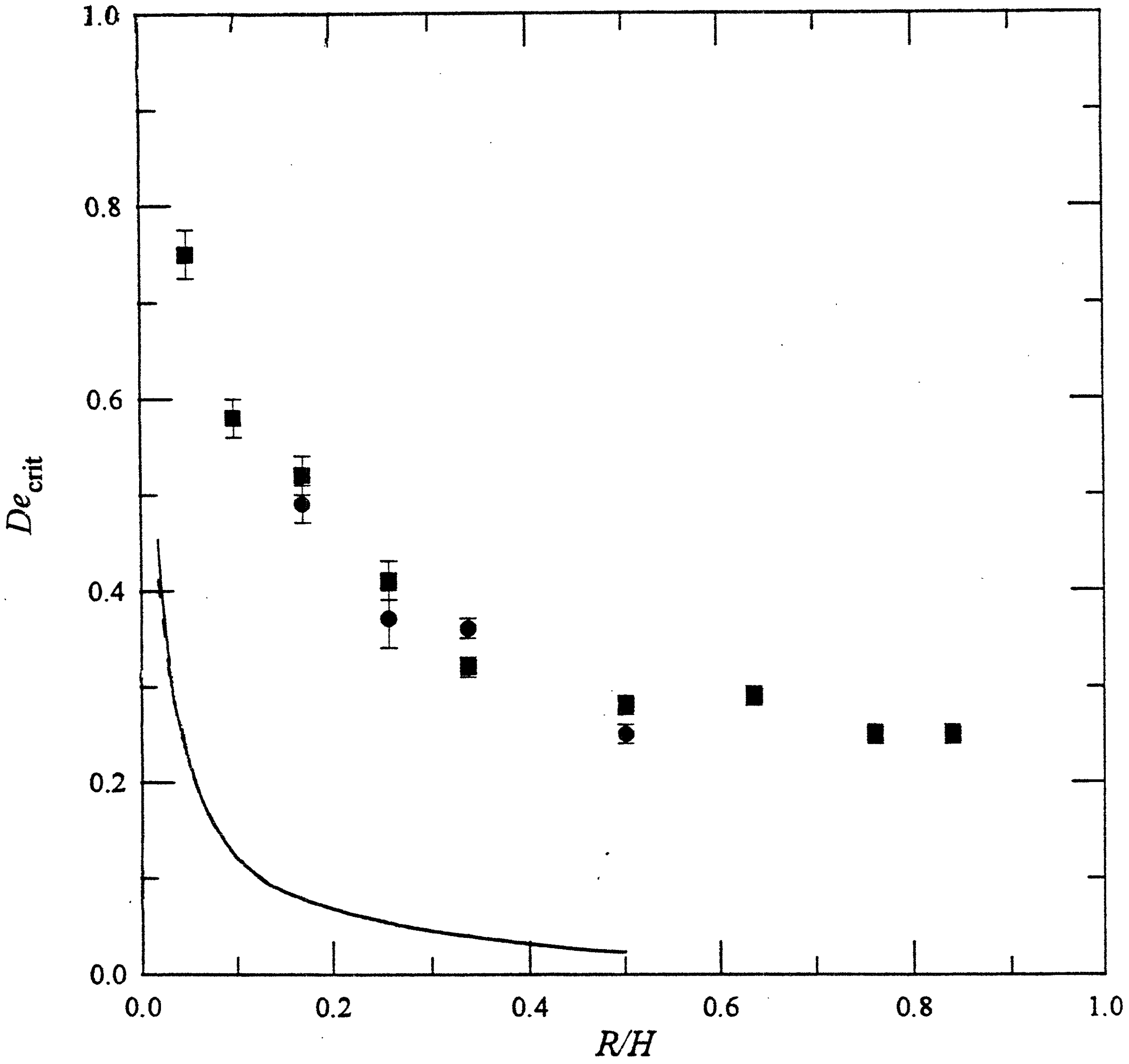

Figure 5.25 Comparison of experimentally-determined and numerically calculated stability diagrams for the onset of the flow past a cylinder in Boger fluid with $\beta = 0.59$. In the figure, dashed line (- - -) indicates the prediction of the Oldroyd-B model, and the solid curve (——) indicates the prediction of the Giesekus model with indicated value of α and symbols indicate experimental measurements of the present work (■) and McKinley, Armstrong & Brown (1993) (●).

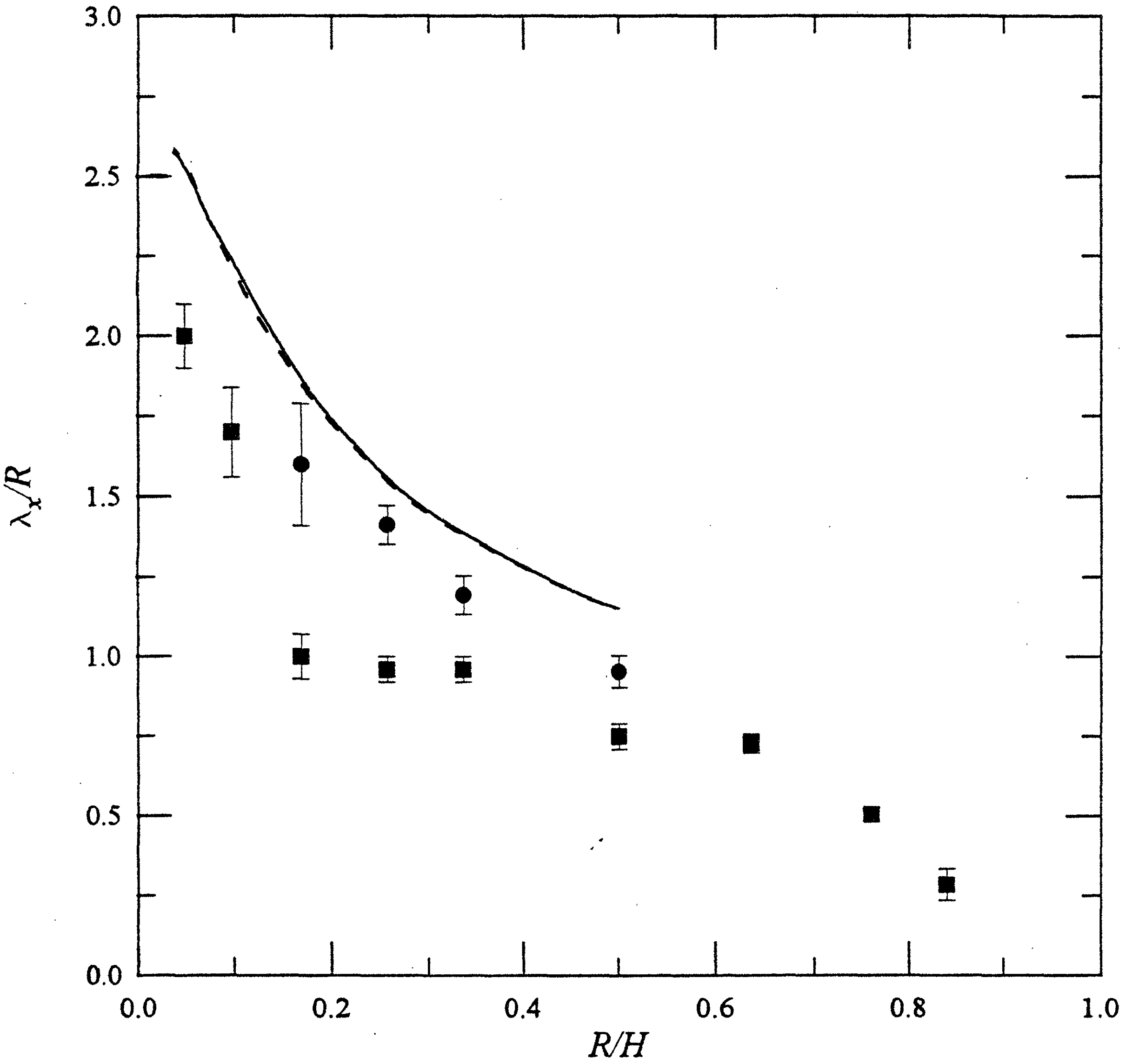

Figure 5.26 Comparison of experimental measurements and predictions from linear stability calculations with Giesekus model ($\beta = 0.59$) for the dimensionless wavelength λ_{crit}. Symbols indicate experimental measurements of the present work (■) and McKinley, Armstrong & Brown (1993) (●) and the solid curve (——) indicates the predictions of the numerical calculation.

Chapter 6

Superposed Plane Poiseuille Flow

The previous studies of superposed plane Poiseuille flow discussed in §2.3 showed that a large number of parameters govern the interfacial stability. The results of this chapter are not intended to provide a comprehensive study of all of the parameters that affect the interfacial instability, but rather to demonstrate that an experimental system has been constructed that can be used to determine the stability of the flow for a range of conditions, and that the growth rate of the instability can be calculated. All of the fluids used here have similar densities and chemical compositions, so the effects of gravity and surface tension are expected to be small, and all experiments have been conducted using pairs of fluids whose viscosities differ by a factor of approximately two. Whereas previous experimental work has considered either low viscosity Newtonian fluids or polymer melts, this chapter presents results for experiments using Boger fluids and Newtonian fluids with similar viscosities. The stability of the flow has been studied by varying the elasticity of each layer, the depth ratio, the vertical position of the separating vane and the wavenumber of the introduced disturbance. All results have been nondimensionalized with respect to the properties of the more viscous fluid (which is also the more elastic fluid for the Boger fluids used here). The Deborah number is defined as $De = \lambda_1 u_{\text{int}}/d_1$, where λ_1 is the relaxation time from Table 3.1, u_{int} is the interfacial velocity, and d_1 is the depth of the more viscous fluid. Disturbance wavenumbers are defined as $\alpha = 2\pi d_1 \nu/u_{\text{int}}$, where ν is the frequency of the disturbance.

The experiments conducted in this system to date do not form as complete a picture of the instability as for the stagnation and rotational flows above, but rather begin to establish the stability boundaries for this system and suggest directions for future study. The results for two Newtonian fluids are presented in §6.1, the effects of elasticity are shown in §6.2 for a Boger fluid and a Newtonian fluid and in §6.3 for two Boger fluids, and §6.4 outlines possible extensions of the current results.

6.1 Two Newtonian Fluids

In order to make meaningful statements about the effects of elasticity on the stability boundaries for this system, experimental results are needed for Newtonian fluids as a basis for comparison. Although linear stability calculations have been performed for the superposed flow of two Newtonian fluids, no experimental data are available to show if these conditions can be achieved experimentally and if the effects of surface tension and gravity can be neglected. The thorough study of the stability required to construct an experimental neutral stability diagram has not been performed, and instead the results of this section are intended to demonstrate the ability to determine the stability of the flow and to provide specific cases for comparison with the results of §§6.2-.3.

Figure 6.1 shows a single frame of the videotape of the flow of two Newtonian fluids with a wavenumber of $\alpha = 1.53$ introduced by sinusoidally varying the flowrate of the bottom fluid (H100 PB). For the fluids used in these experiments, the viscosity ratio is $m = 0.55$, and in this experiment the depth ratio is $n = 1.1$. The upper and lower walls of the channel can be seen by the reflections at the wall/fluid interfaces, and the addition of a dye to the 2.7% C14/H100 fluid in the upper layer results in a clearly visible interface between the two fluids. Although a slight deflection to the interface can be seen, because the wavelength of the disturbance is comparable to the frame length, it is necessary to form a composite image of the flow which compresses the horizontal scale in order to see the spatial structure of the disturbance. Figure 6.2 shows a composite image for the same conditions as figure 6.1, in which a single vertical line of pixels has been taken from the center of the image every 0.2 s and added to the composite image in order to show the flow at a point over a period of two minutes. The image processing algorithm described in §3.4 can be used to obtain the position of the interface as a function of time as shown in figure 6.3(*a*), and the FFT of the interface position yields the frequency and amplitude of the disturbance (figure 6.3(*b*)). For the conditions used here, $u_{\mathrm{int}} = 1.11$ mm/s and $d_1 = 1.69$ mm, so that $\alpha = 1.53$.

The results in figures 6.1-3 were all obtained at a distance of 10 cm downstream of the vane tip where the fluids come into contact with one another, and by taking similar measurements along the length of the channel, it is possible to determine the growth rate for the disturbance. Because of the presence of small amplitude longwave disturbances as seen in figure 6.3(*a*) and the difficulty of accurately determining pixel-sized variations in the amplitude of disturbances, the amplitude of the disturbance is measured in terms of the power spectral density (PSD) of the FFT at a given frequency. The PSD for $\nu = 0.16 \pm 0.01$ s^{-1} as a function of position along the channel is shown in figure 6.4. Also shown is a fit to the measurements at $x = 0.5$, 5 and 10 cm showing that at least initially the amplitude of the disturbance grows exponentially in space. The amplitude, A, of the PSD for $\nu = 0.16$ is given by $A = A_0\exp(\beta_{\mathrm{PSD}}x)$, where β_{PSD} is the spatial growth rate and is found to be $\beta_{\mathrm{PSD}} = 0.038$ cm^{-1} in this case. Because the amplitude of the PSD increases as the square of the amplitude of the disturbance, the growth rate β for the amplitude of the

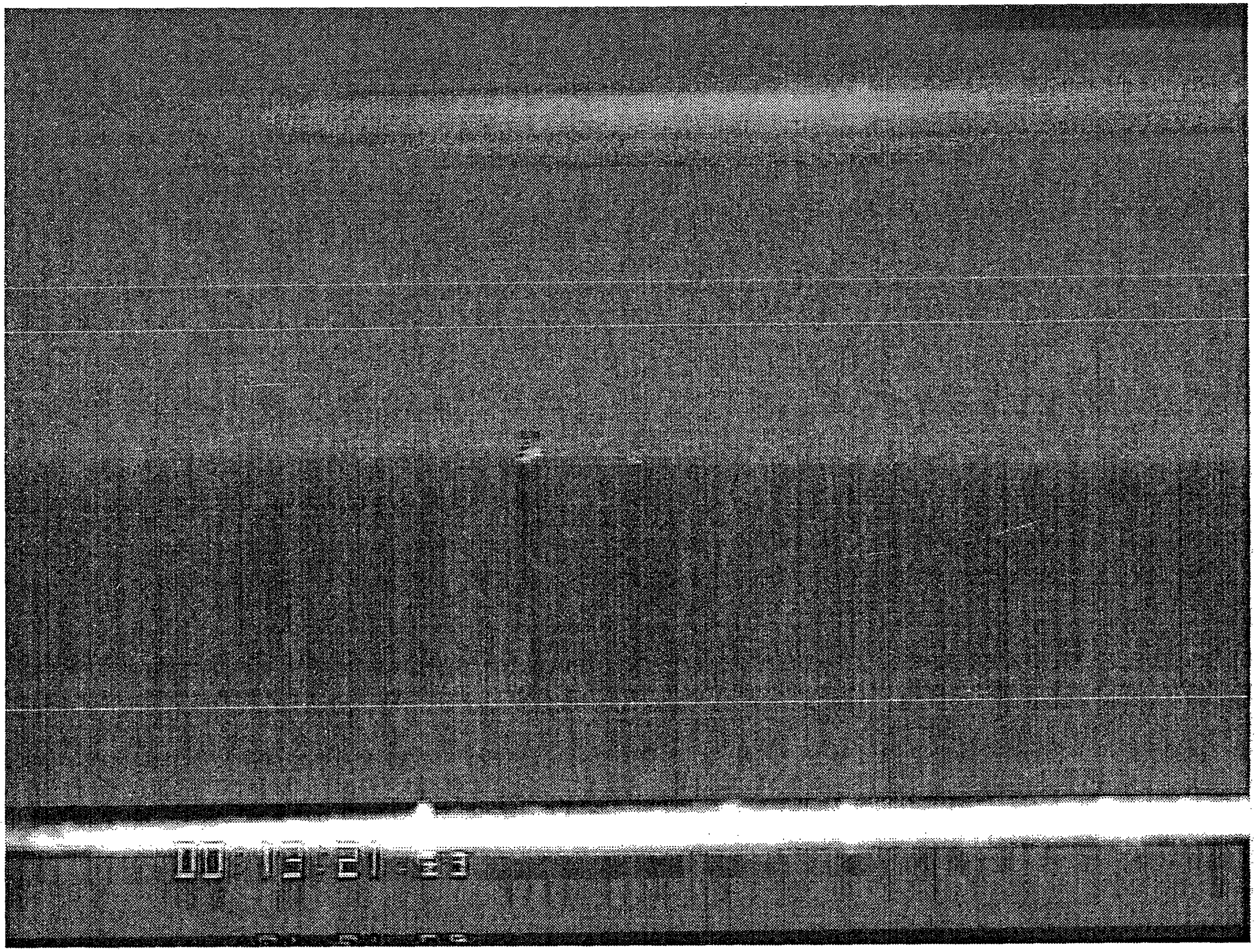

Figure 6.1 Single frame at a distnce 10 cm downstream of the vane tip of the superposed flow of the 2.7% C14/H100 (top layer) and H100 PB Newtonian fluids with an introduced disturbance of $\alpha = 1.53$. The interfacial velocity is 1.11 mm/s and the length of the frame is 5.9 mm. Flow is from left to right.

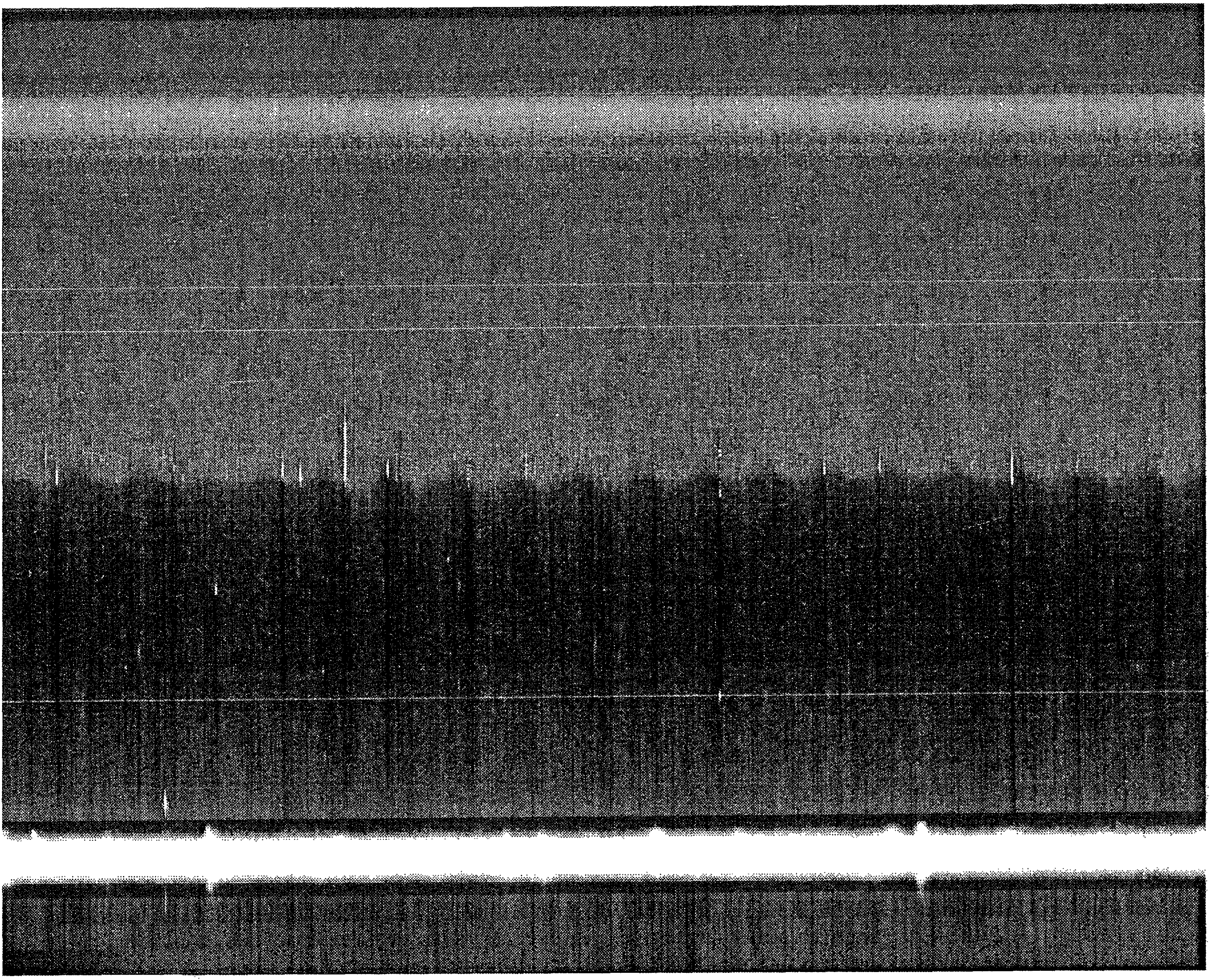

Figure 6.2 Composite image of two minutes of the flow past a point 10 cm downstream of the vane tip for the conditions of figure 6.1.

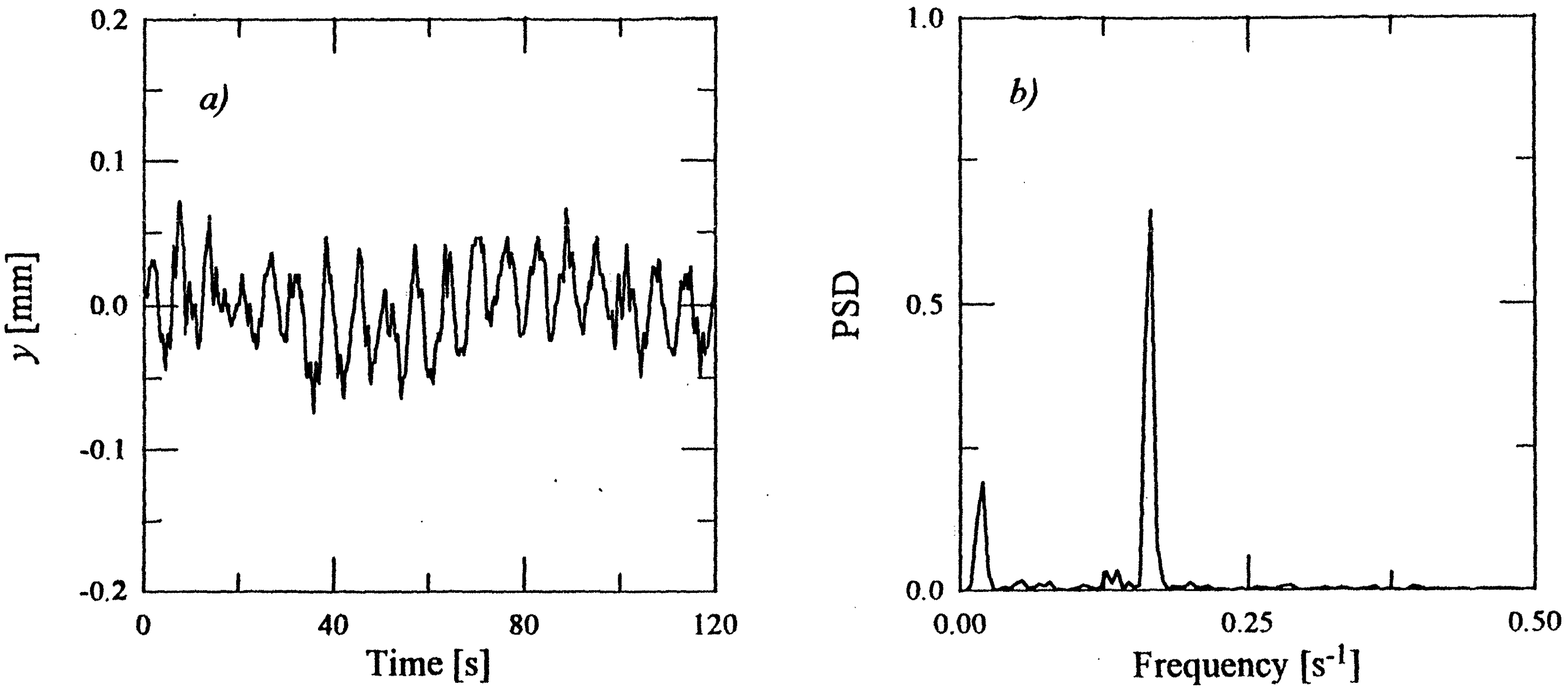

Figure 6.3 (*a*) Position of the interface of the composite image shown in figure 6.2, (*b*) and its FFT showing the primary frequency to be 0.16 s^{-1}.

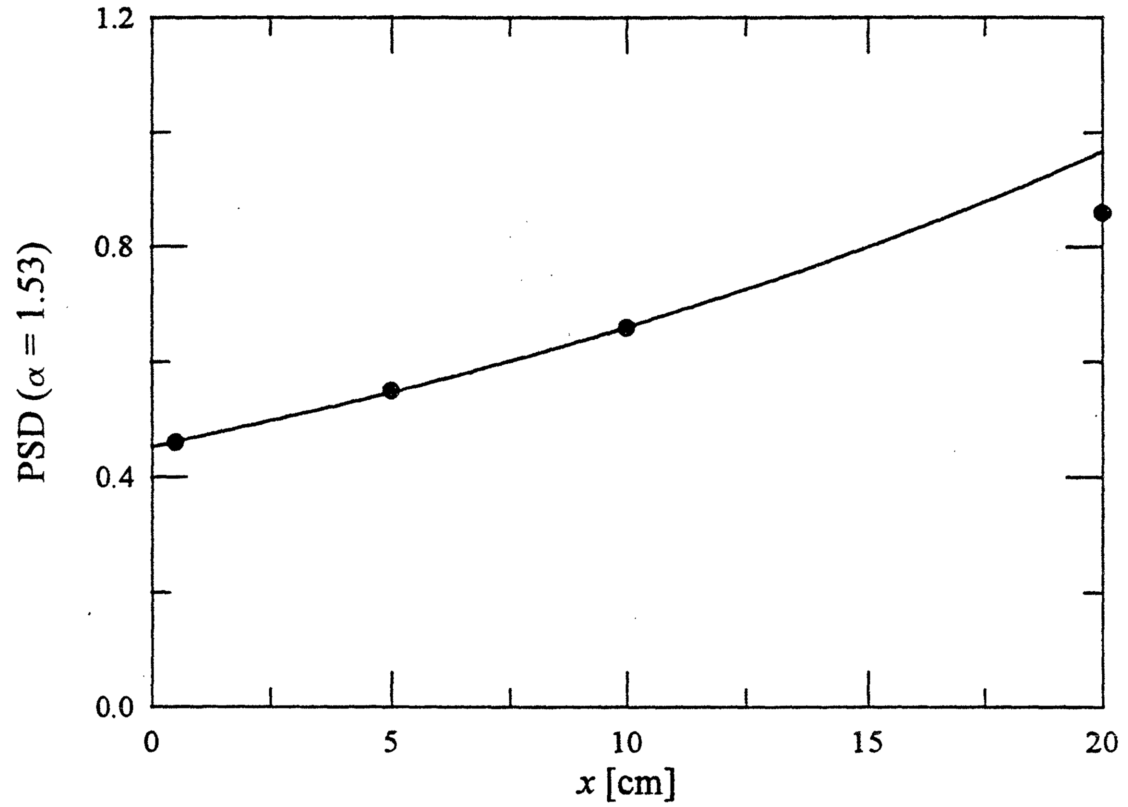

Figure 6.4 Amplitude of the power spectral density (PSD) of the disturbance with wavenumber 1.53 along the length of the channel for the conditions of figure 6.1. The growth rate is $\beta_{PSD} = 0.038$ cm^{-1}.

disturbance is 0.019 cm^{-1}. The spatial growth rate determined from the experiments can be related to a dimensionless temporal growth rate by $\alpha c_i = \beta d_1 = 3.5\times10^{-3}$, where c_i is the imaginary part of the wavespeed. This value is much higher than the value of $O(10^{-5})$ calculated by Su and Khomami (1992a) for two Newtonian fluids with a viscosity ratio of 0.5 and a depth ratio of 1. Their calculations were for $Re = 0.1$, but Su and Khomami (1992b) showed that for Oldroyd-B fluids the growth rate was insensitive to the Reynolds number for $Re \leq 0.1$. Between $x = 10$ cm and 20 cm, it is not possible to determine whether the growth rate has decreased for large x due to nonlinear effects, or if the measurement at $x = 20$ cm should be considered as part of the exponential growth region, in which case $\alpha c_i = 3.0\times10^{-3}$. In either case, it is clear that the flow is unstable for these conditions, as is to be expected from the neutral stability diagram given in figure 2.25(*a*), where the depth ratio is defined as $\varepsilon \equiv n^{-1}$ and the viscosity ratio is $m = 0.5$. For the slightly higher viscosity ratio of the experiments, the critical depth ratio would be $\log\varepsilon = 0.13$, and the critical wavenumber for $\log\varepsilon < 0.13$ would increase slightly. Enlarging figure 2.25(*a*) shows that the experimental condition of $\alpha = 1.53$ and $\log\varepsilon = -0.04$ is expected to be unstable for $m = 0.5$, although further experiments near the stability boundary are required to show that the neutral stability diagram can be reproduced.

Due to the similar chemical compositions of the two fluids, the effects of interfacial tension are expected to be negligible, although no measures of the surface tension have been made. In this and all other experiments, the more dense fluid is in the bottom layer, so any gravitational effects will be stabilizing. For these fluids, the density ratio is $r = 1.0023$, and for the conditions of the experiment $F = (r - 1)gd_1/u_{\mathrm{int}}^2 = 34$. However, it is misleading to compare this value to figure 2.23, because Yiantsios and Higgins show that the gravitational term enters the interfacial stress balance as ReF. For this experiment, $Re = 7.2\times10^{-5}$ and $ReF = 2.5\times10^{-3}$, whereas the smallest value of ReF shown in figure 2.23 is $ReF = 0.1$. The stabilizing effects of gravity are therefore expected to be negligible.

Figure 6.3 shows that there is a small wavenumber disturbance present in addition to the disturbance that is intentionally introduced. As shown below, this wavenumber can grow rapidly for viscoelastic fluids, especially for large depth ratios. Experiments were therefore carried out with Newtonian fluids as a basis for comparison, and although the wavenumber is present even when not forced, its amplitude remains small throughout the channel. Figure 6.5 shows a disturbance near the tip of the vane for a higher depth ratio of $n = 3.6$ ($\log\varepsilon = -0.56$), which has a wavenumber of $\alpha = 0.21$. Although figure 2.25 indicates that this disturbance should be unstable and it in fact seems to grow initially, a growth rate could not be determined because the amplitude of the disturbance is too small

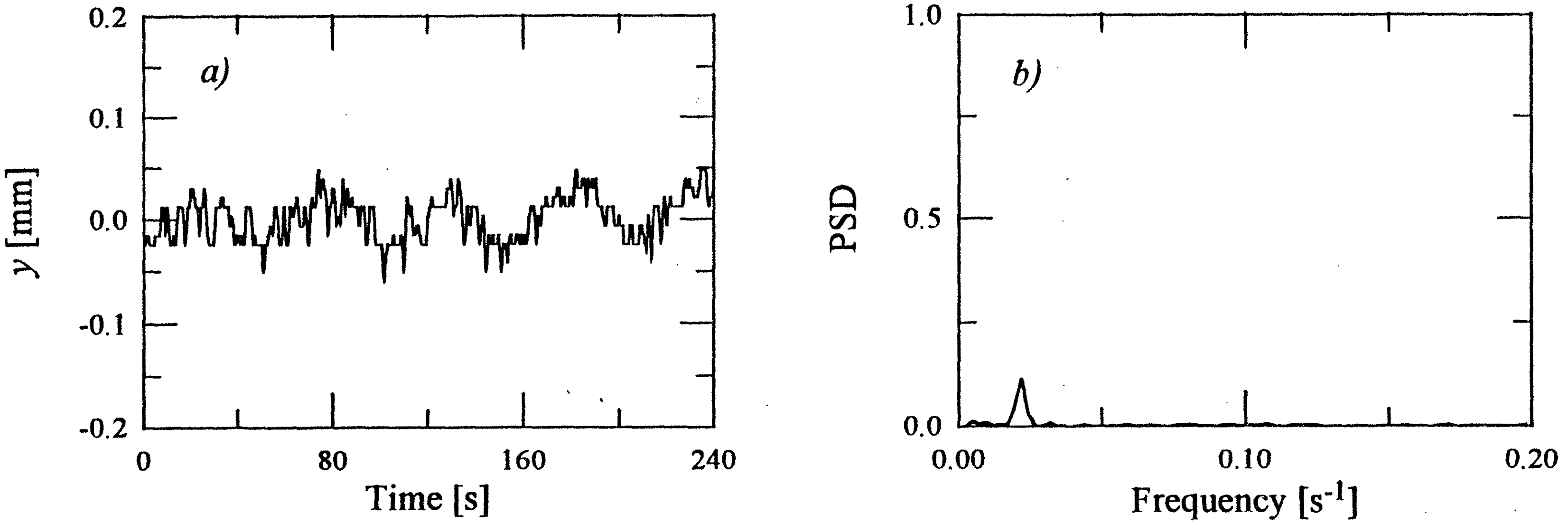

Figure 6.5 (*a*) Position of the interface for two Newtonian fluids with $n = 3.6$, $m = 0.55$ and no external forcing, (*b*) and its FFT showing the primary frequency to be 0.022 s^{-1}.

(~one-fifth of those introduced above) and the growth rate is apparently too small. Small amplitude disturbances with $\alpha \sim 0.2$ were also observed for depth ratios of 2.7 and 4.9.

6.2 A Boger Fluid and a Newtonian Fluid

The effect of elasticity was first investigated by reproducing the conditions of figures 6.1-4, but with the 2.7% C14/H100 fluid replaced by the 0.31% PIB (2) Boger fluid. Composite images were formed of the interface along the channel and the interface position was determined as shown in figure 6.6 for $x = 5$ cm and 20 cm. In contrast to the results for two Newtonian fluids above, it can be seen that the wavenumber $\alpha = 1.53$ corresponding to $\nu = 0.16$ s^{-1} decays, while the smaller wavenumber $\alpha = 0.09$ grows in this case. The growth rate was found to be $\alpha c_i = -4.6\times10^{-3}$ for $\alpha = 1.53$ and although the $\alpha = 0.09$ disturbance is clearly unstable, its growth rate could not be calculated since its period is almost as long as the total measurement time. Although no linear stability calculations exist for these conditions, the results agree at least qualitatively with the calculations of Su and Khomami shown in figure 2.26. For two Oldroyd-B fluids at low Deborah number, when the more viscous is the less elastic, they showed that small wavenumbers are unstable while larger wavenumbers are stable for depth ratios near unity. Although the Newtonian fluid in the experiment is the more viscous, its Deborah number is zero, while the Boger fluid has $De = 0.78$, whereas the calculations were for $De = 0.001$ and 0.01.

In order to determine the effects of the depth ratio on the stability and growth rate, experiments were also attempted at depth ratios of 2.7, 3.6 and 4.9, *i.e.* with a thinner layer of the 0.5% PIB Boger fluid and a thicker layer of the 2.7% C14/H100 fluid. However, with the vane positioned vertically in the center of the channel, the large change in the velocities as the two fluids come together resulted in a large disturbance to the interface immediately downstream of the vane. This is shown in the series of single frames of the flow at the vane tip in figure 6.7 for $n = 4.9$ and $De = 0.69$. Figure 6.7(*a*) shows a smooth interface as the fluids come into contact, with the Boger fluid in the upper layer. However, in figure 6.7(*b*) the Newtonian fluid pushes back into the Boger fluid, until in figure 6.7(*c*) a large amplitude wave can be seen breaking. After this wave breaks, there is no longer a clearly definable interface between the two fluids, and measurements of the disturbance amplitudes further downstream are not possible. The cycle of the Newtonian fluid backing into the Boger fluid and forming a large amplitude wave repeats regularly with a period of ~50 s. This set of experiments shows the importance of adjusting the vane

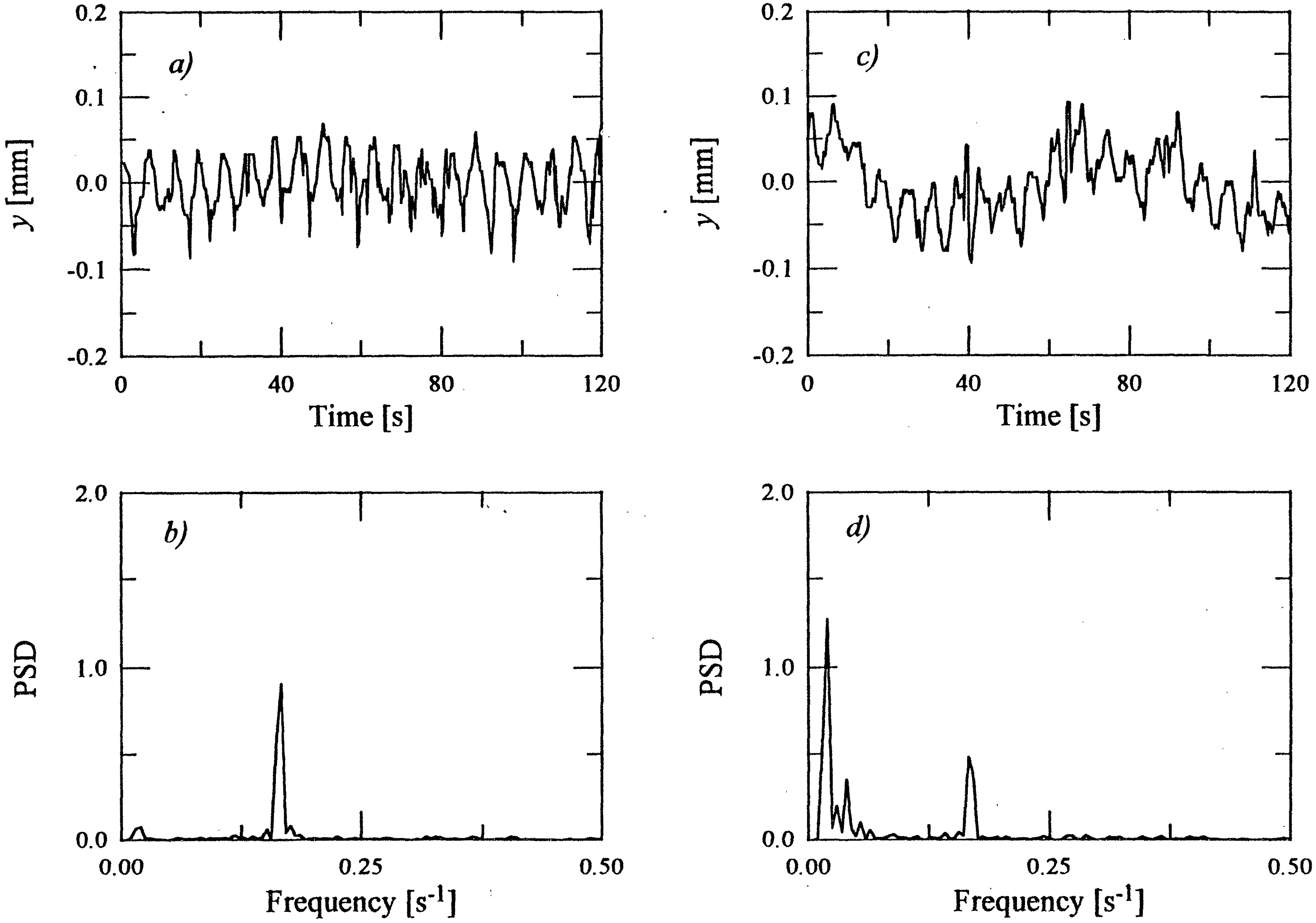

Figure 6.6 Position of the interface for a Boger fluid and a Newtonian fluid with $n = 1.1$, $m = 0.55$ and $De = 0.78$, and its FFT at downstream position of (*a-b*) 5 cm and (*c-d*) 20 cm.

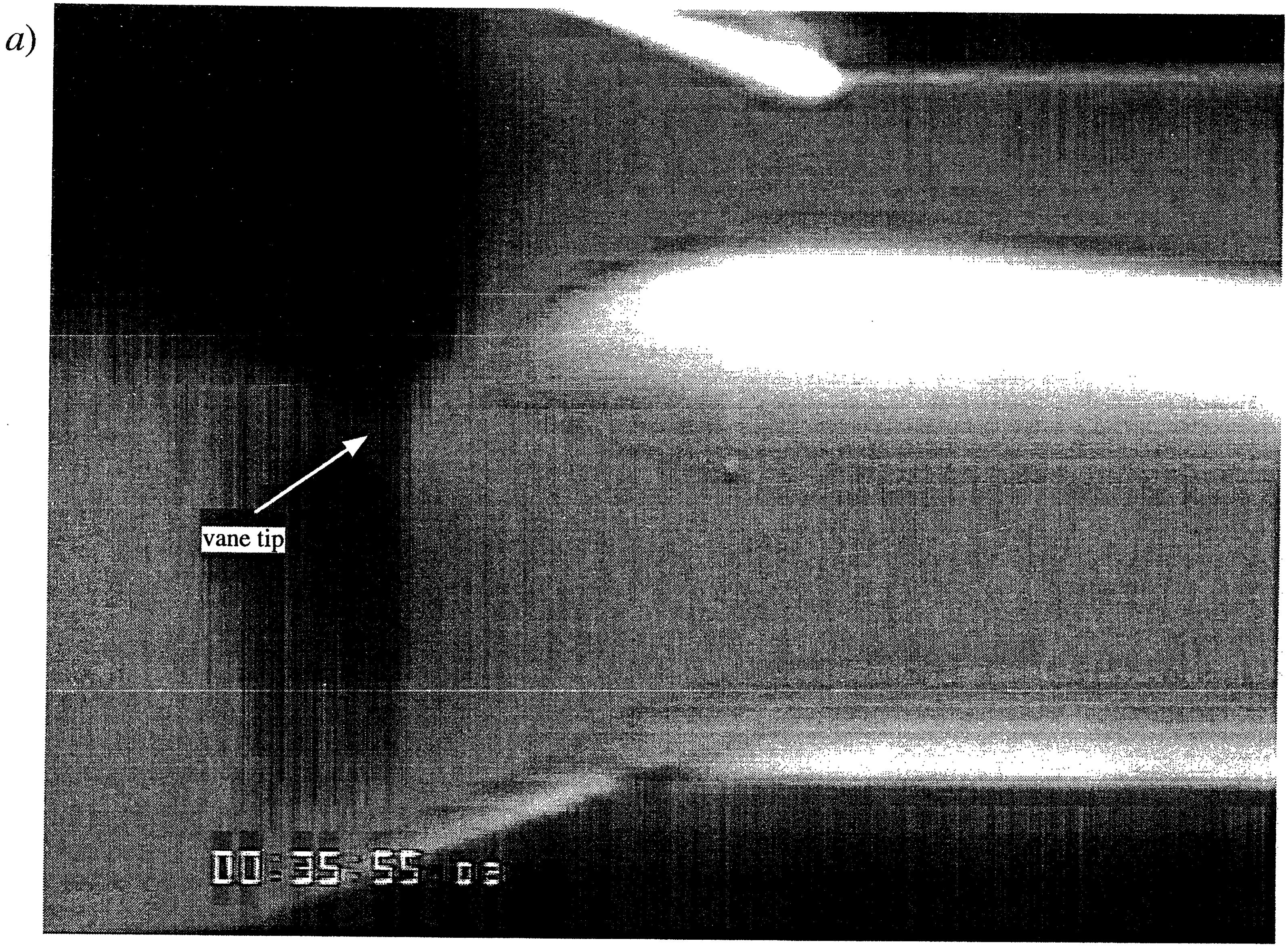

Figure 6.7 Series of images at the vane tip showing the formation of a large amplitude disturbance for a Boger fluid and a Newtonian fluid with $n = 4.9$, $m = 0.55$, $De = 0.69$ and no external forcing. The timer indicates hr:min:sec:sec/100.

b)

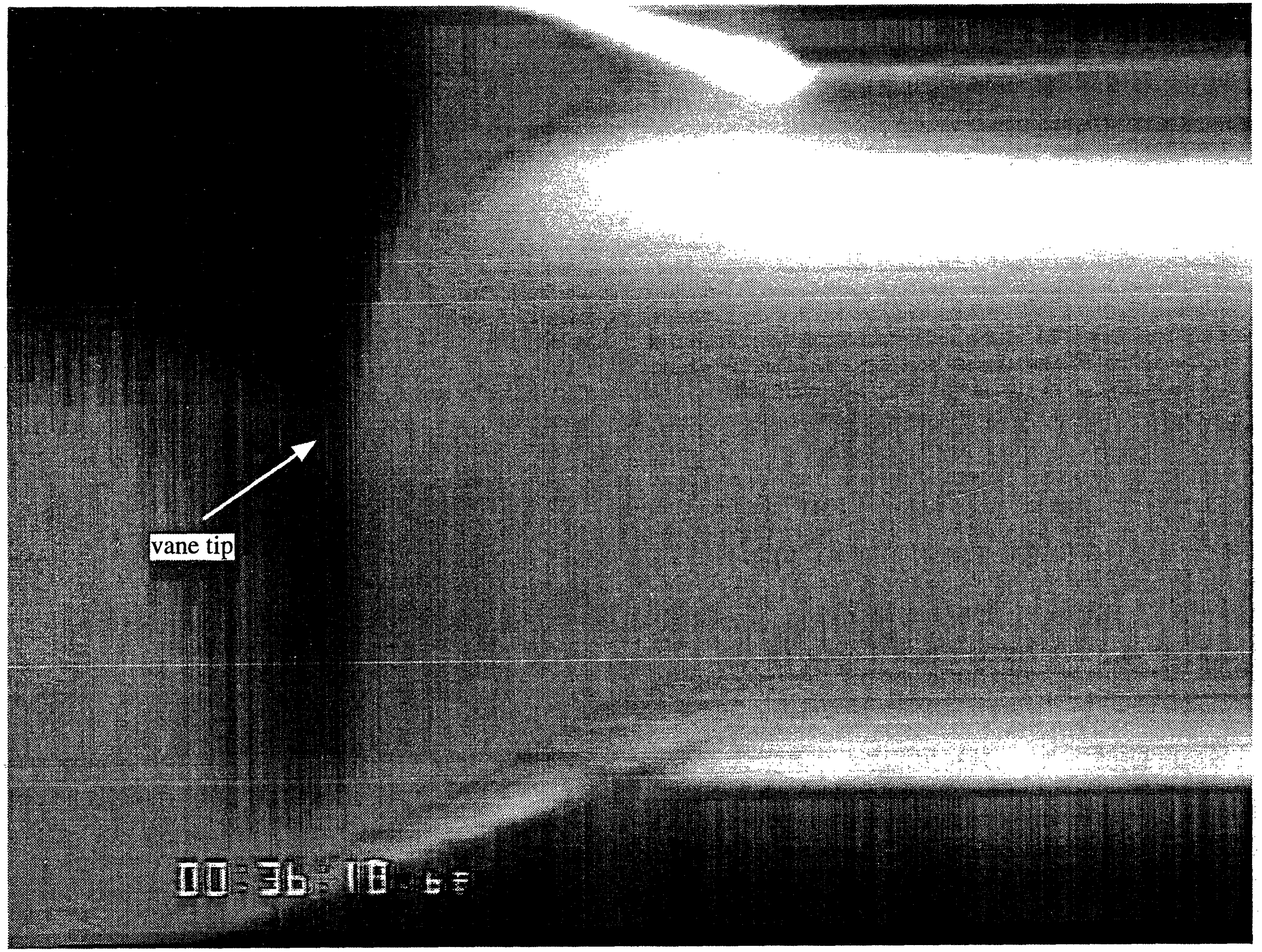

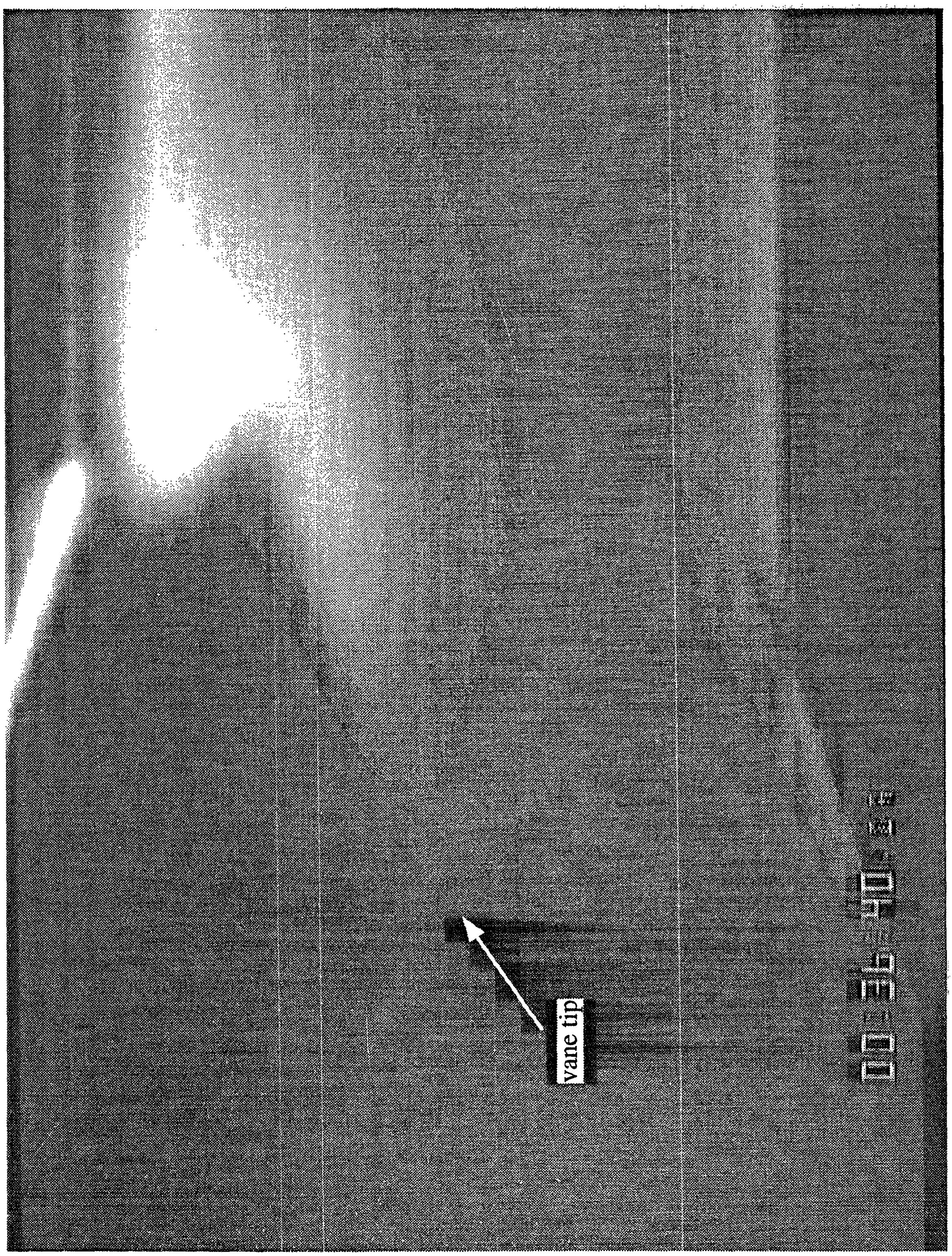

c)

position to establish a stable base flow before conducting experiments with the introduction of a controlled disturbance.

6.3 Two Boger Fluids

When the two Boger fluids were used with the more elastic 0.5% PIB fluid in the thinner layer, a disturbance was also introduced due to the mismatch in the fluid velocities without any external forcing, although in this case the initial amplitude was smaller, which allowed the growth rate of the disturbance to be measured. Three different depth ratios were studied, and in each case the flowrates of the fluids were adjusted so that the Deborah number based on the 0.5% PIB fluid remained constant at 0.81 and the frequency of the disturbance was 0.02 s^{-1} in each case, corresponding to $\alpha = 0.18$.

The effect of the depth ratio on the growth rate of the disturbance is shown in figure 6.8, which shows the growth of the PSD for $\alpha = 0.18$ for depth ratios of $n = 2.7$ and 4.9. For $n = 2.7$, the disturbance grows throughout the geometry at a growth rate $\alpha c_i = 2.6\times10^{-3}$, whereas for $n = 4.9$ the growth rate was $\alpha c_i = 0.017$ and exponential growth was observed only over the first 3 cm. At $x = 6$ cm, the amplitude was still growing at a much lower rate, and beyond 6 cm the wave broke and no further measurements of the interface could be obtained. These growth rates are of the same magnitude as those calculated by Su and Khomami (1992b) for two Oldroyd-B fluids, although their results were for a lower *De* and a greater difference in elasticity between the two fluids. The composition of the PIB/PB/C14 Boger fluids used in these experiments can be tailored to obtain fluids with a wide range of rheological properties. Future experiments can therefore attempt to more closely reproduce the conditions of Su and Khomami, but the purpose of the current experiments was to demonstrate the presence of an elastic instability for Boger fluids and ensure that the growth rates were in the expected range and could be measured in the test geometry. The flow was also unstable for $n = 3.6$, although in this case the initial amplitude and the growth rate were both large enough that the wave had broken within 1 cm downstream of the vane, which was not sufficiently far to allow the growth rate to be determined.

Because of the large growth rate of the $\alpha = 0.18$ disturbance, it was not possible to determine growth rates for other wavenumbers. Disturbances could still be introduced, but the larger amplitude of the $\alpha = 0.18$ disturbance made it more difficult to resolve their amplitude, and after the $\alpha = 0.18$ wave broke, no further measurements could be obtained. In order to explore the stability of a wider range of wavenumbers, it is therefore necessary

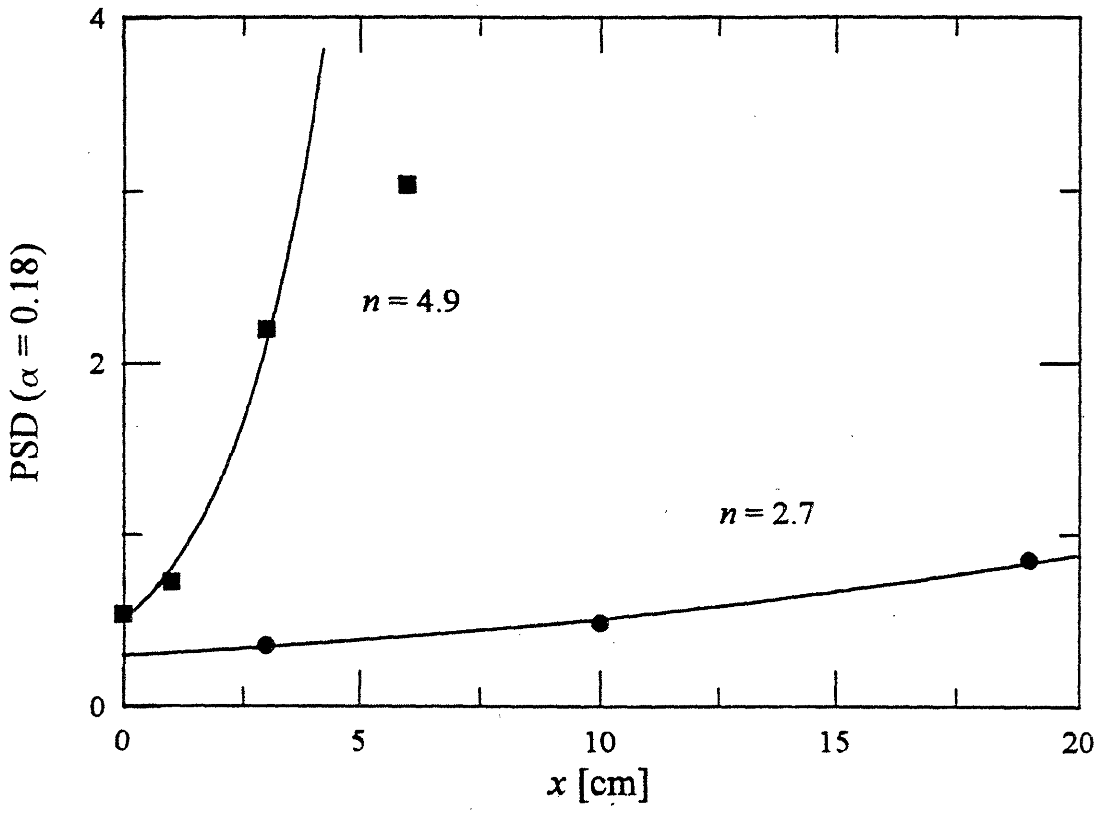

Figure 6.8 Amplitude of the power spectral density of the disturbance with wavenumber $\alpha = 0.18$ along the length of the channel for $m = 0.61$, $De = 0.81$ and $n =$ (■) 4.9 and (●) 2.7. The growth rate is $\beta_{PSD} = 0.480$ cm^{-1} for $n = 4.9$ and 0.055 cm^{-1} for $n = 2.7$.

to minimize any disturbance other than the one introduced by pulsing the flowrate of one of the fluids. Figure 6.7 suggests that the curvature of the interface due to the different depth ratios upstream and downstream of the vane leads to the $\alpha = 0.18$ disturbance, so the position of the vane was changed in order to achieve a more horizontal interface immediately downstream of the vane.

When the vane was repositioned so that the upstream fluid depth more closely corresponded to the downstream depth, no disturbance to the interface was caused near the vane, and the interface remained flat for $x \leq 5$ cm for $n = 2.4$, $De = 0.22$, and constant flowrates. In order to begin to determine the dependence of the growth rate on the wavenumber, experiments were conducted for these conditions with introduced disturbances of $\alpha = 2.9$, 0.97 and 0.29. The flow was stable for $\alpha = 2.9$, but the initial amplitude of the disturbance was too small and it had decayed by 1 cm downstream, so a growth rate could not be determined. Wavenumbers $\alpha = 0.97$ and 0.29 were also stable for these conditions, and their growth rates were found to be $\alpha c_i = -7.1\times10^{-3}$ and -8.7×10^{-3}, respectively. As seen above in §2.3, the neutral stability diagram is sensitive to the Deborah number and differences in elasticity between the two fluids, so it is difficult to extrapolate from the available linear stability diagrams to the conditions of the present experiments. However, the lower growth rate for $\alpha = 0.29$ at $De = 0.22$ compared to that of $\alpha = 0.18$ at $De = 0.81$ agrees qualitatively with the experimental results of Wilson and Khomami and the analysis of Su and Khomami, who found that the growth rate increased for a larger normal stress difference change across the interface. They also found the highest growth rate for $\alpha = O(1)$, although further experiments for more wavenumbers are required to determine the highest growth rate for the current system.

6.4 Future Work

The results presented above clearly demonstrate that the interfacial instability can be studied under a variety of conditions and that the growth rates are in the range that can be measured for this system. However, the limited data currently available can only show qualitative trends for the effects of elasticity and depth ratio, and only a single viscosity ratio has been studied. The relatively large growth rate obtained for two Newtonian fluids very close to the neutral stability curve suggests that further experiments should be conducted with Newtonian fluids in order to gauge the ability of the experimental system to determine accurately neutral stability boundaries. Further experiments also are required in order to determine the effects of elasticity and the viscosity ratio on the stability boundaries and growth rate. Disturbances can be introduced to the flow with a range of wavenumbers at a variety of depth ratios in order to produce a detailed stability diagram, and the Deborah number of the flow can be varied by either using different fluids or changing the flowrates of the fluids. Experiments with polymer melts have shown that chemical compatibility can affect the stability of the flow, and this can be investigated in this system by using Boger fluids based on polyacrylamide and corn syrup.

Chapter 7

Conclusions

This thesis has presented detailed experimental data describing viscoelastic flow instabilities in three different types of test flows that model more complex polymer processing systems. Stability diagrams have been constructed showing the sensitivity of the onset conditions to the flow geometry, and the spatial and temporal characteristics of the instabilities have also been shown. These results coupled with the linear stability analyses conducted in parallel provide a thorough description of the instabilities. The results also serve as a basis for comparison with linear stability analysis, and can help determine what level of detail is required in constitutive models to accurately predict elastic instabilities.

Previous studies of the instabilities in rotating flow geometries focused primarily on the dramatic rise in the torque and normal force associated the instability as measured in rheometry experiments, whereas the current work is concerned with determining the spatial and temporal characteristics of the secondary flow, as well as finding the onset conditions. Video imaging of the flow showed that the instability has the form of traveling spiral cells whose structure depends on the flow geometry and fluid, and digital image analysis gave quantitative measures of the structure and wavespeed.

In the parallel plate geometry, the cells formed Archimedean spirals with a constant radial wavelength. When the Deborah number is increased slightly above its critical value, a single azimuthal mode of the instability is observed for short times, where the azimuthal mode number is the number of nested spirals. The radial wavelength of the cells scaled with the separation between the plates, and decreased slightly for the 0.20 wt% PIB fluid with the higher solvent viscosity ratio. The vortices traveled outward at a constant velocity, which scaled with the separation and the rotation rate, and was also slightly lower for the 0.20 wt% fluid. The cells did not extend across the entire disk, but were confined to an annular region. The linear stability analysis of Öztekin and Brown using the Oldroyd-B model yielded good agreement for the wavespeed, wavelength and azimuthal structure, but predicted that the flow should be unstable for all values of the radius greater than a critical value that depended on the Deborah number. Calculations with the Chilcott-Rallison model showed that the incorporation of a shear-rate-dependent first normal stress coefficient resulted in the prediction of an outer radius beyond which the flow was restabilized. The shear rate increases linearly with radius in this geometry, so at larger radii there is a lower effective Deborah number, which leads to the restabilization.

The cone-and-plate geometry differs from the parallel-plate geometry in that it does not have characteristic length scale corresponding to the plate separation to scale the wavelength or wavespeed. Instead, the instability takes the form of a self-similar logarithmic spiral which fills the entire region between the two fixtures. The wavenumber decreased for both fluids for increasing cone angle, and the measured value agreed well with linear stability predictions using the Oldroyd-B model, although the observed magnitude of the wavespeed was smaller than predicted. Because the shear rate is uniform throughout the geometry, the vortices filled the entire gap, but the effect of shear rate on the instability was measured by changing the cone angle. As the cone angle decreases, the shear rate increases for a given rotation rate, which leads to stabilization of the flow for small angles. As with the parallel-plate geometry, the linear stability analysis for the Oldroyd-B model did not predict the restabilization, but did predict the critical wavenumber well. Calculations for single-mode Chilcott-Rallison and Giesekus models showed restabilization for small cone angles due to shear-thinning of the first normal stress coefficient, and very good quantitative agreement for the critical Deborah number was obtained for a four-mode Giesekus model.

LDV measurements of the wake instability for flow past a cylinder extended previous work by determining the effects of aspect ratio over a larger range, providing greater detail of the structure of the instability and considering the influence of the upstream flow on the instability. An axisymmetric stagnation flow was also studied, and no instability was observed.

Experiments with large cylinder radius to channel height aspect ratios showed that the onset of the instability does not depend on the shearing flow between the cylinder and the channel wall. In the rotational flows discussed above and in the Taylor-Coutte geometry, shearing across curved streamlines can cause elastic instabilities, although that mechanism does not seem to cause the instability for flow past a cylinder. For small aspect ratios, the Deborah number based on the cylinder radius increased as the aspect ratio decreased, as predicted by a linear stability analysis of the planar extensional flow, although the critical Deborah number was lower than that observed experimentally. Even for an aspect ratio of 0.05, the channel walls affect the strain rate in the downstream stagnation region.

The structure of the instability was characterized in terms of its wavelength and spatial extent. The wavelength of the instability did not scale with any characteristic length of the geometry, although the ratio of the wavelength to the cylinder radius increased as the aspect ratio decreased, and for intermediate values of the aspect ratio, the wavelength was nearly equal to the cylinder radius. This was lower than previously reported values, but an experiment designed to introduce a longer wavelength showed that there was a strong selection of the shorter wavelength. The linear stability analysis predicted a larger value of the wavelength that increased with decreasing aspect ratio over the range of the experiments, but reached a plateau for even smaller aspect ratios. The instability was shown to cause fluctuations in the streamwise velocity not only in the stagnation region, but also near the cylinder upstream of the stagnation point, and the upstream extent increased with increasing Deborah number. This was shown to be due to the fact that the downstream velocity was not symmetric about the centerplane, and that the position of the minimum velocity alternated about the centerplane with the same wavelength as the velocity fluctuations.

Experiments with a planar divider with a rounded end had the same downstream stagnation flow as the cylinder, but the upstream flow was modified to be fully developed shearing flow. A similar instability was observed for this geometry, although the details of the structure were slightly different. The axisymmetric analog of the planar divider is a rod with a rounded end in a tube, and measurements of the streamwise velocity in this geometry were both temporally and spatially stable, suggesting that flow past a sphere is also stable.

Whereas the rotational flow and stagnation flows have been thoroughly characterized both experimentally and theoretically, the experimental study of the interfacial instability for superposed plane Poiseuille flow in only in its initial stage. Results are shown that demonstrate the ability to obtain the position of the interface using image analysis, and to calculate growth rates of disturbances. For the rotating flows, the temporal characteristics of only the fastest growing spiral mode could be studied, and for flow past a cylinder, introducing a wavelength other than the one selected by the flow required construction of a cylinder with a radius that varied along its axis. In contrast, a wide range of disturbance wavenumbers can be introduced to this system simply by sinusoidally varying the flowrates of one of the fluids. This system therefore has the potential of providing even more detailed information about the instability, leading to neutral stability diagrams in terms of the fluid properties, the depth ratio and the wavenumber.

Chapter 8

References

Acharya, A., Mashelkar, R. A. and Ulbrecht, J. 1976 Flow of Inelastic and Viscoelastic Fluids past a Sphere; I. Drag Coefficient in Creeping and Boundary Layer Flows, *Rheol. Acta* **15**, 454-470.

Achenbach, E. 1972 Experiments on the Flow past Spheres at Very High Reynolds Numbers, *J. Fluid Mech.* **54**(3), 565-575.

Anturkar, N. R., Papanastasiou, T. C. and Wilkes, J. O. 1990 Linear Stability Analysis of Multilayer Plane Poiseuille Flow, *Phys. Fluids A* **2**(4), 530-541.

Baaijens, F. P. T., Baaijens, H. P. W., Peters, G. W. M. and Meijer, H. E. H. 1994 An Experimental and Numerical Investigation of a Viscoelastic Flow around a Cylinder, *J. Rheol.* **38**(2), 351-376.

Batchelor, G. K. 1967 *An Introduction to Fluid Mechanics*, Cambridge University Press, Cambridge.

Becker, L. E., McKinley, G. H., Rasmussen, H. K. and Hassager, O. 1994 The Unsteady Motion of a Sphere in a Viscoelastic Fluid, *J. Rheol.* **38**, 377-403.

Bird, R. B., Armstrong, R. C. and Hassager, O. 1987a *Dynamics of Polymeric Liquids. Volume 1: Fluid Mechanics,* 2nd Edition, Wiley Interscience, New York.

Bird, R. B., Curtiss, C. F., Armstrong, R. C. and Hassager, O. 1987b *Dynamics of Polymeric Liquids. Volume 2: Kinetic Theory,* 2nd Edition, Wiley Interscience, New York.

Bisgaard, C. 1983 Velocity Fields around Spheres and Bubbles Investigated by Laser-Doppler Anemometry, *J. Non-Newtonian Fluid Mech.* **12**, 283-302.

Boger, D. V. 1977/78 A Highly Elastic Constant-viscosity Fluid, *J. Non-Newtonian Fluid Mech.* **3**, 87-91.

Boger, D. V. and Walters, K. 1993 *Rheological Phenomena in Focus*, Elsevier, Amsterdam.

Bohlin, T. 1960 *Trans. Roy. Inst. Technol.* **155**.

Broadbent, J. M. and Mena, B. 1974 Slow Flow of an Elastico-viscous Fluid past Cylinders and Spheres, *Chem. Eng. J.* **8**, 11-19.

Brown, R. A. and McKinley, G. H. 1994 Report on the VIIIth International Workshop on Numerical Methods in Viscoelastic Flows, *J. Non-Newtonian Fluid Mech.* **52**, 407-413.

Bush, M. B. 1993 The Stagnation Flow behind a Sphere, *J. Non-Newtonian Fluid Mech.* **49**, 103-122.

Bush, M. B. 1994 On the Stagnation Flow behind a Sphere in a Shear-thinning Viscoelastic Liquid, *J. Non-Newtonian Fluid Mech.* **55**, 229-247.

Byars, J. A. 1992 *Viscoelastic Flow past Axisymmetric Obstacles*, Ph. D. Thesis Proposal, MIT.

Byars, J. A., Öztekin, A., Brown, R. A. and McKinley, G. H. 1994 Spiral Instabilities in the Flow of Highly Elastic Fluids between Rotating Parallel Disks, *J. Fluid Mech* **271**, 173-218.

Carew, E. O. A. and Townsend, P. 1991 Slow Viscoelastic Flow past a Cylinder in a Rectangular Channel, *Rheol. Acta* **30**, 58-64.

Caswell, B. and Schwarz, W. H. 1962 The Creeping Motion of a Non-Newtonian Fluid past a Sphere, *J. Fluid Mech.* **13**, 417-426.

Chhabra, R. P. and Uhlherr, P. H. T. 1988 The Influence of Fluid Elasticity on Wall Effects for Creeping Sphere Motion in Cylindrical Tubes, *Can. J. Chem. Eng.* **66**, 154-157.

Chhabra, R. P., Uhlherr, P. H. T. and Boger, D. V. 1980 The Influence of Elasticity on the Drag Coefficient for Creeping Flow around a Sphere, *J. Non-Newtonian Fluid Mech.* **6**, 187-199.

Chiao, S.-M. F. and Chang, H.-C. 1990 Instability of a Criminale-Ericksen-Filbey Fluid in a Disk-and-cylinder System, *J. Non-Newtonian Fluid Mech.* **36**, 361-394.

Chilcott, M. D. and Rallison, J. M. 1988 Creeping Flow of Dilute Polymer Solutions past Cylinders and Spheres, *J. Non-Newtonian Fluid Mech.* **29**, 381-432.

Chmielewski, C. and Jayaraman, K. 1993 Elastic Instability in Crossflow of Polymer Solutions through Periodic Arrays of Cylinders, *J. Non-Newtonian Fluid Mech.* **48**, 285-301.

Chmielewski, C., Nichols, K. L. and Jayaraman, K. 1990 A Comparison of the Drag Coefficients of Spheres Translating in Corn-syrup-based and Polybutene-based Boger Fluids, *J. Non-Newtonian Fluid Mech.* **35**, 37-49.

Clift, R., Grace, J. R. and Weber, M. E. 1978 *Bubble, Drops, and Particles*, Academic Press, New York.

Crewther, I., Huilgol, R. R. and Jozsa, R. 1991 Axisymmetric and Non-axisymmetric Flows of a Non-Newtonian Fluid between Coaxial Rotating Disks, *Phil. Trans. R. Soc. Lond. A* **337**, 467-495.

Davis, P. J. 1993 *Spirals: From Theodorus to Chaos,* A.K. Peters, Wellesley, MA.

Dhahir, S. A. and Walters, K. 1989 On Non-Newtonian Flow past a Cylinder in a Confined Flow, *J. Rheol.* **33**(6), 781-804.

Durst, F., Melling, A. and Whitelaw, J. H. 1981 *Principles and Practice of Laser-Doppler Anemometry,* Second Edition, Academic Press, New York.

Evans, A.R., Shaqfeh, E.S.G. and Frattini, P.L. 1994 Observations of Polymer Conformation during Flow through a Fixed Fiber Bed, *J. Fluid Mech.* **281**, 319-356.

Faxén, O. H. 1946 Forces Exerted on a Rigid Cylinder in a Viscous Fluid between Two Parallel Fixed Planes, *Proc. Roy. Swedish Acad. Eng. Sci.* **187**, 1-13.

Ferry, J. D. 1980 *Viscoelastic Properties of Polymers,* Third Edition, Wiley-Interscience, New York.

Flory, P. J. 1953 *Principles of Polymer Chemistry*, Cornell University Press, Ithaca.

Georgiou, G., Momani, S., Crochet, M. J. and Walters, K. 1991 Newtonian and Non-Newtonian Flow in a Channel Obstructed by an Antisymmetric Array of Cylinders, *J. Non-Newtonian Fluid Mech.* **40**, 231-260.

Giesekus, H. 1963 Some Secondary Flow Phenomena in General Viscoelastic Fluids, *Proc. 4th Int. Cong. Rheology*, Vol. 1, Brown Univ., Wiley, 249-266.

Giesekus, H. 1965 Sekundärströmungen in Viskoelastischen Flussigkeiten bei Stationärer und Periodischer Bewegung, *Rheol. Acta* **4**, 85-101.

Giesekus, H. 1982 A Simple Constitutive Equation for Polymer Fluids Based on the Concept of Deformation-dependent Tensorial Mobility, *J. Non-Newtonian Fluid Mech.* **11**, 69-109.

Griffiths, D. F., Jones, D. T. and Walters, K. 1969 A Flow Reversal Due to Edge Effects, *J. Fluid Mech.* **36**(1), 161-175.

Griffiths, D. F. and Walters, K. 1970 On Edge Effects in Rheometry, *J. Fluid Mech.* **42**(2), 379-399.

Haberman, W. L. and Sayer, R. M. 1958 *David W. Taylor Model Basin Report* no. 1143, Washington.

Han, C. D., Kim, Y. J. and Chim, H. B. 1984 Rheological Investigation of Interfacial Instability in Two-layer Flat-film Coextrusion, *Polym. Eng. Reviews* **4**(3), 177-201.

Han, C. D. and Shetty, R. 1978 Studies on Multilayer Film Coextrusion II. Interfacial Instability in Flat Film Coextrusion, *Polym. Eng. Sci.* **18**(3), 180-186.

Happel, J. and Brenner, H. 1973 *Low Reynolds Number Hydrodynamics*, Martinus Nijhoff, Dordrecht.

Harlen, O. G. 1990 High-Deborah-number Flow of a Dilute Polymer Solution past a Sphere Falling along the Axis of a Cylindrical Tube, *J. Non-Newtonian Fluid Mech.* **37**, 157-173.

Harris, O. J. and Rallison, J. M. 1994 Instabilities of a Stagnation Point Flow of a Dilute Polymer Solution, *J. Non-Newtonian Fluid Mech.* **55**, 59-90.

Hassager, O. 1979 Negative Wake behind Bubbles in Non-Newtonian Liquids, *Nature* **279**, 402-403.

Hassager, O. and Bisgaard, C. 1983 A Lagrangian Finite Element Method for the Simulation of Flow of Non-Newtonian Liquids, *J. Non-Newtonian Fluid Mech.* **12**, 153-164.

Heuser, G. and Krause, E. 1979 The Flow Field of Newtonian Fluids in Cone-and-plate Rheometers with Small Gap Angles, *Rheol. Acta* **18**(5), 531-564.

Hill, C. T. 1972 Nearly Viscometric Flow in the Disk and Cylinder System. II: Experimental, *Trans. Soc. Rheol.* **16**(2), 213-245.

Hooper, A. P. and Grimshaw, R. 1985 Nonlinear Instability at the Interface between Two Viscous Fluids, *Phys. Fluids* **28**(1), 37-45.

Hudson, N. E. and Ferguson, J. 1990 The Shear Flow Properties of M1, *J. Non-Newtonian Fluid Mech.* **35**, 159-168.

Hutton, J. F. 1969 Fracture and Secondary Flow of Elastic Liquids, *Rheol. Acta* **8**(1), 54-59.

Jackson, J. P., Walters, K. and Williams, R. W. 1984 A Rheometrical Study of Boger Fluids, *J. Non-Newtonian Fluid Mech.* **14**, 173-188.

Ji, Z., Rajagopal, K. R. and Szeri, A. Z. 1990 Multiplicity of Solutions in Von Kármán Flows of Viscoelastic Fluids, *J. Non-Newtonian Fluid Mech.* **36**, 1-25.

Jones, D. M. and Walters, K. 1989 The Behaviour of Polymer Solutions in Extension-dominated Flows, with Applications to Enhanced Oil Recovery, *Rheol. Acta* **28**, 482-498.

Joo, Y. L. and Shaqfeh, E. S. G. 1992 A Purely Elastic Instability in Dean and Taylor-Dean Flow, *Phys. Fluids A* **4**(3), 524-543.

Joo, Y. L. and Shaqfeh, E. S. G. 1994 Observations of Purely Elastic Instabilities in the Taylor-Dean Flow of a Boger Fluid, *J. Fluid Mech.* **262**, 27-73.

Kao, T. W. and Park, C. 1972 Experimental Investigation of the Stability of Channel Flows Part 2. Two-layered Cocurrent Flow in a Rectangular Channel, *J. Fluid Mech.* **52**, 401-423.

Kerr, O. S. and Dold, J. W. 1994 Periodic Steady Vortices in a Stagnation-point Flow, *J. Fluid Mech.* **276**, 307-325.

Khomami, B. 1990a Interfacial Stability and Deformation of Two Stratified Power-law Fluids in Plane Poiseuille Flow Part I. Stability Analysis, *J. Non-Newtonian Fluid Mech.* **36**, 289-303.

Khomami, B. 1990b Interfacial Stability and Deformation of Two Stratified Power-law Fluids in Plane Poiseuille Flow Part II. Interface Deformation, *J. Non-Newtonian Fluid Mech.* **37**, 19-36.

Khomami, B. and Wilson, G. M. 1995 An Experimental Investigation of Interfacial Instability in Superposed Flow of Viscoelastic Fluids in a Converging/Diverging Channel Geometry, *J. Non-Newtonian Fluid Mech.* **58**, 47-65.

Kim, I. and Pearlstein, A. J. 1990 Stability of the Flow past a Sphere, *J. Fluid Mech.* **211**, 73-93.

Kobayashi, R., Kohama, Y. and Takamadate, C. 1980 Spiral Vortices in Boundary Layer Transition Regime on a Rotating Disk, *Acta Mech.* **35**, 71-82.

Kocherov, V. L., Lukach, Y. L., Sporyagin, E. A. and Vinagradov, G. V. 1973 Flow of Polymer Melts in a Disk-type Extruder and in Rotational Devices of the 'Cone-plate' and 'Plate-plate' Type, *Polymer Engng Sci.* **13**, 194-201.

Kulicke, W. M. and Porter, R. S. 1979 Irregularities in Steady Flow for Non-Newtonian Fluids between Cone and Plate, *J. Applied Polym. Sci.* **23**, 953-965.

Lagnado, R. R. and Leal, L. G. 1990 Visualization of Three-dimensional Flow in a Four-roll Mill, *Exps. Fluids* **9**, 25-32.

Lagnado, R. R., Phan-Thien, N. and Leal, L. G. 1984 The Stability of Two-dimensional Linear Flows, *Phys. Fluids* **27**(5), 1094-1101.

Lagnado, R. R., Phan-Thien, N. and Leal, L. G. 1985 The Stability of Two-dimensional Linear Flows of an Oldroyd-type Fluid, *J. Non-Newtonian Fluid Mech.* **18**, 25-59.

Lamb, H. 1932 *Hydrodynamics*, Sixth Edition, Cambridge University Press, Cambridge.

Larson, R. G. 1992 Instabilities in Viscoelastic Flows, *Rheol. Acta* **31**, 213-263.

Larson, R. G., Muller, S. J. and Shaqfeh, E. S. G. 1994 The Effect of Fluid Rheology on the Elastic Taylor-Couette Flow Instability, *J. Non-Newtonian Fluid Mech.* **51**, 195-225.

Larson, R. G., Shaqfeh, E. S. G. and Muller, S. J. 1990 A Purely Elastic Instability in Taylor-Couette Flow, *J. Fluid Mech.* **218**, 573-600.

Laun, H. M. and Hingmann, R. 1990 Rheological Characterization of the Fluid M1 and of Its Components, *J. Non-Newtonian Fluid Mech.* **35**, 137-157.

Lee, C. S., Tripp, B. C. and Magda, J. J. 1992 Does N_1 or N_2 Control the Onset of Edge Fracture, *Rheol. Acta* **31**, 306-398.

Leslie, F. M. and Tanner, R. I. 1961 The Slow Flow of a Viscoelastic Liquid past a Sphere, *Quart. J. Mech. Appl. Math.* **14**, 36-48.

Liu, A. W. 1995 *personal communication.*

Lunsmann, W. J., Genieser, L. H., Brown, R. A. and Armstrong, R. C. 1993 Finite Element Analysis of Steady Viscoelastic Flow around a Sphere: Calculations with Constant Viscosity Models, *J. Non-Newtonian Fluid Mech.* **48**, 63-99.

Magda, J. J. and Larson, R. G. 1988 A Transition Occurring in Ideal Elastic Liquids During Shear Flow, *J. Non-Newtonian Fluid Mech.* **30**, 1-19.

Magda, J. J., Lou, J., Baek, S.-G. and DeVries, K. L. 1991 Second Normal Stress Difference of a Boger Fluid, *Polymer* **32**(11), 2000-2009.

Malik, M. R. 1986 The Neutral Curve for Stationary Disturbances in Rotating-disk Flow, *J. Fluid Mech.* **164**, 275-287.

Manero, O. and Mena, B. 1981 On the Slow Flow of Viscoelastic Liquids past a Circular Cylinder, *J. Non-Newtonian Fluid Mech.* **9**, 379-387.

McKinley, G. H., Armstrong, R. C. and Brown, R. A. 1993 The Wake Instability in Viscoelastic Flow past Confined Circular Cylinders, *Phil. Trans. R. Soc. Lond. A* **344**, 265-304.

McKinley, G. H., Byars, J. A., Brown, R. A. and Armstrong, R. C. 1991a Observations on the Elastic Instability in Cone-and-plate and Parallel-plate Flows of a Polyisobutylene Boger Fluid, *J. Non-Newtonian Fluid Mech.* **40**, 201-229.

McKinley, G. H., Öztekin, A., Byars, J. A. and Brown, R. A. 1995 Self-similar Spiral Instabilities in Elastic Flows between a Cone and a Plate, *J. Fluid Mech.* **285**, 123-164.

McKinley, G. H., Raiford, W. P., Brown, R. A. and Armstrong, R. C. 1991b Nonlinear Dynamics of Viscoelastic Flow in Axisymmetric Abrupt Contractions, *J. Fluid Mech.* **223**, 411-456.

Mena, B. and Caswell, B. 1974 Slow Flow of an Elastic-viscous Fluid past an Immersed Body, *Chem. Eng. J.* **8**, 125-134.

Mena, B., Manero, O. and Leal, L. G. 1987 The Influence of Rheological Properties on the Slow Flow past Spheres, *J. Non-Newtonian Fluid Mech.* **26**, 247-275.

Merzkirch, W. 1987 *Flow Visualization,* Second Edition, Academic Press, London.

Muller, S. J., Shaqfeh, E. S. G. and Larson, R. G. 1993 Experimental Studies of the Onset of Oscillatory Instability in Viscoelastic Taylor-Couette Flow, *J. Non-Newtonian Fluid Mech.* **46**, 315-330.

Müller, A. J., Odell, J. A. and Keller, A. 1988 Elongational Flow and Rheology of Monodisperse Polymers in Solution, *J. Non-Newtonian Fluid Mech.* **30**, 99-118.

Northey, P. N., Armstrong, R. C. and Brown, R. A. 1992 Finite-amplitude Time-periodic States in Viscoelastic Taylor-Couette Flow Described by the UCM Model, *J. Non-Newtonian Fluid Mech.* **42**, 117-139.

Olagunju, D. O. 1993 Asymptotic Analysis of the finite Cone-and-plate Flow of a Non-Newtonian Fluid, *J. Non-Newtonian Fluid Mech.* **50**, 289-305.

Olagunju, D. O. 1994 Effect of Free Surface and Inertia on Viscoelastic Parallel Plate Flow, *J. Rheol.* **38**(1), 151-168.

Olagunju, D. O. and Cook, L. P. 1992 Secondary Flows in Cone and Plate Flow of an Oldroyd-B Fluid, *J. Non-Newtonian Fluid Mech.* **46**, 29-47.

Oldroyd, J. G. 1950 On the Formulation of Rheological Equations of State, *Proc. Roy. Soc.* **A200**, 523-541.

Öztekin, A. and Brown, R. A. 1993 Instability of a Viscoelastic Fluid between Rotating Parallel Disks: Analysis for the Oldroyd-B Fluid, *J. Fluid Mech.* **255**, 473-502.

Öztekin, A., Brown, R. A, and McKinley, G. H. 1994 Quantitative Prediction of the Viscoelastic Instability in Cone-and-plate Flow of a Boger Fluid Using a Multi-mode Giesekus Model, *J. Non-Newtonian Fluid Mech.* **54**, 351-377.

Öztekin, A., Byars, J. A., Liu, A. W., Armstrong, R. C. and Brown, R. A. 1995 Three-dimensional Wake Instability in Viscoelastic Flow past a Cylinder: Theory and Experiment, in preparation.

Peitgen, H.-O., Jürgens, H. and Saupe, D. 1992 *Chaos and Fractals*, Springer-Verlag, New York.

Petrie, C.J.S. and Denn, M. M. 1976 Instabilities in Polymer Processing, *A.I.Ch.E. J.* **22**(2), 209-235.

Phan-Thien, N. 1983 Coaxial-Disk Flow of an Oldroyd-B Fluid: Exact Solution and Stability, *J. Non-Newtonian Fluid Mech.* **13**, 325-340.

Phan-Thien, N. 1985 Cone and Plate Flow of the Oldroyd-B Fluids is Unstable, *J. Non-Newtonian Fluid Mech.* **17**, 37-44.

Pinarbasi, A. and Liakopoulos, A. 1995 Stability of Two-layer Poiseuille Flow of Carreau-Yasuda and Bingham-like Fluids, *J. Non-Newtonian Fluid Mech.* **57**, 227-241.

Press, W. H., Flannery, B. P., Teukolsky, S. A. and Vetterling, W. T. 1986 *Numerical Recipes*, Cambridge University Press, Cambridge.

Prilutski, G., Gupta, R. K., Sridhar, T. and Ryan, M. E. 1983 Model Viscoelastic Liquids, *J. Non-Newtonian Fluid Mech.* **12**, 233-241.

Quinzani, L. M. 1991 *Birefringence Studies of Entry Flows of Concentrated Polymer Solutions*, Ph. D. Thesis, MIT.

Quinzani, L. M., McKinley, G. H., Brown, R. A. and Armstrong, R. C. 1990 Modeling the Rheology of Polyisobutylene Solutions, *J.Rheol* **34**(5), 705-748.

Renardy, Y. Y. 1995 Weakly Nonlinear Behavior of Periodic Disturbances in Two-layer Channel Flow of Upper-convected Maxwell Liquids, *J. Non-Newtonian Fluid Mech.* **56**, 101-126.

Riddle, M. J., Narvaez, C. and Bird, R. B. 1977 Interactions between Two Spheres Falling along Their Line of Centers in a Viscoelastic Fluid, *J. Non-Newtonian Fluid Mech.* **2**, 23-35.

Russ, J. C. 1992 *The Image Processing Handbook*, CRC Press, Boca Raton.

Satrape, J. V. and Crochet, M. J. 1994 Numerical Simulation of the Motion of a Sphere in a Boger Fluid, *J. Non-Newtonian Fluid Mech.* **55**, 91-111.

Schrenk, W. J., Bradley, N. L., Alfrey, T. and Maack, H. 1978 Interfacial Flow Instability in Multilayer Coextrusion, *Polym. Eng. Sci.* **18**(8), 620-623.

Sdougos, H. P., Bussolari, S. R. and Dewey, C. F. 1984 Secondary Flow and Turbulence in a Cone-and-plate Device, *J. Fluid Mech.* **138**, 379-404.

Shaqfeh, E. S. G., Muller, S. J. and Larson, R. G. 1992 The Effects of Gap Width and Dilute Solution Properties on the Viscoelastic Taylor-Couette Instability, *J. Fluid Mech.* **235**, 285-317.

Sigli, D. and Coutanceau, M. 1977 Effect of Finite Boundaries on the Slow Laminar Isothermal Flow of a Viscoelastic Fluid around a Spherical Object, *J. Non-Newtonian Fluid Mech.* **2**, 1-21.

Steiert, P. and Wolff, C. 1990 Rheological Properties of a Polyisobutylene in a Kerosene/Polybutene Mixture in Simple Shear Flow, *J. Non-Newtonian Fluid Mech.* **35**, 189-196.

Su, Y. Y. and Khomami, B. 1992a Purely Elastic Interfacial Instabilities in Superposed Flow of Polymeric Fluids, *Rheol. Acta* **31**, 413-420.

Su, Y.-Y. and Khomami, B. 1992b Interfacial Stability of Multilayer Viscoelastic Fluids in Slit and Converging Channel Die Geometries, *J. Rheol.* **36**(2), 357-387.

Sugeng, F. and Tanner, R. I. 1986 The Drag on Spheres in Viscoelastic Fluids with Significant Wall Effects, *J. Non-Newtonian Fluid Mech.* **20**, 281-292.

Tanner, R. I. and Keentok, M. 1983 Shear Fracture in Cone-plate Rheometry, *J. Rheol* **27**(1), 47-57.

Tirtaatmadja, V. and Sridhar, T. 1993 A Filament Stretching Device for Measurement of Extensional Viscosity, *J. Rheol* **37**(6), 1081-1102.

Tirtaatmadja, V., Uhlherr, P. H. T. and Sridhar, T. 1990 Creeping Motion of Spheres in Fluid M1, *J. Non-Newtonian Fluid Mech.* **35**, 327-337.

Townsend, P. 1980 A Numerical Simulation of Newtonian and Viscoelastic Flow past Staionary and Rotating Cylinders, *J. Non-Newtonian Fluid Mech.* **6**, 219-243.

Townsend, P. 1984 On the Numberical Simulation of Two-dimensional Time-dependent Flows of Oldroyd Fluids Part 1: Basic Method and Preliminary Results, *J. Non-Newtonian Fluid Mech.* **14**, 265-278.

Turian, R. M. 1972 Perturbation Solution of the Steady Newtonian Flow in the Cone-and-plate and Parallel-plate Systems, *Ind. Eng. Chem. Fund.* **11**, 361-368.

Ultman, J. S. and Denn, M. M. 1971 Slow Viscoelastic Flow past Submerged Objects, *Chem. Eng. J.* **2**, 81-89.

Van Dyke, M. 1982 *An Album of Fluid Motion*, Parabolic, Stanford.

Walsh, W. P. 1987 On the Flow of a Non-Newtonian Fluid between Rotating Co-axial Disks, *Z.A.M.P.* **38**, 495-511.

Walters, K. and Waters, N. D. 1968 "On the Use of a Rheogoniometer. Part I - Steady Shear", Polymer Systems: Deformation and Flow, , A. D. Wetton and A. Whorlow (eds.).

Wilson, G. M. and Khomami, B. 1992 An Experimental Investigation of Interfacial Instabilities in Multilayer Flow of Viscoelastic Fluids Part I: Incompatible Polymer Systems, *J. Non-Newtonian Fluid Mech.* **45**, 355-384.

Wilson, G. M. and Khomami, B. 1993a An Experimental Investigation of Interfacial Instabilities in Multilayer Flow of Viscoelastic Fluids II: Elastic and Nonlinear Effects in Incompatible Polymer Systems, *J. Rheol.* **37**(2), 315-339.

Wilson, G. M. and Khomami, B. 1993b An Experimental Investigation of Interfacial Instabilities in Multilayer Flow of Viscoelastic Fluids III. Compatible Polymer Systems, *J. Rheol.* **37**(2), 341-354.

Yiantsios, S. G. and Higgins, B. G. 1988 Linear Stability of Plane Poiseuille Flow of Two Superposed Fluids, *Phys. Fluids* **31**(11), 3225-3238.

Yih, C.-S. 1967 Instability Due to Viscous Stratification, *J. Fluid Mech.* **27**, 337-352.

Yu, H. S. and Sparrow, E. M. 1969 Experiments on Two-component Stratified Flow in a Horizontal Duct, *J. Heat Transfer* **91**, 51-58.

Zana, E., Tiefenbruck, G. and Leal, L. G. 1975 A Note on the Creeping Motion of a Viscoelastic Fluid past a Sphere, *Rheol. Acta* **14**, 891-898.

Zandbergen, P. J. and Dijkstra, D. 1987 Von Kármán Swirling Flows, *Ann. Rev. Fluid Mech.* **19**, 465-491.